UNIVERSITÀ
DEGLI STUDI
DI PADOVA

Dipartimento di Scienze Chimiche
_____

SCUOLA DI DOTTORATO DI RICERCA IN SCIENZA E INGEGNERIA DEI MATERIALI
XXVI ciclo

PhD Thesis

NANOFABRICATION AND DEVELOPMENT
OF SURFACE PLASMON RESONANCE PLATFORMS
FOR SENSING APPLICATIONS

Director: Ch. mo Prof. Gaetano Granozzi

Supervisor: Ch. mo Prof. Filippo Romanato

Ph. D. Student: Agnese Sonato

Abstract

In recent decades, surface plasmon resonance has known a growing interest in the realization of miniaturized devices for label-free sensing applications due to the need of increasing the sensitivity of the sensor and limiting the consumption of material.

This work is aimed to the realization of plasmonic nanostructures that can be applied to different sensoristic fields in order to create a starting point for the realization of miniaturized sensors for a wide range of applications. In this context a careful study of geometry and materials suitable for creating the starting plasmonic platforms (i.e. gold sinusoidal gratings) was performed and a characterization method has been optimized. Subsequently a manufacturing strategy that would allow to obtain a large number of versatile substrates in a short time and in a cheap way was designed. Thus by combining interference lithography and soft lithography the required plasmonic substrates were realized and characterized by varying the azimuthal rotation of the grating. The substrates were tested in different application fields: the detection of *M. tuberculosis* DNA using PNA probes, the detection of cystic fibrosis DNA using DNA probes, the detection of explosive trace and the detection of *L. pneumophila* bacteria. The reached optimization and control of the sensing experiment and plasmonic surface preparation procedures, and the obtained results, have shown the extreme versatility of the sensors realized with respect to different applications. This goal is to be considered a good starting point for future studies aimed to the miniaturization and engineering of a sensor suitable for different needs and applications spacing from the biomedical field to the security one, passing through food and pollution analysis.

Riassunto

Negli ultimi decenni la risonanza plasmonica di superficie ha conosciuto un crescente interesse nella realizzazione di dispositivi miniaturizzati per applicazioni sensoristiche *label-free* dettate dalla necessità di aumentare la sensibilità dei sensori e di limitare il consumo di materiale.

Questo lavoro ha come scopo la realizzazione di nanostrutture plasmoniche che possano essere applicate a diversi campi della sensoristica in modo da creare un punto di partenza per la realizzazione di sensori miniaturizzati per molteplici applicazioni. In primo luogo è stato effettuato uno studio accurato della geometria e dei materiali adatti alla realizzare delle nanostrutture (*grating* sinusoidali metallici nella fattispecie) ed è stato ottimizzato il metodo di caratterizzazione delle superfici plasmoniche. Successivamente è stata ideata una strategia di fabbricazione che permettesse di ottenere un grande numero di substrati versatili, in poco tempo e con costi limitati. Così combinando litografia interferenziale e *soft lithography* sono stati realizzati dei substrati plasmonici caratterizzati variando la rotazione azimutale del *grating*. I substrati sono stati testati in varie applicazioni: la rivelazione di DNA della *M. tuberculosis* tramite sonde a PNA, la rivelazione di DNA della fibrosi cistica tramite sonde a DNA, la rivelazione di esplosivi in traccia e la rivelazione del batterio *L. pneumpohila*. L'ottimizzazione delle procedure di *sensing* e di preparazione della superficie plasmonica, e i risultati ottenuti hanno dimostrato l'estrema versatilità dei sensori realizzati nei confronti di molteplici applicazioni sensoristiche anche molto diverse tra loro. Questo traguardo è da considerarsi un ottimo punto di partenza per studi futuri finalizzati all'ingegnerizzazione e miniaturizzazione di un sensore adattabile a diverse esigenze e applicazioni che spazino dall'area biomedica a quella della sicurezza, passando per l'analisi del cibo e dell'inquinamento.

Summary

Preface

In recent years the research and development devoted to the realization of optical chemical and biological sensors has rapidly grown requiring always more device miniaturization and increasing sensitivity and resolution. In this context a large number of optical methods, in which a desired quantity is determined by measuring the refractive index, absorbance and fluorescence properties of analyte molecules or a chemo-optical transducing medium, have been exploited. Ellipsometry, spectroscopy (luminescence, phosphorescence, fluorescence, Raman), interferometry (white light interferometry, modal interferometry in optical waveguide structures), spectroscopy of guided modes in optical waveguide structures (grating coupler, resonant mirror), and surface plasmon resonance are the most explored techniques.

Simultaneously two other scientific fields have known a remarkable growth: nanotechnology and plasmonics.

Nanotechnology is likely to have a profound impact on our economy and society in the early 21st century, comparable to that of semiconductor technology, information technology, or cellular and molecular biology. Science and technology research in nanotechnology promises breakthroughs in areas such as materials and manufacturing, nanoelectronics, medicine and healthcare, energy, biotechnology, information technology and national security.

Plasmonics, that has known an increasing interest in a growing range of scientific fields and its advances and progress have offered promising ideas for applications in many areas (sensing, solar cells, optoelectronics and communication), is defined as the study and application of the interactions of optical-frequency electromagnetic waves with electrons in metals. Indeed one key advantage of plasmonics is the possibility to confine and exploit electromagnetic oscillations at optical frequencies to a size that is much smaller that the wavelength in vacuum. The possibility to exploit material properties at the nanoscale and to control light interaction with matter revealed new unexpected phenomena and opened the route to new research-threads in the sensoristic frontier.

Plasmonic device realization requires the synergy of many disciplines: physics, material science and information engineering, biotechnology, biochemistry and medicine. In this way plasmonics has increasingly become a interdisciplinary research field, where contributions of different backgrounds, engineering and physics as well as biology and chemistry, is needed in order to provide the required knowhow so to design and realize such plasmonic devices.

In general the complete fabrication of a plasmonic device need the following of an accurate method beginning with the device design and ending with the final sensing test. Thus after a preliminary study of design and analysis in order to optimize the optical response of such nanostructures and provide to nanofabrication the proper windows of process for the realization of optimized devices. Once the components have been fabricated and assembled, a characterization step is performed to verify the real optical behaviour and compare results with the theoretical expectations and literature background. Thus the realization of a plasmonic device should consider and overcome each step of this chain of processes: simulation – fabrication – characterization.

This thesis deals with the realization and application of plasmonic gratings to different application fields, from DNA to explosives, passing through bacteria. The whole work is the result of an interdisciplinary work, which was possible thanks to the collaboration with other laboratories and research groups skilled in a specific step of the sensor fabrication process.

Plasmonic gratings are nanostructured metallic surface that support the excitation and propagation of Surface Plasmon Polaritons (SPPs). These modes are localized surface-waves propagating along the interface between a metal and a dielectric medium and have risen in the coupling of electromagnetic-field with electron-plasma oscillations inside the metal. Thanks to the great confinement of the electromagnetic energy at the nanoscale on the surface, these modes are extremely sensitive to interface properties and reveal themselves as a powerful probe for surface analysis and sensing applications.

The change in refractive index of the medium, for example due to a change in concentration of an analyzed solution, or to the binding of molecules to the metal surface, alters the propagation constant of surface plasmon polaritons and changes the coupling conditions of incident light. In this way a variation in resonance conditions can be transduced into a measure of surface functionalization or solution concentration: this is the basic principle of modern Surface Plasmon Resonance (SPR) sensors. Since its first demonstration for the study of processes at the surfaces of metals and sensing of gases in the early 1980s, SPR sensing has made vast advances in terms of both development of technology and its applications for label-free fast and compact sensors. In particular the application for detection of chemical and biological species has gained considerable importance and interest in several fields: medical diagnostics, environmental monitoring, food safe and security. Common SPR affinity biosensors consist of a biorecognition element that is able to interact with a particular selected analyte in solution and an SPR transducer, which translates the binding event into an output signal. The core of the transducer is the optical platform, such as a metallic grating, on which surface plasmon polaritons are optically excited and propagate.

In this work the fabrication of metallic sinusoidal grating was carried out combining laser interference lithography and soft lithography techniques. Using laser interference lithography a sinusoidal master with specific geometrical parameters was fabricated. The master was then replicated by a replica-molding process and the plasmonic behaviour was given to the sensing platform by a bi-metallic layer evaporation. Starting from the realized substrate, an accurate study of the sensing surface preparation and optimization was performed in order to fit different applications (**Figure P. 1**), requiring the combination of chemical, biomedical and physical studies. Specific probes with their specific functional groups and deposition strategies were studied, designed and then optimized for each desired application. After the sensing layer preparation real sensing experiments were performed through the azimuthally-controlled grating-coupling SPR detection method, known to provide a sensitivity higher than the classical grating-coupling configuration. The advantages, the limits, the sensitivity and the efficiency of the sensor realized were then evaluated.

One of the most important results of this thesis work is the demonstration of the applicability of our sinusoidal grating to a wide range of sensing application with results, in term of efficiency, sensitivity and resolution, at the state of the art or above. Starting from this result, the possibility of further develop our detection system and integrate the sensing platform here described into a final miniaturized device is now open and the transfer of our sensing prototype to commercial or medical field could be achieved in the future.

The whole work was inserted into the following projects.

PLATFORMS (*PLAsmonic nano-Textured materials and architectures FOR enhanced Molecular Sensing)*, Strategic Project of the University of Padova.

Aim of this project is the study and development of complex Nano-Structured Architectures (NSAs) able to exploit surface plasmon polaritons propagation (SPPs) and electromagnetic enhancement phenomena, aimed to realize chemical and biochemical sensors. In this project the attention is focused on two important application fields: (a) detection of biological compounds, where a highly efficient qualitative and quantitative identification within complex matrices is of great importance in disease diagnostics and drug discovery; (b) monitoring of the atmospheric pollution, that has become highly strategic in order to guarantee a sustainable development.

SPLENDID (*Surface Plasmonic for Enhanced Nano Detectors and innovative Devices*), Excellence Project of CARIPARO Fundation.

The project aims to exploit the physical phenomena of surface plasmon polaritons to control the interaction of electrons and light on the surface of a nanostructured materials for the developing of biosensors capable of detecting and identifying even a few molecules. Indeed the purpose of the whole project is the development of a typology of integrated sensors for which it is expected a strong industrial fallout for bio-medical and food product analyses.

PROGETTO IRE (Istituto Ricerche Esplosivistiche).

The project has the goal of demonstrating the working evidence of a TNT sensing prototype based on a sinusoidal gold grating characterized under azimuthal control, as potential alternative solution for explosive trace detection.

POR-PROTOLAB, Veneto Nanotech project.

The aim of the project is the realization of a plasmonic sensor for bacteria detection introducing innovative miniaturized and high sensitive techniques in the currently biomedical scenario. The final purpose of the project is the realization of an industrial sensing prototype.

All the sensor realized in this thesis work starting from the same plasmonic substrate are summarized below.
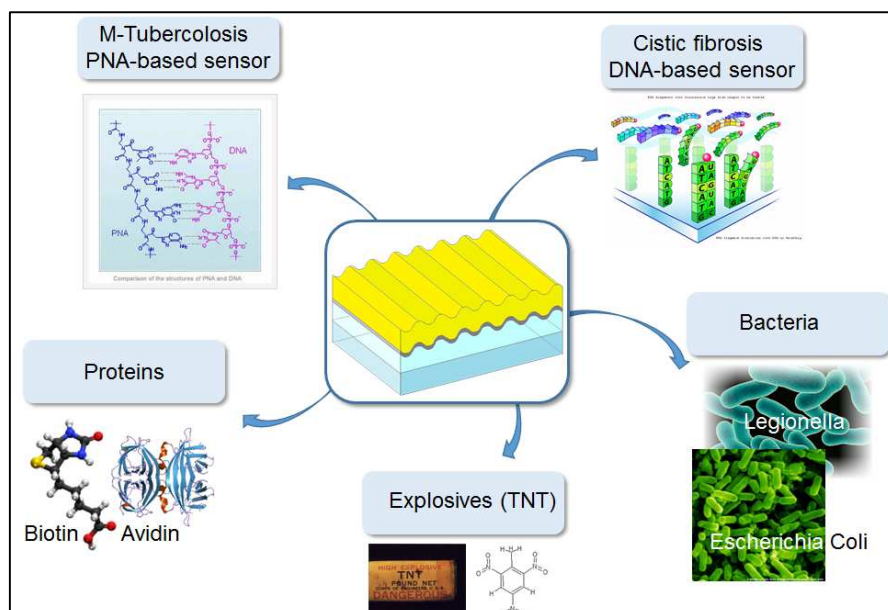
Figure P. 1. Sensors realized in this work starting from the same sensing platform realized in this work.

In summary, the content of this thesis work is organized as it follows.

Chapter 1. *Plasmonics for sensing.* A brief introduction to recent developments in the sensoristic field and to surface plasmon polaritons properties is given. A description of the typical configurations (prism/grating-coupling) for surface plasmon polaritons excitation are described, focusing on the sensing application requirements. The chapter ends with a summary of the most important characteristic of an SPR sensor and a discussion on the comparison between prism and grating coupling SPP excitation methods is reported.

Chapter 2. *Materials and methods.* In this Section the sensing platform realized in this work is described in detail together with the characterization methods necessary for the realization of the final sensor (more details are reported in **Appendix A.1**, **A.2** and **A.3**). Also an overview of sensors realized in this thesis work is shown.

Chapter 3. *Fabrication.* The sensing substrate fabrication strategy is here described in detail for what concern both laser interference lithography (LIL) and soft lithography steps. SEM and AFM images of the resulting substrates obtained by LIL and after the metallic layer deposition are shown. The goodness of fabrication results has to be attributed to the collaboration with TASC-IOM-CNR nanofabrication laboratories of the Area Science Park in Basovizza (Trieste).

Chapter 4. *PNA sensor for M. tuberculosis.* An overview of M. tuberculosis and peptide nucleic acid (PNA)-based sensing is reported in detail. The optimization strategy adopted for the realization of this type of sensor, consisting in the immobilization of a poly(ethylene oxide)-PNA as the probe and of a shorter poly(ethylene oxide) for the protection of surface from non-specific adsorption, is shown from its design to its application. The study was focused on the following steps: sensing surface calibration, complete antifouling achievement, optimization of PNA sensing efficiency and sensing experiments using real samples. The high sensitivity resulting from this work gives a good starting point for the miniaturization of the PNA-based sensor here described and for the possibility of further improving the PNA-based detection in a biomedical field. This work, inserted in the PLATFORMS project, was performed in collaboration with research groups of the Department of

Pharmaceutical Sciences and Industrial Engineering of the University of Padova, for the biological element synthesis, and with Nanofab Laboratory (Veneto Nanotech, Mestre –Venezia), for fluorescence analyses.

Chapter 5. *DNA sensor for cystic fibrosis.* The design and realization of a sensor for the detection of four cystic fibrosis mutations is described from the probe sequence design (details are reported in **Appendix A.4**) to the real sample detection. In this work of particular relevance was the simultaneous detection of the same experiment with both SPR and fluorescence methods, performed for all the experimental steps. The work, inserted in the SPLENDID project, was performed in collaboration with Nanofab Laboratory (Veneto Nanotech, Mestre –Venezia) for the probe design, the sensing strategy optimization and for the fluorescence analyses.

Chapter 6. *Sensors for explosives.* The development of a TNT sensing prototype is here shown, exploiting two different sensing surface strategy: the use of a self-assembled monolayer and the use of a molecularly imprinted polymer (MIP) matrix. Only preliminary tests were performed and are here shown, with the aim of demonstrate the possibility of further develop and apply this type of sensor in a real explosive detection context. The MIP-based sensing layer was realized in collaboration with the Department of Industrial Engineering of the University of Padova.

Chapter 7. *Sensor for L. pneumophila.* Starting from the recent research of new methods for increase the sensitivity in the detection of *L. pneumophila* bacteria, in this Section the study, optimization and application of a grating-based sensing platform for *L. pneumophila* detection is shown. Preliminary results here shown reveal the possibility of improving the detection sensitivity of our system and of applying the sensing strategy adopted to the detection of other bacteria. This work was inserted in the POR-PROTO LAB project and was performed in collaboration with Nanofab Laboratory (Veneto Nanotech, Mestre –Venezia) for the sensing strategy optimization and for the fluorescence analyses.

Chapter 8. *Conclusions.* A summary of all the sensors realized in this work highlighting their advantages and limits is reported. From the results obtained it is clear the applicability of the sensing platform realized in this work to a wide range of application, and the possibility of further improving and being applied in a real biomedical context.

1. Plasmonics for sensing

1.1 Optical label-free sensors

Among the different definitions of biosensors that have been elaborated in recent decades, an updated version of that selected by the International Union of Pure and Applied Chemistry (IUPAC) in 1999 [1] is: "a biosensor is a compact analytical device incorporating a biological or biologically derived sensing element, either integrated within or intimately associated with a physicochemical transducer".

Nowadays we can find a lot of biosensing systems based on different detection methods like electrochemical, colorimetric and optical sensors. Recently the research and development devoted to the realization of optical chemical and biological sensors has rapidly grown from its first applications [2] to more recent ones, exploiting a large number of optical methods, in which a desired quantity is determined by measuring the refractive index, absorbance and fluorescence properties of analyte molecules or a chemo-optical transducing medium: ellipsometry, spectroscopy (luminescence, phosphorescence, fluorescence, Raman), interferometry (white light interferometry, modal interferometry in optical waveguide structures), spectroscopy of guided modes in optical waveguide structures (grating coupler, resonant mirror), and surface plasmon resonance.

In general optical sensors are divided into two categories: *labeled* and *label-free* sensors. In the labeled detection (e.g. fluorescence-based methods [3]), either target molecules or biorecognition molecules are labeled with fluorescent tags, such as dyes; the signal detected indicates the presence of the target molecules (the analyte) and the interaction strength between target and biorecognition molecules. While labeled detection is extremely sensitive, with the detection limit down to a single molecule [4], it needs laborious labeling processes that may also interfere with the function of a biomolecule and with sensor production costs. Quantitative analysis is challenging due to the fluorescence signal bias, as the number of fluorophores on each molecule cannot be precisely controlled [5]. In contrast, in label-free detection [6], target molecules are detected in their natural forms. This type of detection is relatively easy and cheap to perform, and allows for quantitative and kinetic measurement of molecular interaction. There exist a number of label-free optical detection method, including refractive index (RI) detection, optical adsorption detection and Raman spectroscopy detection, and all methods can be compared in term of their sensitivity and detection limit (**Table 1. 1**).

Table 1. 1. Sensitivity and detection limit of optical label-free sensors found in literature. Table is re-printed from Fan, X. et al. [6].

Technology platform	Optical structures	Analyte	Detection limit
Surface plasmon resonance	Surface plasmon resonance	Bulk solution	10^{-5}-10^{-8} RIU
	Long range SPR	Bulk solution	10^{-7}-10^{-8} RIU
	Surface plasmon resonance imaging (SPRI)	Bulk solution	10^{-5}-10^{-7} RIU
	SPRI	Protein	1 nM
	Optical heterodyne SPR	Protein	0.2 nM
	Phase sensitive SPR	Protein	1.3 nM
	Wavelength modulated SPR	DNA	10 pM (Note 1)
	SPRI	DNA and RNA	10 nM
	Flow injection SPR	DNA	54 fM, 1.38 fM (Note 1)
	Angle modulated SPR	Protein (PSA)	0.15 ng mL^{-1} (Note 1)
	SPR	Protein (CA19-9)	66.7 unit mL^{-1}
	SPR	Protein (α-fetoprotein)	50 ng mL^{-1}
	Prism-based SPR	Bacteria (E. coli)	10^6 cfu mL^{-1}
		Salmonella yphimurium	100 cfu mL^{-1}
	BIAcore 2000 SPR	Bacteria	25 cfu mL^{-1}
Interferometer	Mach-Zehnder interferometer	Bulk solution	10^{-7} RIU
		Protein	20 pg mm^{-2}
	Young's interferometer	Bulk solution	$\sim 1 \times 10^{-7}$ RIU
		Virus	1000 particles mL^{-1}
	Hartman interferometer	DNA	4 ng mL^{-1}
		Protein	5 ng mL^{-1}, 0.1 ng mL^{-1} (Note 1)
		Virus	10^7 pfu mL^{-1}
		Bacteria	5×10^8 cfu mL^{-1}, 5×10^5 cfu mL^{-1} (Note 1)
	Backscattering interferometer		
	Porous silicon	DNA	2 pM
	BioCD	Protein	0.1 ng mL^{-1}
	Microchannel backscattering	Bulk solution	7×10^{-9} RIU
		Protein	femto-mole (Note 2)
		Protein	picomolar (Note 3)
Waveguide	Resonant mirror	Protein	~ 0.1 pg mm^{-2}
		Cell	10^6 cells mL^{-1}
	Metal-clad waveguide	Bacterial spore	$\sim 10^5$ spores mL^{-1}
		Cell	~ 10 cells mm^{-2} (Note 2)
	Reverse symmetry waveguide	Cell	60 cells mm^{-2} (Note 2)
	Symmetrical metal-clad waveguide	Bulk solution	2×10^{-7} RIU
Ring resonator	Ring on a chip	Bulk solution	10^{-4} to 10^{-7} RIU
		DNA	~ 100 nM
		Protein	20–250 pg mm^{-2}, 0.1 nM
		Bacteria	10^5 cfu mL^{-1}
	Dielectric microsphere	Bulk solution	10^{-7} RIU
		DNA	1 pg mm^{-2}
		Protein	10 pg mL^{-1} (trypsin), 1 unit mL^{-1} (thrombin)

Technology platform	Optical structures	Analyte	Detection limit	Ref.
Optical fiber	Capillary opto-fluidic ring	Bulk solution	10^{-6}-10^{-7} RIU	[152]
		DNA	4 pg mm^{-2}, 10 pM	[163]
		Protein	~1 pg mm^{-2}, 3 pM (Note 2)	[157]
		Virus	1000 particles mL^{-1}	[164]
	Fiber Bragg grating	Bulk solution	~10^{-6} RIU	[204–209]
		DNA	0.7 µg mL^{-1}, 0.1 µM	[209]
	Long-period grating	Bulk solution	10^{-4} RIU	[219]
		Protein	2 µg mL^{-1}	[218]
	Nanofiber	Bulk solution	10^{-7} RIU	[223]
	Fiber coupler	Bulk solution	4×10^{-6} RIU	[227]
		Protein	0.5 µg mL^{-1}	[227]
	Fiber Fabry-Perot cavity	Bulk solution	10^{-5} RIU	[207,231]
		DNA	76 µM, 1.7 ng	[229]
		Protein	25 µg mL^{-1}	[228]
Photonic crystal	2-D PC	Bulk solution	10^{-5} RIU	[240,241]
		Protein	0.4 pg mm^{-2} (Notes 2 and 4)	[240,241]
	2-D PC microcavity	Bulk solution	~10^{-3} RIU	[234,235]
		Protein	1 fg	[237]
	PC waveguide	Protein	0.15 µM	[239]
	1-D PC microcavity array	Bulk solution	7×10^{-5} RIU	[246]
	PCF	Bulk solution	10^{-4} RIU	[219]

Notes: (1) With gold nanoparticle amplification. (2) Adsorption result. (3) Binding takes place in free solution rather than on a solid substrate. (4) Results obtained after solution containing protein is dried.

RI detection has gained a great interest in optical label-free sensing as its change is induced by molecular interactions in the proximity of a sensing surface and it is related to the sample concentration or surface density, instead of total sample mass. As a result, the detection signal does not scale down with the sample volume. This characteristic is particularly attractive when ultrasmall (femtoliter to nanoliter) detection volume is involved and is advantageous over fluorescence-based detection whose signal usually depends on the total number of analytes in the detection volume or on the detection surface. In this context, RI detection methods currently used include plasmonic sensors, interferometer-based sensors, optical waveguide-based sensors, optical ring resonator-based sensors, optical fiber-based sensors and photonic crystal-based sensors.

In this work we will focused on plasmonic biosensors and more precisely on Surface Plamon Resonance (SPR) sensing as it revealed to be a high sensitive method for label-free sensing [7]. Since the first demonstration in early 1980s, SPR sensors have made vast advances in terms of both development of the technology and its applications. SPR biosensors have become a central tool for characterizing and quantifying biomolecular interactions. Moreover, development of SPR sensors for the detection of chemical and biological species has gained considerable momentum, and the number of publications reporting applications of SPR biosensors for detection of analytes related to medical diagnostics, environmental monitoring, and food safety and security has been rapidly growing.

1.2   Plasmonics
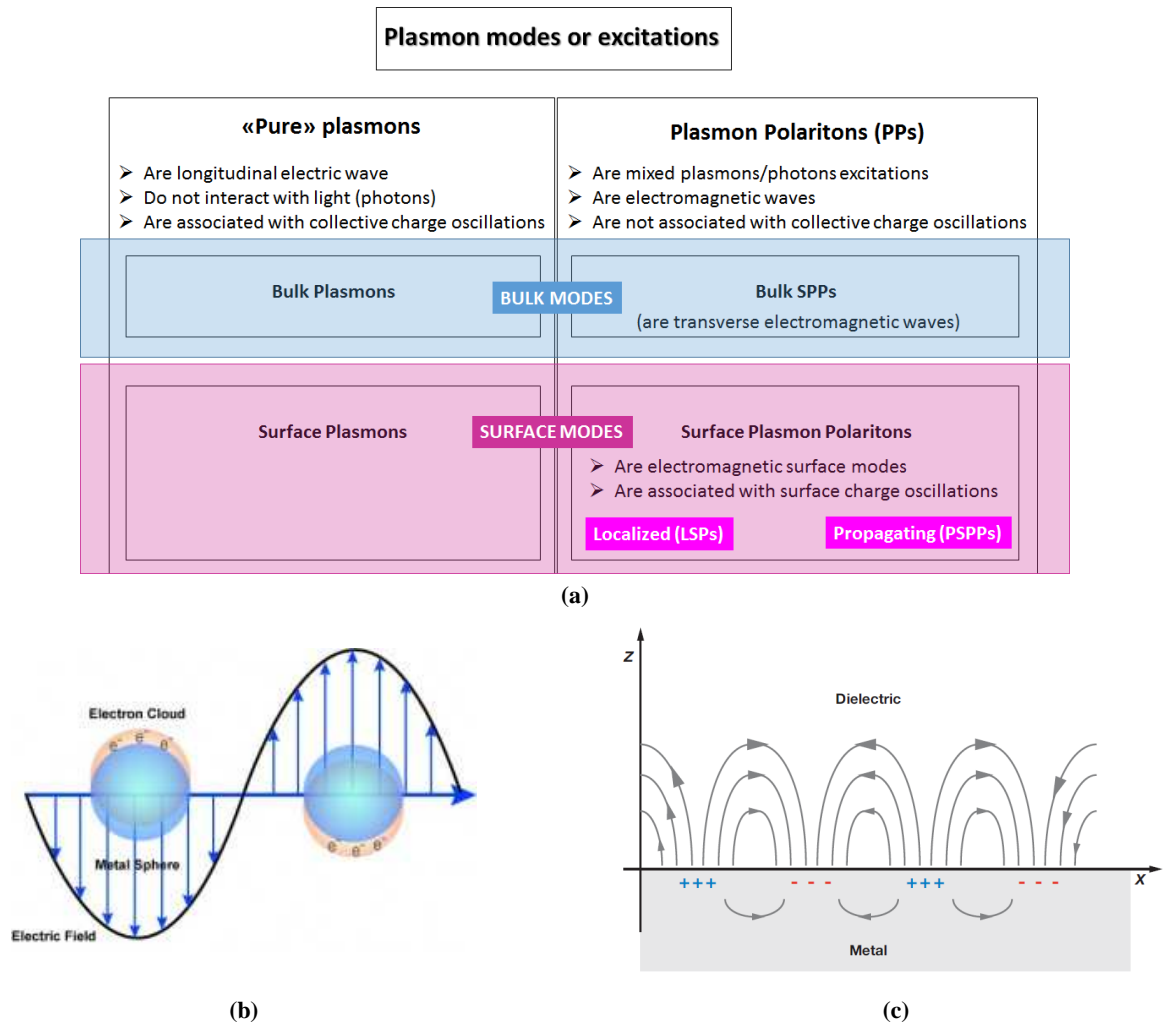
The first use of the term "plasmon" was made by Pines in 1956 [8] when he defined plasmons as "the quantum of elementary excitation associated with high-frequency collective motion of the valence electron oscillation" and the mathematical description of these surface waves was established around the turn of the 20$^{\text{th}}$ [9–13]. Therefore a plasmon is a quantum representing the

elementary excitations, or modes, of the charge density oscillations in a plasma. In **Figure 1. 1 (a)** the types of plasmon excitations, which can be essentially divided in "pure" plasmons and plasmon polaritons (PPs), are shown.

"Pure" plasmons correspond to longitudinal excitations of the electric field, they cannot couple to photons and are associated with collective charge oscillations. Bulk plasmon polaritons (BPPs), which are modes that exist in an infinite metal, belong to "pure" plasmons. When an electromagnetic wave is propagating in a medium, it excites the electron degree of freedom, generating a polarization (P). A photon coupled with the polarization is called "polariton". Considering the charge density, the energy of the electromagnetic wave is shared between the polariton and the plasmon, and the corresponding excitation is known as "plasmon polariton" (PP). If the charge density oscillation is confined to the surface we speak about surface plasmon polaritons (SPPs).

Thus SPPs are electromagnetic surface modes and are associated with surface charge oscillations. They are divided into two categories: the localized SP (LSPs) and the propagating SPPs (PSPPs). Localized surface plasmons are charge density oscillations confined to metallic nanoparticles and metallic nanostructures (**Figure 1. 1 (b)**). Excitation of LSPs by an electric field (incident light) at an incident wavelength where resonance occurs results in strong light scattering, in the appearance of intense surface plasmon absorption bands, and an enhancement of the local electromagnetic fields [14,15]. On the other hand propagating SPPs are typical of metal/dielectric extended interfaces or nanostructures (**Figure 1. 1 (c)**). The significant and analysis of PSPPs will be performed in the following Section in detail.

Plasmon modes or excitations

«Pure» plasmons	Plasmon Polaritons (PPs)
➢ Are longitudinal electric wave ➢ Do not interact with light (photons) ➢ Are associated with collective charge oscillations	➢ Are mixed plasmons/photons excitations ➢ Are electromagnetic waves ➢ Are not associated with collective charge oscillations

BULK MODES

Bulk Plasmons	Bulk SPPs (are transverse electromagnetic waves)

SURFACE MODES

Surface Plasmons	Surface Plasmon Polaritons ➢ Are electromagnetic surface modes ➢ Are associated with surface charge oscillations
	Localized (LSPs) **Propagating (PSPPs)**

(a)

(b) (c)

Figure 1. 1. Plasmon modes excitations can be divided in *bulk* and *surface modes* (a). In the surface modes we have SPPs that can be localized, in the case of nanoparticles for example (b), or propagating, in the case of extended planar or nanostructured surfaces (c).

1.3   Basic of SPR

SPPs are a charge density oscillations that may exist at the interface of two media with dielectric constants of opposite signs (**Figure 1. 1 (c)**), like a metal and a dielectric. The charge density wave is associated with an electromagnetic wave, whose field vectors reach their maxima at the interface and decay evanescently into both media. This surface plasma wave (SPW) is a TM-polarized wave (magnetic vector is perpendicular to the direction of propagation of the SPW and parallel to the plane of interface) [16,17].
SPPs are localized in the direction perpendicular to the interface: field intensity decays exponentially from the surface with an extension length of the same order of the wavelength inside the dielectric and almost one order shorter in the metal (**Figure 1. 2**). These features make SPPs extremely sensitive to optical and geometrical properties of the supporting interface, such as shape, roughness and refractive indices of the facing media.
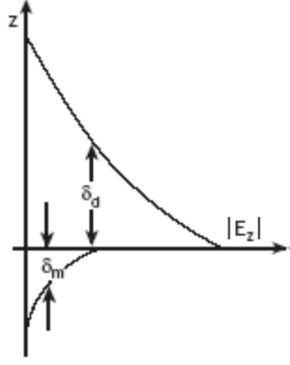
Figure 1. 2. SPPs at the interface between a metal and a dielectric material have a combined electromagnetic wave and surface charge character (*left*). The combined character also leads to the field component perpendicular to the surface being enhanced near the surface and decade exponentially with distance (δ_d for the dielectric and δ_m for the metallic material) away from it (*right*).

Gold and silver show the best plasmonic properties. The comparison of the main characteristic of SPW propagating along the interface between water and the surface plasmon active metal (gold and silver) is reported in **Table 1. 2**. Owing to high loss in the metal, the SPP propagates with high attenuation in the visible and near-infrared spectral regions. The electromagnetic field of an SPP is distributed in a highly asymmetric way and the major art of the field is concentrated in the dielectric medium. An SPP propagating along the surface of silver is less attenuated and exhibits higher localization of electromagnetic field in the dielectric than a SPP supported by gold, thus silver has better plasmonic properties than gold.

Table 1. 2. Optical constants of gold and silver taken from [17].

Metal layer	Gold		Silver	
Wavelength [nm]	**630**	**850**	**630**	**850**
Propagation length [μm]	3	24	19	57
Penetration depth into metal [nm]	29	25	24	23
Penetration depth into dielectric [nm]	162	400	219	443
Concentration of field in dielectric [%]	85	94	90	95

SPPs are confined solutions of Maxwell's equations (Eq. (1. 1)-(1. 4)) at the interface of two semi-infinite media, with the imposition of the associated boundary conditions. In the absence of free charges and currents the equations to solve are:

$$\overline{\nabla} \cdot \overline{D} = 0 \tag{1. 1}$$

$$\overline{\nabla} \times \overline{E} = -\frac{\partial \overline{B}}{\partial t} \tag{1. 2}$$

$$\overline{\nabla} \cdot \overline{B} = 0 \tag{1. 3}$$

$$\overline{\nabla} \times \overline{H} = \frac{\partial \overline{D}}{\partial t} \tag{1. 4}$$

with the constitutive relations:

$$\overline{D} = \varepsilon \overline{E} \tag{1.5}$$

$$\overline{B} = \mu \overline{H} \tag{1.6}$$

where $\varepsilon = \varepsilon_0 \varepsilon_r$, $\mu = \mu_0 \mu_r$, ε_r and μ_r are respectively the relative dielectric permittivity and the relative magnetic permeability of the medium, ε_0 and μ_0 are their values in vacuum.

Using Maxwell's equations and appropriate boundary conditions we are able to describe all SPR theory [16]. In this Section we will focused on SPR theory and phenomena that will be involved in the experimental part of the work and that are interesting for the development of SPR sensors designed in this work.

SPP on a planar metal/dielectric interface

In **Figure 1. 3** the structure of a planar metal/dielectric interface is shown.

Figure 1. 3. Planar metal/dielectric interface.

Analysis of Maxwell's equations with appropriate boundary conditions suggests that this structure can support only a single guided mode of electromagnetic fields of a surface plasmon: a SP is a transversally magnetic (TM) mode, and therefore its vector of intensity of magnetic field lies in the plane of metal-dielectric interface and it is perpendicular to the direction of propagation.

The propagation constant of a surface plasmon at the metal-dielectric interface (β) can be expressed as:

$$\beta = \frac{\omega}{c} \sqrt{\frac{\varepsilon_d \varepsilon_m}{\varepsilon_d + \varepsilon_m}} = k \sqrt{\frac{\varepsilon_d \varepsilon_m}{\varepsilon_d + \varepsilon_m}} \tag{1.7}$$

For metals following the free-electron model:

$$\varepsilon_m = \varepsilon_0 \left(1 - \frac{\omega_p^2}{\omega^2 + i\omega v} \right) \tag{1.8}$$

where v is the collision frequency and ω_p is the plasma frequency expressed as:

$$\omega_p = \sqrt{\frac{N e^2}{\varepsilon_0 m_e}} \tag{1.9}$$

where N is the concentration of free electrons, and e and m_e are the electron charge and mass, respectively. Eq. (1. 8) is fulfilled for frequencies lower than the plasma frequency of the metal, i.e. when the Surface Plasmon Wave (SPW) is supported by a structure providing that

$$\varepsilon_m^{Re} < -\varepsilon_d^{Re} \tag{1. 10}$$

This condition is fulfilled, for example, by silver and gold (**Table 1. 2**).

Considering a metal-dielectric interface with a transverse-magnetic plane wave which propagates in the positive *x-direction*. Since we are looking for localized EM-waves, the magnetic field should have the following form:

$$z > 0 \qquad \overline{H}(x,z,t) = (0, H_1, 0)e^{ik_{1x}x - k_{1z}z}e^{-i\omega_1 t} \tag{1. 11}$$

$$z < 0 \qquad \overline{H}(x,z,t) = (0, H_2, 0)e^{ik_{2x}x + k_{2z}z}e^{-i\omega_2 t} \tag{1. 12}$$

Where k_{1z} and k_{2z} must be positive in order to describe an electromagnetic wave localized to the dielectric-metal interface at $z = 0$. Since $\overline{n} \times (\overline{H}_1 - \overline{H}_2) = 0 \forall (x,t)$ at $z = 0$, it follows that $\omega_1 = \omega_2 = \omega$, $\overline{H}_1 = \overline{H}_2$ and $k_{1x} = k_{2x} = k_x$, and Eqs. (1. 11) and (1. 12) become:

$$z > 0 \qquad \overline{H}(x,z,t) = (0, H_1, 0)e^{ik_x x - k_{1z}z}e^{-i\omega t} \tag{1. 13}$$

$$z < 0 \qquad \overline{H}(x,z,t) = (0, H_2, 0)e^{ik_x x + k_{2z}z}e^{-i\omega t} \tag{1. 14}$$

Calculating the curl of **H** and using Maxwell's equations we find the following expression for the electric field:

$$z > 0 \qquad \overline{E}(x,z,t) = \left(\frac{Hk_{1z}}{\omega \varepsilon_1}, 0, \frac{Hik_x}{\omega \varepsilon_1}\right)e^{ik_x x - k_{1z}z}e^{-i\omega t} \tag{1. 15}$$

$$z < 0 \qquad \overline{E}(x,z,t) = \left(-\frac{Hk_{1z}}{\omega \varepsilon_1}, 0, \frac{Hik_x}{\omega \varepsilon_1}\right)e^{ik_x x + k_{1z}z}e^{-i\omega t} \tag{1. 16}$$

The boundary condition

$$\overline{n} \times (\overline{E}_1 - \overline{E}_2) = 0 \tag{1. 17}$$

imposes

$$\frac{k_{1z}}{\varepsilon_1} + \frac{k_{2z}}{\varepsilon_2} = 0 \tag{1. 18}$$

If we assume that the dielectric function of the metal $\varepsilon_2(\omega)$ is real, it follows, since k_{z1} and k_{z2} must be real and positive, that ε_2 must be negative for this surface electromagnetic waves to exist.

Using the last expression and the definition of k_{zi} obtained substituting the solution into the wave equation:

$$k_{zi} = \sqrt{k_x^2 - \varepsilon_i \left(\frac{\omega}{c}\right)^2}$$

(1. 19)

we obtain an explicit expression for the wavenumber of the SPP as a function of its frequency ω, called *dispersion relation*:

$$k_x = \frac{\omega}{c}\sqrt{\frac{\varepsilon_1\varepsilon_2}{\varepsilon_1 + \varepsilon_2}} = k_{ph}\sqrt{\frac{\varepsilon_1\varepsilon_2}{\varepsilon_1 + \varepsilon_2}} = k_{ph}M$$

(1. 20)

where k_{ph} is the photon momentum. The real and imaginary parts of the dielectric function, $\varepsilon = \varepsilon' + i\varepsilon''$, are given by:

$$\varepsilon'(\omega) = 1 - \frac{\omega_p^2\tau^2}{1 + \omega^2\tau^2}$$

(1. 21)

$$\varepsilon''(\omega) = \frac{\omega_p^2\tau}{\omega(1 + \omega^2\tau^2)}$$

(1. 22)

where, in Drude theory, τ is the relaxation time of the electron sea and it is usually of order 10–14 s.

For ω >> 1/τ imaginary part is negligible and dielectric function reduces to:

$$\varepsilon = 1 - \frac{\omega_p^2}{\omega^2}$$

(1. 23)

Substituting this expression into the SPP momentum relation and rearranging terms we obtain SPP dispersion law (**Figure 1. 4**).
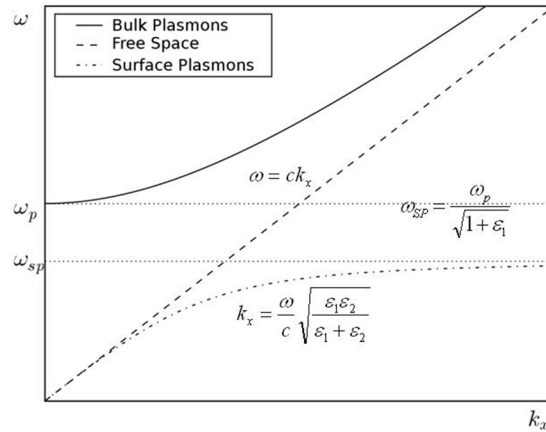
Figure 1. 4. Free photon dispersion law (*dashed line*) compared with BPP (*solid line*) and SPP (*dashed-dotted line*) dispersion law [17].

Dispersion curve lies in the right of the dispersion curve of a free photon (or light in vacuum), $\omega = ck_x$, and there is no intersection between them. Thus surface polaritons are non-radiative waves and cannot be excited directly by incident waves. For $k \to +\infty$ dispersion curve asymptotically approaches the frequency

$$\omega_p^{'} = \frac{\omega_p}{\sqrt{1 + \varepsilon_1}} \qquad (1.\ 24)$$

Since the group velocity $\frac{\partial \omega}{\partial k} \to 0$, as $k \to +\infty$, this is the frequency of steady surface waves (surface plasmons).

At large k_x the group velocity $\frac{\partial \omega}{\partial k}$ decreases going to zero for the limit $k \to +\infty$ (as explained above), and the phase velocity goes to zero as well. In this limit SP resembles a localized fluctuation of the electron plasma.

The characteristic frequency, rewriting Eq. (1. 24),

$$\omega_{SP} = \frac{\omega_p}{\sqrt{1 + \varepsilon_1}} \qquad (1.\ 25)$$

is called *surface plasmon frequency* and can be reduced to $\omega_{SP} = \frac{\omega_p}{\sqrt{2}}$ when the dielectric medium is the air.

1.4   Excitation of SPPs

As SPPs have a non-radiative nature (clearly visible from the non-crossing between SPP and photon dispersion laws in **Figure 1. 4**), the excitation by means of a wave illuminating the metallic surface is possible only in the configurations providing the wavevector-matching between the incident light and SPP dispersion law. Methods adopted for exciting SPPs can be divided into two geometries: the prism and the grating coupling one.

1.4.I   Prism Coupling (PC)

Prism coupling is the most common method for optical excitation of SPPs and it can be performed through two different configurations: the Kretschmann and the Otto geometry.

In the Kretschmann configuration a light wave passes through a high refractive index (n_p) prism and is totally reflected at the base of the prism, interfaced with a metal-dielectric waveguide consisting of a thin metal film with permittivity ε_m and thickness q, generating an evanescent wave penetrating the thin metal film (**Figure 1. 5-(a)**). The evanescent wave propagates along the interface with its propagation constant that can be adjusted to match the SP one by controlling the incoming light incidence angle.

In the Otto geometry, a high refractive index prism with refractive index n_p is interfaced with a dielectric–metal waveguide consisting of a thin dielectric film with refractive index $n_d(n_d < n_p)$ and thickness q, and a semi-infinite metal with permittivity ε_m (**Figure 1. 5-(b)**). A light wave incident on the prism–dielectric film interface at an angle of incidence larger than the critical angle of incidence for these two media, produces an evanescent wave propagating along the interface between the prism and the dielectric film. If the thickness of the dielectric layer is chosen properly (typically few microns), the evanescent wave and a surface plasmon at the dielectric–metal interface can couple. For the coupling to occur, the propagation constant of the evanescent wave and that of the surface plasmon have to be equal.

For both geometries the resonance condition of Eq. (1. 20) can be written as:

$$k_{ph,prism} = \frac{\omega}{c}\sqrt{\varepsilon_p}\,\sin\theta_{inc} \qquad (1.\,26)$$

where θ_{inc} is the light incident angle and ε_p is the prism dielectric function. The resulting dispersion curve of (1. 26) is depicted in **Figure 1. 5-(c)** (upper part). In the photon and SPP momentum matching condition a portion of the incident light energy is transferred to the propagating SPP, resulting in a decrease in the metal reflectivity at the coupling light incident angle (resonance angle - *angular interrogation*) or wavelength (resonance wavelength – *wavelength interrogation*) (**Figure 1. 5-(c)**). The reflectivity decrease is detected as a dip in the metal reflectivity spectrum (**Figure 1. 5-(c)**). When the refractive index at the metal/dielectric interface changes (e.g. after the metal functionalization with a biological layer), the SPP momentum increases producing a transfer in the SP dispersion curve (**Figure 1. 5-(c)**) and a shift in the dip position to a higher resonance angle (or wavelength). The resonance angle shift is the signal of the presence of a new material at the metal/dielectric interface.

(a)

(b)   **(c)**
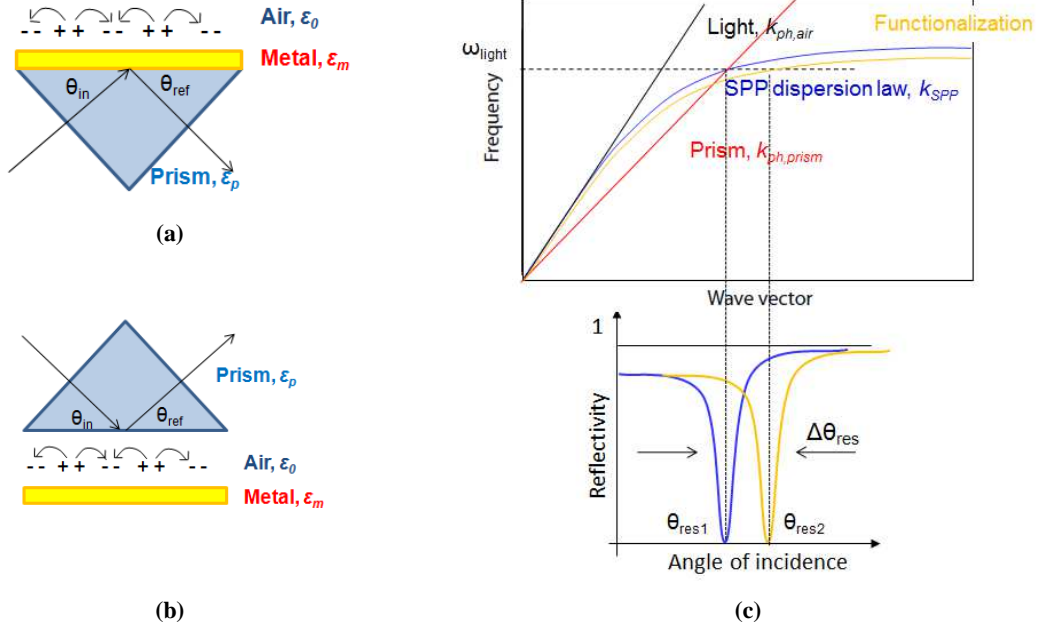
Figure 1. 5. Scheme of SP excitation by PC-SPR. PC-coupling could be performed using the typical Kretschmann geometry (a) or the Otto configuration (b). In both cases the use of a prism allows the matching condition between an incoming photon and a SP momentum (c), visible from the cross between SPP dispersion curve (*blu solid line,* upper part of (c)) and the dispersion curve of light passing through the prism (*red solid line*). For angular interrogation, at the resonance condition, for a particular light incident frequency ω_light (dashed line, upper part of (c)) a portion of the incident light energy is transferred to the SP resulting in a reflectivity dip in the metal reflectivity spectrum at a certain resonance angle θ_res1 (*blu solid line,* lower part of (c)). After refractive index changes at the metal/dielectric interface, a SP dispersion curve transfer occurs (*orange solid line,* upper part of (c)), crossing the ω_light line in a different point, and resulting in the shift of the reflectivity dip to higher resonance angles θ_res2 (*orange solid line,* lower part of (c)). Thus the presence of a new material at the metal/dielectric interface is detected from the resonance angle shift Δθ_res.

1.4.II Grating-Coupling (GC)

The excitation of SPPs on grating (**Figure 1. 6**) is achieved when the *momentum conservation condition* (or *resonance condition*) between an incoming photon and a SPP is satisfied:

$$\bar{k}_{SPP} = \bar{k}_{ph} \pm m\bar{g} \qquad (1.\,27)$$

$\bar{k}_{SPP}$ is the diffracted SPP vector, $\bar{k}_{ph}$ is the incident photon momentum, $\bar{g}$ is the grating momentum and *m* identifies the diffraction order.

The light wave vector is represented by

$$\bar{k}_{ph} = \frac{2\pi}{\lambda}\left(-\sin\theta_{inc},0,\cos\theta_{inc}\right) \qquad (1.\,28)$$

where λ is the incident wavelength and θ_{inc} is the incident angle for which the SPP starts its propagation.

Therefore the component of the wavevector of the diffracted light perpendicular to the plane of the grating $\bar{k}_{SPPz}$ is equal to that of the incident wave, while the component of the wavevector in the plane of the grating $\bar{k}_{xm}$ is diffraction altered by the grating momentum $\bar{g}$:

$$\overline{g} = \frac{2\pi}{\Lambda}(\cos\varphi, \sin\varphi, 0) \tag{1.29}$$

where Λ is the grating pitch and φ is the grating azimuthal orientation angle.

Starting from Eq. (1. 29) we can have two GC-SPR configurations: the null azimuth ($\varphi=0°$) and the rotated azimuth one ($\varphi\neq0°$).

Null azimuth configuration

In the null azimuth configuration (the classical mounting) (**Figure 1. 6 (a)**) Eq. (1. 27) can be simplified giving the following expression for $\overline{k}_{SPP}$:

$$\overline{k}_{SPP} = \overline{k}_{ph} + m\frac{2\pi}{\Lambda} \tag{1.30}$$

The diffracted waves can couple with a surface plasmon when the propagation constant of the diffracted wave propagating along the grating surface k_{SPP} and that of the surface plasmon β^{SPP} are equal:

$$\frac{2\pi}{\lambda}n_d\sin\theta + m\frac{2\pi}{\Lambda} = k_{SPP} = \pm\,\mathrm{Re}\{\beta^{SPP}\} \tag{1.31}$$

where:

$$\beta^{SPP} = \beta^{SPP_0} + \Delta\beta = \frac{\omega}{c}\sqrt{\frac{\varepsilon_d\varepsilon_m}{\varepsilon_d + \varepsilon_m}} + \Delta\beta \tag{1.32}$$

and β^{SPP_0} denotes the propagation constant of the surface plasmon propagating along the smooth interface of a semi-infinite metal and a semi-infinite dielectric, and $\Delta\beta$ accounts for the presence of the grating.

In terms of the effective index, the coupling condition can be written as:

$$n_d\sin\theta + m\frac{\lambda}{\Lambda} = \pm\left(\mathrm{Re}\left\{\sqrt{\frac{\varepsilon_d\varepsilon_m}{\varepsilon_d + \varepsilon_m}}\right\} + \Delta n_{ef}^{SPP}\right) \tag{1.33}$$

where:

$$\Delta n_{ef}^{SPP} = \mathrm{Re}\left\{\frac{\Delta\beta\lambda}{2\pi}\right\} \tag{1.34}$$

As explained for the PC-SPR, at the resonance condition (Eq. (1. 31)), a reflectivity dip in the reflectivity spectrum of the metal can be collected, and after metal functionalization, a shift of the reflectivity dip is detected. For a given incident wavelength, an SPP momentum decrease after the functionalization, gives a reflectivity dip at lower resonance angles (**Figure 1. 6 (b)**).

Null azimuth configuration (φ=0°)

(a)	(b)
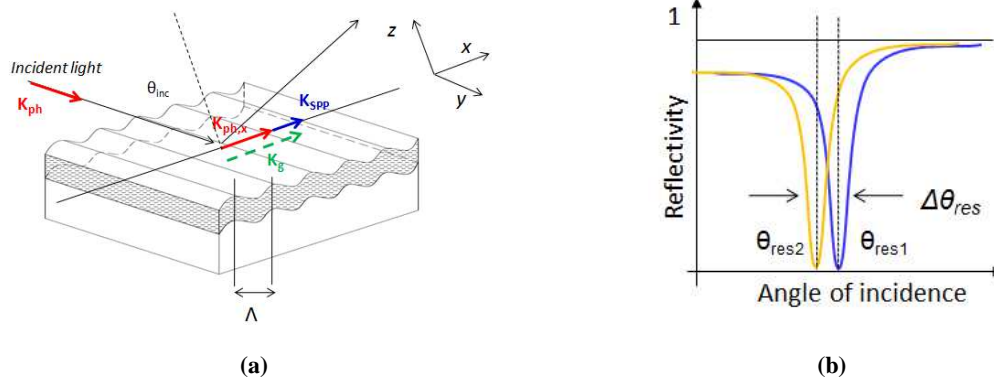
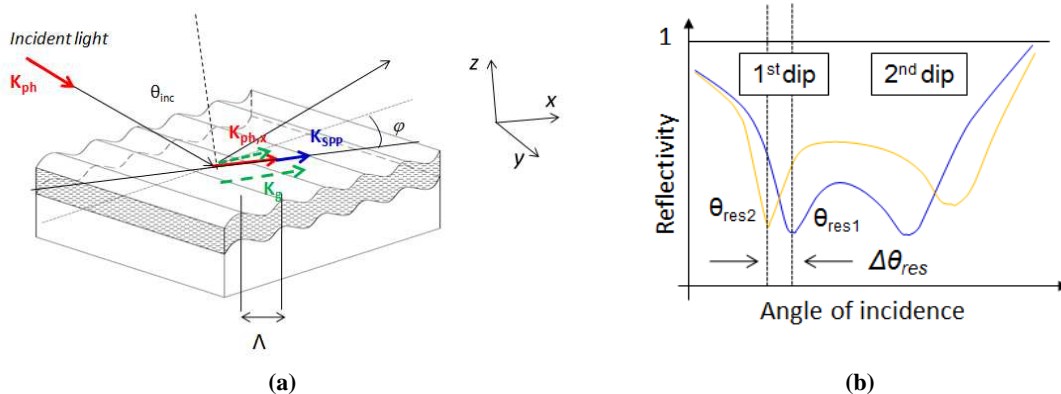**Figure 1. 6.** Scheme of SP excitation by GC-SPR for φ=0° (a). For angular interrogation, at the resonance condition, for a particular light incident frequency a portion of the incident light energy is transferred to the SP resulting in a reflectivity dip in the metal reflectivity spectrum at a certain resonance angle θ_{res1} ((b), *blu solid line*). After refractive index changes at the metal/dielectric interface, the dip shifts to lower resonance angles θ_{res2} ((b), *orange solid line*). Thus the presence of a new material at the metal/dielectric interface is detected from the resonance angle shift $\Delta\theta_{res}$.

Rotated azimuth configuration

In the rotated azimuth configuration (**Figure 1. 7 (a)**), the azimuthal orientation of the sinusoidal grating induces a double surface plasmon polariton (SPP) excitation with a single incident wavelength, leading to a double reflectivity dip in the collected reflectance spectrum as a function of light incident angle (**Figure 1. 7 (b)**).

Rotated azimuth configuration (φ≠0°)

(a)	(b)

Figure 1. 7. Scheme of SP excitation by GC-SPR for φ≠0° (a). For angular interrogation, at the resonance condition, for a particular light incident frequency a portion of the incident light energy is transferred to the SP resulting in a double reflectivity dip in the metal reflectivity spectrum at a certain resonance angle θ_{res1} ((b), *blu solid line*). After refractive index changes at the metal/dielectric interface, the dip shifts to lower resonance angles θ_{res2} ((b), *orange solid line*) in the case of the 1st dip and to higher resonance angles θ_{res2} ((b), orange solid line) in the case of the 2nd dip. Thus the presence of a new material at the metal/dielectric interface is detected from the resonance angle shift $\Delta\theta_{res}$ that can be calculated both for the first and for the second dip. $\Delta\theta_{res}$ in the case of the second dip is higher than one obtained for the first dip. The mechanism of this behaviour is explained in **Figure 1. 8**.

As previously shown, grating-coupled surface plasmon resonance is achieved when the on-plane component $\bar{k}_{ph}^{//}$ of the incident wavevector $\bar{k}_{ph}$ satisfies the momentum conservation law reported in Eq. (1. 27), but the azimuthal rotation of the grating platform opens to unexpected physical phenomena, related to the symmetry breaking of the resonant structure.

Indeed, after the rotation of the grating vector at an azimuth φ≠0° (**conical mounting**), the vector composition in Eq. (1. 27) can be satisfied on the whole grating plane and not only in the direction perpendicular to the grating grooves (as in the classic mounting) [18]. This allows the exploitation of the azimuthal degree of freedom for the excitation of SPPs propagating along almost any direction on the grating plane.

In this case Eq. (1. 27) exhibits the following form on the grating plane:

$$k_{SPP} = \frac{2\pi}{\lambda}\sin\theta_{res}\cdot(1,0) - \frac{2\pi}{\Lambda(\cos\varphi,\sin\varphi)} \tag{1.35}$$

where only the first diffraction order ($n = -1$) is considered because in our cases of interest, the grating momentum $\bar{g}$ is always greater in modulus than $\bar{k}_{SPP}$.

The analysis of the wave-vector components allows a description of double SPP excitation using the schematic shown in **Figure 1. 8**, were all quadrants of the circle can be explored for SPP excitation as long as Eq. (1) is satisfied. For symmetry reason, only $\bar{k}_y$ positive half space is considered. [19,20].

Solving Eq. (1. 35) in the unknown resonance angle, the following expression is obtained as a function of the azimuth angle φ:

$$\theta_{res,-/+} = \arcsin\left(\frac{\lambda}{\Lambda}\cos\varphi_{-/+}\sqrt{M(\lambda)^2 - \left(\frac{\lambda}{\Lambda}\sin\varphi\right)^2}\right) \tag{1.36}$$

where: $M(\lambda) = k_{SPP}\Big/(2\pi/\lambda)$.

The largest circle in the k-space in **Figure 1. 8** (**A**) represents equi-magnitude $\bar{g}$ vectors at different azimuthal orientation. The two smaller circles represent all possible $\bar{k}_{SPP}$ vectors with equal magnitude respectively before (solid line) and after(dashed line) surface functionalization and whose modulus, for shallow gratings, can be approximated by [16]:

$$k_{SPP} = \frac{2\pi}{\lambda}M(\lambda)\frac{2\pi}{\lambda}\sqrt{\frac{\varepsilon_m n_{eff}^2}{\varepsilon_m + n_{eff}^2}} \tag{1.37}$$

where ε_m and n_{eff} are the dielectric permittivity of the metal and the effective refractive index of the dielectric side.

After functionalization, SPP modulus increases because of the small increase in n_{eff} due to the surface coating. The dashed line at the tip of the circle of radius $\bar{g}$ represents the x-component of

the photon wavevector, $\bar{k}_{ph}{}^{//}$, the only component that takes part in SPP excitation. The line scales linearly in $sin\theta$ so that the full length of the line at the incident angle θ of 90°corresponds to the maximum exploitable value of $\bar{k}_{ph}{}^{//}$.

The intersections of the $\bar{k}_{ph}{}^{//}$ dashed horizontal line with the smaller $\bar{k}_{SPP}$ circle determine the conditions for which Eq. (1. 35) is satisfied and allows the identification of the incident resonance angle θ_{res} for SPP excitation.
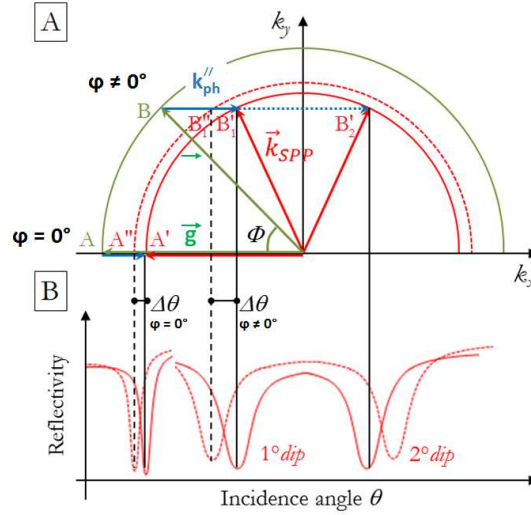
Figure 1. 8. (A) Schematic picture of wave-vector combination at SPP resonance (n = -1) in the wavevector space. The large circle represents equi-magnitude $\bar{g}$ vectors (*solid green line*). The smaller circles represent equi-magnitude k_{SPP} vectors before (*solid red line*), and after (*dashed red line*) surface functionalization of the grating. The blue arrows represent the incident on-plane wavevector $k_{||}{}^{(in)}$ and the red arrows represent the SPP propagation direction. Letters A and B represent vectors with azimuthal rotation $\varphi = 0°$ and $\varphi \neq 0°$ respectively. In (B) the reflectivity curves in correspondence of SPP excitation for the cases depicted in (A) are shown. Focusing on the first dip of the $\varphi \neq 0°$ configuration (B), it is clear that the detected resonance angle shift is higher than the one detected for $\varphi = 0°$.

At first we consider the case of the uncoated sample, the smallest of the semicircles.

For example, point B on the $\bar{g}$ circle, identified by the azimuthal angle $\varphi \neq 0°$, allows the excitation of SPPs at two possible conditions: B'1 and B'2.

On the contrary, at $\varphi = 0°$ (point A) it is clear that the photon wavevector can intersect the SPP circle only in the first quadrant but not the second, thus exciting only a single SPP for each wavelength (point A').

The same argument is applicable in the case of light impinging on the sample after functionalization. Due to the larger $\bar{k}_{SPP}$, a different excitation condition is expected. Therefore the intersection point changes, for instance from B'1 to B'2 and from A' to A''. The condition for double SPP excitation around the circumference of the $\bar{k}_{SPP}$ circle generates a shifts in k-space between points B'1and B''1, which is much larger than that between points A' and A'' provided by a single SPP excitation ($\varphi = 0°$).

Therefore the resonance angle shift in the reflectivity curve is greater in the rotated mounting than in the classical one **Figure 1. 8 (B)**.

Within the double SPP range (point B), as the incident wavelength or the azimuthal orientation φ increase, the points B'1 and B'2 will gradually merge to form a very broad dip with even higher sensitivity as experimentally shown by Romanato et al [19] (**Figure 1. 9**).
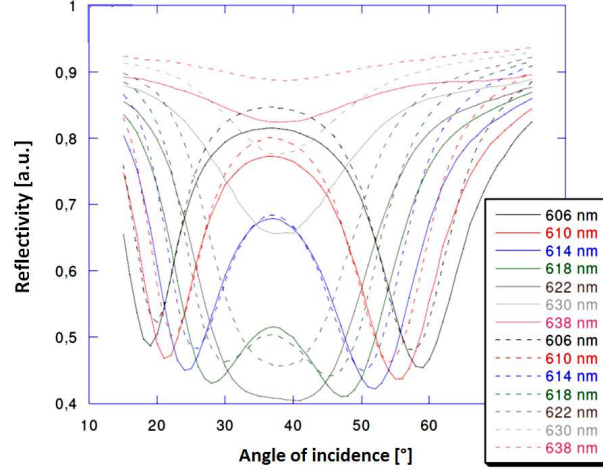
Figure 1. 9. In angular interrogation, as the incident wavelength increase, the two SPP dip will gradually be broader until merging giving a single reflectivity dip. *Dashed lines* represent the reflectivity dip detected for the starting sensing substrate, while *solid lines* are referred to the functionalized surfaces.

As a consequence of the symmetry breaking due to the azimuthal rotation of the grating, the incident polarization must be tuned in order to optimize the coupling with SPP modes [20]. While in the classical mounting p-polarization is the most effective for SPP excitation, after a rotation at an azimuth φ, the incident polarization should be fixed at a value a_{opt} given by:

$$\tan \alpha_{opt} = \tan \varphi \cos \theta_{res} \tag{1. 38}$$

SPP modes just described have been demonstrated to exhibit a greater sensitivity to surface changes with respect to the classic ones because thanks to a geometrical effect related to the azimuthal rotation of the grating vector, the resonance angle shift, for instance consequent to surface functionalization, can be enhanced [19]. Moreover, a double-SPP excitation is allowed, with sensitivity values increasing with the angle of propagation of the surface plasmon with respect to the grating grooves.

1.5   SPR sensor performances: sensitivity and resolution

In this Section we show all SPR sensor performance parameters that can be determined [17]. For our experimental work we chose to focus on the calculation of the system sensitivity and resolution.

Refractive index sensitivity

The refractive index sensitivity (S_{RI}) is defined, in general, as the ratio of the change in sensor output (*Y*) to the change in the measurand (i.e. the refractive index *n* in this case):

$$S_{RI} = \frac{\Delta Y}{\Delta n} \tag{1.39}$$

where n is the refractive index and Y is the sensing experiment output in tern of resonance angle shift or resonance wavelength shift.

The comparison of reflectivity data before and after functionalization provides information about the change of plasmonic resonances such as angular $\Delta\theta$ or wavelength $\Delta\lambda$ shifts of dip position, thus Y could stand for θ or λ. In order to estimate the refractive index sensitivity (Eq. (1. 39)), an estimation of the effective refractive index variation due to a functionalization in necessary. Once surface plasmon polaritons are excited, the confined electromagnetic field experiences a dielectric medium which is different because of the presence of the adsorbed layer. The effective permittivity ε_{eff} is calculated by averaging the permittivity $\varepsilon(z)$ over the depth of the whole multi-layered structure, always weighting the local refractive index with a factor that takes into account the exponential decay of the field [21]. This average is therefore calculated with the depth integral:

$$\varepsilon_{eff} = \frac{2}{L} \int_0^{+\infty} \varepsilon(z) \cdot e^{-\frac{2z}{L}} dz \tag{1.40}$$

where L is the extention length of the excited SPP.

From Maxwell's equations we get an analytical expression for the extension length as a function of the exciting wavelength λ and the surrounding media ([16]):

$$L = \frac{\lambda}{2\pi} \sqrt{-\frac{\varepsilon_{eff} + \varepsilon_m}{\varepsilon_{eff}^2}} \tag{1.41}$$

where ε_m is the dielectric permittivity of the metal side.

For a single-layer functionalization of thickness d and dielectric permittivity ε_l we find out from Eq. (1. 40):

$$\varepsilon_{eff} = \varepsilon_0 + (\varepsilon_l - \varepsilon_0)\left(1 - e^{-\frac{2d}{L}}\right) \tag{1.42}$$

Since the layer thickness is usually much thinner than the SPP extension length in air ($d/L \approx 10^{-2}$) it is reasonable to approximate:

$$\Delta\varepsilon = \varepsilon_{eff} - \varepsilon_0 \cong (\varepsilon_l - \varepsilon_0)\frac{2d}{L} \tag{1.43}$$

After inserting last expression into Eq. (1. 46) and rearranging terms, we get a 3rd degree polynomial equation that could be solved in the unknown L:

$$\pi^2 \varepsilon_0^2 L^3 + \left[4d\pi^2 \varepsilon_0(\varepsilon_l - \varepsilon_0) + 4\pi^2(\varepsilon_l - \varepsilon_0)^2 d^2 + \lambda^2(\varepsilon_0 + \varepsilon_M)\right]L^2 + \frac{d}{2}(\varepsilon_l - \varepsilon_0)\lambda^2 = 0 \tag{1.44}$$

Once L has been calculated with the condition $L \geq 0$, after putting the value into Eq.(1. 43), we get the following estimation for the effective refractive index change:

$$\Delta n_{eff} = \frac{\partial n}{\partial \varepsilon} \Delta \varepsilon_{eff} \cong \frac{\varepsilon_l - \varepsilon_0}{\sqrt{\varepsilon_0}} \cdot \frac{d}{L} \qquad (1.45)$$

Thus if film thickness and optical properties, in term of complex dielectric permittivity are known, it is possible to get an estimation of the corresponding variation n_{eff} in the effective refractive index which is experienced by the excited SPP at the considered wavelength. Inserting Δn_{eff} into Eq. (1. 39) we could obtained the refractive index sensitivity of our sensing system.

An analytical expression of S_{RI} in angular interrogation could also be found from [19]:

$$S_{RI} = -\frac{1}{\cos \theta_{res}} \left(\frac{M}{n_0} \right)^3 \frac{\sqrt{\frac{1}{\Lambda^2} + \frac{\sin^2 \theta_{res}}{\lambda^2} - \frac{2 \cos \varphi \sin \theta_{res}}{\Lambda \lambda}}}{\frac{\cos \varphi}{\Lambda} - \frac{\sin \theta_{res}}{\lambda}} \qquad (1.46)$$

where M is derived from the dispersion relation expressed in Eq. (1. 20), n_0 is the refractive index of the surrounding dielectric medium, λ is the incident wavelength and θ_{res} is the resonance angle (Eq. (1. 36))

Resolution

The sensor resolution (σ_{RI}) is the smallest change in measurand, which produces a detectable change in the sensor output. It can be easily calculated using the following equation.

$$\sigma_{RI} = \sigma_\theta / S_{RI} \qquad (1.47)$$

where σ_θ is the experimental error on the resonance angle shift detected and S_{RI} is the refractive index sensitivity.

Other parameters

Linearity

Sensor *linearity* may concern primary measurand (analyte concentration) or refractive index and defines the extent to which the relationship between the measurand and sensor output is linear over the working range. Linearity is usually specified in terms of the maximum deviation from a linear transfer function over the specified dynamic range. In general, sensors with linear transfer functions are desirable, as they require fewer calibration points to produce an accurate sensor calibration.

Accuracy

Sensor *accuracy* describes the closeness of agreement between a measured value and a true value of the measurand (analyte concentration or refractive index). It is usually expressed in absolute terms or as a percentage of the error/output ratio.

Reproducibility

Reproducibility is the ability of the sensor to provide the same output when measuring the same value of the measurand (analyte concentration or refractive index) under the same operating conditions over a period of time. It is typically expressed as the percentage of full range.

Dynamic range

The *dynamic range* describes the span of the values of the measurand that can be measured by the sensor.

Limit of detection

The *limit of detection* (LOD) is the concentration of analyte C_L derived from the smallest measure Y_L that can be detected with reasonable certainty. The value of Y_{LOD} is given by the equation:

$$Y_{LOD} = Y_{blank} + m\sigma_{blank} \tag{1.48}$$

where Y_{blank} is the mean of the blank (sample without analyte) measures, σ_{blank} is the standard deviation of the blank measures and m is a numerical factor chosen according to the confidence level desired (typically 2 or 3).

As $c_{blank}=0$, the concentration LOD, c_{LOD}, can be expressed as:

$$c_{LOD} = \frac{1}{S_c(c=0)} m\sigma_{blank} \tag{1.49}$$

where S_c denotes the sensor sensitivity to analyte concentration.

Limit of quantification

The *limit of quantification* (LOQ) is sometimes used too. Analyte quantification is generally accepted to begin at a concentration equal to 10 standard deviations of the blank. Thus, the LOQ concentration c_{LOQ}, can be expressed as:

$$c_{LOQ} = \frac{10}{S_c(c=0)} \sigma_{blank} \tag{1.50}$$

In this work refractive index sensitivity and resolution were calculated using the methods described above and were then compared as shown in the Conclusions Chapter.

1.6   PC-SPR *vs.* GC-SPR: a sensitivity comparison

Prism-coupling (PC-SPR) assures refractive index sensitivities (S_{RI}) from 50 to 200°/RIU (resolution of about $2\times10^{-6}-10^{-7}$ RIU) depending on the metal layer composition and thickness [22–25]. GC-SPR, which permits avoiding the use of the prism through the direct illumination of the metallic nano-grating, was initially shown to display slightly lower S_{RI} values [17,24,26–28] than those obtained by PC-SPR. However, more recently, sensitivities of the same order or higher have been demonstrated also with GC-SPR for example, by creating a miniaturized 200 parallel sensing channel system (50°/RIU) [29], by selecting silver-based grating parameters so to create a

surface plasmon bandgap (650°/RIU) [22,30] or by coupling the grating plasmonic field with core-shell nanoparticles [31].

The enhanced-sensitivity of azimuthally-controlled GC-SPR, deducible from the higher resonance angle shift obtained (**Figure 1. 8**), was demonstrated and was firstly shown experimentally by measuring bulk variations of refractive index with saline solution of controlled concentration [19,20,32,33]. A sensitivity enhancement up to 650°/RIU was shown, almost one order of magnitude greater than in the null-azimuth case [34], which was further confirmed by analyzing the response generated by a monolayer of dodecanethiol [19]. The introduction of the conical configuration was demonstrated to result into a double SPP excitation with a crucial role of the incident polarization, which needs proper tuning in order to optimize SPP coupling. Sensitivity values between 500 and 800°/RIU passing from the first to the second resonance dip were easily achieved [19]. This enhanced sensitivity open the way to new SPR biosensing strategies that can allow improving the current biodetection limit.

In the following table typical sensitivity values for currently adopted SPR devices are reported.

Table 1. 3. Theoretical [17] and experimental [19,35] sensitivity and resolution of SPR sensing structure: prism-based system[a]; grating-based system[b]; azimuthally-controlled grating-based system[c].

Detection approach	Angular interrogation	Wavelength interrogation	Reference
Optical system used	Sensitivity [°/RIU]/ Resolution [RIU]	Sensitivity [nm/RIU]/ Resolution [RIU]	
PC-SPR (λ=630 nm) [a]	191 / $5x10^{-7}$	970 / $2x10^{-5}$	
GC-SPR (λ=630 nm) [b]	43 / $2x10^{-6}$	309 / $6x10^{-5}$	
Azimuthally-controlled GC-PR (λ=625 nm) [c]	520 or 653 / $5x10^{-7}$	874.16/1.4 $x10^{-4}$	

(a, b) Model values taken from [17]; (c) Experimental sensitivity reported in the table are referred to the adsorption of a thin monolayer of biological molecules performed with our sensing systems for both angular [19,35] and wavelength interrogation (Section 7.2.IV).

2. **Materials and methods**

2.1 Sensing platform design

An optical biosensor setup, like the one we adopted, basically consists of the following components:

1. The plasmonic sensing surface.
2. The analyte, i.e. the sample that has to be detected.
3. The probe, i.e. the biological element that senses the presence of the analyte.
4. The light source that illuminates the sample and the wavelength changes with respect to the sensing substrate and to the analyte.
5. The detector, for the output signal collection.

In our case we designed and implemented the sensor platform shown in **Figure 2. 1**. The sensing surface consisted of a thiolene resin sinusoidal grating (≈ 6 cm^2) coated by a bi-metallic layer (Chromium (5 nm)/Gold (40 nm)) and supported onto a glass slide. The grating geometry (period of 500 nm and amplitude of 40 nm). The probe was anchored to the gold surface *via* self-assembly of thiol species onto the gold surface, a widely diffused strategy [36]. Although silver is known to have best plamonic properties than gold (**Table 1. 2**)[33], we chose to fabricate our sensing substrate with gold. Indeed gold forms good SAMs as it binds thiols with high affinity ($\sim$40-44 kcal/mol) [37–39] and it does not undergo any unusual reactions with them (e.g., the formation of a substitutional sulfide Interphase) [36]. Finally gold is chemically stable and essentially inert. Indeed it does not oxide at temperature below its melting point (1337,33 K/1064,18°C), a desirable feature due to the fact that some biological binding experiments are performed at high temperature; it does not react with atmospheric oxygen and it does not react with most chemicals. These properties make it possible to handle and manipulate gold samples under atmospheric conditions instead of under UHV and allow the using of liquid cleaning solutions containing for example oxygen peroxide, alcohol, ammonium (often adopted as surface cleaning, an important first step for biosensing experiments [36])

Gold is also compatible with cells, that is, cells can adhere and function on gold surfaces without evidence of toxicity. SAMs formed from thiols on gold are also stable for periods of days to weeks when in contact with the complex liquid media required for cell studies.

Thus the probe was anchored onto the gold surface *via* thiol-gold chemistry and then it was exposed to the analyte. Between the probe and the sensing surface, a spacer molecule, with antifouling function (e.g. poly (ethylene oxide), see Section 4.4.I), was deposited in order to protect the surface from non-specific adsorptions that can be due to the presence of a complex analyte or to non-specific compounds in the analyte solution.

A spectroscopic ellipsometer was used for the light source (in particular wavelengths in the visible range between 600 and 800 nm) and also for the signal detection.

Figure 2. 1 shows the structure and working principle of the sensing platform realized in this work.
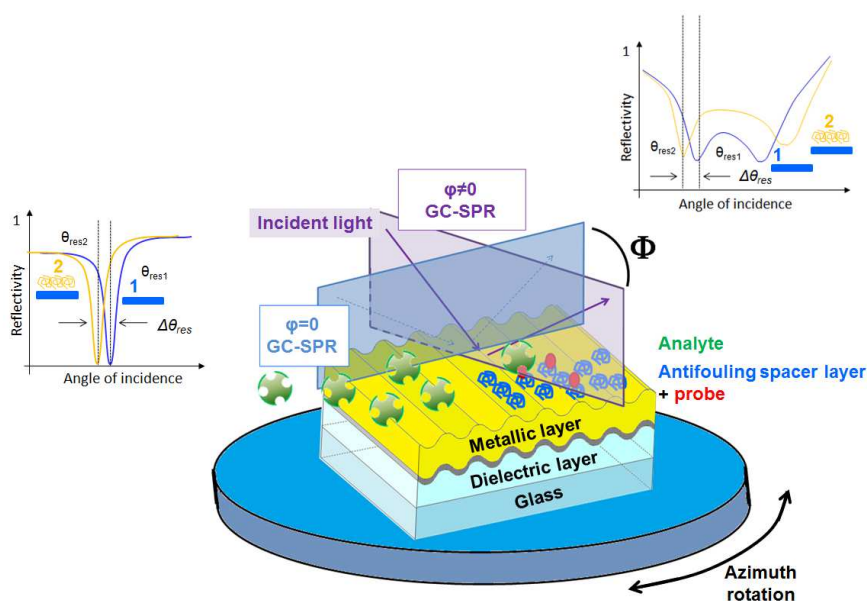
Figure 2. 1. Scheme of the sensing platform realized in this work. The thiolene resin is supported onto a glass slide and it is covered by the metallic layer. In the two insets the two GC-SPR methods are shown: the classic GC-SPR detection (*left*, *blu*-original grating surface; *orange*-functionalized grating surface), and the azimuthally controlled GC-SPR detection (*right*, *blu*-original grating surface; *orange*-functionalized grating surface). The change in the photon scattering plane between the two configurations from orthogonal with respect to the grating "ridges" for simple GC-SPR to rotated for the azimuthally-controlled GC-SPR of a certain azimuthal angle, are indicated with *light blue* and *purple*, respectively. Nell'immagine: spacer anziché spacer Probe può andare maiuscolo come gli altri elementi

Starting from the plasmonic platform described above, all the sensing systems summarized in **Table 2. 1** were realized.

Table 2. 1. Details of the types of sensors investigated in this work.

Type of sensor	Spacer layer (antifouling)	Probe	Analyte	Type of SPR interrogation	Analyte environment	Chapter
Protein	HS-PEO[1]	biotin	avidin	angular	liquid	4
Tuberculosis	HS-PEO	PNA[2]	DNA[3]	angular	liquid	4
Cistic Fibrosis	HS-PEO	DNA	DNA	angular	liquid	5
Explosives	-	6-MNA[4]/MIP[5]	TNT[6]	Angular/wavelength	gas	6
Bacteria	HS-PEO	antibody	L.pneumophila	wavelength	liquid	7

[1]poly (ethylene oxide); [2]peptide nucleic acid; [3]desoxyribonucleic acid; [4]6-Mercaptonicotinic acid; [5]molecularly imprinted polymer; [6]trinitro toluene.

2.2 Characterization methods

In this section all the techniques used to characterize both the biological components and the plasmonic sensing response are described.

Spectroscopic Ellipsometry and SPR reflectivity measurements (Appendix A.1)

Both Spectroscopic Ellipsometry and SPR reflectivity measurements were performed on a J. A. Woollam Co. VASE ellipsometer; with angular and spectroscopic resolution of 0.01° and 0.3 nm, respectively. *Spectroscopic Ellipsometry* was performed onto biological films deposited onto flat gold surfaces for deriving their optical constants. An incident wavelength in the range of 300-1200 nm and a scanning incident angle range of 50°-70° were adopted.

Reflectivity measurements of the plasmonic gratings were performed in the dry state. For the azimuthal angle rotation, a goniometer with a 0.1° precision mounted onto the sample holder was used. This setup consists in a Xenon-Neon lamp (75W) as a light source with a monochromator and focusing system that allow selecting wavelengths in the range 270 – 2500 nm. Polarization state is controlled with a first polarizer and the output light that hits the sample is reflected into a detector arm, consisting in a rotating polarizer (analyzer) and a photodiode system for signal conversion and amplification.

Parameters adopted for SPR sensing experiments are summarized in the following table.

Table 2. 2. Characterization parameters adopted for SPR reflectivity measurements

Type of sensor	Incident wavelength [nm]	Angle of incidence [°]	Azimuth [°]	Light polarization [°]
M. Tuberculosis (PNA/DNA)	625	20-80	45	140
	650-800	20-80	0	-
Protein (biotin/avidin)	625	20-80	45	140
Cystic Fibrosis (DNA/DNA)	625	20-80	45	140
Explosives (6-MNA/TNT)	700-800	70	45	140
(MIP)	300-700	70	45	140
L. pneumophila (antibody/bacterium)	600-800	70	45	140

Scanning Electron Microscopy (Appendix A.2)

SEM micrographs were collected with a dual beam FEI Nova 600i instrument, using a semi-in-lens cold cathode field emission scanning electron microscope source at 30 kV accelerating voltage using in-lens detector in pure secondary electron signal mode.

Atomic Force Microscopy (Appendix A.3)

A VEECO D3100 Nanoscope IV atomic force microscope, equipped with tip having 10 nm curvature radius, 10-15 μm height and curvature angle ≤ 22° was used. All measurements where performed in the non-contact mode with a scan rate between 0.8 and 0.95 Hz and a resolution of 512X512 pixel^2.

Nuclear Magnetic Resonance (NMR)
H^1-NMR analysis was carried out using a Bruker AMX 300 MHz.

Fluorescence analyses

Fluorescence measurements on hybridized array (both DNA or cell targets) were performed using Genepix 4000B laser scanner (Molecular Devices, Sunnyvale, CA) using the characterization parameters reported in

Table 2. 3. Fluorescent spot intensities were quantified using the Gene Pix Pro software after normalizing the data by subtracting local background from the recorded spot intensities.

Microarray glass slides "e-surf" slides (LifeLineLab) were deposited using a microarray spotter robot (Versarray Chip Writer, Biorad) following the instrument and procedure flow depicted in **Figure 2. 2** as control of the process steps and of detection sensitivity for all the described sensors. Moreover, flat gold slides were used as control for PNA-based sensor and for the *L. pneumophila* sensor.

Table 2. 3. Characterization parameters adopted for fluorescence measurements for both cystic fibrosis and *Legionella pneumophila*.

Type of Sensor	Type of sample	Wavelength [nm]
Peptide nucleic acid	Mycobacterium DNA	532
DNA sensor for cystic fibrosis	Cystic Fibrosis DNA (wt/*mut*)	532/635
Sensor for *L. pneumophila*	*L. pneumophila* cells	635
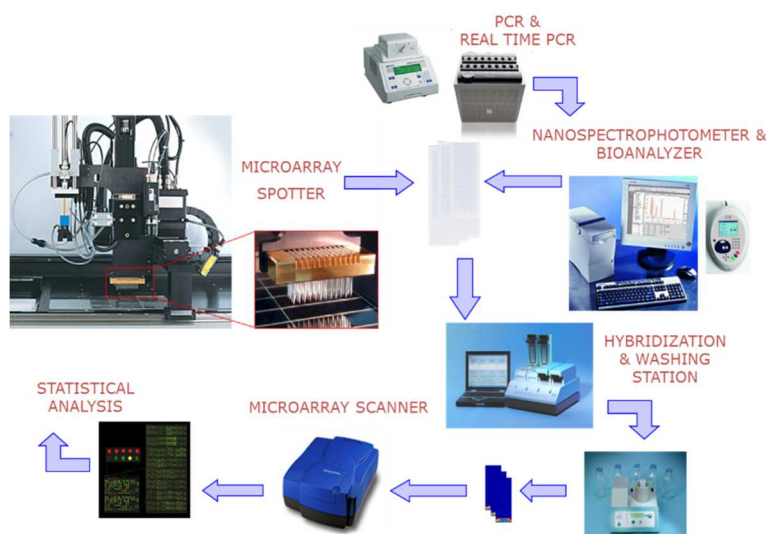
Figure 2. 2. Work-flow of instruments and procedures used for fluorescent microarray analysis. Analyte were DNA oligonucleotides, for which it was enough a sample preparation using a microarray spotter, or PCR amplified DNA. For PCR amplified DNA, PCR instrument, Bioanalyzer and Nanospectrophotometer were used to obtain and quantify the products. After sample preparation, samples were hybridized using Microarray Hybridization and Washing Station (Advalytix), with optimized buffer composition and hybridization temperature, and microarray slides were analyzed with GenePix laser scanner, using both λ 532 nm and 635 nm. Finally statistical data were collected for genotyping.

UV-Vis absorption measurements

Absorption spectra of films deposited (performed for TNT sensor in Chapter 6) on silica glass slides were collected in the range 200–800 nm using a UV–Vis spectrophotometer (JascoV-570) with a resolution of 0.1 nm.
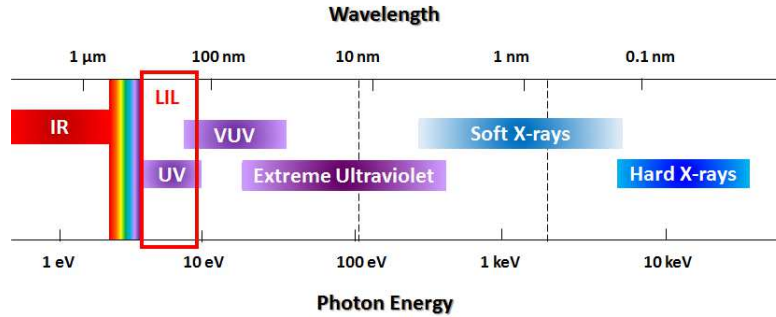
3. **Fabrication**

Abstract

Laser interference lithography is a top down fabrication method that allows to obtain homogeneous and controllable sinusoidal gratings onto large areas (about 4 cm^2) in few times [40–42]. On the other hand soft lithography is a widely used technique for having a large number of replica of a starting nanostructure using simple and cheap materials [43–46]. Starting from these two techniques we developed a fabrication strategy made by the combination of LIL and soft lithography (**Figure 3. 1**). Our strategy allowed us to obtain a large number of reproducible sensing substrates in few steps and resistant to chemical solutions adopted for the sensing applications.
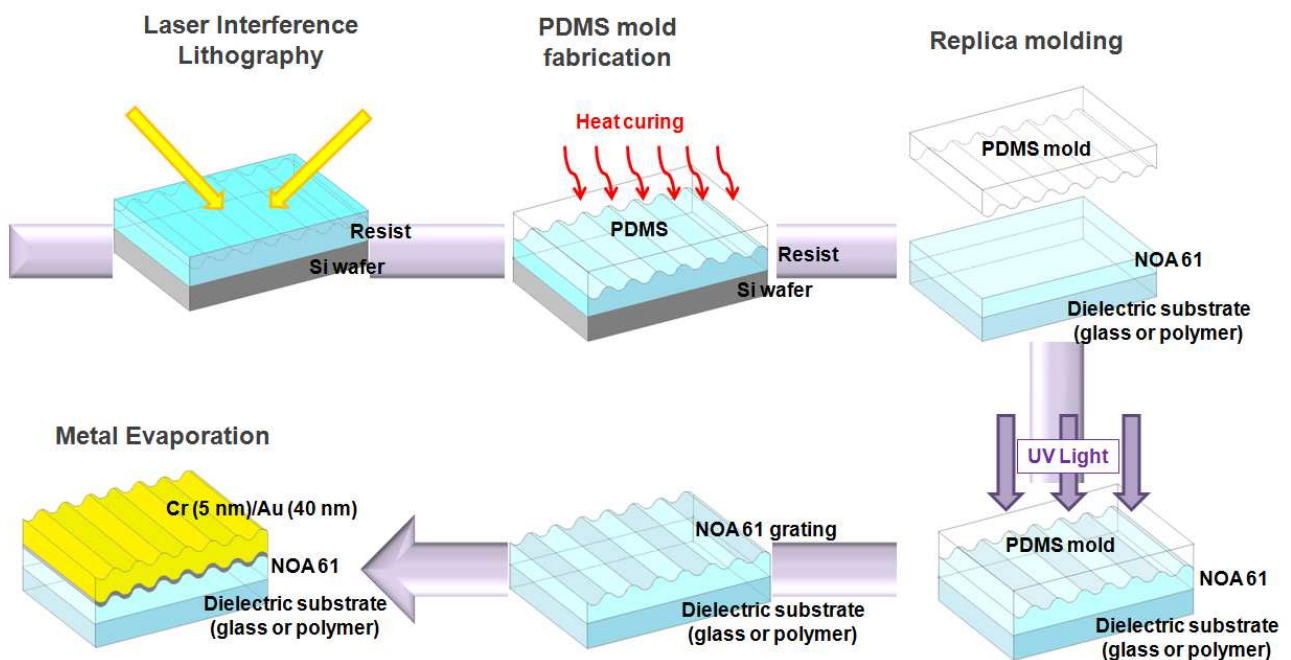
Figure 3. 1. Fabrication strategy adopted for the realization of all the sensing substrates used in this work. The fabrication method consisted into realizing a sinusoidal grating through laser interference lithography, replicating it through soft lithography and then depositing a bi-metallic layer onto the surface.

## 3.1   Laser interference lithography (LIL)

IL is an optical lithography belonging to the *UV photolithography* class (see **Figure 3. 2**) where the light beam is generated by a laser of the desired wavelength (for this reason Interference Lithography is often called Laser Interference Lithography).

Figure 3. 2. Complete spectrum of photon wavelength. IL belongs to the UV photolithography class.

IL is the preferred method for fabricating periodic and quasi-periodic patterns that must be spatially coherent over large areas. It is a conceptually simple process where the interference of coherent light forms a standing wave, which can be recorded in photoresist. The principal advantages of LIL, as it is shown in many [47–49], are the short exposure times, simple experimental equipment and the possibility to pattern large areas. The use of IL offers other numerous advantages over conventional methods: IL is both maskless and lensless, minimizing the cost and eliminating the optical aberrations that accompany a complex system of lenses. The depth of field is determined by the beam diameter, intensity profile, and the angle of intersection, and is typically so large (from tens of microns to centimetres) that for most purposes it may be considered infinite. Finally, the IL technique provides complete control over aerial image contrast. Intersection of intensity-matched beams produces a sinusoidal aerial image with 100% intensity modulation, independent of the grating period. The modulation of the light image can be varied precisely and at will by unbalancing the intersecting beams.

The classical and simplest configuration is the two-beam interference (**Figure 3. 3**): two light beams of wavelength λ are incident on the sample surface with an angle θ. This configuration makes possible the realization of digital or sinusoidal gratings. Through additional exposures, or the interference of more than two beams, the possible patterns increase from simple gratings to a wide variety of periodic structures.
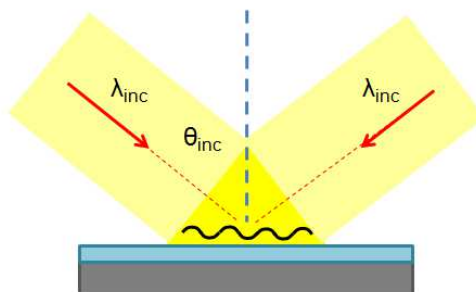
Figure 3. 3. The two-beam IL configuration

The period of the pattern can be varied continuously over a wide range by simple mechanical adjustment of the optical system, allowing systematic studies of behaviour of materials as a function of pitch. The pattern period, p, is described by Eq. (3. 1).

$$p = \frac{\lambda}{2\,sen\,\vartheta}$$

(3. 1)

where λ is the incident beam wavelength and θ is the incidence angle of the two light beams.

Besides the grating period, another important parameter affects the final pattern: the exposure dose D (Eq.(3. 2)), which indicates the amount of energy that hit the sample on an area of 1 cm^2.

$$D = Power \times t$$

(3. 2)

where Power is the laser power measured in μW/cm^2, t is the exposure time expressed in seconds and D is conventionally expressed in mJ/cm^2.

Controlling the angle of light beam incidence and the exposure dose, grating period and amplitude can be tuned fitting the desired features for the final device.

3.1.I   Fabrication procedure by LIL: the resist processing

The final pattern quality depends on the resist processing and properties, so particular attention has to be given to all the resist processing steps, which can be summarized in:

- Substrate preparation (Resist stability, contamination, and filtration)
- Resist coating
- Soft-bake
- Exposure
- Post-exposure bake
- Development
- Post-development treatment

Substrate preparation

In the simplest case the substrate preparation only consists in the cleaning of the substrate surface. Cleaning procedures vary according to substrate surface composition and prior processing, but all procedures have to remove organic and inorganic contaminations and particles, which can damage the printed pattern for example by embedding themselves in the resist.

Cleaning procedures that use solvents, including dipping, vapour degreasing, spraying, and ultrasonic immersion, are the most common. Also plasma cleaning is quickly becoming a popular alternative for removing organic and inorganic contamination. A dehydration bake at 200 °C or higher temperature (with optional vacuum) in an oven or on a hot plate typically follows the solvent-cleaning steps. This bake is necessary to remove traces of absorbed water on the wafer surface.

In other cases the substrate preparation is quite more complex and involves other processes such as the introduction of an adhesion layer or promoter on the substrate surface before the resist coating. Trapped voids, either in the bulk or at the wafer interface, must be removed completely by proper choice of solvent, which

must evaporate slowly to avoid creating internal bubbles. Baking conditions are also selected to minimize the evaporation rate of residual solvent and to promote annealing.

Resist coating

A photoresist can be dispensed by several methods: spin coating, spray coating, and dip coating. The most widely used method is the spin coating one. During spin coating, the resist is dispensed onto a wafer substrate (either statically or dynamically), accelerated to final spin speed, and cast to a desired film thickness. Spin-coating processes use the dynamics of centrifugal force to disperse a polymeric resist material over the entire wafer surface. The wafer is accelerated rotationally to the final spin speed of 2000-4000 rpm typically.

The coating process is essentially influenced by two parameters that could affect the final film properties: the flow properties (rheology) of the resist and the solvent transport through evaporation, which can result in an increase in resist viscosity and consequently in a lower film thinning.

Soft-bake

Baking processes are used to accomplish several functions and generally alter the chemical and/or physical nature of a resist material. Goals of resist baking operations may include the following:

- Solvent removal
- Stress reduction
- Planarization
- Reduction of resist voids
- Reductions of standing waves
- Polymer cross-linking and oxidation
- Polymer densification
- Volatilization of sensitizer, developer, and water
- Induction of (acid) catalytic reactions

A proper choice of the baking temperature, time and method is necessary in order to allow some degree of fluid-like resist behaviour, in which stress in a coated film can be reduced and diffusion of solvents, sensitizer, and photoproducts is enhanced, for example carrying out the baking step at a temperature near the Tg, and in order to avoid polymer decomposition occurring at high baking temperatures.

Exposure

Exposure of a photoresist involves the absorption of radiation and subsequent photochemical change, generally resulting in a modification of dissolution properties.

Both maximum light transmission (to reach to the bottom of the resist) and absorption (to achieve the highest sensitivity) are desired. There is therefore an optimum resist absorbance value for any resist thickness. If a resist film has a thickness t and dt is the thickness of the bottom portion of the resist, the intensity transmitted through the film thickness to dt can be determined from Lambert Beer's law:

$$I = I_0 \cdot e^{-\varepsilon m(t)} \qquad (3.3)$$

where ε is the molar extinction coefficient of the sensitizer, and m is the molar concentration.

The energy density absorbed at the bottom of the resist is

$$E = I_0 \cdot e^{-\varepsilon m(t)} \frac{\left(1 - e^{-\varepsilon m(dt)}\right)}{dt} \qquad (3.4)$$

Because dt is small, $e^{-\varepsilon m(dt)}$ can be approximated as $1 - \varepsilon m(dt)$ and

$$E = I_0 \cdot (\varepsilon m) e^{-\varepsilon m(t)} \qquad (3.5)$$

which is maximized when $\varepsilon m(t) = 1$. Converting to absorbance:

$$Absorbance = \log[\ e(\varepsilon mt)] = 0.434 \qquad (3.6)$$

This is the optimum absorbance for a resist film regardless of thickness. In other words, higher absorption is desired for thinner resists and lower absorption is desired for thicker films.

When light is incident on a resist layer, in addition to the primary standing wave formed in the plane of the substrate, there is a second standing wave that can form perpendicularly to the substrate, due to the interference between the vertical components of the incident light and the light reflected at interfaces in the resist stack. In particular, when light is reflected at the boundary between the photoresist and the underneath substrate, a vertical standing wave forms, which can modify the predict pattern and severely degrade the resist profiles (**Figure 3. 4** and **Figure 3. 5**).
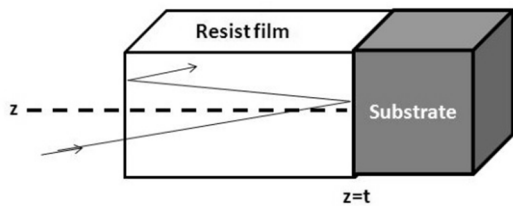
Figure 3. 4. Multiple reflection generation at the resist-substrate interface
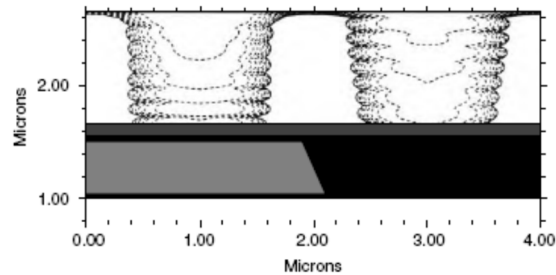
Figure 3. 5. Resist standing waves resulting from coherent inference of incident and reflected radiation within a resist layer. Standing wave phase and amplitude is dependent on the underlying substrate.

The period of the vertical standing wave is determined by the same factors that govern the period of the grating: the light wavelength and the angle of interference.

A higher reflectivity at the resist/substrate boundary leads to a higher contrast standing wave and more damage to the resist pattern. Obviously, one way to decrease the effects of this standing wave is to minimize the reflectivity at this interface. The use of a bottom-anti-reflection coating (BARC) underneath the resist is a standard procedure for reducing the effects of the vertical standing wave. The BARC would be able to reduce the reflectivity at the bottom of the resist.

Post-exposure bake (PEB)

Figure 3. 6 shows the impact that a PEB step can have on resist standing waves.
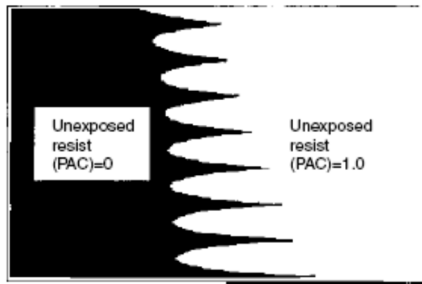
Unexposed regions of the photoresist contain a photoactive compound (PAC), exposed regions contain photoproduct, and the boundaries between them are determined by the constructive and destructive interference nodes of the exposure standing wave.

Figure 3. 6. Distribution of photoactive compound (PAC) as a result of standing-wave resist exposure

If the resist temperature is near or above its Tg, the PAC can effectively diffuse through the polymer matrix and produces an averaging effect across the exposed/unexposed boundary, leveling the pattern profile and giving more uniformity to the pattern. But if the PAC diffusion length is too high the pattern profile would result altered or damaged, so an appropriate and controlled PEB temperature is needed, considering also the resist characteristics.

Development

Resist development is a critical step in lithography, because it exerts great influence on pattern quality. The traditional development method uses a liquid developer solution that preferentially dissolves either the exposed region (positive resists) or the unexposed region (negative resists). Development can be carried out by either spray or immersion techniques. Many operating parameters affect the outcome of resist development, such as developer strength, agitation, temperature and humidity at which development takes place, and the size of developer molecules. All these parameters influence the relative rates of dissolution of both exposed and unexposed regions, as well as the degree of swelling and latent-image distortion.

Developer solutions may be alkaline solutions or commercially available products. To have a better develop control and a less strong effect on the resist the developer could be diluted

The working principle of the developing step is the resist dissolution in the exposed or unexposed region, depending on the resist tone (positive or negative).

Hard-bake

Post-development baking is often utilized to remove remaining casting solvent, developer, and water within the resist. Baking above the resist's Tg also improves adhesion of the resist to the substrate. Because photosensitivity is no longer required, the baking temperature can be elevated toward the solvent boiling point (Tb), effectively eliminating the solvent from the resist and allowing the maximum densification.

3.1.II Experimental setup

A variety of methods exist for the separation and recombination of a beam to produce interference fringes (**Figure 3. 7**). The Lloyd's mirror system (**Figure 3. 7**.a) divides the laser beam using a mirror fixed onto the sample holder. The Mach-Zender IL system (**Figure 3. 7**.b) produces the two light beams with a beam splitter, which divides the source radiation into two parts that, after a system of mirrors, reach the sample giving the two-beam interference. Achromatic IL system (AIL) (**Figure 3. 7**.c) uses a series of phase shifting gratings

(grating interferometer) to produce more light beam starting from a source radiation. Immersion AIL (**Figure 3. 7**.d) combines the use of phase shifting gratings and a fluid in which the radiation can be refracted.
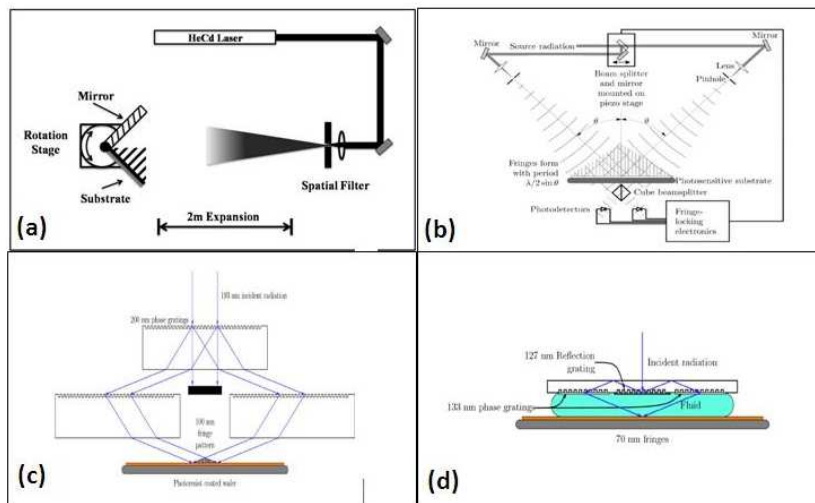

Figure 3. 7. Possible experimental configuration to obtain a 2-beam interference: Lloyd's mirror system (a); Mach-Zender IL system (b); achromatic IL system, AIL, (c); immersion AIL (d)

The method proposed by Lloyd in 1837, involves using a broad beam of light and a mirror to fold a portion of the wavefront back onto itself. **Figure 3. 9** shows a schematic of the Lloyd's mirror interferometer. With the mirror rigidly fixed perpendicular to the surface, the angle of interference, and thus the period of the grating, is set by rotating the mirror/ substrate assembly around the point of intersection of the mirror and the substrate, and the angle of interference is read on a goniometric sample holder situated at the base of the interferometer. Although the light is incident on the substrate at a different angle than the mirror, simple trigonometry guarantees that the light reflected off the mirror is always incident on the substrate at the same angle as the original beam. By having the mirror at a fixed angle to the substrate, the mirror can be brought into physical contact with the substrate to reduce scattering noise.

In this work, the Lloyd's mirror system of National Laboratory IOM-CNR at Basovizza (Trieste), consisting of a laser (HeCd in this work), which emits in the UV range (325 nm), was adopted. The laser beam is deviated by a system of mirrors before passing through a spatial filter that selects the central components of the Gaussian beam and reduces the beam diameter to prevent undesired reflections. The light beam reaches the sample mounted onto a rotating stage: half of the beam is reflected by a mirror fixed on the rotary stage perpendicularly to the sample holder and the other half reaches the sample directly.

In **Figure 3. 8** is schematically reported the Lloyd's mirror interferometer, while in **Figure 3. 9** is reported the picture of the LIL experimental setup used in this work.
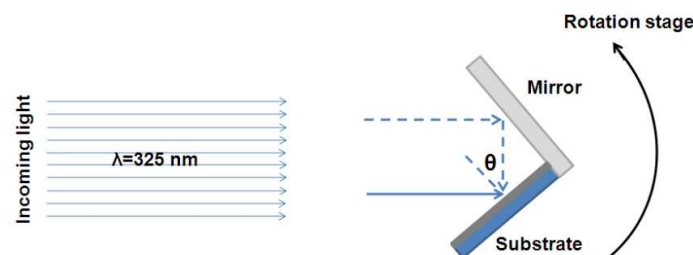
**Figure 3. 8**. Lloyd's mirror IL interferometer
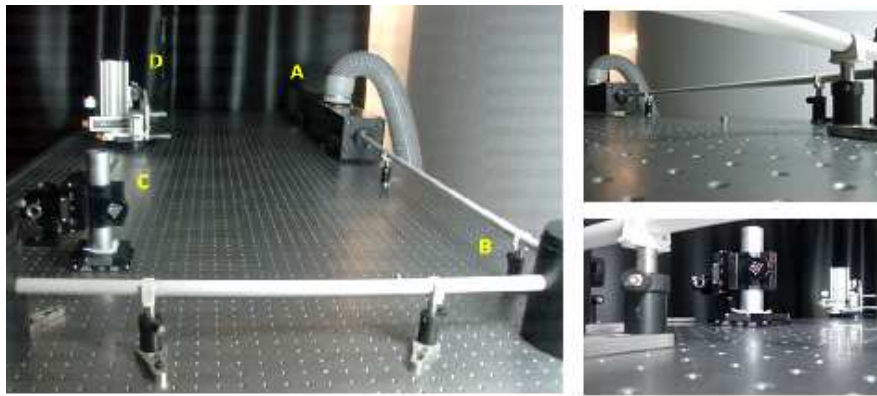
Figure 3. 9. Pictures of the Lloyd's IL system: laser source (A); system of mirrors to deviate the laser beam (B); spatial filter (C); Lloyd's mirror interferometer (D)

3.1.III Fabrication procedure by LIL

The sinusoidal grating fabrication procedure by LIL was optimized for a period of 500 nm and amplitude of 40 nm.

A S1805: PGMEA solution (2:3) was spun onto a silicon wafer with a spin speed of 6000 rpm for 30 s. Sample was exposed to a 50mW Helium Cadmium (HeCd) laser emitting a TEM00 single mode at 325 nm light source with a beam incidence angle of 19° and an exposure dose of 70 mJ/cm^2. Resist developing was performed by immersing the samples in a MF319:Milli-Q water (10:1) solution for 15 s.

In **Figure 3. 10** AFM images of sinusoidal gratings realized by LIL are reported.

(a)   (b)   (c)
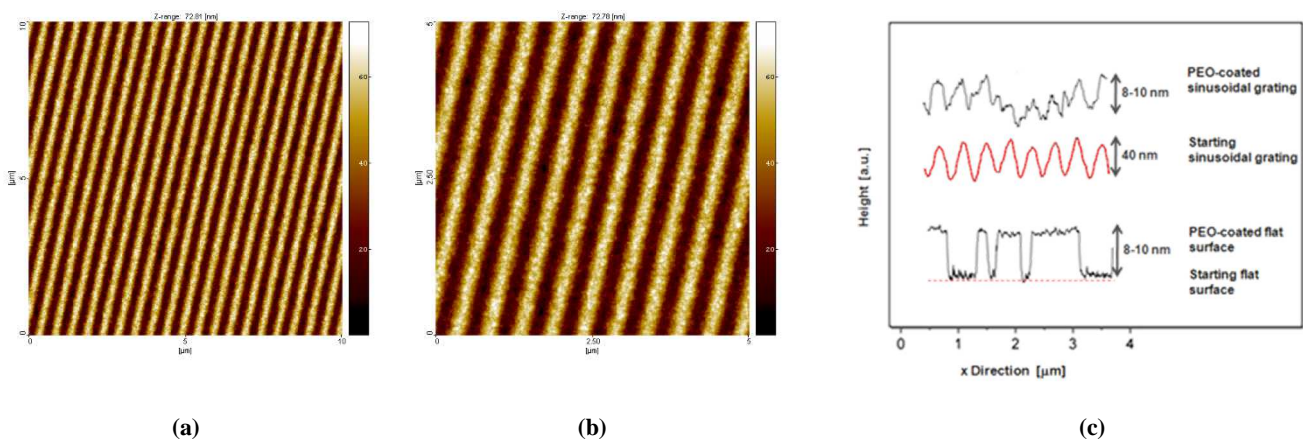
Figure 3. 10. AFM analyses of sinusoidal gratings obtained by LIL: AFM topography (a, b) and sinusoidal profile (c).

3.2 Soft lithography

Soft lithography is a non-photolithographic technology proposed and developed by the [46]. It is based on self-assembly and replica molding for carrying out micro- and nanofabrication and it provides a convenient, effective, and low-cost method for the formation and manufacturing of micro- and nanostructures. In soft lithography, an elastomeric stamp with patterned relief structures on its surface is used to generate patterns and structures with feature sizes ranging from 30 nm to 100 μm [43–45]. Thus through soft lithography we were able to fabricate nanometre-resolution patterns with low cost and high throughput. It creates patterns essentially by replicating the structures present in a patterned elastomeric mold (usually made in PDMS) on a UV-curable polymer.

### *Fabrication procedure by soft lithography*

Starting from the sinusoidal grating realized by LIL a polydimethylsiloxane (PDMS) mold was fabricated curing the PDMS layer dropped onto the resist grating at 60°C for 4 hours.

The nano-pattern was then imprinted onto a thiolene resin film (NOA 61) supported onto a microscope glass slide, illuminating the PDMS mold with Ultra-Violet (UV) light (λ=365 nm) for 30 s, using a standard metal halide 50 mW/cm^2 lamp (DYMAX UV Light flood lamp curing system). A 12 hour thermal treatment at 50°C was then performed in order to increase the resin adhesion onto the glass substrate.

To obtain the final plasmonic substrate, a gold (40 nm) layer was evaporated above the patterned resin film and a thin chromium film (5 nm) was used as adhesion layer between the metal and the underlying dielectric medium. Metal thicknesses were chosen basing on theoretical simulations of SPP coupling on metallic gratings, based on Chandezon's method [50].

3.3 Results

In **Figure 3. 11** SEM and AFM images of the resulting sinusoidal gratings are reported [35,41,51,52].


(a)   (b)
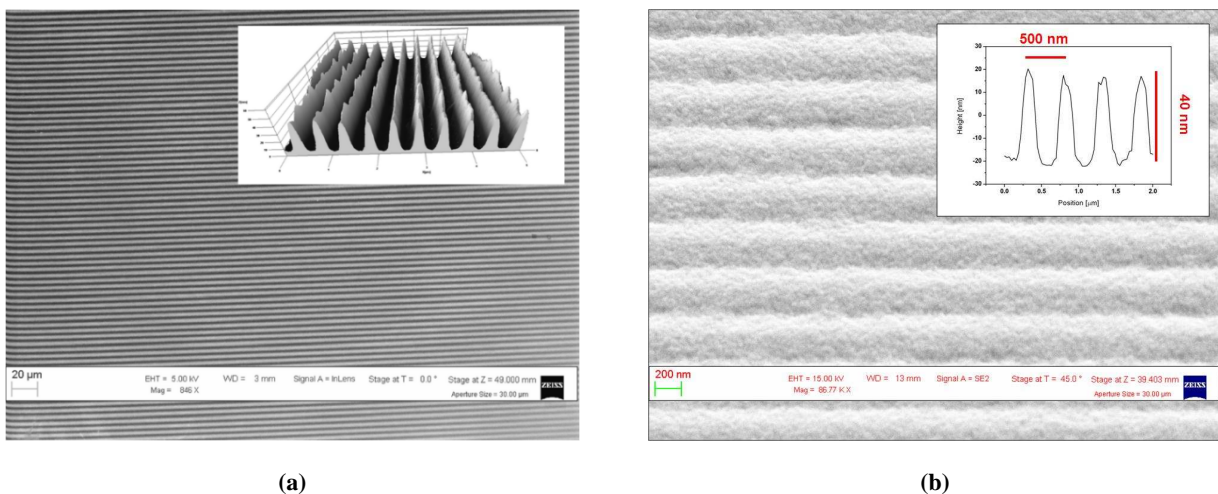
Figure 3. 11. (a) SEM image on a 20 μm scale of a plasmonic sinusoidal grating and AFM 3D image (*inset*); (b) SEM image on a 200 nm scale of a plasmonic sinusoidal grating and AFM profile (*inset*).

Our LIL/soft lithography-combined method allowed to obtain a large number of substrates with high throughput. Both technique adopted were optimized in order to maximize the final available surface area and the reflectivity signal.

A first optimization consisted in the choice of the Lloyd's mirror setup for LIL. Indeed it requires minimal alignment and adjustment. Another advantage of the Lloyd's mirror interferometer is the simplicity with which the period of the grating can be changed. As mentioned earlier, this requires only a rotation of the mirror/substrate assembly. Realignment or repositioning of components is unnecessary.

The second optimization consisted in soft lithography choices: UV exposure time and resin thermal treatment were chosen in order to maximize the resin performance and adhesion to the glass substrate.

In **Figure 3. 12** a scheme of the final plasmonic substrates is reported.
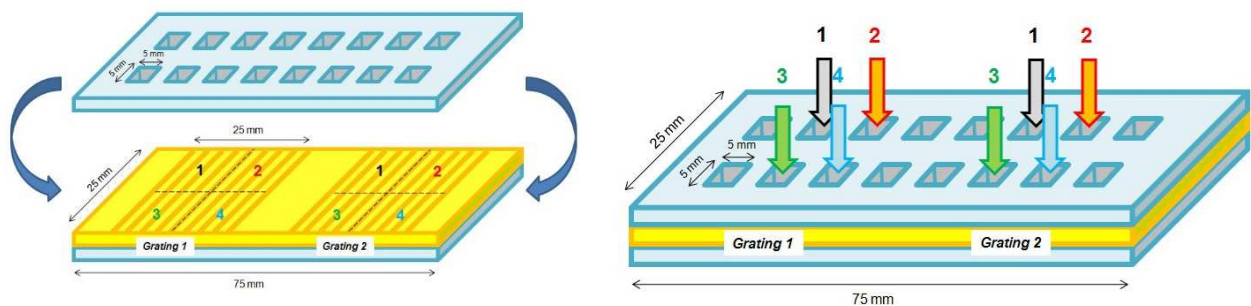
Figure 3. 12. Scheme of the final plasmonic substrate: 2 gratings were realized onto a single glass slide. This strategy allowed to perform a large number of experiments onto the same glass slide using a polycarbonate mask (ProPlate) of 16 o 64 cells.

Using the strategy showed in **Figure 3. 12** we had the possibility of making up to 32 experiments onto the same substrate at the same time. This was a great advantage in terms of statistics and reproducibility of the same experiment using the minimum amount of material needed for the fabrication process.

<div align="right">**Chapter 4**</div>

4. PNA Sensor for *M.tuberculosis*

Abstract

PNA-based biosensors are included in the class of nucleic acid biosensors, those in which the probe molecule is DNA, RNA, or a synthetic polymer analogous to natural nucleic acids [53–56]. The unique physicochemical nature of the peptide-mimetic, neutral PNA backbone has promoted the use of PNA oligomers as capture probes in electrochemical, optoelectronic, and microarray-based biosensors, and in other types of sensor.

Nucleic acid immobilization on the biosensor surface is an important initial step that affects the overall performance of the sensor. In general, nucleic acids are immobilized onto solid surfaces in such a way that a signal is obtained only if they react with their specific target molecules. Hence, experimental conditions must be adjusted for every application, and a large choice of immobilization methods can be used. In this Chapter the optimization of an azimuthally-controlled GC-SPR sensor is shown, from initial tests to final real sensing experiments, performed comparing SPR and conventional microarray (fluorescent) measurements, which lead to a successful detection of *Mycobacterium (M.) tuberculosis*, with its advantages and limits that could be overcome with further studies.

4.1   *M. tuberculosis* sensing

Approximately one-third of the world's population is infected by *M. tuberculosis* and about 3 million people globally die [57] of tuberculosis each year, another 8 million new individuals become infected [58] and tuberculosis has resurged sharply since the mid-1980s [59,60] after its eradication at the end of the twelfth century. Probably, the most serious global problem is a steady increase in the frequency of *M.* tuberculosis strains resistant to at least one of the anti-tuberculosis agents commonly used [58]. The last report prepared by the World Health Organization (WHO) and the International Union Against Tuberculosis and Lung Disease Global Project based on the data from 93 different countries/geographical settings collected between 2002 and 2007 shows that the proportion of drug resistance ranged up to more than 55%. In addition, the multi-drug resistant (MDR) tuberculosis, which is defined as tuberculosis with resistance to isoniazid and rifampicin, the two most powerful first line drugs, is reaching now a critical proportion of more than 20% in some countries. China and India carry approximately 50% of the global burden of MDR cases and the Russian Federation an additional 7% [61]. Due to the fact that, when drug susceptibility testing is culture-based, detection still takes 2–9 weeks [62], the development of a nucleic acid-based sensor for *M. tuberculosis* detection using SPR could respond to the current need for a sensitive, specific, fast and cost-effective method for detection of this pathogen. In addition instead of using classical SPR methods and DNA probes, methods already explored in other works [58,63,64], combining azimuthally-controlled GC-SPR and peptide nucleic acid (PNA) probes could better answer to the tuberculosis sensing requirements becoming a turning point in the *M.* tuberculosis detection scenario [57,65].

4.2   Peptide Nucleic Acid (PNA): properties, limits and challenges

Peptide Nucleic Acid (PNA) was at first designed by Nielsen using computer model building as a reagent to specifically bind double strand DNA (dsDNA) [66] and after the first PNA appearance in the scientific community, a lot of works has followed, from theoretical to applied studies [55,56,65,67–76], all summarized in a recent Briones work [54]. Since it first applications, PNA has become even more popular thanks to its remarkable behaviour and DNA recognition action, a behaviour explained by PNA structure [55].

PNA is an analogue of DNA in which the entire negatively-charged sugar-phosphate backbone is replaced with a neutral "peptide-like" backbone consisting of repeated N-(2-aminoethyl) glycine units linked by amide bonds (**Figure 4. 1 (a)**). The four natural nucleobases (i.e., adenine, cytosine, guanine, and thymine) come off the backbone at equal spacing to the DNA bases. Methylene carbonyl linkages connect the bases to the central amine of the backbone. Thus, PNA contains the same number of backbone bonds between bases (i.e., six) and the same number of bonds between the backbone and the bases (i.e., three), as in DNA. Such structure is not prone to degradation by nucleases or proteases, hence offering high biological stability. The unique structure and the resultant hybridization properties of PNA (discussed below), open up many important biological and diagnostic applications, not achievable with traditional oligonucleotides [55].

Owing to its neutral backbone and proper interbase spacing, PNA binds to its complementary nucleic acid (DNA or RNA) sequence with higher affinity and specificity compared to traditional oligonucleotides.

- It was shown that such hybridization to complementary oligonucleotides obeys the Watson–Crick base-pairing rules with the PNA and DNA strands joined through hydrogen bonds (**Figure 4. 1 (b), (c)**) [77].
- It was demonstrated also that the thermal stability of the resulting PNA/DNA duplex is essentially independent of the salt concentration and pH in the hybridization solution [54]. Such independence of the ionic strength is the result of the uncharged nature of the PNA backbone.
- The neutral backbone also implies a lack of electrostatic repulsion between the PNA and DNA strands (compared to that existing between two negatively charged DNA oligomers), and hence a higher thermal stability of PNA/DNA duplexes. On average, the melting temperature (tm) of a PNA/DNA duplex is 1°C higher per base pair compared to that of the corresponding DNA/DNA duplex [69].

| (a) | (b) | (c) |
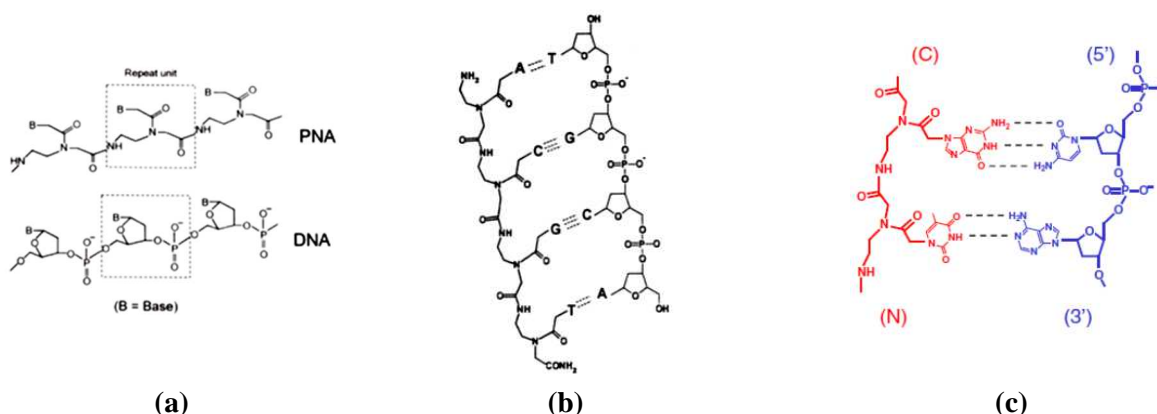
Figure 4. 1. Schematic chemical model of PNA and DNA. The entire negatively-charged sugar-phosphate backbone replacement with a neutral "peptide-like" backbone is shown in (a), while PNA (red)-DNA (blue) bonding with the hydrogen bonding between complementary nucleobases is depicted in (b) and (c) (*dotted lines*).

The thermal stability of the PNA/DNA duplexes is strongly affected by the presence of imperfect matches. Such presence of mismatches in a PNA/DNA duplex is much more destabilizing than a mismatch in a DNA/DNA duplex. For example, a single base mismatch results in 15 and 11°C lowering of the tm of PNA/DNA and DNA/DNA duplexes, respectively. This property of PNA is responsible and maybe it's the

unique way for the remarkable discrimination between perfect matches and mismatches offered by PNA probes, and makes them so attractive as oligonucleotide recognition elements in biosensor technology.

For perfectly sequence-matched duplexes of different lengths (6–20 bp) and sequences, the average free energy of PNA/DNA binding (ΔG) per base pair was determined to be -6.5 ± 0.3 kJ mol^{-1} at 25°C [78], unlike -6.2 ± 0.3 (37°C) [79] and -5.9 (25°C) [80] kJ mol^{-1} for DNA/DNA binding. X-ray crystallography, nuclear magnetic resonance, fluorescence energy transfer, and other, complementary techniques have shown that the typical structures of PNA/DNA heteroduplexes are extended double helices whose features are intermediate between those of the A and B forms of dsDNA. Thus, the PNA/DNA duplex has a helix diameter of 2.3 nm and a helical rise of 4.2 nm with 13 bp per turn [78,81,82].

For the application of PNA in the biosensoristic context, the interaction of PNA with surfaces has been investigated. Thiol-modified PNA oligomers have unprecedented capability for self-assembly on gold surfaces, adopting a standing-up conformation [75]. Furthermore SAMs of PNA on surfaces tend to interact specifically with complementary nucleic acid molecules, and are, for these two reasons, useful for biosensing applications[54,72–75,83]. Although the usefulness of PNA SAMs, it is generally recommended to add a link or spacer molecule to the immobilized PNA to physically separate the hybridization sequence from the biosensing surface. The spacer addition avoids or limits steric hindrance during the process and assures the sensing surface protection from non-specific adsorptions (named *antifouling* property), a strategy widely adopted for biosensors (Section 4.3).

Beyond PNA extraordinary properties, there are also some disadvantages that have to be taken into account while preparing a PNA-based biosensor. Advantages and disadvantages of PNA are reported in **Table 4. 1** [54–56].

Table 4. 1. Advantages and disadvantages of PNA.

	Advantages	Disadvantages
1.	PNA has a high thermodynamic stability, i.e. it is a more sequence-specific binder; and single-point mismatches are better discriminated by PNA than by DNA or RNA.	PNA has lower solubility compared to both DNA and RNA due to the lack of charge in the backbone; PNA solubility enhancers can alleviate this problem [84]. PNA solubility is also related to the length of the oligomer and purine/pyrimidine ratio [85].
2.	The higher destabilizing effect of base mismatches in PNA-containing heterodimers improves discrimination in genotyping.	PNA length must comprise between 6 and 18 monomers ref [54]).
3.	PNA is generally more chemically stable than DNA or RNA fragments. Being a polyamide-based molecule, PNA is very stable under acid and moderately stable under basic conditions, as well elevated temperatures. This property made PNA suitable for the detection of a large number of biological samples.	To impair PNA aggregation, sequences with a purine content higher than 60% must be avoided; for the same reason, the maximum sequence of purines is four in a row [54].
4.	PNA is also biochemically stable: it is not a substrate for proteases, peptidases or nucleases.	PNA has very low cellular permeability, thus limiting its applications for antigene or antisense therapies [86,87].
5.	The lack of charges in the PNA backbone results in the lack of electrostatic repulsion between the hybridising PNA-DNA (RNA) strands, and thus in a greater affinity towards its targets. Actually, introduction of a positive charge in the PNA strand could be beneficial for the formation and the stability of duplex and triple helices.	In biological system, the triplex formation is limited only to guanine-poor targets, since the physiological pH does not affect the protonation of cytidine residues [77].
6.	PNA molecules are also stable over a wide pH range.	Because of the strength of PNA–PNA interactions, neutral PNA molecules have a tendency to aggregate to a degree that is dependent on the sequence of the oligomer [88], thus self-complementary sequences (inverse repeats, palindromes, or

		hairpins) must be avoided if they involve six or more consecutive monomers [54].
7.	PNA binding to its complementary single-stranded targets is rather unaffected by the ionic strength of the medium.	Even if (chemical and biochemical stabilities) facilitate synthesis, purification, storage and application of PNA oligomers, PNA synthesis is expensive.

The unique physicochemical nature of the peptidomimetic, neutral PNA backbone have promoted the use of PNA oligomers as capture probes in electrochemical, optoelectronic, and microarray-based biosensors, and in other types of sensors. Recent PNA-based sensors results are summarized in **Table 4. 2** [54].

Table 4. 2. Most developed PNA-based biosensor [54].

Detection method	Target	Limit of detection
Electrochemical (redox indicator)	dsDNA oligomers	1.8×10^{-12} mol L^{-1}
	PCR amplicon	4.8×10^{-12} mol L^{-1}
Electrochemical (nanowire)	DNA oligomer	10^{-13} mol L^{-1}
Electrical (nanowire)	DNA oligomer	5×10^{-14} mol L^{-1}
Optoelectronic (QCM)	HBV genomic DNA (no PCR)	8.6×10^{-12} mol L^{-1}
Optoelectronic (SPR)	DNA (PCR)	7.5×10^{-9} mol L^{-1}
Optoelectronic (Localized SPR)	ssDNA	6.7×10^{-13} mol L^{-1}
Optoelectronic (SPR Imaging-SPRI)	ssDNA	10^{-15} mol L^{-1}
Microarray (fluorescent)	HBV genomic DNA from real samples	10^2 copies mL^{-1}
Nanomechanical	DNA oligomer	10^{-15} mol L^{-1}

From literature studies [54] we derived that a controlled sensing surface preparation is needed in order to have the best sensing performances. In particular the PNA-based sensor requirements could be summarized in the following four points:

1. A quantitative evaluation of the final amount of available probes anchored to the sensing surface is desirable;
2. A complete surface protection from non-specific adsorptions has to be achieved;
3. Due to the strength of PNA-PNA interactions, also a spacer between PNA probes is fundamental;
4. The application of PNA-based sensors to complex and real samples is required for a clinical application of this recent type of sensor.

In the following Section the strategy that we adopted in order to satisfy PNA-based sensor requirements is described.

4.3   PNA-based sensor realization strategy

A large number of deposition strategies for the deposition of thiolated PNA (HS-PNA) or thiolated PEO-PNA (HS-PEO-PNA) for biosensoristic purposes are described in literature as they depend on the type of sensors (i.e. on the sensor geometry, materials and characterization technique), the probe concentration, process temperature, deposition time, dilution buffer and deposition strategy adopted [69,71,72,83,89–102]. We performed an accurate study in order to obtain a careful and precise protocol for the development and optimization of our sensing prototype, answering to PNA-based sensor four requirements.

1.   In order to obtain even better performances from the PNA-based sensor, we chose to combine the high PNA/DNA binding sensitivity with GC-SPR under azimuthal rotation, known for its high sensitivity [19], with high sensitivity given by PNA performances.

2.   We used a thiolated poly (ethylene oxide) (HS-PEO -or HS-PEG-) as antifouling layer to assure a complete protection of the surface from non-specific adsorptions, directly linking PEO to PNA (HS-PEO-PNA) in order to have a single-step procedure for the probe deposition.

In fact it is widely accepted that a hydrophilic polymeric layer needs to be inserted between the probe and the metal surface (**Figure 4. 2**) [103–108] for the prevention of nonspecific adsorptions onto the SPR sensing surface, that is very important along the device optimization [26,109,110].
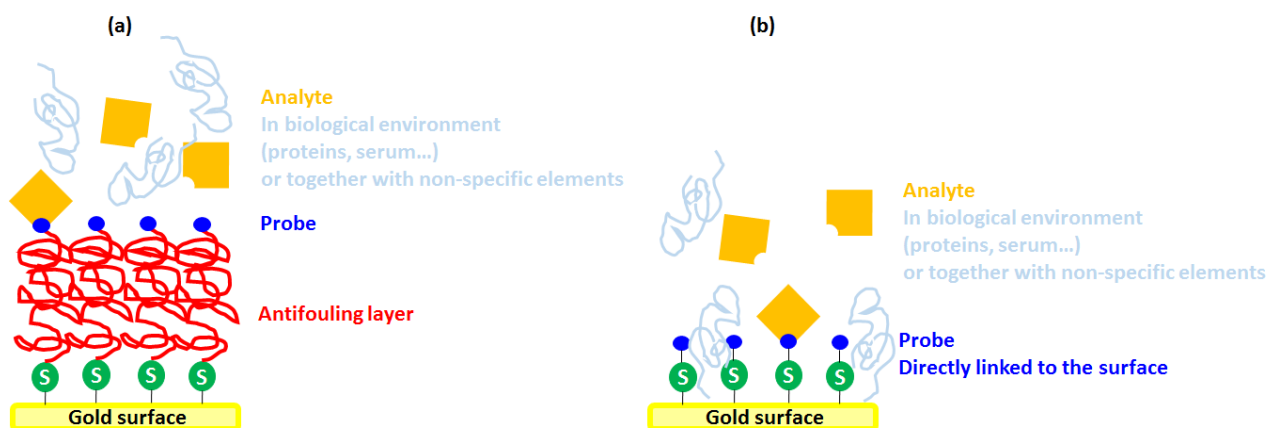
Figure 4. 2. Antifouling mechanism. The presence of an antifouling layer (a) prevent non-specific adsorption onto the surface due to components of the sample containing biological environment or to non-specific elements that could be found in complex or real samples. Such non-specific adsorptions can occur when an antifouling layer is not present and the probe is directly inked to the surface (b), making the discrimination between specific and non-specific signal, both contributing to the final signal, difficult.

One of the polymers used for this purpose is precisely PEO. Among all, PEO is the only antifouling polymer characterized by bi-functionality, and this gives it the advantage of allowing fine tuning the tethered surface reactivity [51]. The use of PEO for inhibiting protein adsorption onto flat surfaces has been widely demonstrated since the '80s [111–117], and it is now known that its antifouling efficacy depends on the polymer chain length, its surface packing density and the fouling protein size [112–115].

As a general rule, in order to achieve surfaces with both optimal and reproducible antifouling and sensing performances, it is important to be able to control the surface coating process. Indeed, exhaustive investigation on the grafting kinetics of short chain thiol-PEOs onto gold has been carried along the years [36,110,118–121]. At first we optimized the sensing capability of our sensing platform only for HS-PEO (Mw 5 kDa) assembly onto the surface. Through this study we were able to estimate the amount of PEO molecules adsorbed in term of surface density (σ [ng/nm^2]) from SPR measurement output (i.e. resonance angle shift) using a mathematical

model [35]. After sensor calibration we compared the antifouling behaviour of three different Mw PEOs (0.3, 2 and 5 kDa) in the presence of BSA and serum, biological elements often present in the analyte solution. We also compared and quantified the sensing ability of our system using biotin/avidin binding as a model interaction [51].

3.   To overcome the problem of high PNA/PNA affinity that leads to the tendency of PNA to aggregate, we decided to keep the PNA probes separated from each other using a shorter HS-PEO.

Backfilling procedure (i.e. the immobilization of two different thiolated species onto a surface) is currently performed following two strategies [36]: the *sequential backfilling*, in which the backfiller molecule is deposited after the deposition of the probe molecule; and the *co-immobilization process*, in which a single mixture of the backfiller and probe molecule is used to obtain a 2-component active layer simultaneously.

Both backfilling methods are limited by the adsorption rate constant of the two molecules used and thus they require a particular attention in order to get a perfect surface control, and we chose to exploit the co-immobilization method as it requires shorter deposition times and less procedures onto the same sensing surface (like cleaning steps and functionalization). The problem of this approach is that the simultaneous adsorption of two thiolated species is competitive, due to the different adsorption rate constants, which lead to different adsorption mechanisms. For this reason it is difficult to control the co-immobilization process, in particular for what concern the final amount of adsorbed material and in literature there are many works in which the co-immobilization results as a successful approach, but a surface chemistry control is often missing. Thus we realized a co-immobilization mathematical model (Section 4.9.II) to control the simultaneous adsorption of HS-PEO$_{2kDa}$ and HS-PEO$_{5kDa}$-PNA [122].

4.   We tested our sensor in the presence of non-specific component (non-specific DNA and BSA), oligo DNA and PCR amplified and genomic DNA. Sensing experiments were measured through SPR and microarray (fluorescent) techniques, and a comparison between HS-PNA and HS-PEO-PNA performances was also performed.
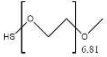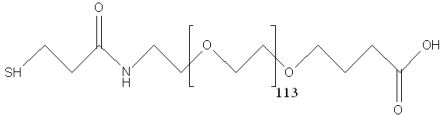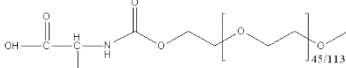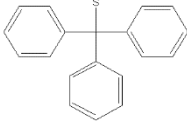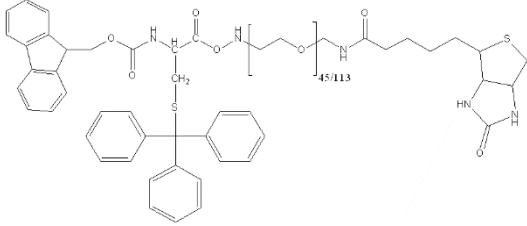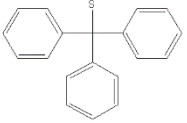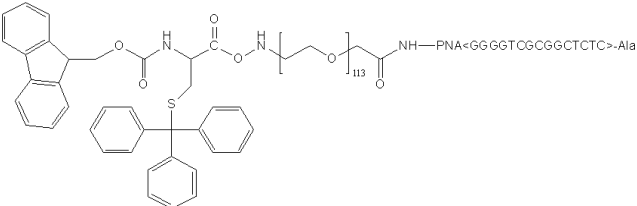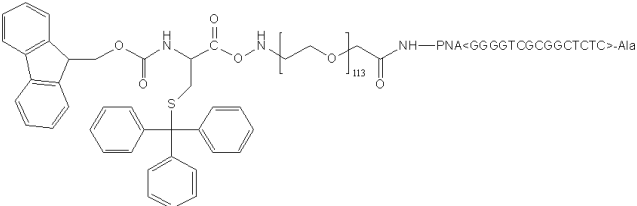
4.4   Materials and methods

4.4.I   Biological elements

In this section the synthesis strategies and the application protocols in term of surface functionalization, antifouling and hybridization experiments are described. For each experiment the same configuration and the same functionalization strategy were adopted: we always started from a thiol-PEO derivative linked to the sensing element (e.g. Biotin or PNA). The thiol group, at first protected by a trytil (trt) group, was used for the probe-gold binding. In the following Table all the molecules adopted for the whole work are shown.

Table 4. 3. PEO derivatives used in this work. In the Table the analyte for which they were used, their chemical structure and the reference describing their applications are reported.

PEO derivative	Analyte	Function	Structure	Provenience	References
mPEO$_{0.3kDa}$-SH	-	Protection from non-specific adsorptions		Commercial (Plasmachem)	
Fmoc-Cys(trt)-PEO$_{5kDa}$-COOH	-	TBO test		Commercial (Sigma Aldrich)	[35,41,51,52]
mPEO$_{2kDa}$-Cys(trt) mPEO$_{5kDa}$-Cys(trt)	-	Protection from non-specific adsorptions		Synthesized	
fmoc-Cys(trt)-PEO$_{2kDa}$-(CH$_2$)$_6$-Biotin fmoc-Cys(trt)-PEO$_{5kDa}$-(CH$_2$)$_6$-Biotin	Avidin	Probe for Avidin binding		Synthesized	[51]
fmoc-Cys(trt)-PEO$_{2kDa}$-PNA fmoc-Cys(trt)-PEO$_{5kDa}$-PNA	DNA (rpoB15wt)	Probe for DNA binding		Synthesized	[65,123]

Synthesis of PEO-Cys(trt) derivatives

PEO 0.3 derivative was purchased from Sigma Aldrich, while the 2 and 5 kDa ones were synthesized by prof. Margherita Morpurgo and dott. Davide Silvestri of the Department of Pharmaceutical Sciences.

Unless otherwise specified, all reagents were purchased from Sigma Aldrich and were of analytical grade. The reaction pathway leading to the PEO derivatives of this work is summarized in **Figure 4. 3.** Similar protocols were adopted for the 2 and 5 KDa derivatives.
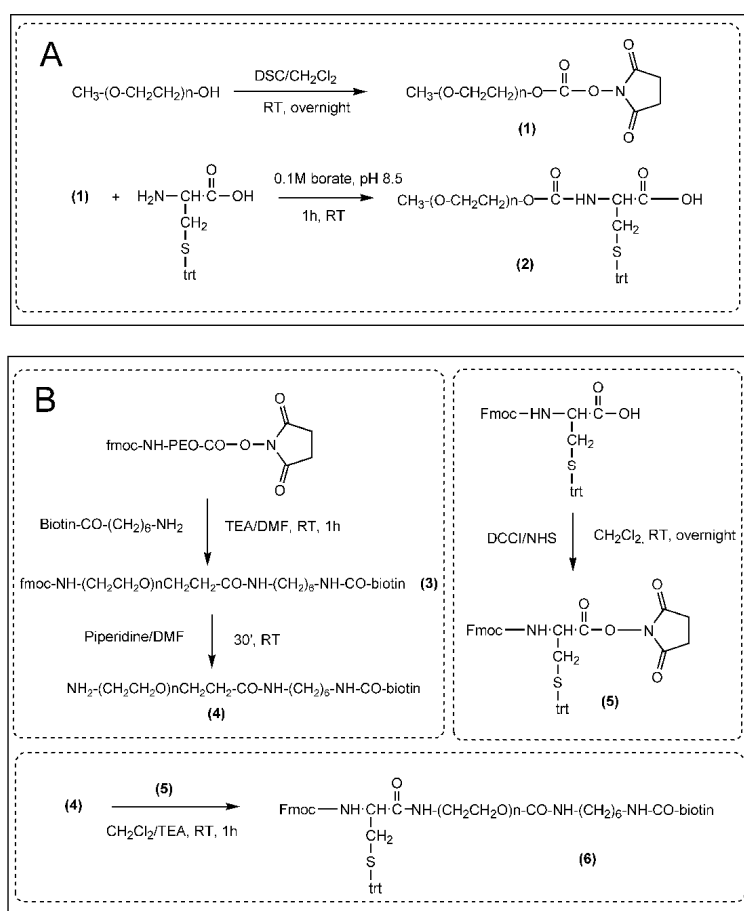
Figure 4. 3. Synthesis of mPEO-Cys(trt) (A) and biotin-PEO-Cys(trt) (B).

n is 45 and 113 for the 2 and 5KDa derivatives, respectively.

α-methoxy, ω-trt-S-Cys polyethyleneoxide (mPEO-Cys(trt), (2), (Figure 4. 3 (A)) was synthesized by coupling S-trityl-cysteine to the hydroxyl end of monomethoxy-PEO (mPEO-OH). The starting mPEO-OH was dissolved in anhydrous chloroform and activated as *N*-hydroxy-succinimidylcarbonate by adding two equivalents of di-succinimidylcarbonate (DSC) in the presence of triethylamine (TEA). The reactive intermediate (1) was isolated by diethylether precipitation and later added, under mixing, to a 2mM trt-cysteine solution in 0.1M borate buffer, pH 8.5. After 2h at room temperature the final product (2) was extracted with dichloromethane (CH_2Cl_2), the organic solution was dried over magnesium sulfate ($MgSO_4$), filtered, concentrated by rotary evaporation, and the product was isolated after diethylether precipitation and characterized by ^{1}H-NMR.

α-biotinammidohexylamido, ω-cys-trt-PEO (**b-PEO$_{2and\ 5KDa}$-Cys(trt)**), (6), (**Figure 4. 3** (B)) were synthesized starting from the bifunctional PEO derivative, fmoc-NH-PEO$_{2\ or\ 5KDa}$-CO-NHS (Rapp Polymer, Germany). Biotinamidohexanolalamine was synthesized according to a published procedure [124] and was mixed with one equivalent of fmoc-NH-PEO$_2$ or $_{5KDa}$-CO-NHS in dry dimethylformamide (DMF), in the presence of 1 equivalent of TEA. After a 2 hours reaction at room temperature, the product (3) was isolated by diethylether precipitation. It was then treated for 30 minutes with 20% piperidine in DMF to remove the fmoc residue. The solution was then diluted with water and the fmoc-deprotected product (4) was isolated by CH$_2$Cl$_2$ extraction, followed by diethylether precipitation.

In a separate vessel, fmoc-trt-S-cysteine was activated as *N*-hydroxysuccinimidyl ester with 1 equivalent of both diciclohexylcarbodiimide (DCCI) and *N*-hydroxysuccinimide (NHS) in dry CH$_2$Cl$_2$. The activated compound (5) was added to 1 equivalent of (4) previously dissolved in dry CH$_2$Cl$_2$, followed by 2 equivalents of TEA. Product isolation was achieved by diethylether precipitation. All product identities were confirmed by ^{1}H-NMR.

Synthesis of PNA derivatives

While DNA oligonucleotides were purchased from IDT Integrated DNA Technologies (Leuven, Belgium), PNA derivatives were synthesized in the lab[65].

Probe Design

In **Figure 4. 4** the structure of the designed probe is reported. It is composed of three main elements: a thiol function for gold attachment, the high MW trt-protected PEO chain meant to prevent non-specific interactions and a sequence for DNA recognition. With respect to the DNA binding element, a PNA analogue was selected on the basis of its ability to improve duplex stability and base mismatch discrimination.

Selection of the PNA Sequence and Length

We selected a 15 bases long probe within an 81-bp fragment of the gene encoding the beta subunit of RNA polymerase (RpoB) whose mutations are involved in rifampicin resistance [125]. The probe (RPOB15wt) was analyzed by BLAST to avoid high homology with other genomes. We selected a 15 base length probe as a compromise between affinity and specificity for the target analyte. In fact, oligomers of 12 to 17 bases are suitable for most applications whereas longer sequences (from 25 to 40 units) are rarely required to improve the stability of the hybridized duplex. In addition, for the discrimination of single base mutations as those that generate drug resistance, the impact of a mismatch is greater on a shorter sequence than a longer one. It is generally accepted that relatively short sequences (less than 15 residues) can discriminate single base mismatch through hybridization at room temperature with appropriate control of salt concentration [126]. On the other hand, if longer probes are used, salt concentration modification may not be sufficient to destabilize unpaired duplex for single mismatch discrimination and higher temperature or the addition of denaturants such as formamide must be used, and both the use of high temperature or formamide may not be feasible within common SPR experimental set-ups [126–128]. From the chemical point of view it has to be pointed out that purine-rich PNA oligomers display a tendency to aggregate, with guanine-rich oligomers having the greatest tendency [129]. As a consequence, the selected 15-mer (PNA-RPOB15wt) can be considered a "difficult" one to synthesize because it includes more than three guanine (G) residues in a row and it also includes more than six purines in any stretch of ten units. In addition, the sequence contains a palindrome trait (GCGC) that could potentially give problems such as self-hybridization with consequent difficulties in purification and characterization.

In **Table 4. 4** all the sequences and the name of PNA and DNA oligomers used in this work are reported.

Table 4. 4. Name, sequence and abbreviation of DNA and PNA oligomers used in this work.

Molecule name	Sequence	Abbreviation
myco wt PNA probe	H_2N-CTGTCGGCGCTGGGG-Ala-Ala-$CONH_2$	myco PNA
myco wt ω-thiol PNA probe	Cys-PNA(CTGTCGGCGCTGGGG)-Lys_4	myco HS-PNA
myco wt PEG_{5000}-PNA probe	Fmoc-Cys(trt)-PEG_{5000}-PNA(CTGTCGGCGCTGGGG-Ala-Ala-$CONH_2$)	myco PEG-PNA
myco wt DNA probe	5'-/H_2NC6/TGTCGGCGCTGGGG-3'	myco DNA-NH_2
myco wt DNA complementary	5'-CCCCAGCGCCGACA-3'	myco DNAc
myco wt DNA complementary Cy3	5'-/Cy3/CCCCAGCGCCGACA-3'	myco DNAc Cy3
non-complementary DNA probe	5'-AGCTGTGTCTGTAAACTGATGG-3'	DNAnc
quenching test DNA probe	5'-/H_2NC6/GATCGGGTGTGGGTGGCGTAA AGGGAGCATCGGACA/Cy3/-3'	quench DNA
myco forward primer	5'-CGCAGACGTTGATCAACATCCGGC-3'	mFw
myco reverse primer	5'-GGTTTCGATCGGGCACATCCGGC-3'	mRev

Synthesis of Avidin/Nucleic acid nanoassemblies (ANANAS)

Synthesis of ANANAS particles was realized by prof. Margherita Morpurgo of the Department of Pharmaceutical Sciences and the synthesis details are not discussed in this work. The detailed synthesis is reported elsewhere [130].

4.4.II   Functionalization and hybridization protocols

Grafting of PEO-thiol reagents on gold surfaces for SPR measurements

PEO depositions were carried using five ω-thiol ending polymer derivatives of 0.3, 2 and 5KDa Mw, from commercial (0.3KDa) or synthetic (2 and 5 KDa) source. The 2 and 5 kDa derivatives possess a S-trt protected cysteine residue at their ω end that allows fast and quantitative deliverance of the gold reactive SH group upon TFA treatment. In this way a single gold reactive species is present in solution and its degree of oxidation is negligible as SH de-protection is carried out immediately before deposition. This kind of S-protection was selected also because the leaving triphenylmethanol does not interfere with gold as opposed to other thiol protecting leaving groups.

Thus thiol de-protection was performed prior to their use by mixing the polymers in powder form with the minimum amount of TFA (about 10µl every 5 mg of PEO) for 20 minutes at room temperature. N_2-saturated dd-H_2O was then added up to reach 1 mM final thiol concentration and the insoluble trt residue was removed by centrifugation (10000g, 4°C, 10 min). For homogeneity, the commercial 0.3kDa PEO-SH was used at the same 1 mM concentration in N_2-saturated H_2O containing a small amount of TFA, so to reproduce the same environment of that used with the high Mw derivatives.

Gold-coated substrates were pre-cleaned in a basic peroxide solution (5:1:1 double distilled water (ddH$_2$O), 30% H$_2$O$_2$ and 25% NH$_4$OH) for 10 minutes, rinsed in ddH$_2$O and dried under N$_2$ flux. Depositions were then carried out in a N$_2$-fluxed incubation chamber by immersing the substrates in 1mM polymer solutions obtained as above described. At scheduled times, samples were removed and rinsed thoroughly with dd-H$_2$O in order to remove physisorbed molecules. They were then dried in vacuum (10^{-7} atm) in a desiccator for 90 minutes and stored under N$_2$ atmosphere and far from light until characterization.

In **Figure 4. 4** the probe and antifouling layer functionalization scheme is reported, for both PEO-biotin and PEO-PNA procedure.
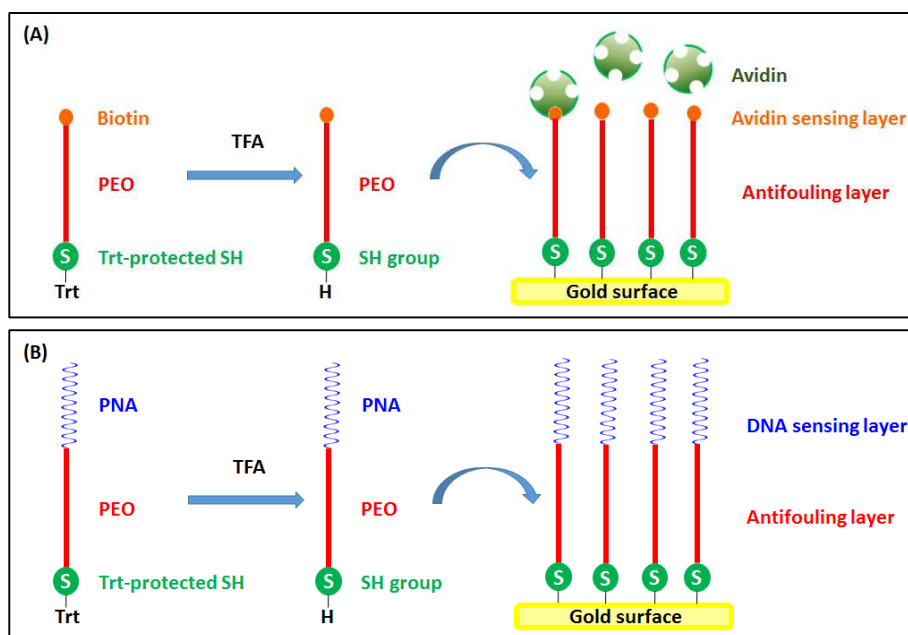
Figure 4. 4. Surface functionalization scheme for PEO-biotin (A) and PEO-PNA (B).

Microarray surface functionalization

Microarray deposition was performed both for myco PEO-PNA and for myco DNA NH$_2$, on gold surfaces and on commercial microarray slides, respectively. Surfaces were printed by VersArray Chip Writer Pro System (Biorad, Hercules, CA), using Telechem SMP3 microspotting pins (Arrayit Corporation, Sunnyvale, CA).

Concerning flat gold surfaces, prior of their usage, they were cleaned with basic piranha solution and a PEO-PNA/PEO solution, prepared with different dilutions as described in Section 4.4.II, was loaded into micro-plates and printed. Slides were incubated overnight in a 75% humidity incubation chamber and then the surface was blocked with BSA 2% for 45 minutes, rinsed with PBS 1 X, with milliQ water and N$_2$ flux dried.

Printing of e-surf commercial LifeLine slides (25 mm × 75 mm, LifeLineLab, Pomezia, Italy) was performed with myco DNA NH$_2$, diluted in Microarray Printing Buffer 1.5X, to a final concentration of 20 µM. Printed slides were incubated overnight in a 75% humidity incubation chamber, blocked and washed according to standard protocols as specified by the supplier with microarray blocking and washing solutions, respectively.

Fouling and specific binding experiments for biotin-avidin experiments

Substrates covered with PEO at selected densities were immersed at room temperature in 10 mM phosphate, 150 mM NaCl, pH 7.4 (PBS) alone or containing either 0.1% BSA (PBS-B) or 1% goat serum (PBS-GS). After 2 hours, samples were rinsed with double distilled water, dried under nitrogen flux and their resonance angle shift was measured by SPR. The same protocol was followed using bPEO-Cys coated surfaces, which were incubated in the same buffers as above containing also avidin (4 µg/ml).

When also avidin/nucleic acid nanoassemblies were adopted for binding events (Section), Avidin and avidin nanoassembly 4 mg/ml solutions in a BSA/PBS dilution buffer 0.1% were deposited onto plasmonic gratings for 60, 80, 120 or 180 minutes. Sensing surfaces were then dried under nitrogen flux.

Oligonucleotide and PCR hybridization

Mycobacterium tuberculosis DNA extracts from a wild type strain was kindly provided by Professor Riccardo Manganelli (University of Padova).

200 ng of DNA extract were PCR amplified using the following reagent final concentrations: 1X PCR buffer, 1.5 mM $MgCl_2$, 200 µM dNTPs, 500 µM of both mFw and mRev primers, 1 unit of Taq polymerase. Reagents for PCR amplification reaction (AmpliTaq Gold 360 DNA Polymerase kit) were purchased from Applied Biosystem (Life Technologies, Milan, Italy). The following thermal cycle was performed: 5 minutes at 95 °C; 40 cycles of 30 sec at 95 °C, 30 sec at 58 °C and 1 minute at 70 °C; 7 minutes at 70°C and hold at 4 °C. PCR product was purified with silica spin column (PureLink PCR Purification Kit, Life Technologies) and run on Agilent Bioanalyzer with DNA chip (Agilent Technologies, Santa Clara, CA) to check fragment integrity, dimensions and amount. Fluorescent *M. tuberculosis* wild type PCR product was obtained amplifying genomic DNA in the same conditions, but using a mix of dNTPs including Cy3 dCTP (GE Healthcare, Little Chalfont, UK). Fluorophore incorporation was verified spectrophotometrically (NanoPhotometer, Implen, München, Germany).

Human genome from a lung carcinoma cell line (CCL-185 cell line, LGC standards, UK) was extracted with QIAamp DNA Mini Kit (Qiagen, Hilden, Germany), and fragmented with a mix of restriction enzymes in the conditions indicated by the supplier (PvuII, Eco RI, NcoI, NaeI, MwoI, all from New England Biolabs, Ipswich, MA). Obtained fragments ranged from 200 bp to 1000 bp, as verified by capillary gel electrophoresis with Agilent Bioanalyzer, and used as interferent DNA in the subsequent preparations.

Complementary DNA oligonucleotide (myco DNA Cy3) was diluted in hybridization buffer (1X SSC, 0.1% SDS, 0.2X BSA) in the following final concentrations: 10 nM, 2 nM, 0.4 nM, 0.08 nM, 0.016 nM, 0.0032 nM and 0 nM. The same dilutions were performed for myco PCR fragments, considering its length of 224 bp. Myco PCR fragments (Cy3-labeled or unlabeled) were incubated alone or co-hybridized in the presence of 100 ng of fragmented human interferent DNA, in a hybridization buffer consisting in 4X SSC, 0.1% SDS, 0.2X BSA. Mixtures were denatured for 5 minutes at 95°C, placed on ice and hybridized for 3 hours at 50°C in the Array Booster AB410 hybridization station (Advalytix, Munich, Germany). Slides were removed from the chamber and washed in the Advawash Station AW400 (Advalytix) for 5 minutes in 1X SSC 0.1% SDS at 50°C, 2 minutes in 0.2X SSC, 2 minutes in 0.1X SSC and 30 seconds in dd-H_2O. Microarray slides were finally spin-dried using Microarray High-Speed Centrifuge (Arrait Corporation, Sunnyvale, CA) and submitted to SPR analysis or scanned for fluorescent emission.

Toluidine Blue O (TBO) test

The carboxyl layer (deposited following the procedure described in Section 4.4.II) was incubated for 5 hours in humid chamber at 30°C with a TBO (**Figure 4. 5**) solution (5×10^{-4} M, pH 10). The incubation liquid

was removed and the substrate surface was at first cleaned with potassium hydroxide (NaOH 10^{-4} M, pH 10) to remove non-bounded dye, and then incubated with a known volume of acetic acid (CH_3COOH 50%, pH 2). Changing pH, the ionic interaction between the carboxyl groups and TBO is lost causing the detachment of TBO from the surface ad its dispersion in the acetic acid solution. The amount of detached TBO was determined measuring the solution optical density using a Varian Cary 50 UV-Vis spectrophotometer at λ = 633 nm. The value obtained indicates the available –COOH groups onto the sensing surface. Through an appropriate calibration curve and normalizing the results considering the sample surface area, it was possible to obtain the number of –COOH groups, and thus of HS-PEO-COOH molecules adsorbed onto the surface.
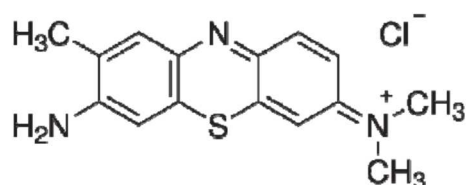
Figure 4. 5. Toluidine Blue O chemical structure

4.5 Refractive index and thickness of biological elements: a spectroscopic ellipsometric study

The refractive index and thickness of biological elements used in this work were derived through spectroscopic ellipsometry analyses. Biological films characterized were:

- Biotin-PEO$_{2kDa}$

- Biotin-PEO$_{5kDa}$

- Biotin-PEO$_{2kDa}$ + Avidin

- Biotin-PEO$_{5kDa}$ + Avidin

Each layer was deposited onto the same glass/chromium/gold substrate using the method described in Section 4.2.II, thus the starting substrate characterization was performed only at the beginning of the work, and its results were used for the fitting of all biological layers.

In **Figure 4. 6** and **Table 4. 5** the 3-layer model used for starting substrate fitting and related derived thicknesses are reported.

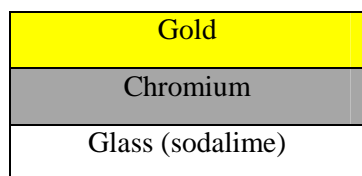| Gold |
| :---: |
| Chromium |
| Glass (sodalime) |

Figure 4. 6. Scheme of the model used for the starting substrate fitting

Table 4. 5. Resulting Thicknesses for adopted metals

Material	Thickness [nm]
Chromium	2.16±0.22
Gold	38.16±0.11

In the following Table the refractive index used for the fitting of biological layer curves are reported.

Table 4. 6. Literature refracive index used for the biological layer fitting procedure

Material	Refractive index		Reference
	Solution	*Crystalline*	
Methoxy-PEO 2/5kDa	1.47		[120]
Biotin-PEO 2/5 kDa	1.47		[120]
Avidin	1.42	1.45	[131]
DNA	1.7		[132]
bPEO+Avidin	1.46		Calculated

The A and B constant values for the Cauchy model here used, which is the model used in literature for the modeling of biological layers, were those found in literature: 1.45 (A) and 0.001 (B) [120,131,132].

Methoxy- and Biotin-PEO 2/5 kDa

For methoxy- and Biotin-PEO 2/5 kDa, the same fitting model and the same fitting parameters were adopted (**Figure 4. 7**).

Figure 4. 7. Fitting model scheme for methoxy- (*left*) and for Biotin- (*right*) PEO 2/5 kDa. For A and B Cauchy model parameters, values of 1.45 (corresponding to a wavelength of 620 nm) and 0.01 were used respectively.[120]

Biotin-PEO 2/5 kDa + Avidin

In the case of the Biotin-PEO 2/5 kDa + Avidin system, two different fitting model were adopted and results deriving from both models were then compared.

The first fitting model was named "*Single-Cauchy Model*" and it consisted of the following assumption: the Biotin-PEO/Avidin multilayer is considered as a single layer in which the refractive index could be assumed as a medium value between Biotin-PEO and Avidin ones (i.e. 1.46 for λ=620 nm).

The second fitting model is the "*Multi-Cauchy Model*", based on the assumption that the Biotin-PEO/Avidn multilayer is considered as a double layer, so that a refractive index of 1.47 and 1.45 have to be taken for Biotin-PEO and Avidin respectively. In this case the thickness of Biotin-PEO layer was the one derived before Avidin binding.

In **Figure 4. 8** the schemes of Single- and Multi- (Double-) Cuchy Model are reported.

bPEG+avidin
Gold
Chromium
Glass (Sodalime)

Avidin
bPEG
Gold
Chromium
Glass (Sodalime)

Figure 4. 8. Fitting model scheme for the Single- (left) and Multi- (right) PEO 2/5 kDa. For A and B Cauchy model parameters, values of 1.45 (corresponding to a wavelength of 620 nm) and 0.01 were used respectively.[120]

In **Table 4. 7** all resulting optical constants are reported.

Table 4. 7. Resulting refractive index (n) and thickness (t) of all biological elements characterized

			bPEG+avi	bPEG+avi	Avidin	bPEG+nano	bPEG+nano
	mPEG	bPEG	*Single-Cauchy Mod.*	*Double-Cauchy Mod.*	*Double-Cauchy Mod.*	*Single-Cauchy Mod.*	*Double-Cauchy Mod.*
2 kDa PEO							
n	1.47	1.47	1.46	1.47/1.45	1.45	1.475	1.47/1.48
t [nm]	2.70±0.05	2.49±0.094	5.47±0.10	5.28±0.18	2.7±0.09	3.59±0.12	3.92±0.20
5 kDa PEO							
	mPEG	bPEG	*Single-Cauchy Mod.*	*Double-Cauchy Mod.*	*Double-Cauchy Mod.*	*Single-Cauchy Mod.*	*Double-Cauchy Mod.*
n	1.47	1.47	1.46	1.47/1.45	1.45	1.475	1.47/1.48
t [nm]	5.53±0.12	2.21±0.03	4.72±0.04	4.57±0.08	2.36±0.04	3.87±0.19	4.14±0.12

Comparing the *Single-* and *Double-* Cauchy models, we found that differences in the thicknesses were negligible for both PEO 2 and 5 kDa: 5.47±0.10 nm and 5.28±0.18 nm (*Single-* and *Double-*Cauchy models for PEO 2kDa), 4.72±0.04 nm and 4.57±0.08 nm (*Single-* and *Double-*Cauchy models for PEO 5kDa) respectively.

Differences between PEO 2 and 5 kDa thicknesses could be attributed to differences in the conformation of the two polymers onto the surface. Although, spectroscopic ellipsometry could be not considered as a perfect technique to derive optical and morphological parameters of biological elements that are really variable on surface condition deposition, assembly onto the surface and characterization condition. Thus all the data obtained through Spectroscopic Ellipsometry analyses could be considered good results for having an idea of our system features.

4.6   Sensing substrate calibration

Here, for the first time, we tested the ability of the azimuthally-controlled GC-SPR sensing to distinguish between surfaces covered to different extent by the same thiolated molecule[35].

In this way, a quantitative calibration correlating the GC-SPR output signal to the amount of molecules grafted onto the surface was be obtained. To this end, we functionalized sinusoidal gold gratings with different amounts of monomethoxy-thiol-poly(ethylene oxide) (mPEO-SH, Mw 5 kDa).

We deposited various amounts of mPEO molecules by immersing the grated surface into increasing concentration solutions (from 500 nM to 2.5 mM). We monitored the surfaces through Atomic Force Microscopy (AFM) and SPR reflectivity measurements, both in null and rotated azimuth configuration, and the polymer surface density was then calculated by combining an Effective Medium Approximation (EMA) with the theory shown by Jung[21]. For the calculation, we took into consideration the molecular conformation assumed by PEO, that is known to change from a mushroom- to a folded-chain-like one as the number of adsorbed molecules increase[133]. Finally the GC-SPR system calibration curve, correlating the number of molecules (or surface sensitivity - σ) with the SPR measurement output signal (resonance angle shift, $\Delta\theta$) was obtained.

4.6.I   Grafting of PEO 5kDa

For mPEO layer formation we chose to vary the mPEO-SH solution concentration from 500 nM to 2.5 mM upon an incubation time of 24 hours to mimic similar experimental conditions described in literature[36].

In Figure 2 SPR measurement results after mPEO films formation, both in the null and in the rotated azimuth configuration are shown.
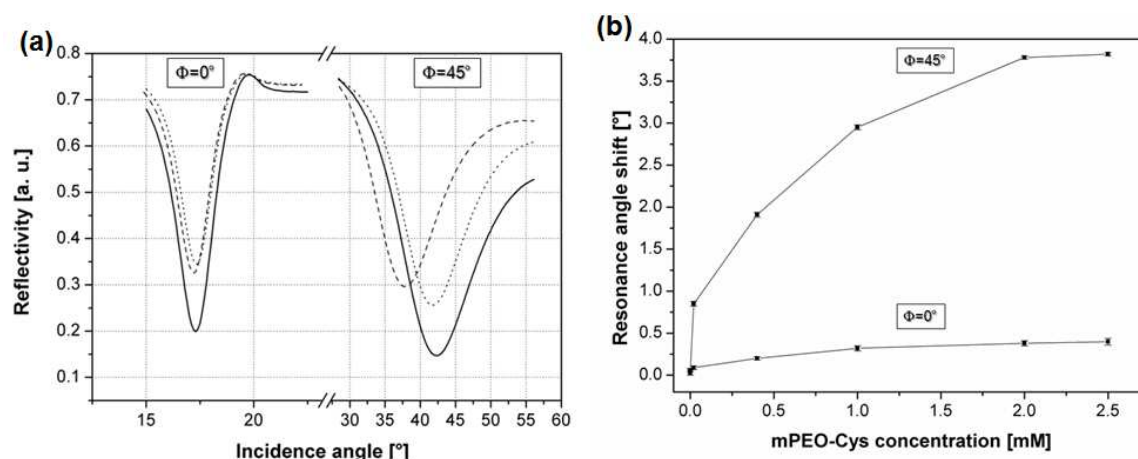
Figure 4. 9. Results of the SPR measurements. (a) Reflectivity dips detected in the null (φ=0°, λ=725 nm) and in the rotated (φ=45°, λ=625 nm; α=140°) azimuth configuration collected before (*solid line*) and after (from 500 nM mPEO-SH deposition *-dotted line-* and from 2.5 mM mPEO-SH deposition-*dashed line*) mPEO-SH coating. (b) Resonance angle shifts collected after mPEO film formation (for φ=0° and θ=45°) as a function of mPEO-SH solution concentrations.

The Δθ range covered from the lowest to the highest concentration is of 0.37° and 3.76° for the φ=0° and φ=45° detection respectively. Δθ gradually increased with mPEO-SH solution concentrations until reaching a plateau between 2 and 2.5 mM, suggesting that at these concentrations the polymer surface saturation was reached.

4.6.II   mPEO surface density calculation

It is known that during its assembly process onto a surface, a polymer exhibits a transition from a mushroom-like molecular conformation to a brush-like one, as the number of adsorbed molecules increases. The dynamics of this assembly is quite complex as it depends on different parameters related to the tethered surface (metal used, surface cleaning, roughness, nanostructuration...), the type of polymer (molecular weight, dimension, hydrophilicity, functional groups…), its concentration in the deposition solution, the solvent used, the deposition time, and other environment-related variables (e.g. temperature, pH and so on) [36,133]. Figure 3 shows the AFM images of mPEO films obtained from different concentration mPEO-SH solutions (500 nM and 2 mM). The images of flat gold substrates covered by mPEO films prepared using the same experimental protocols adopted on the nanostructured ones, which were used to help interpreting the morphology information, are also shown.
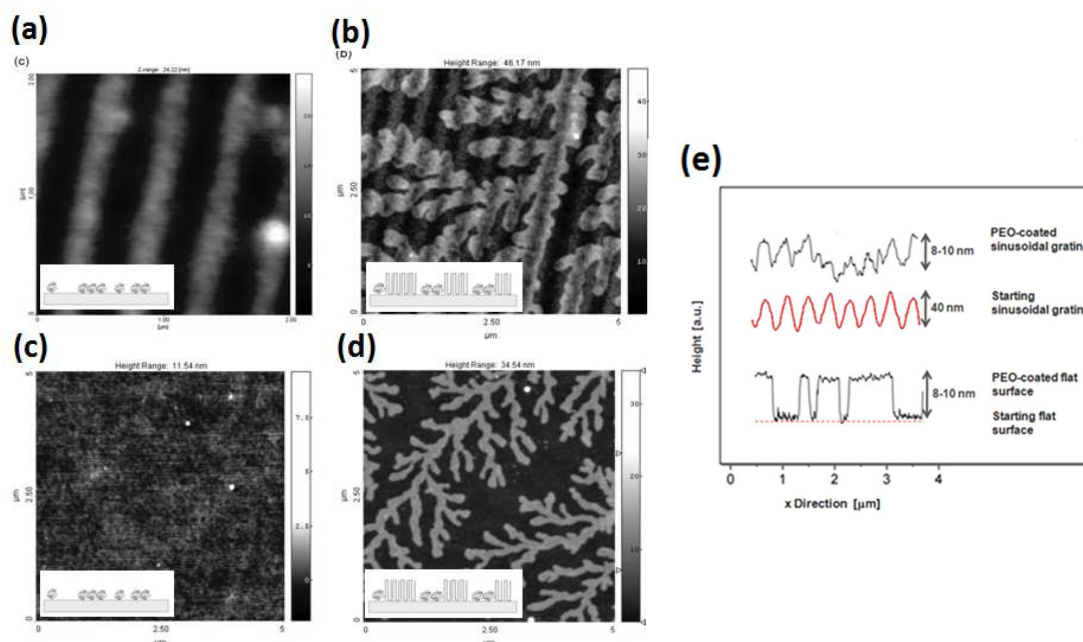
Figure 4. 10. Examples of mPEO film morphology conformation variation onto nanostructured and flat gold surfaces. A polymer mushroom-like conformation is obtained when the solution concentration adopted is 500 nM (a, c), while a mushroom- and folded-chain-like one in obtained from a 2 mM solution concentration (b, d) for both nanostructured (a, b) and flat surfaces (c, d). The insets in the AFM images are schematic representations of the relative polymer conformation. In (e) changes in the surface profiles before and after the mPEO film formation are reported.

The results observed on flat and grated surfaces were similar: dendrimer-like structures, typical of mixed brush/folded mPEO layers [120,133,134], were visible on both surface types, when incubated with the higher concentrated polymer solution. On the contrary, this structure was not visible on the surfaces incubated at low (500 nM) mPEO-SH concentration, indicating that, in this case, a mushroom conformation was obtained. The thickness of the folded-chain-like conformation was about ≈ 10 nm, indicating about a 3-time folded chain. A full brush-like conformation was never observed experimentally, and this is likely due to the high molecular weight of the polymer. Indeed, full brush films are expected to form only for PEO derivatives having a lower Mw than the one here used which is limited by its long chain and high tendency in forming folded coils [36,135].

4.6.III Calculation of surface density from experimental SPR measurements

Starting from Jung's theory for a non-homogeneous surface coverage [21] was combined with the information on the mPEO film morphology obtained experimentally to correlate the resonance angle shifts with the polymer surface density. Indeed, based on the AFM information, the surface coverage was assumed to consist of two different coverage fractions, depending on the adsorbed polymer conformation: *f* for the mushroom-like and *(1-f)* for the folded-chain one. Thus the number of molecules ($N/_{cm^2}$) adsorbed onto the surface was calculated from Eq. (4. 1):

$$N/_{10^{14}} = \frac{f}{A_M} + \frac{1-f}{A_F} \quad [\text{cm}^{-2}]$$

(4. 1)

where A_M and A_F are the surface areas occupied by a molecule in the mushroom-like and in the folded-chain-like conformation respectively.

f (and consequently *(1-f)*) was derived by applying the Jung's model, from which *Δn* results in:

$$\Delta n = \frac{\varepsilon_{PEO} - \varepsilon_0}{\varepsilon_0} \left[\frac{d_F}{L_F} + f \left(\frac{d_M}{L_M} - \frac{d_F}{L_F} \right) \right] \tag{4.2}$$

where ε_0 and ε_{PEC} are the surrounding medium (air) and PEO dielectric constants respectively, L_F and L_M are the extension lengths of the excited SPP into the mPEO layer in the mushroom (L_M) and in the three-folded chain (L_F) conformation, d_M and d_F are the thicknesses of the mPEO layer in the two different conformations respectively. *Δn* is the refractive index variation estimated through an Effective Medium Approximation (EMA) (Section 1.5).

Once *Δn* was derived from SPR measurements, the value of *f* and *(1-f)* can be calculated (Eq. (4. 2)) and thus N (cm^{-2}) and σ (ng/cm^2) (Eq.(4. 1)) were calculated.

For the calculation, a Flory radius of 4.7 nm ($A_M \approx \pi R_f^2$) [111,120] and a film thickness $\approx Rg$ [133] were assumed for the polymer mushroom conformation, while a molecular diameter of 0.45 nm[112] and a 3-times chain folding, were taken into account in the case of the folded-chain-like mPEO conformation. A PEO RI of 1.47 was adopted, considering the polymer film as a Cauchy layer [120,136] (see Section 4.5).

In **Figure 4. 11**, the theoretical calibration curve obtained by means of the above equations is reported, together with the experimental Δθ measured on the surfaces generated upon incubation with different mPEO-SH concentrations. The experimental data are also summarized in detail in **Table 4. 8**.
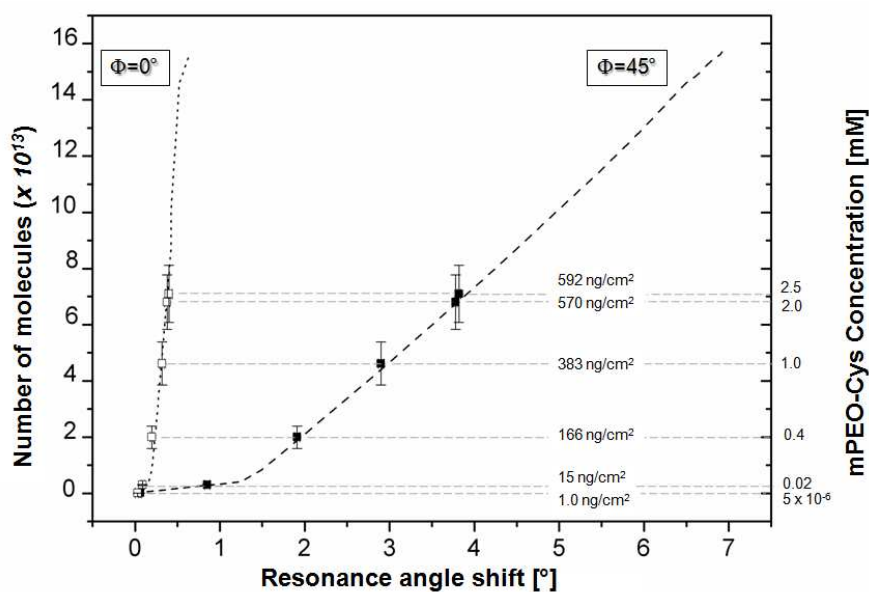
Figure 4. 11. Theoretical (*dotted* and *dashed lines*) and experimental (*symbols*) calibration curves. The number of mPEO molecules grafted onto the surface is plotted as a function of the SPR measurement output signal both for φ=0° (*dotted line* and *empty symbols*) and φ=45° (*dashed line* and *full symbols*) detection. To each experimental point, the corresponding surface grafting density and solution concentration are reported.

Table 4. 8. mPEO number of molecules adsorbed onto the grating surface and corresponding surface densities as a function of solution concentration and resonance angle shifts for both null and rotated azimuth detection.

mPEO-SH Concentration	$\Delta\theta_{res}$ [°]		Surface density		Mushroom contribution*
	Null azimuth ($\Phi=0°$)	Rotated azimut ($\Phi=45°$)	N/cm^2 ($\times 10^{11}$)	σ [ng/cm^2]	[%]
500 nM	0.03±0.03	0.06±0.02	1.3±0.1	1±0.1	3
20 µM	0.09±0.02	0.85±0.03	19.0±2.3	15±2	47
400 µM	0.20±0.02	1.91±0.03	200±40	166±17	87
1 mM	0.32±0.03	2.90±0.03	462±77	383±25	65
2 mM	0.38±0.03	3.78±0.02	680±97	570±35	45
2.5 mM	0.40±0.04	3.82±0.02	710±101	592±37	44

*the mushroom contribution increases when is the only one existing onto the surface (from a 500 nM to a 20 µM concentration), while it gradually decreases when also the folded-chain conformation is present (from 400 µM).

Since the angular range covered by the azimuthally-controlled detection (from 0.06° to 3.82°) is higher than the one covered by the null-azimuth one (from 0.03° to 0.40°), the discussion below focuses onto the more sensitive detection method, taking into account that the same considerations could be done for the other detection method results.

In the theoretical calibration curve, three polymer conformation regimes can be identified along the SPR response range. From 0.01° to 1.25° the grating surface is partially covered by mPEO molecules in a mushroom-like conformation only, and the contribution to the conformation fraction in Eq. (4. 1) is only given by *f*. When $\Delta\theta$ reaches the value of 1.25°, *f* is equal to 1, which means that the surface is completely covered by a mushroom-like polymer layer. From 1.25° to 6.2° a new conformational regime appears, in which the mushroom-like and folded-chain-like conformations co-exist. Here, both *f* and *(1-f)* contribute to Eq. (4. 1): *f* gradually decreases while *(1-f)* increases until it is equal to 6.2° and *f* approaches zero. For $\Delta\theta > 6.2°$ another transition occurs: a mixed folded-chain/brush-like conformation is present and any increment in the amount of tethered polymer results in an increase of the brush-like percentage, until a full brush layer is reached at $\Delta\theta=6.9°$.

In the experimental measurements (*full symbols* in **Figure 4. 11**) we never reached resonance angle shifts greater than 3.82°, meaning that, even at saturation, the polymer film did not reach a full brush, in agreement with the information gathered by AFM (**Figure 4. 10**). Indeed the tendency of long chain polymers, as the one here used, to form folded coils is known to limit the formation of the full brush-like conformation.

By using the theoretical calibration, the amounts of tethered mPEO corresponding to the experimental shifts were calculated, resulting between 1 (500 nM mPEO-SH) and 592 ng/cm^2 (2.5 mM mPEO-SH). Finally, the amount of PEO at the above maximum surface coverage was used to calculate the sensing platform refractive index (S_{RI}) and a mass (S_M) sensitivities, which were of 63 ($\varphi=0°$) and 603 ($\varphi=45°$) °/RIU, and 6.7×10^{-4} ($\varphi=0°$) and 6.4×10^{-3} ($\varphi=45°$) °/ng, respectively. The corresponding resolutions were also calculated, resulting to be 3.3×10^{-5} ($\varphi=0°$) and 6.3×10^{-6} ($\varphi=45°$) RIU, and 59.7 ($\varphi=0°$) and 3.1 ($\varphi=45°$) ng, respectively.

4.7 Protein sensing: the first application

After sensing platform calibration described in the previous section, we applied for the first time GC-SPR φ≠0° to a series of (bio) sensing experiments, which we devoted at optimizing the process of surface dressing so to minimize non-specific interactions with non-analyte molecules and maximize the analytical biosensing signal to background noise (S/N) ratio. Here the term *"noise"* includes not only the typical instrumental factors (photons rate, angular spread etc…) but also the *bio-signal* generated by "background" *non-analyte* components in the sample.

The kinetics of gold coating with higher molecular weight (Mw) PEO-thiol derivatives (which are generally considered the most efficient surface protectors [113,137]) has also been investigated to some extent [136], but a relationship between PEO density and anti-fouling efficacy has not been precisely established. Some information in this direction was provided by Uchida [110] who investigated the antifouling behaviour of a combination of 2 kDa and 5 kDa thiol PEOs using a Biacore® apparatus. By carrying multiple incubations of the two derivatives on the same gold substrate, he obtained several surfaces at different polymer density, which he related to the antifouling response against bovine serum albumin (BSA) (0.1%). However, the surfaces prepared by Uchida contained a mixture of the two polymers so that the individual contribution of each species cannot be extrapolated from his data.

In light of these considerations, we devoted the novel high sensitivity GC-SPR φ≠0° detection set-up to characterize the kinetics of different Mw thiolated-PEOs (0.3, 2 and 5 kDa) grafting onto nanostructured gold surfaces [17,19,20,27] and to study in a quantitative manner their individual antifouling capability using goat serum (GS) or BSA containing buffers. A real biodetection event in the above buffers was also investigated using the avidin/biotin couple and the analytical signal to background noise ratio was calculated at different polymer densities.

4.7.I Kinetics of PEOs binding onto the surfaces

ω-S terminating PEOs of different Mw - 0.3, 2 and 5 KDa – here tested are shown in .
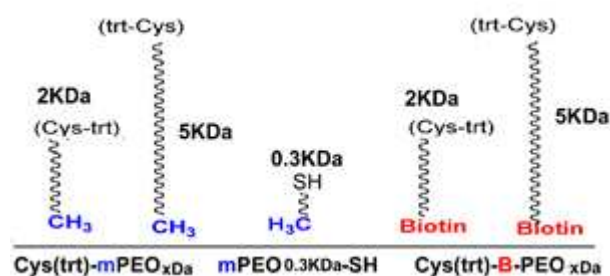
Figure 4. 12. Cartoon (not in scale) depicting the PEO derivatives used in this work for surface functionalization.

All kinetics studies have been carried out using 1 mM PEO solutions. This concentration was selected so to mimic experimental conditions adopted in other studies of thiol-gold tethering [28, 47, 50] and was followed the PEO deposition protocol described in Section 4.2.II. The amount of adsorbed PEO after different deposition times (up to 48h) was calculated (**Table 4. 9**) from the

change in the reflectivity minima depth using the Jung model [21,35] as previously discussed (Section 4.4.II) and the resulting kinetics are shown in **Figure 4. 13**.

The SPR resonance angle shifts increased with deposition time, with different kinetics for each Mw derivative. The high sensitivity of the analytical set-up allowed highlighting even minor variations occurring at the surface. The 0.3 kDa derivative reached a flat plateau after 8h of deposition with a final angle shift of about 2°, whereas the 2 and 5 kDa started to plateau at 24h and 30h, respectively; after then, the resonant shifts continued to increase very slowly (3% and 1.3% increase between 30 to 48h), indicating that layer build-up was still evolving, even if at very slow pace. After 48h, the angle shifts registered were 1.67±0.05° and 3.8±0.02° for the 2 kDa and 5 kDa derivatives, respectively. Polymer surface densities at the end of the process were calculated to be about 379, 310 and 590 ng/cm^2 for the 0.3 kDa, 2 kDa and 5 kDa PEOs respectively. The high final density of the 0.3 kDa PEO indicates that the molecule assembles in a full brush configuration. On the contrary, the 2 and 5 kDa PEOs assemble in the mixed mushroom-brush conformation that, being more disordered generates a smaller or comparable surface density. When analyzing the deposition process in terms of number of molecules/area, the relative grafting rate was inversely related to the molecule size, with a dramatically faster process for the 0.3 kDa derivative.
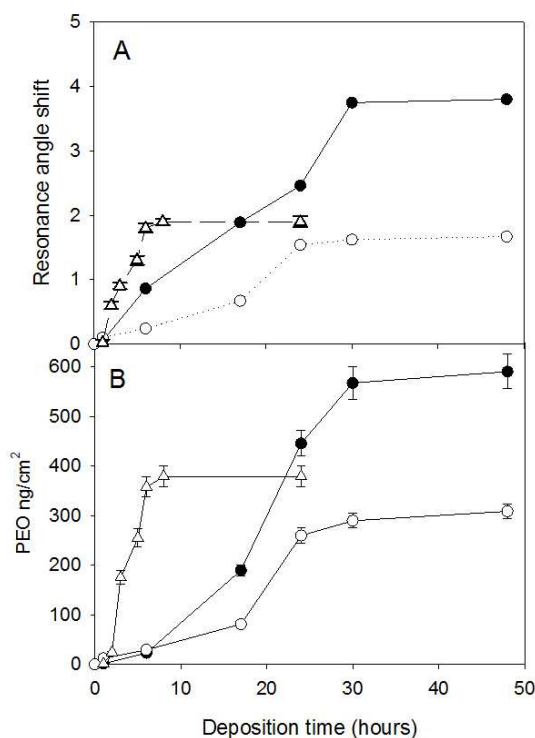
Figure 4. 13. Results of mPEO Cys deposition experiments. The adsorption kinetics of mPEO 0.3 kDa (*triangles*), 2 kDa (*empty circles*) and 5 kDa (*full circles*). Data are reported as crude resonance angle shifts (a) an ng /cm^2 (b).

Table 4. 9. PEO 5, 2 and 0.3 kDa surface densities and adsorbed molecules as a function of resonance angle shift and grafting time.

PEO 2/5kDa	PEO 5kDa			PEO 2kDa			PEO 0.3kDa			
Time [h]	$\Delta\theta$res [°][1]	Surface density σ [ng/cm^2] [2]	Molecules N / nm^2 [3]	$\Delta\theta$res [°][1]	Surface density σ [ng/cm^2] [2]	Molecules N / nm^2 [3]	Time [h]	$\Delta\theta$res [°][1]	Surface density σ [ng/cm^2] [2]	Molecules N / nm^2 [3]
1	0.05 ±0.02	1.3±0.1	0.002	0.10 ±0.06	12±1	0.04	1	0.02 ±0.05	0.79±0.04	0.01
6	0.86 ±0.03	22±1	0.03	0.24 ±0.06	29±2	0.09	2	0.60 ±0.06	24±2	0.4
17	1.89 ±0.03	190±11	0.23	0.67 ±0.05	81±5	0.24	3	0.90 ±0.05	175±14	2.9
24	2.46 ±0.03	446±26	0.54	1.54 ±0.06	260±14	0.78	5	1.33 ±0.07	255±18	4.3
30	3.75 ±0.02	568±33	0.68	1.62 ±0.05	290±15	0.87	6	1.80 ±0.07	358±20	5.9
48	3.80 ±0.02	590±35	0.71	1.67 ±0.05	309±17	0.93	8	1.90 ±0.05	379±21	6.0
-	-	-	-	-	-	-	24	1.90 ±0.09	379±21	6.0

[1] The angular shift error is derived from the instrumental one; [2] The surface density error was estimated from the formula used for the surface density calculation [35]; [3] The molecular dimensions used as input in the Jung model were: a molecular diameter of the polymer in the extended conformation of 0.45 nm [112]; Flory radii for the surface area occupied by mushroom molecules 4.75, 2.70 and 0.89 nm for the 5, 2 and 0.3 kDa [133] derivatives, respectively; and gyration radii for the mushroom film thickness of 2.8, 1.6 and 0.60 for the 5, 2 and 0.3 kDa [133] derivatives, respectively. In the case of the 2 and 5 kDa PEOs only, we assumed also the existence of a folded chain conformation [35].

The adsorption process registered is in line with what indicated by Love and Whitesides for short thiols [36] but, to our surprise, it was dramatically slower than what described in the literature for high Mw PEOs. For example, Tokumitsu [136], using a 50 μM solution of 2 kDa PEO-alkanethiol in dimethylformamide, reached total surface coverage within 2h. Uchida [110], using a 1 mM solution of 5 kDa thiol-PEO in a microfluidic chamber reached a surface density of 230 ng/cm^2 in 20 minutes, a value that in our case necessitated more than 17h deposition.

The higher sensitivity of the rotated angle detection cannot be accounted for the difference observed. Indeed, it is more likely that other factors, e.g. the nature of the thiol at the end of the polymer, the solution used for the deposition, the fluidics, or the surface nanostructuration, alone or in combination, are responsible for this different behaviour. For example, high salinity buffers are described to favour PEO deposition thanks to a salting out effect. Probably by changing some

parameters, like buffering to neutrality the TFA solution or increasing its ionic strength would improve the process and yield a kinetic behaviour more similar to what reported in the literature.

4.7.II   Fouling response

The antifouling behaviour of the surfaces at different PEO coverage prepared along the kinetics study was tested in two kind of buffer solutions, namely PBS containing either 0.1% (w/v) serum albumin (PBS-B) or 1% (v/v) whole animal (goat) serum (PBS-GS). The first diluent is the one that is most commonly used in immunoassays, when antibodies or other protein reagents are used as the recognition elements. In this type of experiments, BSA is added to the medium mainly to prevent the active biorecognition element (antibody or protein) from denaturation. The second diluent, PBS-GS, was selected as a model for direct (label-free) biorecognition (sensing) assays, in which the analyte is found in the biological medium, which is normally analyzed upon dilution. 1% GS concentration mimics the condition of a 100-fold dilution of the unprocessed biological sample, a target that is considered reasonable for a sensitive bioassay.

The dip reflectivity angles were measured before and after their immersion for 2 hours at 37°C in the above buffers (**Figure 4. 14**). The differences in dip reflectivity angles represent the SPR resonance angle shifts that account for the fouling effect. By normalizing these values with the shifts generated by incubating the same buffers on bare gold gratings (θ = 2.9° and 3.4° for PBS-B and PBS-GS, respectively), the antifouling efficacy fraction was also calculated.
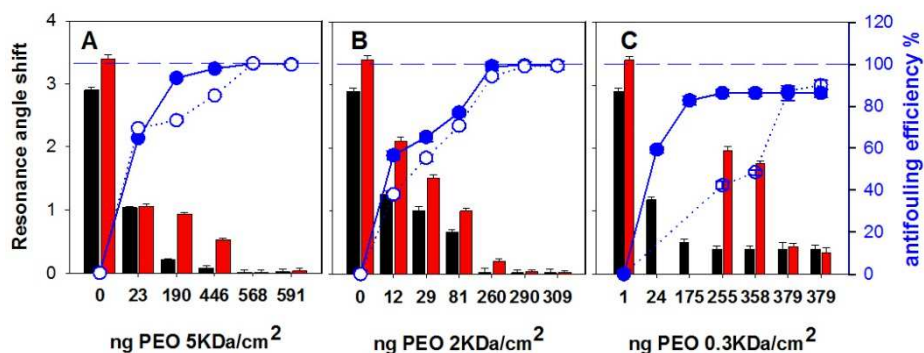
Figure 4. 14. Fouling SPR response of the 5 kDa (A) 2 kDa (B) and 0.3 kDa (C) mPEO layers incubated in the presence of PBS-B (*black bar, full line*) and PBS-GS (*grey bar, dotted line*). The resonance angle shifts generated after 2h incubation at 37°C of the above buffers on surfaces coated with PEO at different density (ng/cm²) are shown as bars, black for PBS-B and grey for PBS-GS. The antifouling efficiency (%) of each surface towards PBS-B (●) and PBS-GS (○) was calculated by normalizing the shift measured onto them with that generated in the absence of PEO. Only the organic components in the buffers (BSA and Serum) are responsible for the shifts, since incubation in PBS alone, carried out as a control, (data not shown) did not modify the resonance angle. A two hour incubation time was selected through preliminary experiments (not shown), so to ensure reaching equilibrium (maximum angle shift) in both diluting buffers.

In the case of the high Mw polymers, the resonance angle shift varied from 1° at the lowest PEO concentrations to null at the highest ones, indicating that both derivatives were capable of full surface protection (namely the condition in which the signal generated upon incubation was of the same order of magnitude as the instrumental error) in both buffers, but only at the highest densities investigated. These conditions were reached only at PEO density $\geq$ 570 ng/cm² (5 kDa) and $\geq$290

ng/cm^2 (2 kDa), namely in the plateau situation of the PEO deposition kinetics process. On the contrary, the 0.3 kDa PEO derivative was inefficient in protecting from fouling, at all surface densities tested. In this case, the smallest resonance shifts, which were registered on the 0.3 kDa PEO saturated surface ($\sigma \approx$ 379 ng/cm^2), were about 0.40° and 0.34° in PBS-B and PBS-GS, respectively. By normalizing these values with the shifts generated by incubating the same buffers on bare gold gratings ($\theta = 2.9°$ and 3.4° for PBS-B and PBS-GS, respectively), it comes out that at PEO 0.3 kDa saturation, the antifouling efficacy is never higher than 90% (86% for PBS-B and 90% for PBS-GS), whereas the 2 kDa and 5 kDa derivatives yield >99% protection.

Overall, these results are not totally surprising, as it was previously shown that the protection efficacy of PEOs strongly depends on the conformation they assume on the surface [36]. Brush like films - like the one here obtained with the 0.3 kDa PEO- even if densely packed (here 6 molecules/nm^2), do not guarantee protection from non-specific interactions, whereas mixed mushroom/brushed systems (as those here obtained with the higher Mw PEOs) do. 5 kDa and 2 kDa PEOs full antifouling was reached at about 0.7 and 0.9 molecules/nm^2 respectively, namely the smaller derivative required higher molecular density than the higher Mw one to achieve the same protective effect.

It is noteworthy that in all surfaces tested, PBS-GS displayed much stronger fouling potency than PBS-B. This is likely due to its higher complexity in composition: as compared to PBS-B (that contains one type of protein only - BSA, Mw 66 kDa), PBS-GS has an overall higher protein load and contains different types of proteins characterized by different size and physico-chemical properties, together with other kind of compounds (e.g. lipids and low Mw compounds) with a wide distribution of Mw. Indeed it is known [116,117] that for a given PEO size and surface density, non-specific binding depends also on the kind and concentration of fouling elements. In general terms, the difference observed in the two buffer fouling strength underlines the importance of validating the negative control buffer when applying SPR sensing to quantitative analysis.

It is noteworthy, that the high analytical sensitivity of the φ=45° measurement allowed to highlight small phenomena that would have remained undetected by other analytical configurations. For example, it is likely that the incomplete protection of the 0.3 kDa PEO or the fouling effects at intermediate polymer densities (eg. 5 kDa at 450 ng/cm^2 and 2 kDa at 260 ng/cm^2, which protected the surfaces from PBS-B but not from PBS-GS) are all likely to remain underestimated when using less sensitive classic SPR detection configurations.

4.7.III Specific binding and analytical signal-to-background noise

These experiments were carried out to evaluate the ability of the entire sensing platform to detect a model analyte and to quantify how the signal-to-background noise value - intended as the ratio between the signal related to the analyte and the one generated by the diluting buffer- varies by changing the fouling polymer density. Biotin and avidin were selected as the ligand/analyte couple. Based on the antifouling results, these experiments were carried out using the two high Mw polymers only. We created surfaces coated with different densities of biotin-PEO (bPEO) by performing depositions for different lengths of time, similarly to what done with mPEO. For the 5 kDa derivative, we obtained three surfaces, two at *"low"* (39 and 222 ng/cm^2) and one at *"high"* (567 ng/cm^2) bPEO density. In the case of the 2 kDa derivative we generated only one surface at *"high"* bPEO density (354 ng/cm^2). The *low* bPEO density surfaces were used to perform avidin binding in the "less fouling" PBS-B, and the two *high* ones were used for the "more complex" PBS-GS. The same incubation time as of that adopted in the antifouling experiments was used, so that

the contribution of non-specific binding to the overall signal at each individual PEO density could be extrapolated from the data of **Figure 4. 14**. The latter was mathematically subtracted from the angle shift generated upon incubation in the presence of avidin, so to obtain the net avidin contribution to the signal (*net avidin* $\Delta\theta_{res}$). The reflectivity dips obtained after bPEO deposition and avidin binding and the contribution to the SPR signal, given by the each individual component on the surface (bPEO, buffer components and avidin) are shown in **Figure 4. 15**. In order to compare quantitatively the antifouling efficacy of all substrates, the contribution of the buffer to the total signal and the signal to background noise, defined as the ratio between the contribute of the analyte and that of the buffer were also calculated (**Table 4. 10**).
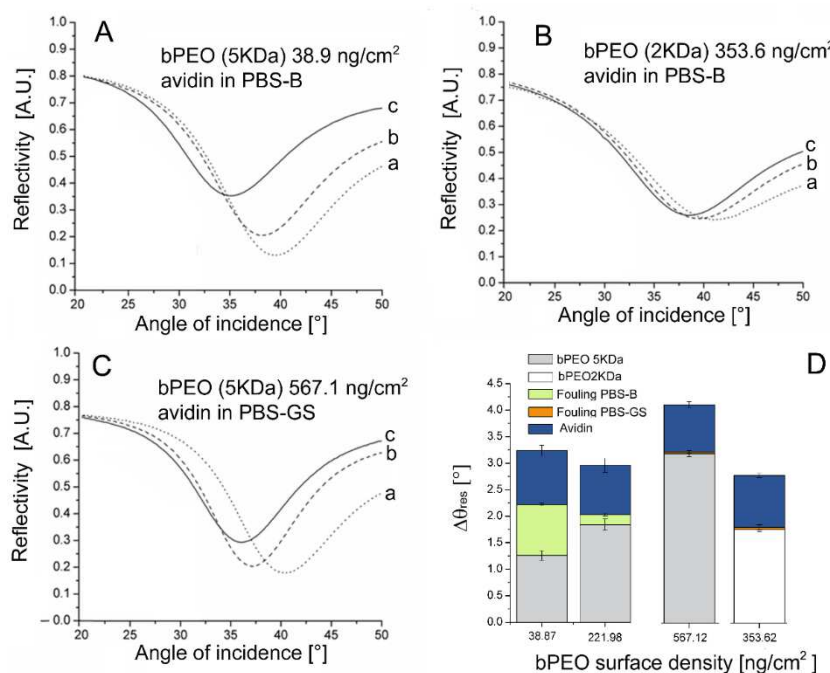
Figure 4. 15. Results of the avidin binding experiments on bPEO coated surfaces. A, B and C show the reflectivity dips of a selected pool of samples, collected on bare substrates ((a)-dot line), after bPEO-Cys deposition ((b)-dashed line) and after incubation of avidin diluted in the fouling buffer ((c)-solid line). The precise conditions of each experiment are summarized in the individual graphs; D) Bar chart showing the contribution of the individual components to the total resonance angle shift ($\Delta\theta_{res}$) in all of the experiments carried out.

Table 4. 10. Quantitative evaluation of specific and non-specific binding events

| Underlying polymer	bPEO density [ng/cm^2]	Buffer type	$\Delta\theta_{res}$ after incubation of avidin in buffer [°][1]	$\Delta\theta_{res}$ contribution from buffer only	Net avidin $\Delta\theta_{res}$ [°][2]	Contribution of buffer to the total signal [%]	S/N (Δ avidin/ $\Delta\theta_{res}$ buffer
bPEO 5 kDa	39	PBS-B	1.98±0.08	1,04	0.94±0.10	52.53	0,90
	222	PBS-B	1.12±0.10	0,21	0.91±0.12	18.75	4,30
	567	PBS-GS	0.92±0.04	0,03	0.89±0.08	3.26	29,7
bPEO 2 kDa	354	PBS-GS	1.05±0.10	0,02	1.03±0.04	1.90	52,5

[1]Experimental; [2]Calculated.

The signal due to the buffer alone (PBS-GS) on the two *high*-density bPEO layers was calculated to be within the instrumental error (0.03° and 0.02° $\Delta\theta_{res}$ for the 5 kDa and 2 kDa PEO surfaces respectively). On the contrary, the contribution to the signal of PBS-B on the two *low* 5kDa bPEO density surfaces was quite high (1.04° and 0.21° $\Delta\theta_{res}$ at 39 and 222 ng/cm^2 of 5 kDa bPEO, respectively). Nevertheless, when these values were subtracted from the total signal obtained in the

presence of avidin, the resulting *net avidin* $\Delta\theta_{res}$ remained centred around the same value, independently of the underlying 5 kDa bPEO layer and the dilution buffer. This is not surprising since all bPEO densities tested were high enough to guarantee the formation of an avidin monolayer so that no dose/response curve was expected.

The mean *net avidin* $\Delta\theta_{res}$ value registered on the bPEO 5 kDa surfaces (each in duplicate) was 0.91±0.03°. Its consistency along the whole range of 5kDa bPEO densities indicates a good reproducibility in the sensing signal generated by the device. In the case of the bPEO 2 kDa surface, the *net avidin* $\Delta\theta_{res}$ was 1.05±0.02°, slightly higher than that registered on the 5 kDa PEO surfaces, likely because the smaller PEO allows the analyte to get closer to the plasmonic surface.

4.8 An innovative approach for protein sensing

One limitation of the avidin–biotin technology is the "low" number of biotin binding sites (BBS) per protein, so that only up to 4 biotinylated moieties can be linked together in one assembly. A possibility to overcome this limit is to obtain polymerized forms of the proteins, and several approaches to obtain supramolecular poly(strept)avidin systems have been described. Micron size avidin or streptavidin coated particles have indeed become commercially available, and colloidal polymeric systems have been described in the literature. A novel colloidal poly avidin system that has recently been described in the literature is the Avidin-Nucleic-Acid Nano Assembly (ANANAS) [130]. This poly avidin is obtained by exploiting a stoichiometrically defined double self-assembly process dictated by high affinity interactions (**Figure 4. 16** (a)). In the process of ANANAS preparation, the high affinity of avidin for the nucleic acids drives the formation of assemblies in which several avidins bind to a nucleic acid filament with precise avidin/DNA base pairs relationship. Even if the protein biotin binding ability is maintained after DNA interaction,9 the avidin-nucleic acid complex is unusable as such, due to its poor solubility in aqueous buffers. However, if the assembly is obtained sing plasmid DNA as the nucleating agent, and controlled amounts of biotinylated hydrophilic polymers (e.g., biotin-poly(ethylene oxide)) to cover a small percentage of the biotin binding sites, buffer-soluble toroid-shaped nanoparticles (Ø ~ 100 nm) are formed, 10 in which most of the biotin binding ability is maintained. A unique property of this system is that, for a given nucleating DNA, the number of protein units/particle is precisely defined [130] as opposed to poly avidin systems obtained by chemical cross-linking whose composition is defined by statistical rather than high affinity rules. Although the composition and the number of biotin binding sites in the core ANANAS particle can be calculated from the stoichiometry of the assembly reagents, the number of BBS truly available for binding biotin derivatives has not been shown yet, and so has the influence of steric or chemical constraints in the particle loading capability. On the other hand, knowing the loading capability of the assembly would allow formulating multifunctional assemblies with stoichiometric precision "in one pot" (**Figure 4. 16** (b)), namely without the need for purification steps. In this work the ANANAS particle synthesis will be not discussed in detail.
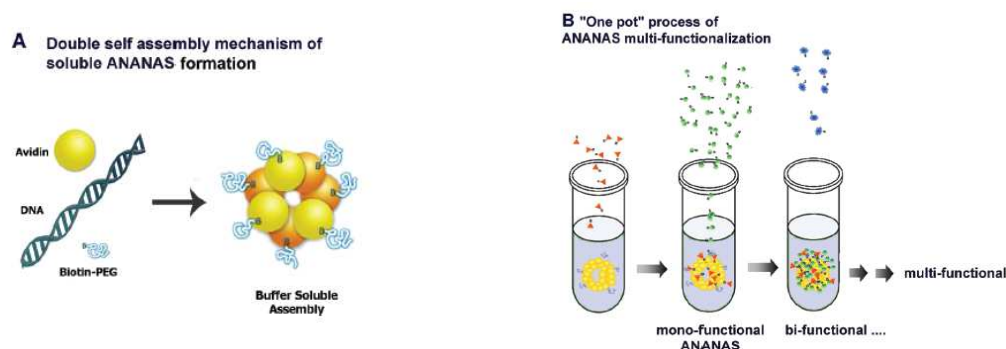
Figure 4. 16. Diagram (not in scale) representing the soluble core ANANAS double self-assembly formation (A) and the general principle of the "one pot" multi-functionalization process (B). Re-printed from *Morpurgo, M. et al. Analytical Chemistry (2012)* [130]

ANANAS particles are currently used in diagnostic thanks to their possibility to increase the final detected signal. Starting from this consideration we applied ANANAS particles to our SPR sensing platform, testing the system sensitivity in the presence of Avidin or Avidin/nucleic acid nanoassemblies.

In this experiment we used a b-PEO5kDa/mPEO5kDa film as sensing layer changing the ratios between the two species in the starting solution (0.034 and 0.006 and 0.001 were the ratios adopted). The three sensing layers were deposited twice in order to perform experiments both with Avidin and ANANAS in the same time. The experiment scheme is reported in **Figure 4. 17**.
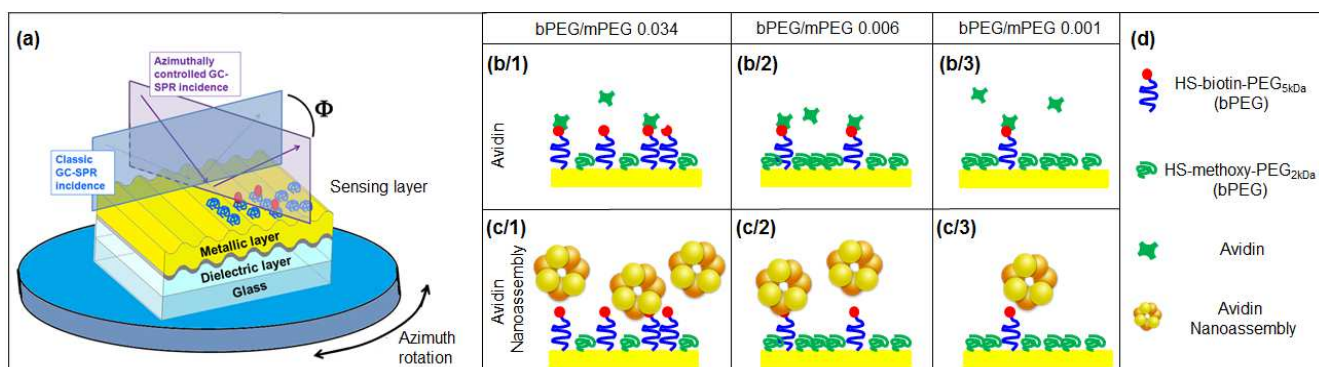
Figure 4. 17. Experimental scheme. The whole sensing architecture adopted (a) consisted in a sinusoidal metallic grating functionalized with a sensing layer and azimuthally rotated for the bio-detection. The sensing surface consisted in a mixed bPEG/mPEG layer obtained by depositing three different molar ratios of the two species: bPEG:mPEG 0.034 [(b/1) and (c/1)], bPEG:mPEG 0.006 [(b/2) and (c/2)] and bPEG:mPEG 0.001 [(b/3) and (c/3)]. Sensing tests were performed with avidin (row - b-) and avidin nanoassembly (row - c-)).

In **Table 4. 11** SPR resonance angle shifts detected and experimental sensitivities obtained for both systems are reported. Only the 0.006 ratio was analyzed changing analyte incubation time because it was considered the most interest regime considering both SPR signal obtained and the number of available probes.

Table 4. 11. SPR response to bPEG/mPEG-aividin and bPEG/mPEG-avidin nanoassembly sensing systems.

In the Table resonance angle shifts, molecular and molar sensitivities are reported for both sensing systems: bPEG/mPEG –avidin and bPEG/mPEG-avidin nanoassembly ones.

bPEG/mPEG molar ratio	Analyte incubation time [min]	Avidin		Avidin nanoassembly		Nanoassembly sensitivity/avidin sensitivity
		Resonance angle shift [°]	Resonance angle shift [°]	Resonance angle shift [°]	Resonance angle shift [°]	
0.034	60	1,17±0,16	1,17±0,16	2,4±0,12	2,4±0,12	2.05±0.19
	60	0,03±0,02	0,03±0,02	0,47±0,06	0,47±0,06	17.7±0.79
	80	0,04±0,02	0,04±0,02	0,87±0,05	0,87±0,05	21.8±0.56
	120	0,08±0,06	0,08±0,06	1,09±0,13	1,09±0,13	13.6±0.87
0.006	180	0,09±0,07	0,09±0,07	1,12±0,14	1,12±0,14	12.4±0.90
0.001	60	0,02±0,07	0,02±0,07	0,03±0,07	0,03±0,07	-

In **Figure 4. 18** the ratio between experimental sensitivity obtained with Avidin and the sensitivity obtained using ANANAS particles is reported.
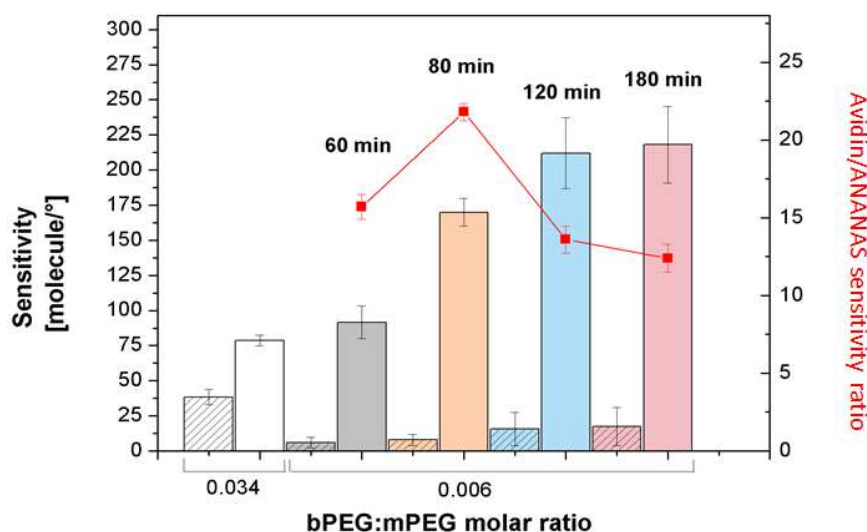
Figure 4. 18. Bar chart showing the sensitivity calulated as the ratio between detected molecules and resonance angle shifts obtained (molecules/°) as a function of bPEG:mPEG molar ratio, for both sensing systems: avidin (patterned bars) and avidin nanoassembly ones (empty bars). Avidin/avidin nanoassembly sensitivity ratio for each incubation time is also reported (red squares).

Saturation condition for analyte-probe binding was reached from 120 minutes for both Avidin and ANANAS, but the SPR signal in the case of ANANAS was significantly higher than in the case of Avidin: SPR sensitivity (molecule/°) was 12.4 times higher for the ANANAS. This result was the first application of ANANAS particles to GC-SPR and it could be a starting point for the development of a sensitive diagnostic system.

In this work we successfully achieved the optimization of an azimuthally controlled GCSPR sensing platform for nucleic acid detection. Various dressing conditions with PNA-based probes and a

PEG$_{2000}$-based backfiller were explored both for sensing and antifouling capabilities, calculating their S/N ratios. The optimal conditions were found to be in the use of a molar ratio of 1:9 between a (trt)Cys-PEG$_{5000}$-conjugated probe and the backfiller, with a S/N ratio of 19.05.

4.9   PEO-PNA deposition

As previously described (Section 4.3), our choice for the deposition of PEO-PNA probes was the co-immobilization strategy, in which both PEO-PNA (the probe) and PEO (the backfiller and antifouling component) are deposited at the same time, starting from the same solution.

In order to have a control on final surface composition in term of PEO-PNA amount, we carried out an accurate study for the optimization of our co-immobilization protocol. We started from a kinetics study of our PEO derivatives, we derived the kinetics adsorption constants of our molecules, and then we realize a mathematical model for predicting the final surface condition of our system. The model was a way for having a better control on deposition protocol, experiment reproducibility and final results, in our experimental conditions.

4.9.I   Thiol adsorption onto gold: theory and experimental

The adsorption reaction of thiols binding onto a gold surface could be summarized as reported in (4. 7) [36] and it is described by the Langmuir adsorption kinetics model [36,121,138–146].

$$R-SH+Au \Leftrightarrow R-S-Au+\frac{1}{2}H_2 \qquad (4.3)$$
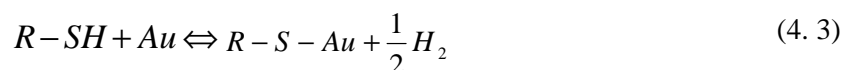
Starting from Langmuir adsorption model, a lot of adsorption models were described in literature in order to get a precise description for thiol adsorption onto gold mechanism [36,118,119]. In particular, changes in the Langmuir model were performed because the thiol adsorption occurs into 2 steps: during the first one (the fastest step) thiol species start to adsorb to the surface in a random and non-homogeneous way, while during the second one (a lower step) the molecules tend to form a compact and high density monolayer [36]. In the following study we will focus on the classical Langmuir adsorption model.

The adsorption kinetics of thiols is described by the Langmuir adsorption equation [145]. [146]:

$$\frac{d\theta}{dt}=k_a(1-\theta)C-k_d\theta \qquad (4.4)$$

where θ is the surface coverage expressed as fraction (unitless), $1-\theta$ is the surface portion uncovered by the thiol, t is the molecule grafting time, C is the thiol bulk concentration [$mol \cdot L^{-1}$], k_a and k_d are the adsorption and desorption rate constants.

Integration of Eq. (4. 8) gives the time-dependent surface coverage:

$$\theta(t)=\left[\frac{k_aC}{(k_aC+k_d)}\right][1-\exp(-(k_aC+k_d)t)] \qquad (4.5)$$

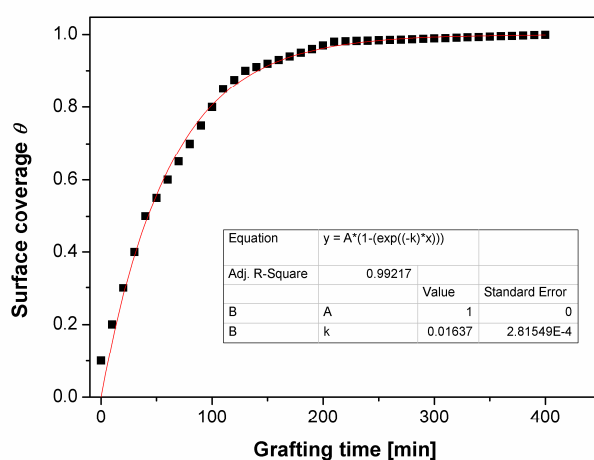As the thiol desorption process is negligible: $k_d \ll k_a$.

Thus, Eq. (4. 5)can be simplified as:

$$\theta(t) = 1 - \exp(-k_{obs} \cdot t)$$
(4. 6)

where $k_{obs} = k_a C + k_d$.

k_{obs} is the *observed* rate constant, i. e. the rate constant of a specific molecule in specific experimental conditions, so it is the parameter directly derived from the experiment. Eq. (4. 6) could be used to fit experimental data of surface coverage plotted as a function of the grafting time.

An example of $\theta(t)$ fitting is reported in **Figure 4. 19**, in which are reproduced the experimental results reported by Hu and Bard [145].

| Equation	y = A*(1-(exp((-k)*x)))		
Adj. R-Square	0.99217		
		Value	Standard Error
B	A	1	0
B	k	0.01637	2.81549E-4

Figure 4. 19. Mercapto-Undecanoic Acid (MUA) adsorption from 0.5 mM solution in deionized water. The curve is plotted starting from raw data showed by *Hu, K. and Bard, A. J.* [145].

To have a correct estimation of k_a and k_d kinetics study for different thiol concentrations are necessary.

By this way, the linear fitting of the plot made by k_{obs} ($k_{obs} = k_a C + k_d$) values *vs* thiol molar concentrations C will give a slope equal to k_a and an intercept equal to k_d .

An example of this procedure is reported by Karpovich and Blanchard [146] (**Figure 4. 20**).
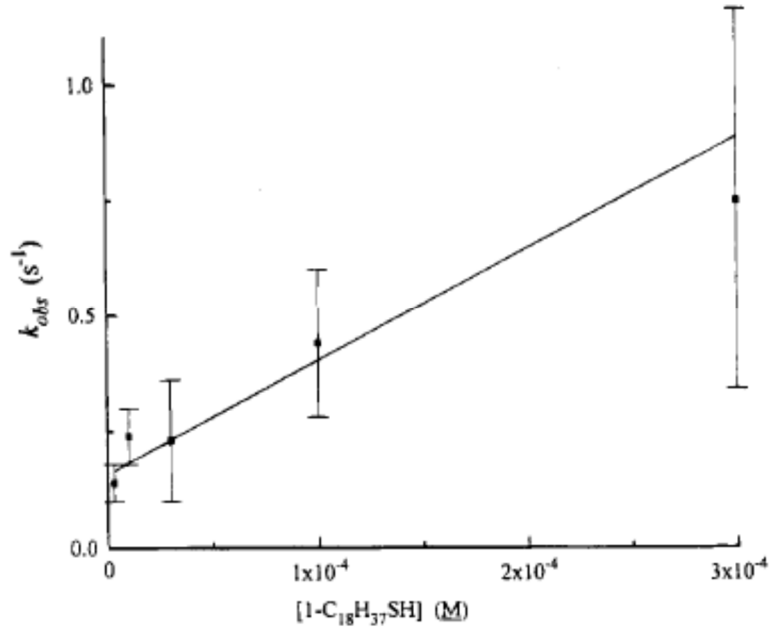
Figure 4. 20. Linear plot of k_{obs} vs thiol molar concentration showed by Karpovich and Blanchard [146].

Observations:

- Since the exact expression of k_{obs} is $k_{obs} = k_a C + k_d$, a plot of k_{obs} $[s^{-1}]$ vs C for a series of experimental concentrations results in a linear dependence between k_{obs} and C where the slope is $k_a [L \cdot mol^{-1} \cdot s^{-1}]$ and the intercept is $k_d [s^{-1}]$.

- In the absence of adsorption kinetics with a series of concentrations k_d could be approximate as $k_d \approx 0$, starting from the fact that $k_d \ll k_a$ (see eq. (3)). Thus we get:

$$k_{obs} \approx k_a C.$$

  The approximation $k_d \approx 0$ is valid for high molecular weight or long chain thiols (as for HS-PEGs), i. e. in the presence of molecules for which the desorption process is negligible.

- On the other hand, in the case of alkanethiols forming SAMs, could results $k_d > 0$, meaning that alkanethiolate-gold SAMs are equilibrium systems, and therefore at any given instant in time, some fraction of the adsorbed sites in the surface is unoccupied.

   Starting from previous considerations we studied the adsorption kinetics of all thiolated-PEO derivatives adopted in this work.

We measured the SPR response in term of resonance angle shift as a function of grafting time for mPEO$_{5kDa}$-Cys (0.825 mM), mPEO$_{2kDa}$-Cys (0.93 and 1.86 mM), bPEO$_{2kDa}$-MPA (1.84 mM), PNA-

PEO$_{5kDa}$-Cys (0.5 mM) and HS-PNA (0.1 mM). Considering the maximum resonance angle shift detected for each molecule as the maximum surface coverage (θ_{max}), the angle shift detected at the instant t (θ_i) could be converted in a surface coverage fraction applying the following equation:

$$\theta(t) = \frac{\theta_i}{\theta_{max}} \qquad (4.7)$$

We derived the surface coverage at each deposition time for all the molecules tested, obtaining a plot of $\theta(t)$ as a function of deposition time (t [s]). All experimental adsorption kinetics curve are plotted in **Figure 4. 21**.
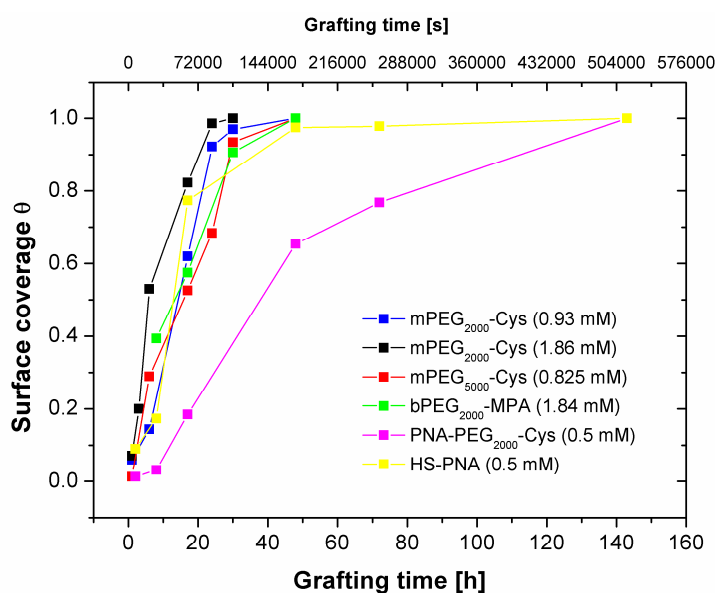
Figure 4. 21. Adsorption kinetics in term of surface coverage as a function of deposition time for all the molecules tested.

Similar adsorption curves were obtained for all PEO derivatives, except for PEO-PNA. This difference is probably due to the relevant difference in PEO-PNA molecule dimensions.

mPEO$_{5kDa}$-Cys (0.825 mM) has a lower adsorption kinetics than mPEO$_{2kDa}$-Cys (0.93 mM) as expected evaluating the chain lengths of the two polymers (about 32 and about 12 nm for PEO$_{5kDa}$ and PEO$_{2kDa}$ respectively). Focusing on PEO$_{2kDa}$, we could observe that the surface coverage saturation condition is reached before for a concentration of 1.86 mM than for a concentration of 0.93 mM.

bPEO$_{5kDa}$-MPA has a lower kinetics adsorption than mPEO$_{5kDa}$-Cys even if bPEO concentration is higher (1.84 mM *vs* 0.825 mM).

The derivation of rate adsorption constants for each molecule, was performed by fitting the experimental curves according to Langmuir adsorption model. The use of this model is usually adopted for simple thiols or alkanethiols [36,118,119,138–142,144–149] and rarely for PEO [150] was possible assuming the following Langmuir validity principles reported by Karpovich and Blanchard [146]. The Langmuir isotherm is based on the assumptions that

- adsorption is limited to one monolayer,
- all surface sites are equivalent,
- and adsorption to one site is independent of the occupancy condition of the adjacent sites.

The first assumption is clearly valid based on the chemical identity of the adsorbate species. For the second assumption we can also say that the surface is defect-free. This assumption is known to be not physically realistic. While there are a variety defects at the gold surface associated with grain boundaries, step edges, adatoms, vacancies and also the substrate nanostructuration could affect the deposition kinetics. Although we can assume that the resultant modulation of surface site energies is apparently small enough that the Langmuir approximation holds and that, due to the fact that our experiments are always performed onto nanostructured surfaces, our results can be considered consistent. Also the third assumption is open to significant questions. In fact PEO chains are not completely independent from the adjacent ones, but what is important to notice is that inter-chain interactions occur on a time scale significantly longer than the time scale associated with the formation of the gold-thiolate bond [146].

The same considerations could be done for HS-PNA.

Starting from these assumptions, the fitting of HS-PEOs and HS-PNA adsorption kinetics curves with the Langmuir model was possible. We use the Langmuir adsorption model based on Eq. (4. 6).
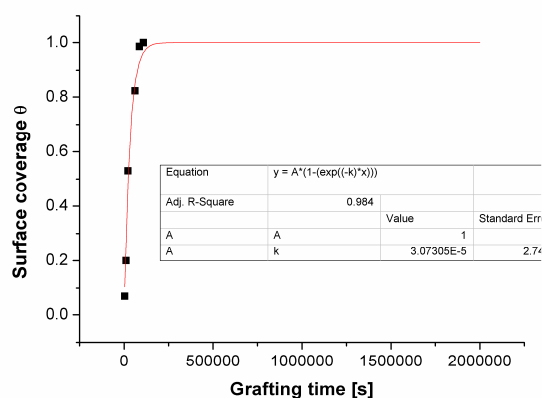
$$\theta(t) = 1 - \exp(-k_{obs} \cdot t)$$ (4. 8)

From the fitting we derived the k_{obs} [s^{-1}] for each used polymer. The fit was performed setting the kinetics ending point at a grafting time approaching an "infinite" value.

From **Figure 4. 22** to **Figure 4. 27** all adsorption curves together with their fitting are reported.
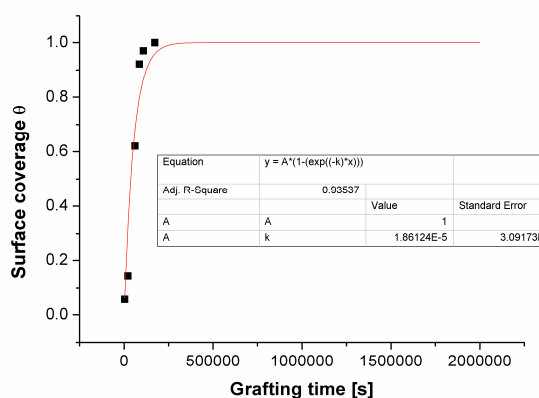
Figure 4. 22. Fitting of adsorption kinetics curve of mPEO$_{2kDa}$-Cys 0.93 mM (χ^2=0.97).

Figure 4. 23. Fitting of adsorption kinetics curve of mPEG$_{2kDa}$-Cys 1.86 mM (χ^2=0.98).
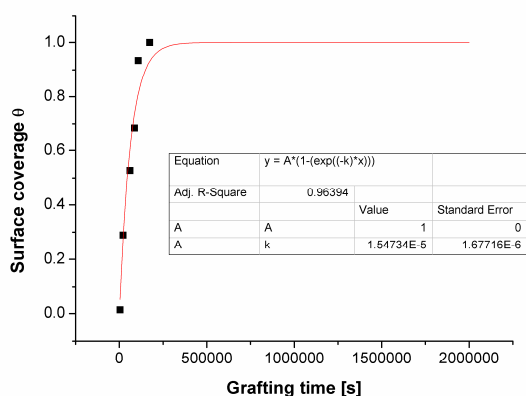
Figure 4. 24. Fitting of adsorption kinetics curve of mPEO$_{5kDa}$-Cys 0.825 mM (χ^2=0.96).
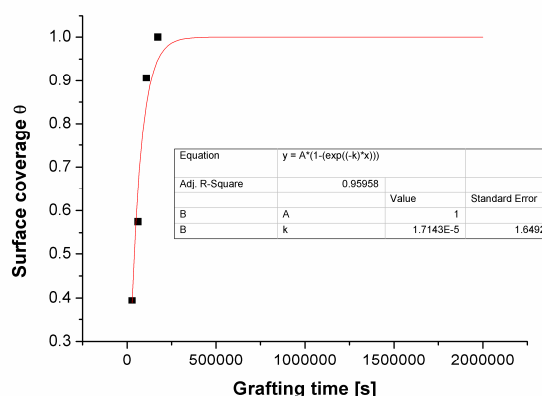

Figure 4. 25. Fitting of adsorption kinetics curve of bPEO$_{5kDa}$-MPA 1.84 mM (χ^2=0.98).
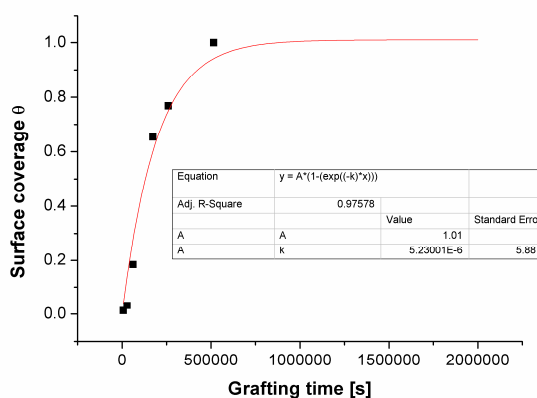

Figure 4. 26. Fitting of adsorption kinetics curve of PNA-PEO$_{5kDa}$-Cys 0.5 mM (χ^2=0.98).
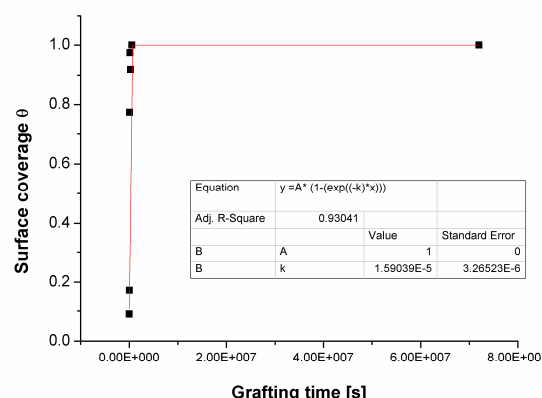
Figure 4. 27. Fitting of adsorption kinetics curve of HS-PNA 0.1 mM (χ^2=0.93).

Adsorption rate constants were calculated assuming that $k_d << k_a$, so that k_a value results:

$$k_a = \frac{k_{obs}}{C} \tag{4. 9}$$

where *C* is the concentration of PEO derivatives and HS-PNA in the solutions adopted for deposition experiments.

In the following table the adsorption rate constants obtained are summarized.

Table 4. 12. Adsorption rate constants of all molecules used

Molecule	Concentration [M]	$k_{obs} \times 10^{-5}\ [s^{-1}]$	$k_a \times 10^{-2}\ [L \cdot mol^{-1} \cdot s^{-1}]$
mPEG$_{2000}$-Cys	0.00093	1.86±0.34	1.83±0.02
	0.00186	3.07±0.3	
mPEG$_{5000}$-Cys	0.000825	1.55±0.184	1.88±0.02
bPEG$_{5000}$-MPA	0.00184	1.71±0.176	0.929±0.02
PNA-PEG$_{5000}$-Cys	0.0005	0.523±0.068	1.05±0.002
HS-PNA	0.25	1.59±0.33	6.35±0.02

4.9.II The co-immobilization model: from theory to preliminary PNA/DNA sensing experiments

Adjusting Eq. (4. 4) to the simultaneous adsorption of two molecules onto the surface we realized a mathematical model to obtain an evaluation of the surface portion occupied by both molecules at the end of the deposition process.

When a competitive adsorption of two different species (specie 1 and specie 2) is occurring onto a surface, the uncovered surface fraction seen by one species could be written as:

$$1 - \theta_1 - \theta_2 \qquad (4.\ 10)$$

where θ_1 and θ_2 are the coverage fraction for specie 1 and specie 2, respectively.

The description of the competitive adsorption mechanism will be given by a system of Eq. (4. 11) and Eq. (4. 12), in which the coverage fraction of each molecule is dependent not only on the specie concentration and on its adsorption and desorption rate constants, but also on the surface fraction occupied by the other molecule during the adsorption process.

$$\frac{d\theta_1}{dt} = k_{a,1}\left(1 - \theta_1 - \theta_2\right)C_1 - k_{d,1}\theta_1 \qquad (4.\ 11)$$

$$\frac{d\theta_2}{dt} = k_{a,2}\left(1 - \theta_2 - \theta_1\right)C_2 - k_{d,2}\theta_2 \qquad (4.\ 12)$$

where θ_1 and θ_2 are the coverage fraction for specie 1 and specie 2.

Re-arranging the above equations we get:

$$\frac{d\theta_1}{dt} = -(k_{a1}C_1 + k_{d1})\theta_1 - k_{a1}C_1\theta_2 + k_{a1}C_1 \qquad (4.\ 13)$$

$$\frac{d\theta_2}{dt} = -k_{a2}C_2\theta_1 - (k_{a2}C_2 + k_{d2})\theta_2 + k_{a2}C_2 \qquad (4.\ 14)$$

and then:

$$\begin{pmatrix} \dot{\theta}_1 \\ \dot{\theta}_2 \end{pmatrix} = \begin{pmatrix} -k_{a1}C_1 - k_{d1} & -k_{a1}C_1 \\ -k_{a2}C_2 & -k_{a2}C_2 - k_{d2} \end{pmatrix} \begin{pmatrix} \dot{\theta}_1 \\ \dot{\theta}_2 \end{pmatrix} + \begin{pmatrix} k_{a1}C_1 \\ k_{a2}C_2 \end{pmatrix} \qquad (4.\ 15)$$

$$\begin{pmatrix} \dot{\theta}_1 \\ \dot{\theta}_2 \end{pmatrix} = \begin{pmatrix} \alpha & \beta \\ \gamma & \delta \end{pmatrix} \begin{pmatrix} \theta_1 \\ \theta_2 \end{pmatrix} + \begin{pmatrix} -\beta \\ -\gamma \end{pmatrix} \qquad (4.\ 16)$$

Solving the calculation, we get the following equations for surface coverage of specie 1 and surface coverage of species 2:

$$\theta_1(t) = -c_1\beta e^{\lambda_+ t} - c_2\beta e^{\lambda_- t} + \frac{\beta}{\lambda_+ \lambda_-}(\lambda_+ + \lambda_- - \alpha - \gamma) \qquad (4.\ 17)$$

$$\theta_2(t) = c_1(\alpha - \lambda_+)e^{\lambda_+ t} + c_2(\alpha - \lambda_-)e^{\lambda_- t} + \frac{(\alpha - \lambda_-)(\alpha - \lambda_+) + \gamma\alpha}{\lambda_+ \lambda_-} \qquad (4.18)$$

Where:

- $\lambda_\pm$ are the eigenvalues:

$$\lambda_\pm = \frac{\alpha + \delta \pm \sqrt{(\alpha - \delta)^2 + 4\gamma\beta}}{2} \qquad (4.19)$$

- $\alpha, \beta, \gamma, \delta$ are the components of the following matrix:

$$\begin{pmatrix} \alpha & \beta \\ \gamma & \delta \end{pmatrix} = \begin{pmatrix} -k_{a1}C_1 - k_{d1} & -k_{a1}C_1 \\ -k_{a2}C_2 & -k_{a2}C_2 - k_{d2} \end{pmatrix} \qquad (4.20)$$

- Defining the initial conditions (i. e. $\theta(t=0)=0$), the coefficients c_1, c_2 result:

$$c_1 = \frac{\alpha + \gamma - \lambda_-}{\lambda_+(\lambda_+ - \lambda_-)} \qquad (4.21)$$

$$c_2 = \frac{\alpha + \gamma - \lambda_+}{\lambda_-(\lambda_- - \lambda_+)} \qquad (4.22)$$

Starting from this model (Eq. (4.17) and Eq. (4.18)) we were able to tune and predict the resulting surface coverage for each thiol species, setting the specie concentration in solution and the functionalization time.

The theoretical calculation was then implemented in a Mathematica Code and it was used for all DNA-PNA sensing experiments.

Validity of the co-immobilization model

The validity of the model described in the previous section was confirmed by a Toluidine Blue O (TBO) test, commonly adopted for evaluating the amount of carboxyl groups (-COOH) adsorbed onto a surface [151,152]. If a molecule adsorbed onto a surface contains –COOH ending group, using a simple procedure, it is possible to derive the number of molecules anchored to the surface [153,154].

We can summarize this type of test in the following steps:

- TBO is able to link carboxyl groups anchored to the surface in a 1:1 ratio, when they are de-protonated in basic environment, through charge interactions.
- Lowering the solution pH, the TBO is released in the solution.
- UV measurements (λ=633 nm) make the quantification of carboxyl groups anchored to the surface possible.

In our case we functionalized nanostructured gold surfaces with a mixed PEO$_{5kDa}$-COOH/PEO$_{2kDa}$ at five () different ratios, following the prediction of the co-immobilization model, and we derived the amount of PEO$_{5kDa}$-COOH molecules anchored to the surface. The mixed PEO$_{5kDa}$-COOH/PEO$_{2kDa}$ was chosen to mimic the DNA-PNA sensor surface.

Table 4. 13. Experimental parameters used for the TBO test

Sample	Surface coverage fraction predicted*		Solution concentration [mM]*	
	PEO$_{5kDa}$-COOH	PEO$_{2kDa}$	PEO$_{5kDa}$-COOH	PEO$_{2kDa}$
1	0.0	1.0	-	1
2	0.25	0.75	0.18	0.87
3	0.50	0.50	0.43	0.43
4	0.75	0.25	0.85	0.18
5	1.0	0.0	1.0	-

*Parameters decided using the co-immobilization theoretical model (Setion 4.7.II). Solution concentration are the same for the two molecules because kinetics adsorption trends of PEO 5 and 2 kDa are almost the same, as it is clearly visible from the adsorption curves in **Figure 4. 21** and from adsorption rate constants in **Table 4. 12**.

Starting from the study showed in Section 4.5.I, we evaluated the predicted number of molecules (as N/nm^2) of PEO$_{5kDa}$-COOH deposited onto the surface. We used the average values between the maximum number of PEO 2 and 5 kDa molecules reported in **Table 4. 9** (0.71 and 0.93 for PEO 5 and 2 kDa, respectively, giving an average value of 0.82) as reference to evaluate the number of PEO$_{5kDa}$-COOH chain adsorbed onto the surface for each desired coverage fraction.

In **Table 4. 14**, the comparison between the number of PEO$_{5kDa}$-COOH molecules predicted and that obtained from TBO test is reported.

**Table 4. 14.** PEO5kDa-COOH number of molecules predicted and obtained from TBO test

Sample	PEO$_{5kDa}$-COOH Surface coverage fraction predicted	Absorbance [a. u.]	PEO$_{5kDa}$-COOH Predicted number of molecules [N/nm^2]	PEO$_{5kDa}$-COOH Number of molecules from TBO test [N/nm^2]
1	0.00	0.060±0.002	0.00	0.00
2	0.25	0.065±0.004	0.20	0.18
3	0.50	0.075±0.011	0.41	0.36
4	0.75	0.080±0.010	0.62	0.54
5	1.00	0.090±0.030	0.82	0.71

Results obtained show that our theoretical model for the co-immobilization is confirmed by the TBO test with good approximation so that the model can be used for real sensing experiments.

4.9.III From theory to experiment: PNA-DNA preliminary sensing experiments

PEO-PNA vs. HS-PNA

Two different mixtures of probes, HS-PNA/mPEO$_{2kDa}$ and PNA-PEO/mPEO$_{2kDa}$ were deposited on SPR surfaces, as described. For each mixture 6 different probe:backfiller ratios were tested (1:0; 0.43:0.57; 0.20:0.80; 0.10:0.90; 0.05:0.95; 0.02:0.098: 0:1). Each series was incubated with three different types of biomolecules: a complementary DNA (DNAc), a non-complementary DNA (DNAnc) and a protein (BSA) (**Figure 4. 28**). All data are reported in **Table 4. 15** in detail.
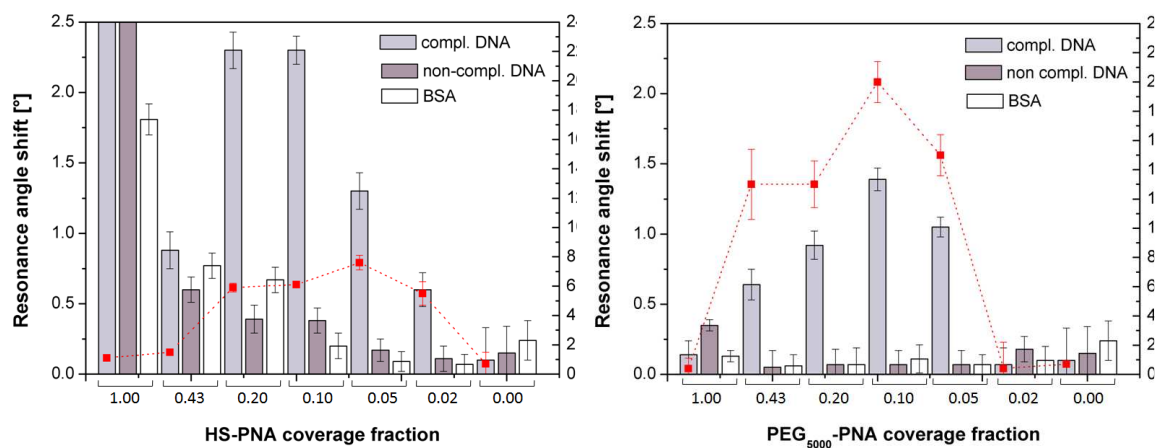
Figure 4. 28. Resonance angle shifts obtained on gratings functionalized with HS-PNA/mPEO$_{2000}$ (*left*) and PEO-PNA/mPEO$_{2000}$ (*right*) after incubation in complementary DNA (compl. DNA) (light grey bars), non-complementary DNA (non-compl. DNA) (dark grey bars) and 0.1% BSA in PBS (white bars). The curves of S/N ratio, calculated as the ratio between SPR signal detected from DNAc and SPR signal detected for DNAnc, as a function of probe surface coverage fraction are reported for both PNA probes (*red curve*).

Table 4. 15. Resonance angle shifts detected for each sensing layer and incubation step.

| Sample	Probe	Resonance angle shift for each robe surface coverage fraction [°]						
		1	0.43	0.20	0.10	0.05	0.02	0
DNA compl.	PEG$_{5000}$-PNA	0.14±0.1	0.64±0.11	0.92±0.1	1.39±0.08	1.05±0.07	0.07±0.12	0.1±0.23
	HS-PNA	4.16±0.08	0.88±0.13	2.3±0.13	2.3±0.1	1.3±0.13	0.6±0.12	
DNA non compl.	PEG$_{5000}$-PNA	0.35±0.04	0.05±0.12	0.07±0.11	0.07±0.1	0.07±0.1	0.18±0.09	0.15±0.19
	HS-PNA	3.68±0.16	0.6±0.09	0.39±0.1	0.38±0.09	0.17±0.08	0.11±0.09	
BSA in PBS	PEG$_{5000}$-PNA	0.13±0.04	0.06±0.08	0.07±0.12	0.11±0.1	0.07±0.07	0.1±0.1	0.24±0.14
	HS-PNA	1.81±0.11	0.77±0.09	0.67±0.09	0.20±0.09	0.09±0.07	0.07±0.07	
S/N ratio	PEG$_{5000}$-PNA	0.4±0.7	12.8±2.4	13.1±1.6	20±1.4	15±1.4	0.4±1.8	0.7±2.6
	HS-PNA	1.1±0.05	1.5±0.2	5.9±0.3	6.1±0.2	7.6±0.5	5.5±0.8	
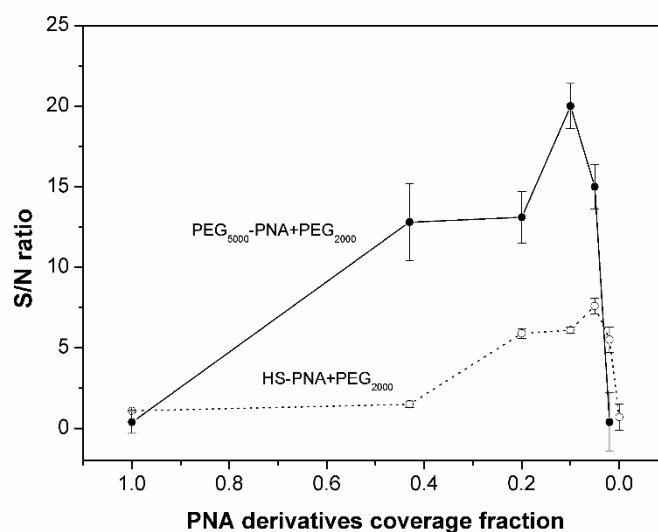
Figure 4. 29. S/N ratio curve as a function of probe surface coverage fraction of PEO$_{5000}$-PNA (solid line, full circles) and HS-PNA (dotted line, empty circles).

Resonance angle shifts detected in the presence of HS-PNA layers were significantly higher than which detected in the presence of PEO-PNA layer, referring both to specific (i.e. complementary DNA) and non-specific (non-complementary DNA and BSA) events. However the S/N ratio related to PEO-PNA layer was higher than the ratio related to HS-PNA layer, reaching a value of ~ 20 with respect to ~ 6 (HS-PNA) in the case of 10% content of PNA onto the surface.

Thus we concluded that the deposition of a PEO-PNA:PEO (0.1:0.9) layer was the most appropriate strategy for our purpose of obtaining an accurate and specific SPR signal, with the minimum amount of non-specific adsorption contributions.

In **Figure 4. 30** and **Figure 4. 31** the differences in hydrophilicity of the sensing surfaces as a function of PNA or PEO content, in the presence of a DNA drop (10 μl), are shown.

(A)

(B)
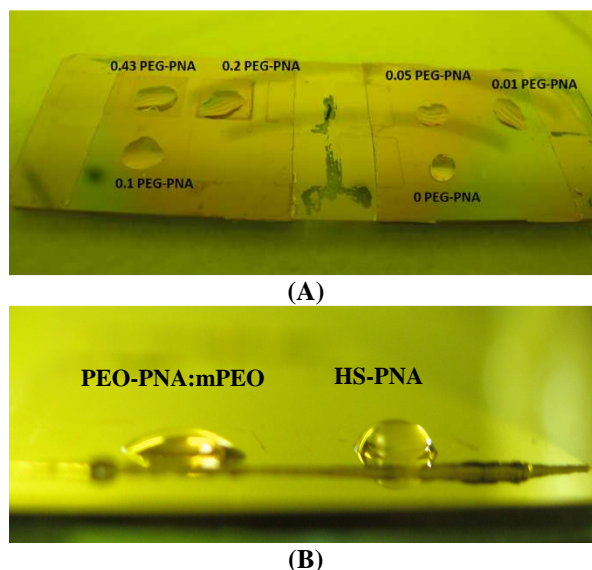
Figure 4. 30. DNA drops (10 μl) onto PEO5kDa-PNA/ layers (A) and comparison between a DNA drop (10 μl) onto a PEO5kDa-PNA/PEO2kDa and onto a HS-PNA layer (B). The fully PNA covered surface showed high hydrophobicity with respect to a surface with a certain PEO content.

PEO$_{5kDa}$-PNA/PEO$_{2kDa}$	**HS-PNA**
(a) Only mPEO	(a) 2 hour deposition
(b) 0.1 PEO-PNA 0.9 mPEO	(b) 8 hour deposition
(c) 0.2 PEO-PNA 0.8 mPEO	(c) 17 hour deposition
(d) 0.4 PEO-PNA 0.6 mPEO	(d) 48 hour deposition
(e) Only PEO-PNA	(e) 72 hour deposition

Figure 4. 31. Trend of DNA drops (10 μl) onto PEO$_{5kDa}$-PNA/PEO$_{2kDa}$ layers at different ratios (*left*) and onto HS-PNA layers after different deposition times (*right*). When the surface is covered only by PEO$_{2kDa}$ (*left/a*) the DNA drop is extended onto the polymer surface due to polymer hydrophilicity. When the surface is only formed by a PEO-PNA layer (*left/e*) the DNA drop is well-defined due to PNA hydrophobicity. PNA hydrophobicity is also clear from the DNA drop shape onto HS-PNA layers obtained with different deposition times (*right*). As the deposition time increases the drop shape remains well-defined.

4.10 PNA-DNA hybridization

4.10.I Detection of oligonucleotide DNA

Sensing of complementary oligo DNA was performed for seven different concentrations: 10, 2, 0.4, 0.08, 0.016, 0.0032 and 0 nM, and a sensing layer with a 10% content of PEO-PNA was used (Section 4.9.III). Obtained results (**Table 4. 16** and **Figure 4. 32**) showed a reliable detection from 2 nM to 0.0032 nM. At higher concentration (10 nM), the recorded signal reaches the saturation level, settling to a mean value of $0.71° \pm 0.11°$. Noteworthy at the lowest concentration the shifts are still more than 5 times higher than their standard deviation (0.11 ± 0.02) and still one order of magnitude higher than the instrumental error (hundredth of a degree). These results suggest that the system can be investigated also to lower concentrations.

Table 4. 16. Resonance angle shifts obtained for the detection of oligo nucleotide DNA by SPR measurements

Oligo DNA concentration [nM]	Resonance angle shift [°]
10	0.68 ± 0.10
2	0.74 ± 0.15
0.4	0.40 ± 0.03
0.08	0.22 ± 0.03
0.016	0.21 ± 0.01
0.0032	0.11 ± 0.02
0	0.002 ± 0.01
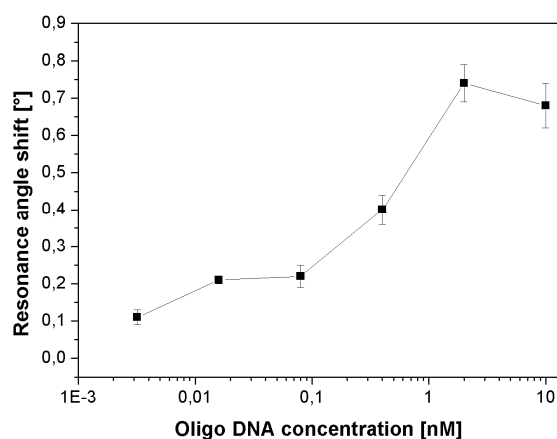
Figure 4. 32. SPR detection output after incubation with oligo DNA as a function of DNA concentration.

A parallel experiment to evaluate the response of a fluorescent-based system in comparison to the label-free SPR system was performed. Onto flat gold surfaces, used as substrates, were deposited the same PEO-PNA mixtures tested for the SPR setting. The sensing layers were then incubated with myco DNAc Cy3 at seven different concentrations.

Results obtained in this configuration are reported in **Figure 4. 33** and **Table 4. 17** and indicate a very low sensing ability of the fluorescent platform built on flat gold substrates, since only dilutions up to 2 nM were detectable.

Myco DNAc Cy3 concentration (nM) – hybridization on flat gold slide

| 10 nM | 2 nM | 0.4 nM | 0.08 nM | 0.016 nM | 0.0032 nM | 0 nM |
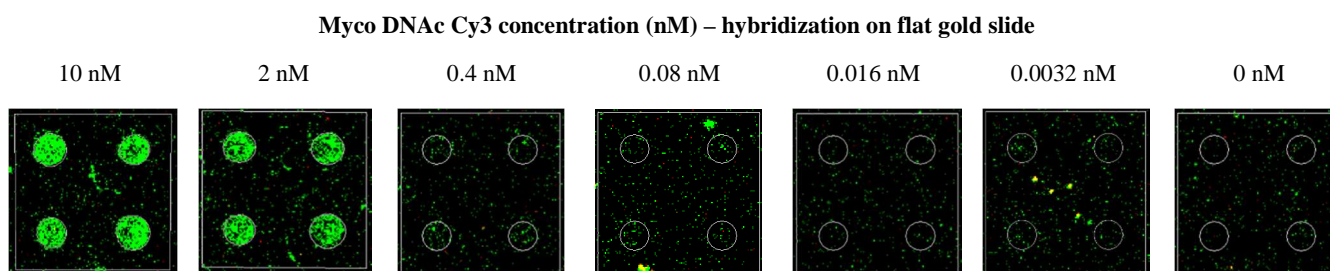
Figure 4. 33. Microarray images obtained after hybridization of myco DNAc Cy3 on a PEG-PNA functionalized flat gold slides.

Table 4. 17. Microarray signal fluorescence intensities obtained after hybridization of myco DNAc Cy3 on a PEG-PNA functionalized flat gold slides.

Myco DNAc Cy3 concentration [nM]	F532 Mean - Bkg	sd
10	14825	25.20
2	121.50	31.84
0.4	11.00	2.16
0.08	6.50	2.08
0.016	1.75	0.50
0.0032	5.75	0.96
0	2.00	0.82

In order to evaluate the reason of the quenching phenomenon, gold flat surfaces were printed in parallel with commercial array slides with a NH_2-DNA-Cy3 probe to verify the entity of the observed phenomenon. Gold flat slides were functionalized by depositing a SH-PEG$_{5kDa}$-COOH monolayer in order to ensure both the successfully DNA amino-modified probe anchorage (through coupling of –COOH and –NH_2 groups) and the achievement of a distance between the surface and the DNA probe comparable to that achieved on the gold SPR gratings functionalized with the PEO-PNA/PEG probe. A 5'NH_2 and 3' Cy3 modified probe (quench DNA) was deposited both on gold and on commercial slides. Concerning gold surface, after substrate cleaning, a 1mM solution of SH-PEG$_{5kDa}$-COOH was deposited for 24 hours. Carboxyl groups were activated with a 5mM solution of EDC and sulfo-NHS in MES 1X buffer for 15 minutes. Substrates were deeply rinsed with Milli-Q water, and N_2 flux dried. Quench DNA probe was finally diluted in Microarray Printing Buffer as described in the experimental section, loaded into micro-plates and submitted for printing. The same probe was directly printed in parallel on ready to use commercial slides.

Results illustrated in **Figure 4. 34** demonstrate that on gold surfaces, fluorescent signals due to fluorescent probe presence were almost 4 times lower than the one observed on commercial slides. Furthermore s signal from gold flat surfaces decreased to a 200 time lower after removing unspecifically adsorbed probes through slide washing, and thus observing the signal due only to covalently bound molecules located in a closer proximity to the surface.

Gold slide		Commercial slide		Graphical plot
Post printing	Post washing	Post printing	Post washing	

Substrate	F532 Mean - Bkg	sd
Gold post print	14936.92	3783.12
Gold post wash	203.13	113.63
Commercial post print	56883.29	2804.08
Commercial post wash	44670.54	5546.50

A **B**
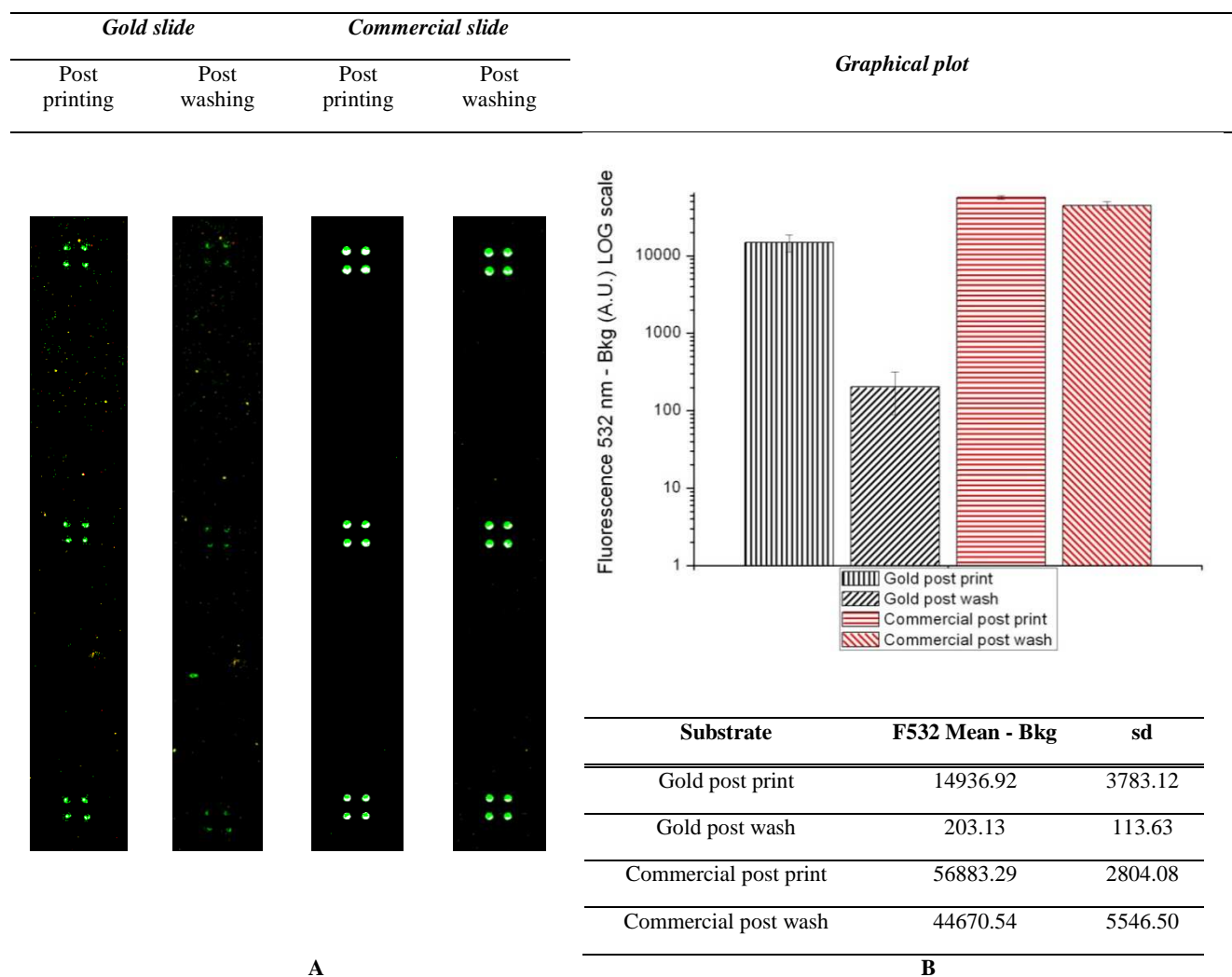
Figure 4. 34. Microarray images (**A**) and signal fluorescence intensities (**B**) obtained after printing of a NH_2-DNA-Cy3 probe (quench DNA) on gold and commercial slides. Signal intensities (mean of 12 identical sub arrays of 4x4 spots) were recorded both after printing and slide washing in water, to remove unspecifically bound probes.

Despite the use of SH-PEG$_{5kDa}$-COOH as a spacer between the gold surface and the DNA probe, the effect of fluorescence quenching for the printed probe is remarkable. Obtained results indicate that the more performing control fluorescence revelation system is obtained functionalizing with the proper DNA probe conventional commercial array slides. In fact, even when a SH-PEG$_{5kDa}$-COOH filler is deposited on gold surface, the fluorescence signal due to the attached DNA probe is too low and does not allow the proper usage of the system as sensing platform.

Results obtained in this configuration demonstrate the presence of a great quenching effect on the emitted fluorescence due to the metal surface. Only target dilutions up to 2 nM were detectable. This result make the use of flat gold surfaces for the detection of fluorescent molecules not suitable, operating in the surface distance range proper of the PEO-PNA molecules used for the deposition. Thus a proper fluorescent-based microarray control was chosen in order to verify and compare SPR sensing ability.

Thus the control microarray slide was therefore hybridized with the same seven different oligonucleotide concentrations of myco DNAc Cy3 on a commercial glass surface functionalized with myco DNA-NH$_2$ probe. Results (**Figure 4. 35**, **Figure 4. 36** and **Table 4. 18**) demonstrated that the fluorescent based detection was achieved up to 0.016 nM concentration of myco DNAc Cy3. The lower concentration (0.0032 nM) was not detected and signal deriving from this subarray was comparable to the zero of the system.

Myco DNAc Cy3 concentration (nM) – hybridization on microarray glass slide

10 nM	2 nM	0.4 nM	0.08 nM	0.016 nM	0.0032 nM	0 nM
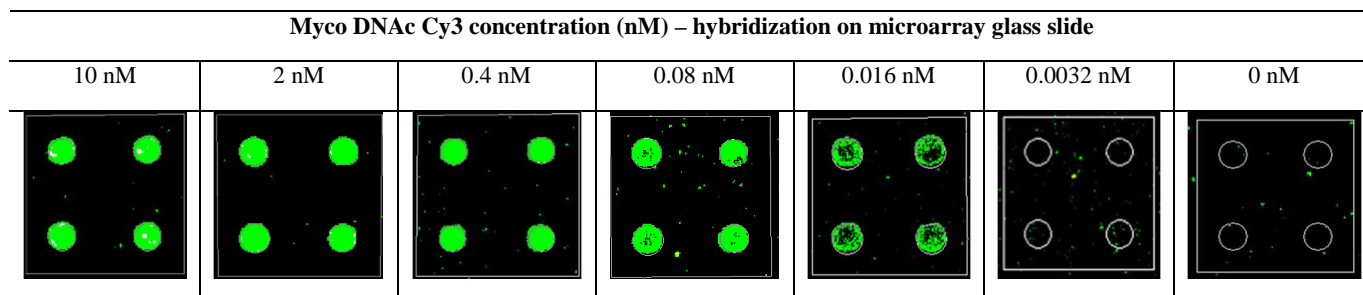
Figure 4. 35. Fluorescent scan image of microarray results after hybridization of myco DNAc Cy3 oligonucleotide

Table 4. 18. Resonance angle shifts obtained for the detection of oligo nucleotide DNA by fluorescent analyses

Myco DNAc Cy3 concentration [nM]	F532 Mean - Bkg	sd
10	31826.13	4144.13
2	24002.38	5472.95
0.4	8715.63	1566.26
0.08	485.75	27.98
0.016	85.63	29.37
0.0032	20.88	10.25
0	24.25	1.71
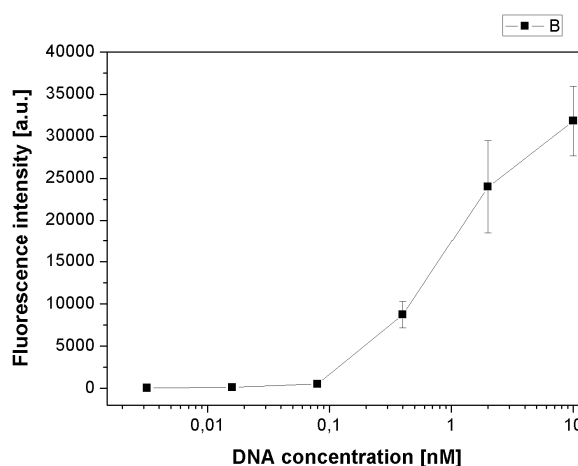
Figure 4. 36. Fluorescence intensities after incubation with oligo DNA as a function of DNA concentration.

The SPR sensing platform allows to obtain a 5 time higher sensitivity (0.0032 nM) if compared to the fluorescent based platform (0.016 nM), and even lower concentrations could be investigated with the SPR method, since the shift obtained from the 0.0032 nM dilution is significantly higher that the zero of the system (0.002±0.01).

4.10.II Detection of *M. tuberculosis* PCR amplified DNA

SPR and fluorescence sensing platforms were tested also for the recognition ability towards a PCR fragment of *M. tuberculosis* genome, containing the target sequence in RpoB gene, site of possible mutations that confer resistance to the rifampicin antibacterial agents.

For SPR sensing experiments, shifts obtained from the pure PCR fragment hybridization were higher than the ones registered hybridizing the corresponding oligonucleotide (myco DNAc) concentration ($1.51° \pm 0.04°$ vs $0.71° \pm 0.11°$ for the 10 nM concentration, **Figure 4. 37** and **Figure 4. 32**, respectively), and this could be possibly explained considering the greater dimensions of the PCR fragment itself. In this experimental setting, the detection system is able to efficiently distinguish the presence of myco-PCR amplified DNA up to 0,016 nM (**Figure 4. 37**).

Table 4. 19. Resonance angle shifts obtained for the detection of M. tuberculosis PCR and PCR+genomic DNA by SPR measurements

Oligo DNA concentration [nM]	Res. Angle mean shift [°] PCR	Res. Angle mean shift [°] PCR+genomic
10	1.51 ± 0.04	-
2	-	0.89 ± 0.06
0.4	1.40 ± 0.02	0.80 ± 0.03
0.08	-	0.57 ± 0.02
0.016	0.83 ± 0.07	0.55 ± 0.09
100 ng genomic	1.14 ± 0.12	
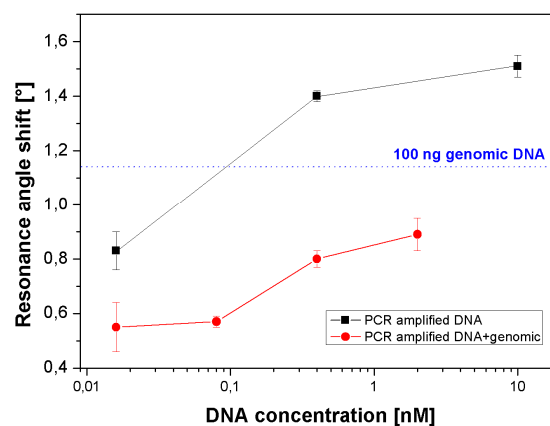
Figure 4. 37. SPR detection output after incubation with M. tuberculosis PCR amplified DNA (PCR only and PCR+genomic) as a function of DNA concentration.

To simulate PCR unamplified clinical samples, we added a fix quantity of fragmented human genome to myco PCR samples prepared at the same concentrations as above. When samples were analysed through SPR detection, the presence of the human genome causes a remarkable decrease of the shift when compared to the results obtained in samples with PCR fragments only (**Table 4. 19** and **Figure 4. 37**). For example, the shift observed incubating the 0.4 nM solution decreases from 1.40° to 0.8° in the presence of human contaminant DNA (**Figure 4. 37**, *empty dots*). The control solution, containing only genomic DNA, turned out in high nonspecific adsorption value: $1.14° \pm 0.12°$ (**Figure 4. 37**, *dotted line*).

A control fluorescence microarray slide was hybridized with the same different concentrations of myco PCR used in the SPR test described above to verify and compare sensing ability of the two systems. As shown in **Figure 4. 38** and **Table 4. 19**, for the fluorescence platform, the detection limit was 2 nM, at least 125 times higher than that recorded for SPR detection (0.016 nM). When the same experiment was performed using the fluorescent sensing platform, the sensitivity of 2 nM was observed as for samples without human genomic DNA (**Figure 4. 39**, *empty dots*).

Myco PCR Cy3 concentration (nM) – hybridization on microarray glass slide

	10 nM	2 nM	0.4 nM	0.08 nM	0.016 nM	0 nM
PCR						
PCR + human genome						

Figure 4. 38. Fluorescent scan of microarray results after hybridization of myco PCR Cy3 are reported.

Table 4. 20. Resonance angle shifts obtained for the detection of M. tuberculosis PCR and PCR + genomic DNA by fluorescent analyses

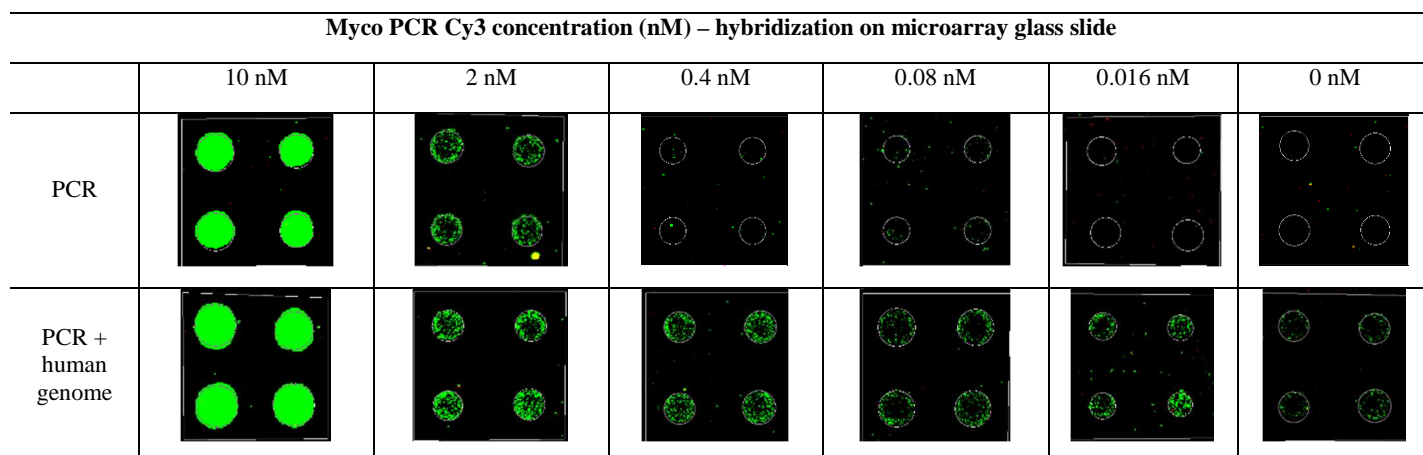| Myco PCR Cy3 [nM]	PCR		PCR plus human genome	
	F532 Mean-Bkg	sd	F532 Mean-Bkg	sd
10	1573.25	115.95	1461.00	209.18
2	1573.25	115.95	86.25	4.57
0.4	26.50	2.00	68.40	5.98
0.08	19.00	4.34	53.50	3.25
0.016	13.64	1.30	50.25	17.89
0	7.00	0.82	44.25	3.77
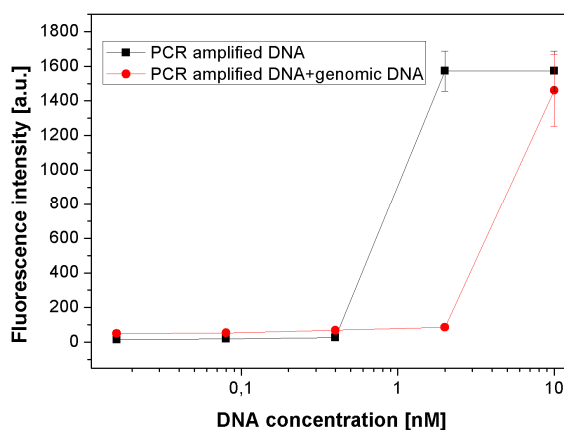
Figure 4. 39. Fluorescence intensities after incubation with M. tuberculosis PCR amplified DNA (PCR only and PCR+genomic) as a function of DNA concentration.

For the SPR PNA-based platform, we verified that, when myco-related sequences are present in unamplified mixtures with contaminant human DNA, the signal due to the presence of target specific sequences is lowered below the signal recorded in presence of human DNA alone. It is possible that partial and random pairings occurring between the genomic DNA and the PNA probe compete with the probe-target binding reaction, lowering the overall shifts due to the specific hybridization. PNA molecules are in fact able to interact with DNA creating complex structures (i.e. adducts like triplex, triplex invasion, duplex invasion, double duplex invasion) and the environmental conditions like low salt concentration, pH and temperature, may affect the specificity of those pairings [66,155]. The shift obtained with the genomic DNA alone, higher than that observed for the tested samples, suggest that the system is not efficiently discriminating in the presence of contaminant double strand DNA in which several sequences of possible partial homology with the 15-mer PNA could be present. Nevertheless, such interaction between the PNA and the contaminant DNA could not be reduced even applying post hybridization washing

procedures longer and/or at higher temperatures than those routinely used in order to reach high stringency performances for conventional DNA probe array (data not shown). Up to date, only few literature examples of non-amplified DNA detection through PNA probes can be found, and it has to be underlined that most of them use specific sandwich hybridization and amplification strategies to achieve higher sensitivity [156]. These strategies have been investigate also on SPR surfaces and to overcome the lack of sensitivity for unamplified DNA the system is coupled with electrochemically based techniques [157], fluorescence-based SPR technique known as surface plasmon fluorescence spectroscopy [158] or a double-recognition strategy coupled with Au-nanoparticles signal amplification [159,160].

4.11   Conclusions

We obtained a theoretical calibration of an azimuthally-controlled GC-SPR sensing platform that correlates the SPR measurement output signal to the amount of mPEO molecules (also in term of surface sensitivity [ng/cm^2]) grafted onto sinusoidal gratings.

After the sensing surface calibration the antifouling behaviour was optimized testing three PEO derivatives of different chain lengths: PEO 0.3, 2 and 5 kDa. The results showed that full surface protection in multiple buffer conditions can be achieved only by using high Mw PEOs deposited at high surface density - as the 2 and 5 kDa here used. On the other hand, short PEOs - as the 0.3 kDa, are not capable to fully protect the surface from fouling at any surface concentration. Protection was achieved by both the 2 and 5 kDa polymer derivatives. However, 2 kDa one provided the best compromise between fouling protection and signal detection in fact it was chosen as the antifouling layer for real sensing applications.

The protection achieved with the high-density polymers is high enough to allow envisioning application of this powerful sensing configuration for analyte quantification directly from complex matrices, for which a true 'negative control', that is classically used for background correction in SPR experiments, does not exist. The most "aggressive" buffer used contained 1% goat serum. It is likely that highly protected layers, as the ones here obtained, may be able to resist to even less diluted serum. If this were the case, this would permit to dilute less a real biological sample prior to testing, with advantages for the overall assay sensitivity.

Starting from the optimized sensing surface we applied it to real DNA/PNA sensing. At first we studied the adsorption kinetics of all the molecules of interest: PEO-PNA (the probe), HS-PNA (the probe for comparison) and PEO 2 kDa (the backfiller). In order to optimized the PNA probe detection efficiency we realized a co-immobilization model that allowed us to control the surface composition on term of probe/backfiller ratios. Comparing surfaces covered by different PEO-PNA:PEO or HS-PNA:PEO, we deduced that the best surface composition for DNA sensing was made by a 10% of PEO-PNA and a 90% of PEO. Using these results we analyzed both oligo and genomic or PCR-amplified DNA, comparing SPR and fluorescence measurements. The optimized set-up was able to detect a purified, complementary oligonucleotide DNA at concentrations down to 3.2 pM by SPR measurements and down to 16 nM by fluorescence analyses, and we expect a reliable detection capability even at lower concentrations with our SPR detection method.

Detection of PCR-amplified *Mycobacterium tuberculosis* DNA containing the target sequence gave shifts even higher than the corresponding concentrations of oligonucleotide DNA, highlighting the possibility of sensing even lower concentrations of target. However, experiments done using samples containing fragmented human genomic DNA as a model of a real, unamplified clinic sample, showed high levels of interferences, with lowered shifts and a high nonspecific adsorption value, indicating the capability of the developed system to efficiently work only in the presence of PCR amplified and purified samples.

Results obtained in this work highlight that a very efficient detection of target sequence could be achieved with the sensing platform realized, when using purified and amplified DNA. Illustrated results, not only demonstrate the strength of the sensing platform for nucleic acid detection, but they also suggest the reliability of the system for a future development of real-time samples analysis

with minimal manipulation and preparation, thanks to the possible integration of microfluidic-based platforms for extraction, amplification and sensing.

5. DNA sensor for cystic fibrosis

Abstract

In this Section the study for the realization of a sensing prototype for cystic fibrosis (CF) is showed. A gold sinusoidal grating was chosen as substrate and the sensor was developed from the CF probe choice until the detection of real samples. All the experiments were characterized using both azimuthally rotated GC-SPR and fluorescence techniques to compare results of complex samples obtained with a new detection method with the results obtained with a standard characterization technique.

5.1 Introduction

Cystic fibrosis (CF) is one of the most common life-shortening, childhood-onset inherited diseases in the Caucasian population, as it occurs once in 2,000–2,500 live births and affects a number of organs, such as the lung airways, gut, pancreas, and sweat glands [161]. It is caused by mutations in a gene called the *cystic fibrosis transmembrane conductance regulator* (CFTR) which has the function of coding a chlorine ion channel protein [162,163]. Almost 1,000 mutations have been identified in the CF gene, but only a few common mutations can be identified as a cause of the disease in the majority of cases: ΔF508, which is the most common one [164], 2183 AA->G; R1162X and N1303K [165–167].

CF genotyping has known a rapid and efficient growth in recent years and it is currently performed by a variety of approaches, including the polymerase chain reaction (PCR) [168], allele-specific oligonucleotides (ASO) [169–171], dot-blot and reverse dot-blot hybridization [172], methylene blue (MB)-DA interaction [164], heteroduplex formation [173], single-stranded conformation polymorphism (SSCP) [174,175], denaturing gradient gel electrophoresis (DGGE) [176], PCR sequencing [177,178], and SPR [167,179–182].

As the most important requirements for CF sensors are quality of services, speed, accuracy, and low cost, SPR has demonstrated to be the most promising high sensitive technique for the CF mutation detection.

However few data are available on the possible use of SPR and biosensor technologies to discriminate between homozygous and heterozygous state in the case of hereditary disease caused by genetic mutations [167,183].

Recently also the PNA/DNA interaction has been investigated as it could be a solution for the sensitivity improvement of current CF sensors [180,181].

We chose to focus our study on the development of a DNA/DNA azimuthally GC-SPR-based sensor. This choice allowed us to test a common strategy adopted in this sensing field together with the innovative contribution of azimuthally-controlled GC-SPR. Thanks to the choice of DNA/DNA interaction we had the possibility of monitoring and controlling our SPR response also by standard fluorescence analyses protocols, which allowed us also to evaluate the advantages and limit of both techniques.

5.2   Materials and methods

5.2.I   Biological elements

Poly (ethylene oxide)

A carboxyl and thiolated poly (ethylene oxide) (HS-PEO-COOH) Mw 3 kDa was used (purchased from Sigma Aldrich) (chemical formula in **Table 4. 3**).

Selection of CFTR mutations

The four most frequent mutations of the CFTR gene were selected looking at statistical data from literature [165,166]: ΔF_508; 2183_AA->G; R1162X and N1303K. Also the mutation localization was found via database, for both wild-type (wt) and mutant (mut) sequence (**Table 5. 1**).

Table 5. 1. CFTR mutation sequences selected

The wild-type sequence is indicated in green and the mutant sequence is in-between brackets, the PCR primers are shown in blue.

ΔF 508 (EXON 13)
ATA**ATGATGGGTTTTATTTCCAGAC**TTCACTTCTAATGGTGATTATGGGAGAACTGGAGCCTTCAGAGGGTAAAATTA AGCACAGTGGAAGAATTTCATTCTGTTCTCAGTTTTCCTGGATTATGCCTGGCACCATTAAAGAAAATATCAT`CTT`TG GTGTTTCCTATGATGAATATAGATACAGAAGCGTCATCAAAGCATGCCAACTAGAAGAGGTAAGAAACTATGTGAAA ACTTTTTTGATTATGCATAT**GAACCCTTCACACTACCCAAAT**TAT

2183 AA->G (EXON 13)
TAA**AGCTGTGTCTGTAAACTGATGG**CTAACAAAACTAGGATTTTGGTCACTTCTAAAATGGAACATTTAAAGAAAGC TGACAAAATATTAATTTTGCATGAAGGTAGCAGCTATTTTTATGGGACATTTTCAGAACTCCAAAATCTACAGCCAGA CTTTAGCTCAAAACTCATGGGATGTGATTCTTTCGACCAATTTAGTGCAGAAAGAAGAAATTCAATCCTAACTGAGAC CTTACACCGTTTCTCATTAGAAGGAGATGCTCCTGTCTCCTGGACAGAAACAAAA`AA(delAA>g)A`CAATCTTTTAAAC AGACTGGAGAGTTTGGGGAAAAAAGGAAGAATTCTATTCTCAATCCAATCAACTCTATACGAAAATTTTCCATTGTG CAAAAGACTCCCTTACAAATGAATGGCATCGAAGAGGATTCTGATGAGCCTTTAGAGAGAAGGC**TGTCCTTAGTACC AGATTCTGAG**CAG

R1162X (EXON 19)
AAA**GCCCGACAAATAACCAAGTGA**CAAATAGCAAGTGTTGCATTTTACAAGTTATTTTTTAGGAAGCATCAAACTAA TTGTGAAATTGTCTGCCATTCTTAAAAACAAAAATGTTGTTATTTTTATTTCAGATGCGATCTGTGAGC`C(t)GA`GTCTTT AAGTTCATTGACATGCCAACAGAAGGTAAACCTACCAAGTCAACCAAACCATACAAGAATGGCCAACTCTCGAAAGT TATGATTATTGAGAATTCACACGTGAAGAAAGATGACATCTGGCCCTCAGGGGGGCCAAATGACTGTCAAAGATCTCA CAGCAAAATACACAGAAGGTGGAAATGCCATATTAGAGAACATTTCCTTCTCAATAAGTCCTGGCCAGAGGGTGAGA TTTGAACACTGCTTGCTTTGTTAGACTGTGTTCAGTAAGTGAATCCCAGT**AGCCTGAAGCAATGTGTTAGC**AG

N1303K (EXON 21)
AAA**AATGTTCACAAGGGACTCCA**AATATTGCTGTAGTATTTGTTTCTTAAAAGAATGATACAAAGCAGACATGATAA AATATTAAAATTTGAGAGAACTTGATGGTAAGTACATGGGTGTTTCTTATTTTAAAATAATTTTTCTACTTGAAATATT TTACAATACAATAAGGGAAAAATAAAAAGTTATTTAAGTTATTCATACTTTCTTCTTCTTTTCTTTTTTGCTATAGAAA GTATTTATTTTTTCTGGAACATTTAGAAAAAAA`C(g)`TTGGATCCCTATGAACAGTGGAGTGATCAAGAAATATGGAAAG TTGCAGATGAGGTAAGGCTGCTAACTGAAATGATTTTGAAAGGGGTAACTCATACCAACACAAATGGCTGATATAGC TGACATCATTCTACACACTTTGTGTGCATGTATGTGTGTGCACAACTTTAAAATGGAGTACCCTAACATACC**TGGAGC AACAGGTACTTTTG**ACT

For each mutation, a pair of primers capable to amplify the genomic portion of interest through PCR method has been selected in order to allow subsequent analysis. Each pair of primers was designed considering particular physical and chemical thermodynamic characteristics to make them suitable for a PCR and potentially for a multiplex PCR and selected primer characteristics are summarized in **Table A.4. 1**(**Appendix A.4**).

Selection of DNA oligonucleotide probes for the recognition of wt and mut sequences of CF gene

Specific probes for DNA microarrays were selected, using the Array Designer software. According to literature's [184] information for the design of the *allele specific oligonucleotide* (ASO) probes for the identification of genetic mutations and polymorphisms, we found that 18-22 nucleotides is the optimal length for probes: short probes are in fact able to discriminate with greater accuracy single base mutations. This parameter was then used for the design of probes required for analysis. It should be pointed out that the design of these probes was highly constrained by the position of the mutation itself, to be placed in the central region of the probe (in order to maximize mutation discrimination capability), and by the nucleotide composition of the sequence immediately before and after the mutation itself, that can not obviously be changed.

The characteristics of the selected probes, with their chemical and physical properties, are listed in **Table A.4. 2** (**Appendix A.4**). Selected probes were analyzed for their specificity through Basic Local Alignment Search Tool (BLAST), in order to evaluate the ability of those sequences to identify the desired mutations.

Hairpins structure design

The portion of each hairpin probe was designed as indicated in literature regarding the length of the portion and we set a length of 6 bp [185,186]. We also examined the stability of the structure in order to standardize the Tm and ΔG of the hairpin region of all the structures created (**Table A.4. 3**, **Appendix A.4**).

The probes with the hairpin portion show excellent uniformity regarding the average Tm, of $59.91 \pm 1.13°$ C, i.e. $10°$ C higher than the probes Tm without the hairpin portion as reported in the following table.

Table 5. 2. Primers characteristics for exon 10, 13, 19 and 21 products, chosen for both fluorescence and SPR analyses

Name	Sequence 5'-3'	nt	GC%	Tm [°C]
1 Ex10 F	ATGATGGGTTTTATTTCCAGAC	22	36.4	50.9
2 Ex10 R	ATTGGGTAGTGTGAAGGGTTC	21	47.6	54.6
3 Ex13 F	AGCTGTGTCTGTAAACTGATGG	22	45.5	54.8
4 Ex13 R	CTCAGAATCTGGTACTAAGGACA	23	43.5	53.3
5 Ex19 F	GCCCGACAAATAACCAAGTGA	21	47.6	55.5
6 Ex19 R	GCTAACACATTGCTTCAGGCT	21	47.6	55.8
7 Ex21 F	AATGTTCACAAGGGACTCCA	20	45.0	53.9
8 Ex21 R	CAAAAGTACCTGTTGCTCCA	20	45.0	52.9

5.2.II   Surface preparation protocols

Gold surface preparation for fluorescence analyses

75x25 mm microarray slides were deposited with the same sub-array scheme as shown in **Figure 5. 1**.

AL	10W	10M	13W	13M	AL
AL	10W	10M	13W	13M	AL
AL	10W	10M	13W	13M	AL
V	V	V	V	V	B
V	V	V	V	V	B
V	V	V	V	V	B
V	19W	19M	21W	21M	V
V	19W	19M	21W	21M	V
V	19W	19M	21W	21M	V

Figure 5. 1. Sub-array deposition scheme on an e-surf slide (LifeLineLab). AL=alignment probe-reference, V= empty, B=buffer, W=wild type probe, M=mutant probe.

Six replicas of alignement probes were spotted, plus three replica of each investigated *wt* or *mut* probe, to ensure statistical analysis. Microarray slides were printed and blocked according to protocols reported in Section 4.4.II. Shortly, each NH$_2$-modified DNA probe was diluted in microarray printing buffer 1.5X (75 mM sodium phosphate, 0.005% Triton, pH 8.5) at the concentration of 20 μM and printed on e-surf commercial LifeLine slides (25 mm × 75 mm, LifeLineLab, Pomezia, Italy) Afterwards, slides were incubated overnight in a 75% humidity incubation chamber, blocked and washed according to standard protocols as specified by the supplier with microarray blocking (0.1 M Tris, 50 mM ethanolamine, pH 9) and washing solutions (4X SSC, 0.1% SDS), respectively.

On a single slide, 16 to 64 identical sub-array can be printed on the slide, and during the hybridization phase they can be physically isolated from each other through ProPlate 16 or 64 slide chamber multi-wells (ProPlate, Sigma Aldrich).

Gold surface preparation for SPR analyses

Two identical gratings were located on a microscope glass slide of *75mm x 25mm* (Section 3.3), and 16 wells of *3.5mm x 3.5mm* were obtained for each grating. In one slide up to 30 samples were therefore analysed and 2 empty cells were left as reference.

Substrates were preliminary cleaned with a basic piranha solution (H$_2$O: H$_2$O$_2$: NH$_3$ solution in 5:1:1 ratio) for 10 minutes, rinsed and dried under nitrogen flux. A hetero bifunctional thiol-PEG (SH-PEG-COOH) was used to functionalize the surface, upon an incubation of 24 hours in humidified environment. Amino modified oligonucleotide CFTR probes were covalently linked to the –COOH surface groups, previous EDC-SNHS activation in MES buffer for 15 minutes. An example of the plasmonic surface organization is showed in **Figure 5. 2**.
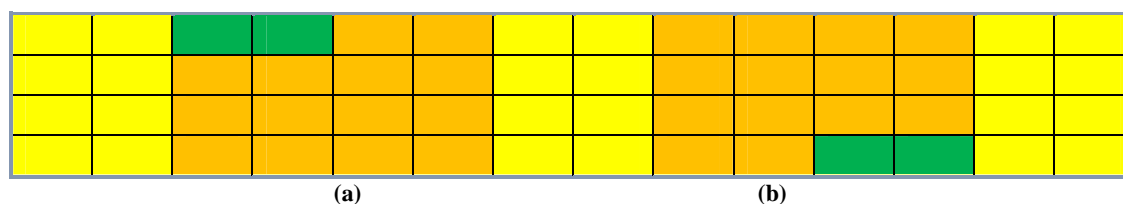
Figure 5. 2. Example of SPR surface scheme created on a microscope glass slide (*75mm x 25mm*), with 2 gratings, having 16 wells each. Flat gold wells (*yellow*) divide the two gratings (*orange* and *green cells*), in which reference cells are highlighted in green.

Each well was functionalized with a single specific probe, and testing was performed hybridizing each specific DNA PCR fragment on two cells: for example 10 wt PCR fragment was hybridized on 10 wt functionalized cell and on 10 mut functionalized cell. Plasmonic signals were collected from both cell for each sample and compared, to obtain a DR also as result of the SPR measurements.

Hybridization was performed with a local control of the temperature granted by an external device, not integrated in the device, incubating the slide with the ProPlate multiwells slide system into Arraybooster.

Surfaces were then characterized using a VASE J. A. Wollam Spectroscopic Ellipsometer after each experimental step (i.e. after piranha cleaning just before PEG deposition, after PEG functionalization, after probe anchoring and after analyte/probe binding) with parameters reported in **Table 2. 2**.

5.3   **Optimization of hybridization protocols**

In this Section all the experiments performed to find the optimal hybridization conditions for both DNA oligonucleotides and PCR amplified samples were monitored through fluorescence measurements.

5.3.I   Hybridization protocol for synthetic complementary DNA oligonucleotides

The first set of experiments was performed using synthetic complementary DNA oligonucleotides. All wild-type complementary oligos Cy3 labeled (green) and all mutant complementary oligos Cy5 (red) were purchased with the desired modification and HPLC purification (**Table 5. 3**). These perfect match oligos were used to preliminary test the ability of the deposited probes to recognize specifically the wt or mut strand, and potentially to correctly genotype the subsequent samples.

Table 5. 3. Oligonucleotide sequences of the DNA probes used for microarray printing and fluorescent complementary target (Cy3 or Cy5) used for hybridization experiments.

| CFTR	Type	sequence 5'-3' of the NH₂ modified probes	sequence 5'-3' of the complementary probes
10	Wt	**CAATCG**AATATCATCTTTGGTGTTTCCT**CGATTG**	AGGAAACACCAAAGATGATATT-Cy3
10	Mut	**CAATCG**ATATCATTGGTGTTTCCTATG**TCGATTG**	CATAGGAAACACCAATGATAT-Cy5
13	Wt	**CACTCG**CAGAAACAAAAAAACAATCTTT**CGAGTG**	AAAGATTGTTTTTTTGTTTCTG-Cy3
13	Mut	**CATCG**ACAGAAACAAAAGACAATCTTT**CGATG**	AAAGATTGTCTTTTGTTTCTGT-Cy5
19	Wt	**CCATCA**TCTGTGAGCCGAGTCTTT**TGATGG**	AAAGACTCGGCTCACAGA-Cy3
19	Mut	**CCATCA**ATCTGTGAGCTGAGTCTTTA**TGATGG**	TAAAGACTCAGCTCACAGAT-Cy5
21	Wt	**CAAGCA**TTTAGAAAAAACTTGGATCCCT**TGCTTG**	AGGGATCCAAGTTTTTTCTAAA-Cy3
21	Mut	**CAAGCA**TTTAGAAAAAAGTTGGATCCCT**TGCTTG**	AGGGATCCAACTTTTTTCTAAA-Cy5

Conditions were optimized for oligos hybridization, considering the contribution to the melting temperature (Tm) that is given by the monovalent cations concentration (Na+), the formamide percentage, the probe length and the guanine-cytosine content (GC%).

Tm was calculated using the following formula as described in the online software for oligonucleotide design [187]:

$$T_m = 81.5 + 16.6 x log(Molarity\ [Na^+]) + 0.41 x GC\% - 0.72 x formamide\% - {500}/{length_{oligo}} \quad (5.1)$$

Hybridization temperature (T_{hyb}) was calculated to obtain a difference (Δ) between T_m and T_{hyb} of 20-25°C (moderate stringency) or 15-20°C (high stringency).

Buffer composition was set to operate with a hybridization temperature ranging from 25°C to 37°C (temperature range lower than theoretical melting temperature of the hairpin probes, see **Table A.4. 3** in **Appendix A.4**) in order to ensure hairpin's probe structure maintenance. Moreover, through the described strategy, it was possible to obtain a theoretical better discrimination between perfect match and mismatch (**Figure 5. 3**), and at the same time to operate with a possible portable device at room temperature, or above.
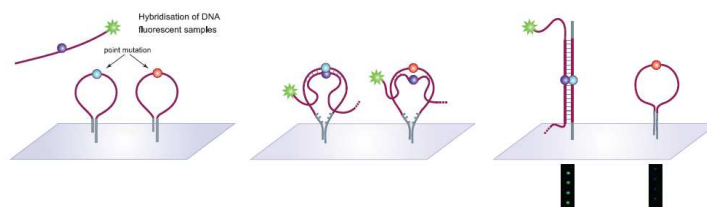
Figure 5. 3. Example of a perfect match hybridization obtained using hairpin loop probes.

The complementary oligonucleotides hybridization has to be considered only as a preliminary evaluation of the probe performances, since hybridization kinetics using short oligos DNA *vs* long PCR products are different, and an accurate optimization protocol is needed.

Complementary oligonucleotides were hybridized in different conditions, modifying the hybridization temperature and time, the oligonucleotide concentration and the hybridization buffer in term of SSC and formamide concentration.

Various settings were tested and the best results in terms of discrimination among wild type and mutant sequences were obtained using the conditions reported in **Table 5. 4**.

Table 5. 4. Hybridization parameters

Hybridization temperature	25°C
Incubation time	3 hours
Oligonucleotide concentration	5 nM
Hybridization buffer	SSC 3X, 50% formamide

The chosen conditions allowed to obtain a theoretical Δ (T_m-T_{hyb}) of 15-20°C, ensuring high stringency. Obtained results, in terms of fluorescence images and statistical data analysis, are reported in
Figure 5. 4.
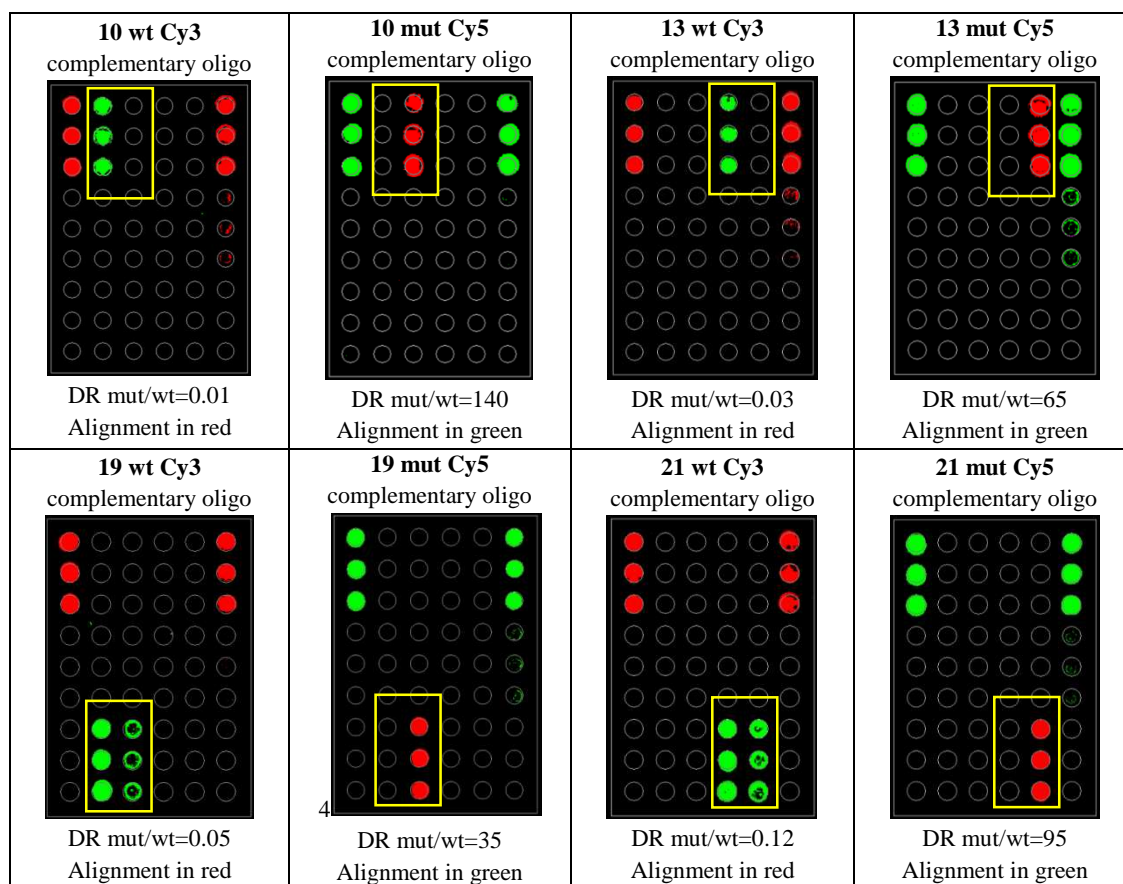
Figure 5. 4. Microarray hybridization results (both images and DR data) obtained with complementary DNA oligonucleotides. Alignments spots are in red (Cy5) when hybridizing wt probes (Cy3), or green (Cy3) when hybridizing mut probes (Cy5). Discrimination ratios (DR) (mut/wt probe signal ratio) for each experiment are reported.

In the optimized experimental condition for oligonucleotide hybridization, correct sequence identification was achieved for all the tested samples.

Discrimination ratios (DR) mut/wt for wt probes were always under the value of 0.12, indicating the ability to detect the hybridization of a wt target with a signal almost 10 times higher on the wt probe, if compared to the mutant one. Best results were obtained with the 10 wt probe (DR=0.01), in fact signals reported after the hybridization of a wt target on the wt probes were 100 times higher than the one reported on the mutant one.

DR for mutant probes were all above 35, meaning that signals reported on mut probe hybridizing a mut target were 35 times higher than those reported on the wt probes. Also for mutant probes best results were obtained for the 10 mut probe (DR=140), as signals detected after the hybridization of a mutant target on the mutant probes were 140 times higher than the one reported on the wt one.

All the tested probes reveal to be successfully able to identify the presence of a wt or mut oligonucleotide fluorescent target.

5.3.II Hybridization experiments with PCR amplified DNA from clinical genetic material

In the previous paragraph, results demonstrating the reliability and specificity of probe recognition were illustrated in the case of complementary oligo sequences.

To verify the reliability of the probe discrimination power in the presence of complex samples simulating real human PCR-amplified extracts, PCR amplicons were obtained using samples or DNA extracts from human cells already genotyped. Four homozygous wt samples (10, 13, 19, 21) and four heterozygous samples (10, 13, 19, 21) were obtained. No homozygous mutant samples were available.

For each of the four investigated exons, a pair of primer was identified and then used to obtain PCR amplified fragments (**Table A.4. 4** in **Appendix A.4**).

After PCR product purification, amplification (through PCR with Cy3 or Cy5 labeled deoxy-cytosine-tri-phosphate –dCTP- and deoxy-nucleotide-tri-phosphate –dNTP- mix) and analysis, amplicons for both wild type and heterozygous samples were incubated on microarray slides pre-functionalized as described in Section 5.2.II, using the same hybridization condition developed for DNA complementary oligonucleotides.

Results illustrated in **Figure 5. 5** demonstrated the ability of the probes in the discrimination between the wild type and the mutant allele.

In particular, for wt Cy3 PCR sample, the signal is detectable on the wt probes with cross hybridizations on the mutant ones all below 5-10%. For the two tested heterozygous samples (19 and 21), containing both a wt and a mutant allele, hybridization is detected correctly on both probes with a mut/wt signal ratio of ~0.5 for exon 19 and of ~1 for exon 21.

The mut/wt signal ratio for heterozygous samples should theoretically be ~1, meaning that the two alleles in the sample, wt and mut, are able to hybridize with comparable efficiency on the wt and on the mut probes, respectively. Signals ~1 were not always obtained in literature, since chemical-physical characteristics of the probes, constrained by mutation position, could be different and affect the hybridization kinetics in different ways. Also if mut/wt ratio of ~1 are not always achievable, a cut-off limit is generally fixed to establish if the sample have to be genotyped as heterozygous or homozygous.
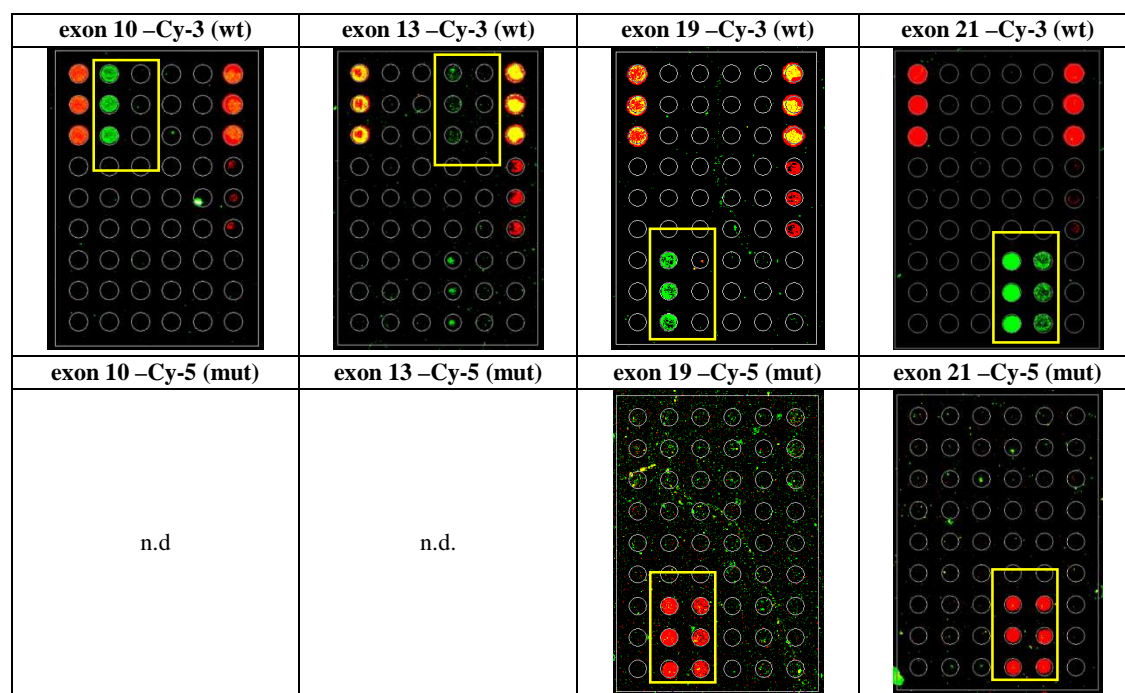
Figure 5. 5 Microarray hybridization results obtained with PCR labelled fragments.
Alignment spots are highlighted in red (Cy5) when hybridizing wt PCR product (Cy3).

Although our experiments underlined the possibility to correctly genotype homozygous wt sample and heterozygous samples, the fluorescent signals obtained were quite low, and in particular they were lower than signals obtained using the complementary oligonucleotides. This fact probably highlights a too high stringency in the hybridization condition used for PCR fragments.

5.3.III   Definition of the hybridization parameters for CFTR amplicons

As discussed above, considering the lenght and complexity of the sample, the hybridization conditions needed to be further optimized to achieve a higher probe discriminination activity compared to those established for oligo DNAs. Indeed, genome regions containing the sequences to be identified as mutated or normal (wild type) are usually sereval hundred nucleotide-long and could undergo complex phenomena like the DNA helix secondary structure formation. The formation of loops, duplexes, or complex foldings of the target DNA sequences during the hybridization processes could be prevented working on the stringency of the saline buffer condition or temperature.

To define the optimal working conditions different hybridization conditions has been tested using PCR amplified regions around the mutated CFTR susceptibility loci.

Hybridization conditions can differ for salt and formamide concentration or hybridization temperature, all parameters that affects the stringency of the specific recognition.

Starting from the hybridization condition optimized for the complementary oligo DNA (Section 5.3.I), and working at temperatures from 25°C (room temperature) to of 37°C, amplicons were hybridized using the following conditions (**Table 5. 5**). The choice of these two temperatures by changing SSC and formamide concentrations allowed to test conditions with stringency ranging from 18°C (high stringency condition) to more than 30°C (low stringency condition).
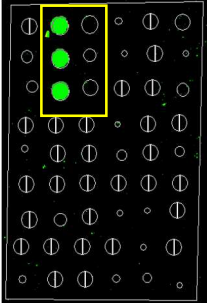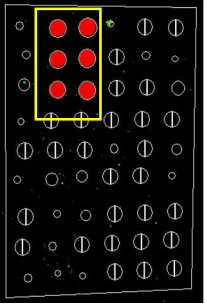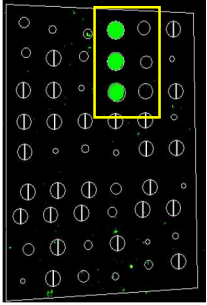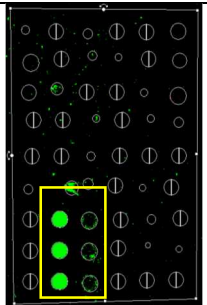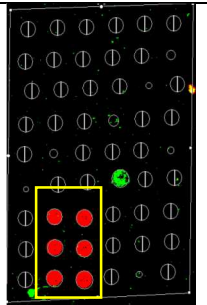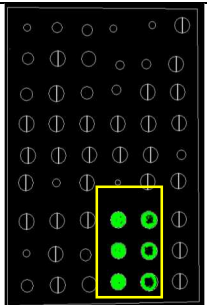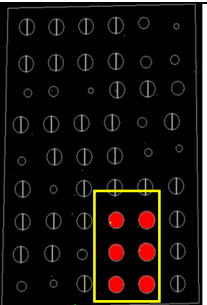
Table 5. 5. Conditions tested for the hybridization of homozygous wt and heterozygous sample genotyping optimization through fluorescent microarray technique.

Hybridization protocols	SSC concentration	Formamide concentration [%]	Hybridization temperature [°C]	Δ temp (T_{melt}-T_{hyb}) [°C]
1	3X	50	25	18
2	3X	40	25	25
3	5X	40	25	29
4	3X	30	25	32
5	3X	30	37	20
6	5X	30	37	24
7	2X	20	37	25
8	3X	20	37	28
9	3X	15	37	31

Signal intensities were analyzed both at 532 and 645 nm in order to reveal hybridization signals deriving from Cy3 labelled sample (green, usually used for homozygous wt samples) or from Cy5 labelled samples (red, usually used for heterozygous samples) at the same time.

The hybridization condition that allowed to detect with the higher specificity only the proper allele was the one with low salt concentration (SSC 2X), low formamide concentration (20%) and a hybridization temperature of 37°C (protocol no. 7 in **Table 5. 5**) as shown in **Figure 5. 6**. The discrimination ratios (DR) calculated in this condition are the most suitable for genotyping are compatible with those recorded hybridizing complementary oligo wt DNA on the corresponding wt probe (see Section 5.3.I).

Figure 5. 6. Microarray hybridization results obtained with PCR labelled fragments, labeled with Cy3 (green, homozygous wt samples) or with Cy5 (heterozygous samples) in the optimized hybridization conditions (SSC2X, formamide 20%, hybridization temperature 37°C 3h). Results are shown both as images and numerically as discrimination ratios (DR). the detection of
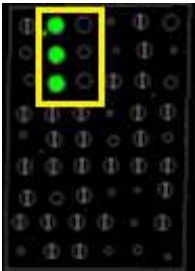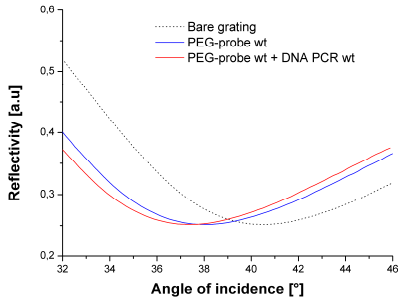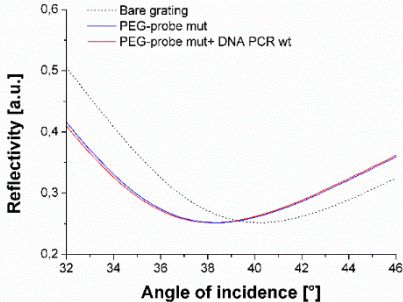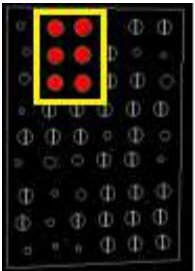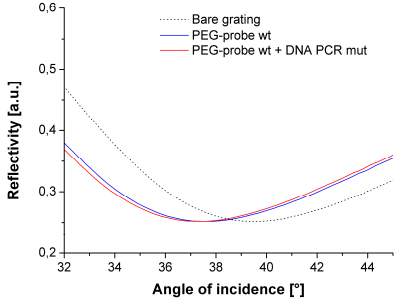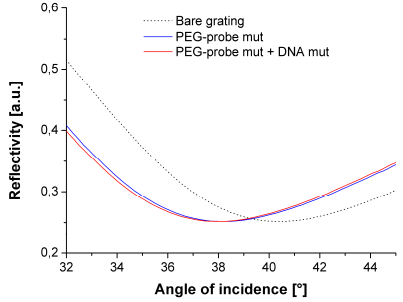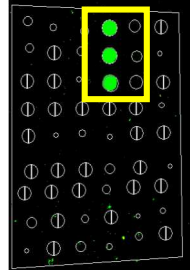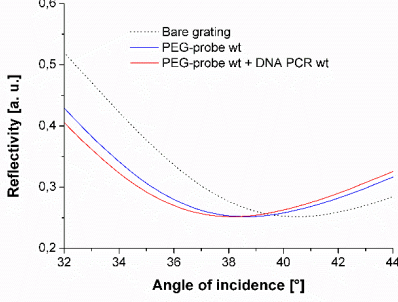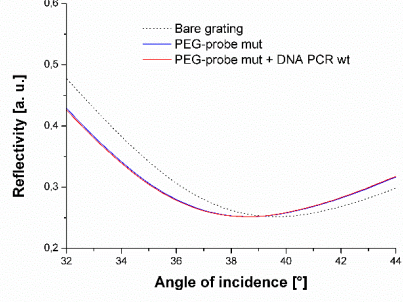
Reported DR demonstrates that for all the *homozygous wt* tested samples obtained values are suitable for genotyping. In particular for wt exon 10, 13 and 19, all reported values are included between 0.01 and 0.08, meaning that the hybridization of a wt PCR on the array generates a signal on its specific wt probe – and not on other wt probes – that is always 12-100 times higher than the signal registered on the mut probe. Concerning PCR 21 wt sample, the obtained DR is 0.4, relatively higher if compared to DR rate obtained for the other wt samples, but still able to genotype correctly the sequence. A higher DR was obtained also using the complementary DNA oligo for 21 wt probe, demonstrating that this can be attributed to the chemico-physical characteristics of the 21 wt and mut probe couple, obviously constrained by the mutation position itself, and by the surrounding nucleotides.

Concerning instead *heterozygous* samples for all the three tested PCR, DR included from 0.9 to 1.3 were achieved: considering that a theoretical DR of 1 should be an ideal results, obtained DR are absolutely in line with this value and are particularly suitable to achieve a precise genotypization of the samples.

The tested hybridization optimized condition was used for the final hybridization tests, as described in the following Section.

5.4   Hybridization experiments

In **Figure 5. 7** results obtained after ex situ hybridization of CFTR related PCR products are shown. Shifts were collected after substrate cleaning, after SH-PEG-COOH plus amino modified probe immobilization on the surface, and after sample incubation. For the *wt* sample tested a clear shift is recorded after incubation of the sample on the related *wt* probe, while no significant signal is detected on the *mut* one. DR obtained using SPR technique for *wt* samples are all included between 0.1 and 0.2 (also for exon 21 *wt* that gave higher DR using fluorescent technique) underlining genotyping ability of the *wt* probes. Concerning *mut* probes, DR range from 0.7 to 3, meaning that also in this case genotypization can be achieved with precision.

Sample		Fluo	SPR on wt probe	SPR on mut probe
Δ F508 (exon 10)	wt	DR mut/wt=0.01		
Δ F508 (exon 10)	hetero			
2183 AA (exon 13)	wt			
2183 AA (exon 13)	hetero	nd.	nd.	nd.
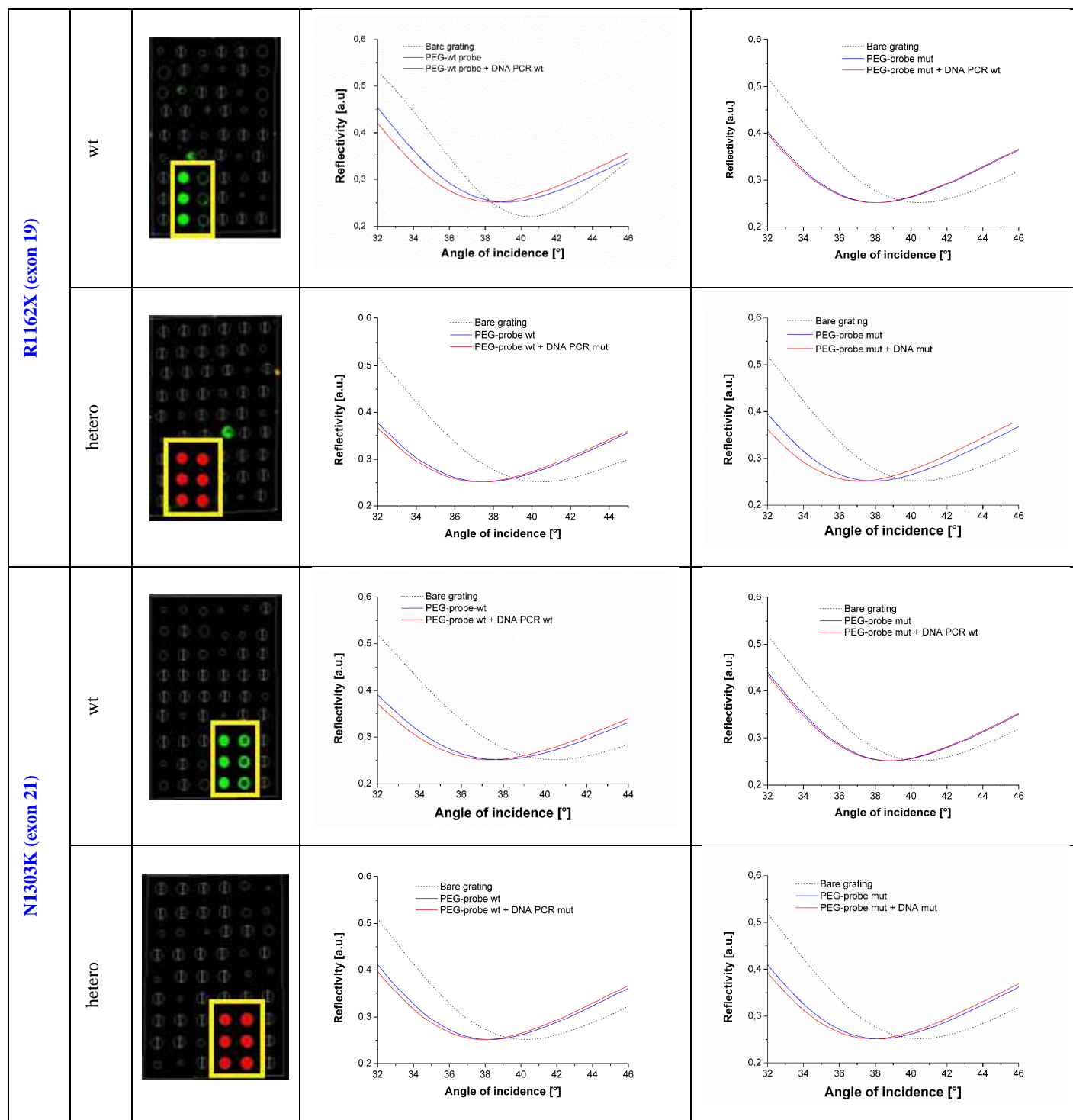
Figure 5. 7. Fluorescence results (*left*) and SPR shift (*right*) obtained after ex situ hybridization of CFTR related PCR products. Each sample was incubated both on wt and on mut related probe. Shifts were collected after substrate cleaning (*Bare grating, black dotted line*), after SH-PEG-COOH plus amino modified probe immobilization on the surface (*solid blue line*), and after sample incubation (*solid red line*).

5.5   Conclusions

In this work we chose the probes for CFTR screening and their structure was evaluated. A precise and reproducible method for plasmonic gold surface functionalization has been optimized, and hybridization conditions for correctly genotyping PCR fragments deriving by DNA extracted from culture cells and from clinical samples were properly set using fluorescent microarray technique. Once optimized, hybridization conditions were used for sample analysis on SPR substrates. Genotypization results are summarized in **Table 5. 6**.

Table 5. 6. Summary of genotypization DR obtained using fluorescent technique (a) and SPR technique (b)

Fluo analysis	**(a)** DR output result		*SPR analysis*	**(b)** DR output result	
	wild type	heterozygous		wild type	heterozygous
wt/mut probe signal	**< 0.40**	**0.50 - 1.50**	wt/mut probe signal	**< 0.40**	**0.50 - 3.50**

A DR cut off for wt sample genotypization can be set at 0.4: all the obtained DR below 0.4 genotype univocally a wt sample, *viceversa* a DR above 0.5 genotype univocally a mutant sample (in our case an heterozygous sample). These results clearly showed the possibility of employing azimuthally-controlled GC-SPR for the genotypization of CF mutations, even if the discrimination between homozygous and heterozygous state could be improved by finely controlling and changing the working temperature. In any case these experiments gave us the starting point for the realization and improvement of a CF SPR sensor.

6.   Sensor for explosives

Abstract

In this work we investigated and developed two trinitrotoluene (TNT) sensing configurations based on azimuthally rotated GC-SPR. The two methods tested differed in the sensing layer adopted: the first method employed a self-assembled monolayer with specific TNT-sensitive ending groups; the second one employed a molecularly imprinted polymer. The aim of the work was to preliminary test the possibility of using the sensing strategies proposed by us in the explosive sensor field, in particular testing their efficiency, feasibility and applicability in a sensing device.

6.1   Sensors for explosives

Recently the need in the explosive traces detection became of great importance due to the increasing use of explosives in terrorism, in addition to the environmental detection and monitoring of traces of explosives from unexploded land mines, industrial leakage at manufacturing facilities, improper disposal, etc [188–190]. Thus currently adopted explosive detection system require an improvement in term of sensitivity, costs, handiness and analyses, in order to make the traces of explosives detection easier.

Commonly used explosives are organic compounds and can be classified into six broad classes based on their chemistry [190–192], most of them having extremely low vapour pressures at ambient temperature, indicating that these molecules are extremely sticky and tend to be adsorbed onto surfaces very easily:

- Aliphatic nitro compounds, such as nitromethane, hydrazine nitrate;
- Nitroaromatic compounds, such as 2,4,6-trinitrotoulene (TNT), dinitrobenzene (DNB), Hexanitrostilbene and picric acid;
- Nitramines or nitrosamines, such as octogen (HMX) or hexogen (RDX);
- Nitrate esters, such as pentrite (PETN), ethylene glycol dinitrate (EDGN), nitroglycerine, and nitroguanidine (NQ);
- Acid salts, such as ammonium nitrate; and
- Organic peroxides, such as triacetone triperoxide (TATP) and hexamethylene triperoxide diamine (HMTD).

Among all the types of explosives, TNT has become of great importance, as it is a potent explosive for which techniques for detection on a person's body or in one's baggage is considered important for assuring safety of airports and air travel. [193].

Currently, the most common technique for the explosive detection include ion mobility spectrometry (IMS), mass spectrometry (MS), and gas chromatography (GC). Most of these devices

are, however, rather bulky, expensive, and require time-consuming procedures. Thus, the research in explosive trace detection has been moved to nanosensors, thanks to their potentially high sensitivity, miniaturization and scalability. Specific colour reaction between explosive compounds and a specific organic reagent/dye [188], laser photoacoustic spectroscopy [193] and cantilever-based sensors [194–196] are examples of the recent explosive detection research in the nanosensor field.

In general explosive nanosensors can be divided into two categories [190]: *receptor-free* and *receptor-based* nanosensors.

Receptor-free nanosensors are based on detecting physical properties of explosives (e.g. thermodynamic, chemical, or optical properties [197]), while *receptor-based nanosensors* achieve selectivity through the specific interaction between the receptor molecule and the explosive analyte. The latter is the most currently explored type of explosive sensors.

Chemical selectivity in explosive detection based on receptors originates from the chemical interaction between the explosive molecules and the receptor molecules. For reversible detection, explosive molecules must bind to the receptors with weak chemical bonds that can be broken at room temperature, for example, van der Waals interactions, hydrogen bonding, etc. Self-assembled monolayers (SAMs) are a widely adopted type of selective sensing layers in this field like in the bio-detection one (Section 2.1). In this context 4-mercaptobenzoic acid (4-MBA) and 6-mercaptonicotinic acid (6-MNA) monolayers are already adopted and diffused [190,198].
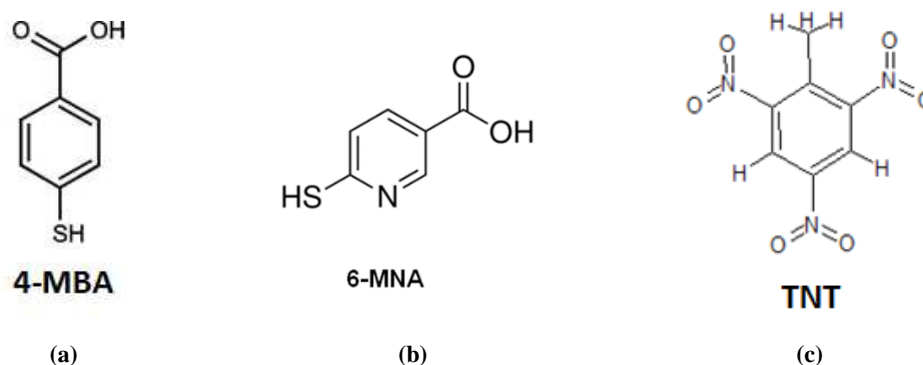
Figure 6. 1. Chemical formulas of 4-mercaptobenzoic acid (4-MBA) (*a*), 6-mercaptonicotinic acid (6-MNA) (*b*) and TNT (*c*).

Molecularly imprinted polymers (MIPs) are another way of obtaining chemical speciation. MIPs for explosives are specially generated via the interaction of functional monomers, explosive molecule templates, and a cross-linking agent. The templates are then removed prior to sensing. Only the molecules that match the template shape and properties can occupy the cavity, providing high selectivity (see Section 6.2 for a detailed description).

In this context we performed some preliminary experiments aimed to the realization of a new TNT sensor prototype by combining the high sensitivity of azimuthally rotated GC-SPR with both sensing SAM and MIP. Thus to strategies will be described in the following Section:

　　1.　SAM-based TNT sensor. A 6-MNA SAM was deposited onto a gold sinusoidal grating and the whole system was then characterized under azimuthal control. The adsorption kinetics of TNT onto the SAM sensing layer was monitored as a function of sensor exposition time to TNT gaseous flow. Through this strategy we explored a well-known method in the TNT detection field (i.e. the

use of 6-MNA as sensing layer) combined with the innovative high sensitive azimuthally-controlled GC-SPR.

2. MIP-based TNT sensor. A MIP layer was deposited onto a gold sinusoidal grating and the whole system was then characterized under azimuthal control. Through this method we wanted to combine the high sensitivity of molecular imprinted polymers with the high sensitivity of azimuthal control GC-SPR.

6.2   Molecular Imprinted Polymers

The technique of molecular imprinting consists in creating specific molecular recognition sites in solid materials by using template molecules. The most significant advantages of molecularly imprinted materials are mechanical/chemical stability, low cost, and ease of preparation and hence have attracted extensive research interest due to the potential applications in separation, sensors, bioassay, and drug delivery [199]. MIP typically involves the copolymerization of functional and cross-linking monomers in the presence of template molecules. Subsequent removal of template molecules from the polymer matrix generates the recognition sites (cavity) complementary to the shape, size, and functionality of the template [199,200] (**Figure 6. 2**).
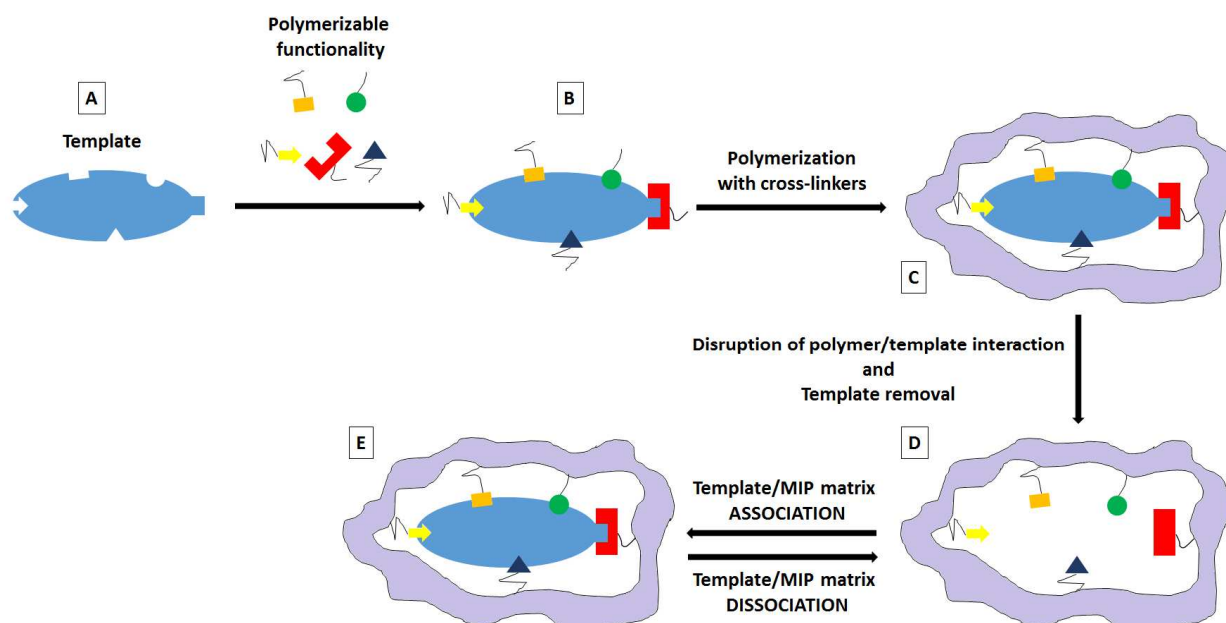
Figure 6. 2. Schematic representation of the molecular imprinting process. Starting from a template (A) the formation of reversible interactions between the template and polymerizable functionality is performed (B). A subsequent polymerization in the presence of crosslinkers, a cross-linking reaction or other process, results in the formation of an insoluble matrix in which the template sites reside (C). Template is then removed from the polymer through disruption of polymer-template interactions and extraction from the matrix (D). The template can be linked again to the MIP matrix (association – D➔E) and removed again (dissociation – E➔D).

Many attempts have been made to exploit this class of materials in sensor's applications, focusing the attention to the systems optimization for obtaining high sensitivity, large binding capacity, and rapid binding kinetics [201]. However, a typical problem is the extraction of the original templates in bulk samples located in areas with increasing distance from the surface: the highly cross-linked rigid structure does not allow these molecules to move freely. Furthermore, if the generated cavities are not in the proximity of the materials' surface, target species need long times to access the empty

cavities within the MIP system. As a result, MIPs most often exhibit high selectivity but low binding capacity (amount of recognition sites), poor site accessibility, and slow binding kinetics [200]. Anyway, moving the imprinted materials toward the nanometric domain is expected to possess several remarkable advantages over normal imprinting materials. Some advantages are the (1) easy removal of template molecules because of extremely high surface-to-volume ratio; (2) higher binding capacity because of more recognition sites in the proximity of the surface; (3) faster binding kinetics due to easy accessibility to the target molecules; (4) well-defined morphology for feasible installation onto the surface of nanodevices.

MIP were applied also to TNT detection, using TNT as template for the matrix synthesis [202,203]. Usually the exposure of MIP-based sensors to TNT is performed by immersing the sensitive substrate in a liquid TNT sample and the response is then evaluated by liquid chromatography or Surface Enhanced Raman Scattering techniques [202]. Just recently, few works appear on the exploitation of MIP combined with localized plasmons of metal NPs to enhance the SPR response and to amplify SPR-based sensors [202,203].

Starting from previous considerations, we chose to combine the MIP-based sensing approach with the high sensitivity of GC-SPR technique, exploiting a new sensing approach for the TNT detection.

6.3   Calculation of TNT saturation concentration

The simplest way to perform preliminary TNT detection experiments is working in a TNT saturated environment, achieved when equilibrium between a TNT source that sublimates and the environment of a small chamber is established.

At the equilibrium, the TNT gas concentration can be derived from the ideal gas law with good approximation, since low pressures are involved [204].

$$c = \frac{P}{k_B T} \qquad (6.1)$$

where P is the pressure, T the temperature and k_B the Boltzmann constant.

For a generic substance, the pressure under saturation condition, called "saturated vapour pressure", depends itself on the temperature, according to the Antoine equation [205]:

$$P_{sat} = 10^{\left(A - \frac{B}{C+T}\right)} \qquad (6.2)$$

The A, B and C parameters are the "Antoine constants" and depend on the material.

In literature different values of TNT Antoine constants are reported, originating from different slopes in the curve of P_{sat} as a function of temperature [191,205]. The reason for the discrepancy is unclear [206] and the only common information is that $C = 0$ in the temperature range of our interest (the temperature is expressed in the absolute scale, which implies that P_{sat} only vanishes at the absolute zero). Two sets of the Antoine constants at room temperature are identified (**Table 6. 1**).

Table 6. 1. Sets of Antoine constants reported in literature

Temperature range	A	B [K]	Reference
Da 293 a 353 K	16.596	5874.238	[205]
Da 287 a 330 K	14.435	5175	[191]

Inserting Eq. (6. 2) in Eq. (6. 1) the saturated vapour concentration we can gather that it rapidly increases as temperature increases:

$$c_{\text{sat}} = \frac{10^{\left(A - \frac{B}{T}\right)}}{k_B T} \tag{6. 3}$$

If A and B are given in SI units, this formula gives the concentration in m^{-3}. The conversion into mass fraction expressed in ppb is obtained introducing the TNT molecular mass (m$_{TNT}$ = 227 amu = 3.769x10^{-25} kg) and the air density, ρ = 1.3 kg/m^3, into the equation:

$$c_{\text{ppb}} = \frac{m_{TNT}}{\rho} \cdot c_{\text{sat}} = \frac{m_{TNT}}{\rho \, k_B} \cdot \frac{10^{\left(9 + A - \frac{B}{T}\right)}}{T} \tag{6. 4}$$

With the Antoine constants reported in **Table 6. 1**, the concentration is calculated and reported in **Figure 6. 3**. Due to the exponential growth, a wide range of concentration values can be provided heating the chamber with a common hot-plate, ranging from some tens to some thousands of ppb.
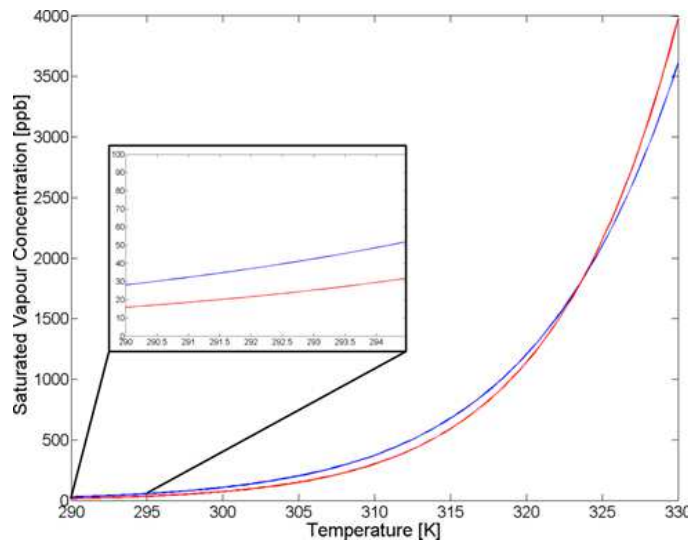
Figure 6. 3. Saturated vapour concentration as a function of the temperature in the chamber. The two different curves are obtained from the first (*red solid line* [205]) and the second (*blue solid line* [191]) Antoine constant sets reported in **Table 6. 1**. In the inset the detail of the curves at low temperatures is shown.

In conclusion, Eq. (6. 4) allowed to estimate the TNT concentration in a saturated environment, with the limitation that, since the correct Antoine constants for our specific TNT sample are unknown, the concentration under our experimental conditions will fall into a certain range of variability.

In order to reach the saturation condition for the predicted TNT concentration, two other parameters have to be taken into account: the diffusion time needed for the incubation chamber saturation and the sublimation rate necessary for TNT to saturate the incubation chamber.

The diffusion time can be estimated as:

$$t \approx \frac{d^2}{D} \tag{6. 5}$$

where d is the dimension of the system (i.e. 10 cm, **Figure 6. 4**), and D is the diffusion coefficient that in our case can be approximated to 5x10^{-6} m^2/s [206]. From Eq. (6. 5) the diffusion time results 2000 s, i.e. about 30 minutes, in our system.

The TNT sublimation rate from a disk-shaped support is given by [206]:

$$\frac{dm}{dt} = 4D \cdot r \cdot c_{\text{sat}} \qquad (6.6)$$

where m is the TNT mass and r is the disk radius. As the total mass needed to saturate the volume (V) of the chamber is

$$M = c_{sat} \cdot V \qquad (6.7)$$

the total time τ can be extracted by the integrated expression:

$$\frac{M}{\tau} = \frac{c_{\text{sat}} V}{\tau} = 4D \cdot r \cdot c_{\text{sat}} \qquad (6.8)$$

From Eq. (6. 8):

$$\tau = \frac{V}{4Dr} \qquad (6.9)$$

meaning that τ is temperature-dependent as both the sublimation rate and the saturated vapour concentration depend on the temperature.

Taking as an example a chamber volume of 10 cm^3 and $r = 1$ cm, the time is estimated in about 1 minute.

According to these calculations, the sublimation is relatively fast and the dominant factor is the diffusion. In our case, one hour is a quite reasonable time scale to ensure the saturation of the chamber.

6.4   TNT adsorption kinetics

Since Antoine equation (Eq. (6. 2)) gives a relation between the temperature and the TNT concentration into the chamber, a correlation between the sensor output (i.e. the resonance angle shift $\Delta\theta$) and the concentration has to be provided in order to have an estimation of the TNT concentration detected with our sensing prototype. We start from the Langmuir adsorption model for gas molecules onto a solid surface [207–209], from which the adsorption of a number of molecules (N_a) can be expressed as a function of time:

$$\frac{dN_a}{dt} = k_a N_g (N_{\text{sat}} - N_a) - k_d N_a \qquad (6.10)$$

where N_a is the number of adsorbed molecules, N_g is the number of free gas molecules, N_{sat} is the maximum number of adsorbed molecules (i.e. the saturation condition), k_a and k_d are the adsorption and desorption rate constants, respectively. In our experimental conditions, since the environment is saturated by a TNT source, the molecules reservoir N_g will remain constant in spite of the adsorption. The desorption rate parameter k_d, that can be rewritten as $1/\tau_r$ for a certain mean residential time of an adsorbed molecule before being released, is expected to be much smaller than k_a, because the sensitive layer is optimized in order to bond to the TNT molecules and hold them for a relatively long τ_r.

Taking into account that the resonance shift is proportional to the number of adsorbed molecules,

$\Delta_\theta \equiv \sigma N_a$ [21] we can consider $s \equiv \sigma N_{\text{sat}}$ as the maximum shift at saturation condition. Considering the saturation condition

$$k_a N_g \equiv K_a c_{\text{sat}} \tag{6.11}$$

Eq. (6. 10) can be written in term of the TNT concentration into the incubation chamber as:

$$\frac{d\Delta_\theta}{dt} \approx K_a c_{\text{sat}}(s - \Delta_\theta) \tag{6.12}$$

After integrating Eq. (6. 12) we get:

$$\Delta_\theta = s \cdot \left(1 - e^{-\tau \cdot c_{\text{sat}} \cdot K_a}\right) \tag{6.13}$$

Eq. (6. 13) can be used to fit the resonance angle shift plotted as a function of incubation time for a constant temperature. For our specific experiment, the incubation time is fixed while temperature is varied. Studying the dependence of Eq. (6. 13) on the temperature we get the following equation:

$$\Delta_\theta(T) = s \cdot \left(1 - e^{-\tau \cdot c_{\text{sat}}(T) \cdot K_a(T)}\right) \tag{6.14}$$

where the resonance angle shift at the saturation condition (s) is not dependent on the temperature, K_a can be considered proportional to $\sqrt{T}$ [209] and c_{sat} is temperature-dependent and Eq. (6. 3) can be re-written as:

$$c_{\text{sat}}(T) \propto \frac{10^{(-B/T)}}{T} \tag{6.15}$$

Introducing a parameter C including all the constants, the final relation between resonance angle shift and temperature becomes:

$$\Delta_\theta(T) = s \cdot \left(1 - e^{-\frac{10^{(-B/T)}}{\sqrt{T}} \cdot C}\right) \tag{6.16}$$

It can be linearized and the re-arranged giving the following equations.

$$\ln\left(1 - \frac{\Delta_\theta}{s}\right) = -\frac{10^{(-B/T)}}{\sqrt{T}} \cdot C \tag{6.17}$$

$$\log_{10}\left[\sqrt{T} \cdot \ln\left(\frac{s}{s - \Delta_\theta}\right)\right] = -\frac{B}{T} + \log_{10} C \tag{6.18}$$

In this way the fit of the (T, Δ_θ) data set is reduced to a linear fit from which we can determine B and C constants.

6.5   Experimental part

6.3.I   Sensing experiment setup

We performed TNT sensing measurements in a TNT gas saturated incubation chamber (**Figure 6. 4**) mounted onto a spectroscopic ellipsometer sample holder. An aluminium box containing the TNT powders was inserted into the chamber and the plasmonic grating was fixed onto the sample holder. After sealing the incubation chamber, the system was left at room temperature for the time needed to reach the environment saturation and then sensing measurements were performed.

(a) **(b)**
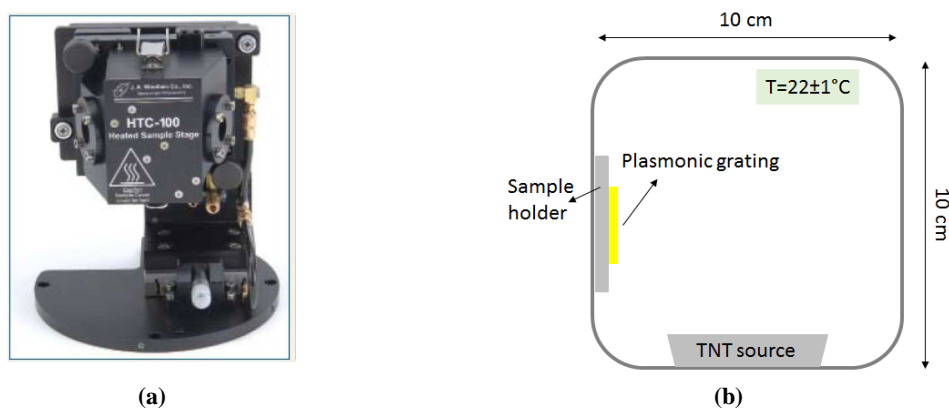
Figure 6. 4. Woollam HTC-100 heat stage and chamber adopted for the TNT sensing experiments (a) and experimental scheme inside the incubation chamber (b).

Starting from considerations of Section 6.3 and considering our working temperature of 22 ± 1 °C, the working TNT concentration was estimated to be in the range 45 ± 15 ppb, depending on the chosen set of Antoine constants.

6.3.II   First approach: SAMs as sensing layers

Sensing layer deposition

6-Mercaptonicotinic acid - 6-MNA - (**Figure 6. 1 (c)**) was purchased from Sigma Aldrich.

After sinusoidal grating cleaning (10 minutes in a 5:1:1 dd-H_2O:NH_4OH:H_2O_2 solution), the surface was immersed in an ethanol 6-MNA 6 mM solution for 24 hours. After layer deposition, SPR response was detected (**Figure 6. 5**)
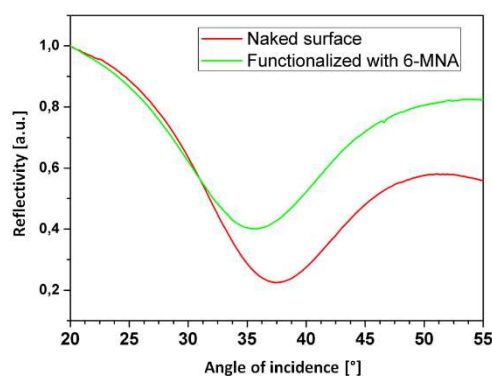
Figure 6. 5. Resonance angle shift detected after 6-MNA deposition onto the plasmonic surface. The *red solid line* is referred to the naked surface, while the *green solid line* is referred to the presence of 6-MNA layer.

TNT detection

SPR TNT detection was performed by mounting an incubation chamber onto the ellipsometer, in which the sensing substrate was fixed and exposed to a TNT flux. Measurements were performed at scheduled times after the TNT flux beginning (30, 45, 60, 90, 120 min and 1 night) at room

temperature (i.e. low TNT concentration regime). In **Figure 6. 6** and **Table 6. 2** the results of the TNT adsorption kinetics are reported.

The first TNT response was detected after 30 minutes and the wavelength shift continued to increase until reaching a maximum value after one night of sensor exposition.

(a)

(b)
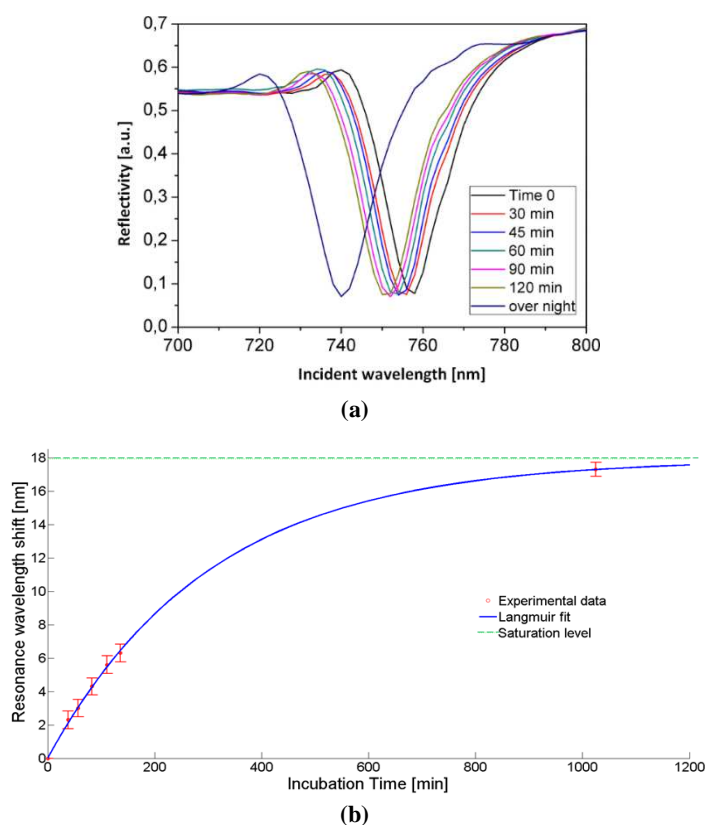
Figure 6. 6. Reflectivity dip detected for the TNT adsorption onto 6-MNA sensing layer. Each exposition time is highlighted with a different colour, from 30 minutes to one night (a) and adsorption kinetics curve fitted using the Langmuir equation (b), where the *green dashed line* underlines the surface saturation level.

Table 6. 2. Resonance wavelength shifts obtained in the TNT adsorption kinetics study.

TNT incubation time [min]	Resonance wavelength shift [nm]
30	2.3±0.38
45	3.0±0.37
60	4.3±0.38
90	5.6±0.35
120	6.3±0.36
Over night	18.08±0.37

Even if the complete surface saturation by TNT was not reached (**Figure 6. 6**), we can conclude that the limit of the detectable concentration can be further improve as the lowest shift detected after 30 minutes of exposition to TNT is not null but it is 2.3 nm.

6.3.III Second approach: MIP as sensing layer

MIP synthesis

The MIP system has been synthesized by the sol-gel method based on the hydrolysis and condensation reaction of silicon alkoxides. In **Figure 6. 7** precursors adopted in our work are reported. The synthesis conditions and the precursors have been selected in order to obtain different properties: (1) a cross-linked inorganic SiO_2 network with pendant amino groups able to interact with TNT molecules (the sensitive element); (2) the presence of thiol functionalities to promote the adhesion of the MIP film to the gold sinusoidal grating (the plasmonic substrate); (3) the addition of a TNT templating solution in order to create binding sites with a specific shape after the completion of sol-gel reactions and network formation.
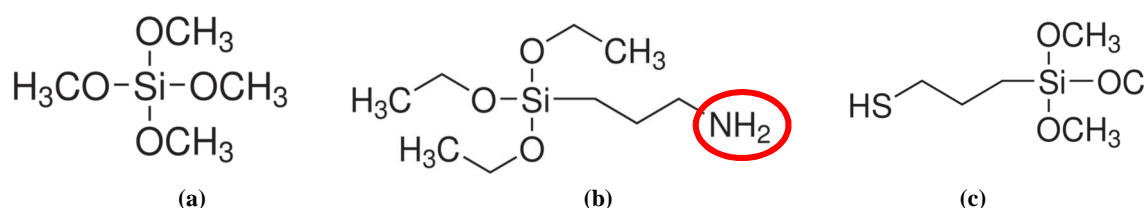
Figure 6. 7. Molecular formulas of the selected sol-gel alkoxides precursors for the synthesis of MIP system: tetramethoxysilane (TMOS) (*a*), aminopropyltriethoxysilane (APTES) (*b*), mercaptopropyltrimethoxysilane (MPTMS) (*c*).

In particular, APTES has been chosen thanks to its ability to form Meisenheimer complex between amino groups and the TNT molecules, through a strong charge transfer. This interaction lead to the appearance of an absorption band in the visible region, and to the deep red coloring of the sol just after the addition of the TNT templating solution (see the figure 14). Following the absorption band due to the Meisenheimer complex it is possible to monitor the extraction of the template molecules from the matrix in the first step and then the presence of TNT after the exposure to explosive vapours.

(a)   **(b)**
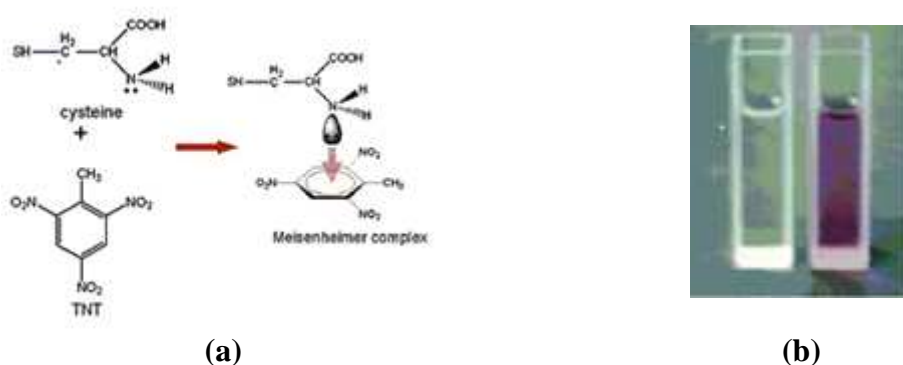
Figure 6. 8. Meisenheimer complex formation mechanism (*a*) and coloring of the sol after the addition of TNT (*b-left*) and its interation with amino group (*b-right*).

Sensing layer deposition

The final MIP was deposited onto plasmonic gratings with different thicknesses ($100 \div 50$ nm). The same system was spin coated onto a glass slide in order to optimize the extraction protocol and to follow the TNT removing within the matrix through UV-Visible spectroscopy. The same procedure was applied to the plasmonic samples used to reveal the presence of TNT in air. **Figure**

6. 9 shows the UV-Vis spectra of MIP after immersion in the extraction sol increasing incubation time. An evident reduction of the absorption band due to Meisenheimer complex, typical of the interaction between the TNT and amino groups, was observed. In fact, the assembly of TNT molecules on the pore wall is based on the very strong non-covalent interaction between the electron-deficient nitroaromatics and the electron-rich amino groups of APTES. By this way, it is possible to detect TNT template molecules onto the pore sites modified with APTES. In particular, the sol used for the TNT removing was based on an alcoholic acid solution (Methanol or Ethanol: Acetic Acid = 9:1).
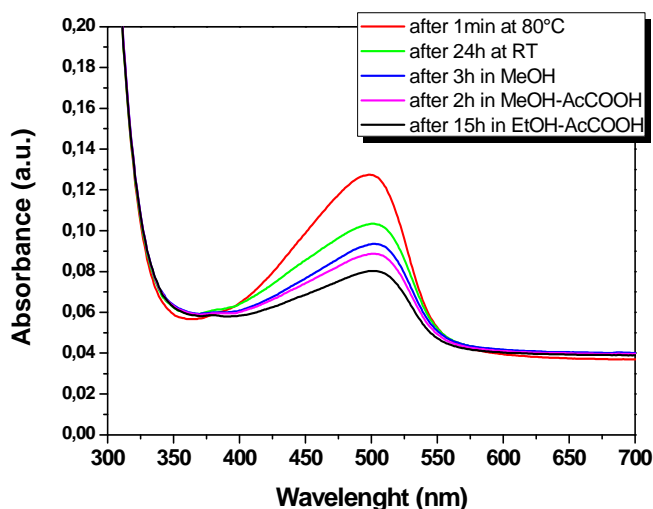
Figure 6. 9. UV-Visible spectra of MIP: evolution of the absorption band due to amino groups-TNT intermolecular interaction for increasing extraction time. After 15 hours a good TNT extraction from the MIP matrix was obtained.

TNT detection

The extracted sample was exposed to TNT molecules in steady state conditions for 2 hours. In **Figure 6. 10**, the reflection spectra acquired are reported for the pristine sample and after the TNT exposure. There was an evident shift of the resonance deep due to a change of matrix refractive index, indicating the ability of MIP to detect the presence of TNT molecules in air. The same sample was also regenerated by immersion, for some hours, in the same sol used for the extraction. The experiment was repeated after some days and the functionalized substrate showed an even better response, probably due to a more efficient extraction or desorption of TNT molecules compared with the first NT extraction.

The resonance angle shifts of 1.4±0.02° and 2.3°±0.04° for the first (**Figure 6. 10 (a)**) and for the second **Figure 6. 10 (b)** experiment respectively, highlighting the potentiality of this architecture to reveal much lower concentrations, considering the order of magnitude of the measurement error.

(a)   **(b)**
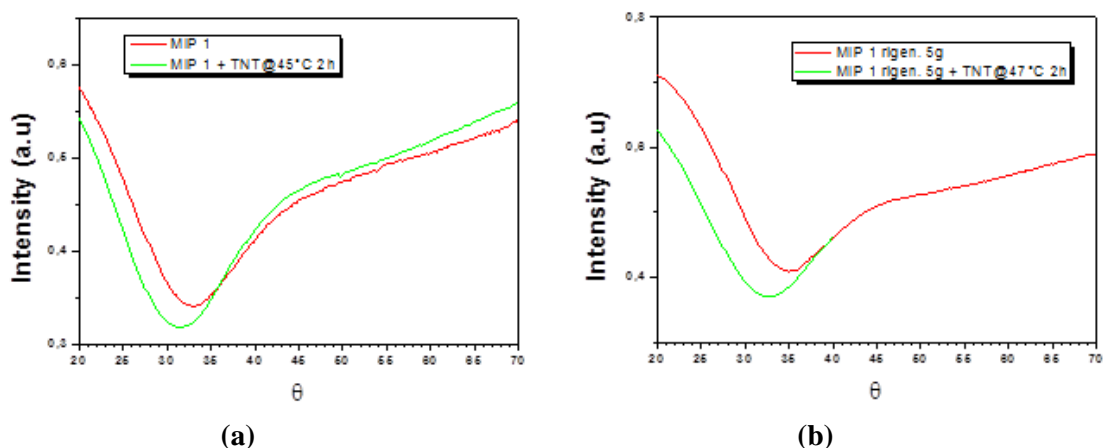
Figure 6. 10. Resonance angle shift detected after MIP deposition onto the plasmonic surface and exposure to TNT vapours in steady-state conditions. The red line is referred to the functionalized MIP surface, while the green line is referred to MIP after the TNT exposure. The measurements were performed at first with the just prepared MIP matrix (*a*) and after the regeneration of the functionalized substrate (*b*).

6.6   Conclusions

We were able to detect TNT traces through both sensing strategies investigated up to a concentration of about 45 ± 15 ppb. Combining the well-known SAM-based method with the azimuthally-rotated GC-SPR one we were able to monitor the adsorption kinetics of TNT having an idea of the time required by our system for the sensor saturation at room temperature. Starting from these preliminary results we could further improve our TNT sensing platform in future studies. Also the preliminary application of MIP to TNT sensing could be easily improved as it demonstrated its feasibility to explosive detection. As the whole TNT study was at its early stages, future studies and experiments are needed to have an accurate estimation of the sensitivity and to make our sensing substrates an efficient miniaturized device for explosive sensing.

7. Sensors for L. pneumophila

Abstract

In this Section the realization of a preliminary azimuthally-controlled GC-SPR system for the detection of *Legionella pneumophila* (*L. pneumophila*, **Figure 7. 1(a)**) is described. The aim of the work was to test the efficiency of our device in term of lowest bacterium detectable concentration (colony-forming unit – CFU). Furthermore, to verify the system specificity, samples to control the substrate adsorption and samples containing *Escherichia coli* (*E. coli*, **Figure 7. 1(b)**) cells, used as unrelated negative control organism for capture antibody binding, were run.

| (a) | (b) |
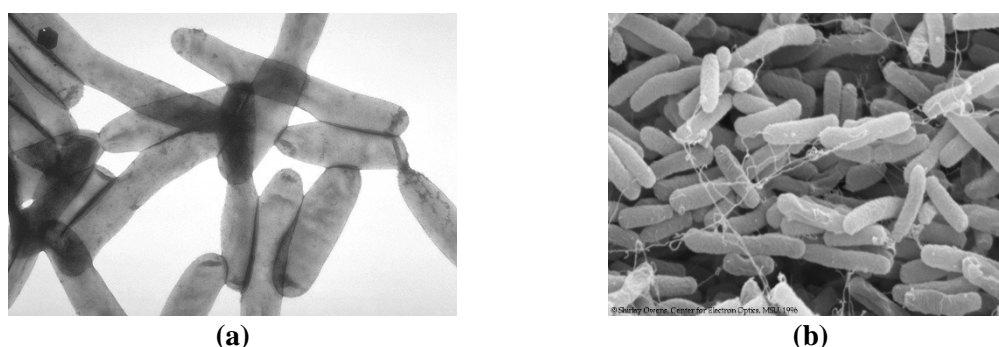
Figure 7. 1. (a) Legionella pneumophila TEM image (Centers for Disease Control and Prevention, part of the United States Department of Health and Human Services) and (b) Escherichia coli (Shirley Owens, Center for Electron Optics, MSU, SEM image). L. pneumophila has a coccobacillary shape with variable dimensions from 0.3 to 0.9 μm (width) and 1.5-5 μm (length). E. coli is significantly smaller: ~1 μm (width) and ~2 μm (length) [210].

7.1   Legionella pneumophila sensing

Legionella pneumophila, the causative agent of Legionnaires' disease and Pontiac fever (an acute, self-limiting, influenza-like illness without pneumonia [211]), was first recognized in 1977 following an outbreak of acute pneumonia in Philadelphia. *L. pneumophila* is responsible for more than 90% of cases of Legionnaires' disease [212], therefore the detection of legionellae by water sampling is important in epidemiological investigations of Legionnaires' disease and its prevention. Actually, ''the gold standard'' for identification of *L. pneumophila* remains the culture method, a method that is known to exhibit a number of problems [213]. To overcome this issue, new sensing strategies were recently explored. An optic biosensor, based on imaging ellipsometry (IE), has been developed for the multiple detection of various pathogens such as *E. coli* O157:H7, *S. typhimurium*, *Y. enterocolitica*, and *L. pneumophila*, with a detection limit of 10^3–10^7 CFU/mL. Moreover Oh [214] demonstrated the use of an optical biosensor based on SPR for the detection of *L.*

pneumophila in artificially contaminated waters with a sensibility of 10^5 cells/mL. Some other preliminary SPR-based methods recently appeared in the Legionella biosensing scenario, all of them leading to a minimum concentration of *L. pneumophila* of 10^3 [213] or 10^1 CFU [215].

At the present the legal limit of *L. pneumophila* in a high risk hospital environment in Italy is 10^2 CFU/L [216], and methods for the bacterium detection under this limit are not currently developed as they are at their preliminary stage. Starting from these considerations we tried to apply our high sensitive azimuthally-controlled GC-SPR system to the detection of *L. pneumophila* to test the detection limit of our sensing device in term of detectable bacterium CFU.

7.2 Materials and methods

7.2.I Biological elements.

Poly (ethylene oxide)

Carboxyl and thiolated poly (ethylene oxide) (HS-PEO-COOH) Mw 3.4 kDa was used purchased from Laysan bio (chemical formula in **Table 4. 3**).

Legionella Pneumophila

L. pneumophila strain was purchased from American Type Culture Collection (ATCC). A rabbit polyclonal IgG anti-Legionella antibody, specific for antigens of intact microorganism, was purchased from Virostat.

Escherichia coli

A strain of non-pathogenic *E. coli* DH10-beta was purchased from New England Biolabs (NEB) to be used as unrelated organism to verify the anti-*Legionella* antibody specificity.

7.2.II Gold surface preparation for *Legionella* detection by SPR and fluorescence analyses

Gold-coated substrates were pre-cleaned in a basic peroxide solution (5:1:1 double distilled water (ddH$_2$O), 30% H$_2$O$_2$ and 25% NH$_4$OH) for 10 minutes, rinsed in dd-H$_2$O and dried under N$_2$ flux just prior to use. PEO-COOH depositions were carried leaving the plasmonic surfaces in a 3.4 kDa thiolated PEO-COOH (**Table 4. 3**) 1mM aqueous (MilliQ water) solution in a wet chamber (75%) at 35°C for 24 hours. In the case of samples for SPR analyses. The polymer solution was poured onto the plasmonic surface in a limited area of the available surface (**Figure 7. 2**). After PEO deposition, surfaces were activated by immersing them in an EDC/sulfo-NHS 5 mM solution in 2-(*N*-morpholino)ethanesulfonic acid (MES) 1X for 10 minutes. Surfaces were then immersed in anti-*Legionella* polyclonal antibody (Virostat) 1mg/mL in printing buffer (Na$_2$PO$_4$ 0.1 M, NaCl 0.3 M, Triton X-100 0,01%, pH 7.2) solution for the PEO-COOH/antibody binding overnight in the wet chamber at room temperature. After antibody deposition surfaces were incubated with a blocking solution (2% BSA in Na$_2$PO$_4$ 50mM a pH 7.2) for one hour at room temperature and then the functionalized part was fixed with absolute ethanol at -20°C for 10 minutes.
The same functionalization protocol was adopted for substrates used for the fluorescence analyses but the functionalized areas were selected using a ProPlate multi-well mask in order to have the possibility of making multiple experiments simultaneously.
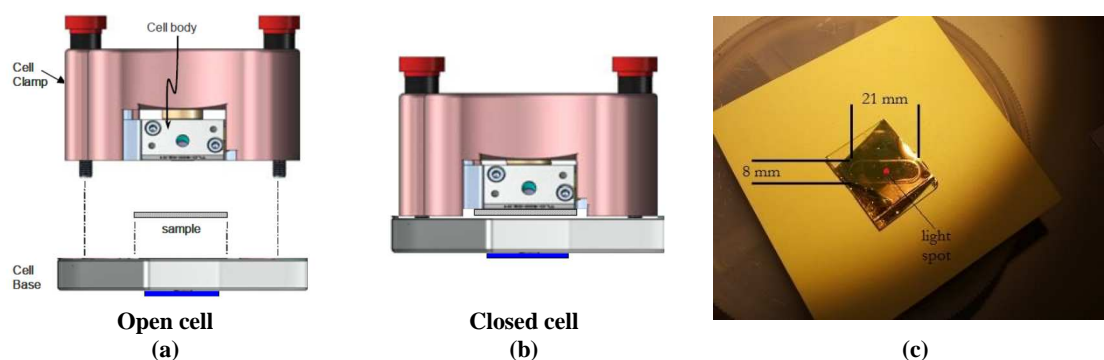
Figure 7. 2. PEO and bacteria deposition in the case of Legionella Pneumophila was performed onto a well defined area, related to the beam incident area derived from the detection chamber adopted ((a) and (b) from [217]) for safety reasons. The functionalization area was defined by drawing an ellipse-like shape with an alcohol resistant marker (c), considering the exact area available from the detection cell features and the incident light spot position.

7.2.III Gold surface preparation for E. Coli detection

For *E. Coli* detection the same sensing surface preparation protocol, as for *Legionella* detection, was followed.

7.2.IV Bacteria capture

Legionella pneumophila

Bacterium concentrations of 10^6, 10^4, 10^2, 10^1 CFU of unlabelled or Alexa Fluor-647 labeled cells were the samples tested for SPR and fluorescent analyses run in parallel, respectively. A negative control sample was set using 10^4 CFU of *L. pneumophila* incubated on substrates functionalized with non-specific capture antibody. After cleaning and resuspension in PBS/BSA (1%) the cells were deposited on functionalized the plasmonic surface (7.2.II). After incubation, the substrates were cleaned with a washing buffer (50 mM Tris , 250 mM NaCl , 0,05% Tween 20, pH 7.0) once and in 1X PBS pH 7.0 twice, rinsed in MilliQ water and incubated for 10 minutes in absolute ethanol (-20 ° C). The slides were then dried and analyzed by SPR measurements or fluorescence analysis following the characterization reported in Section 2.2.

E. coli

Bacterium concentration of 10^4 CFU was tested through SPR analysis as controls for anti-*Legionella* antibody capturing specificity. After cleaning and re-suspension in PBS/BSA (1%) the cells were deposited on the plasmonic surface (7.2.II). After incubation, the substrates were cleaned with a washing buffer (50 mM Tris, 250 mM NaCl , 0,05% Tween 20, pH 7.0) once and in 1X PBS pH 7.0 twice, rinsed in MilliQ water and incubated for 10 minutes in absolute ethanol (-20 ° C). The slides were then dried analyzed by SPR measurements.

7.3   Results

In **Figure 7. 3**, **Figure 7. 4** and **Table 7. 1** SPR and fluorescence detection results are reported. Through azimuthally-controlled GC-SPR we were able to detect a Legionella concentration of 10^1 CFU, a value under the legal limit of 10^2 CFU, while in the case of fluorescence analysis a null signal was detectable already for 10^3 CFU. The shift corresponding to 10^1 CFU (i.e. 2.46±0.04) gives the possibility to further improve the SPR detection sensitivity.

SPR measurements

(a)

(b)

(c)

(d)
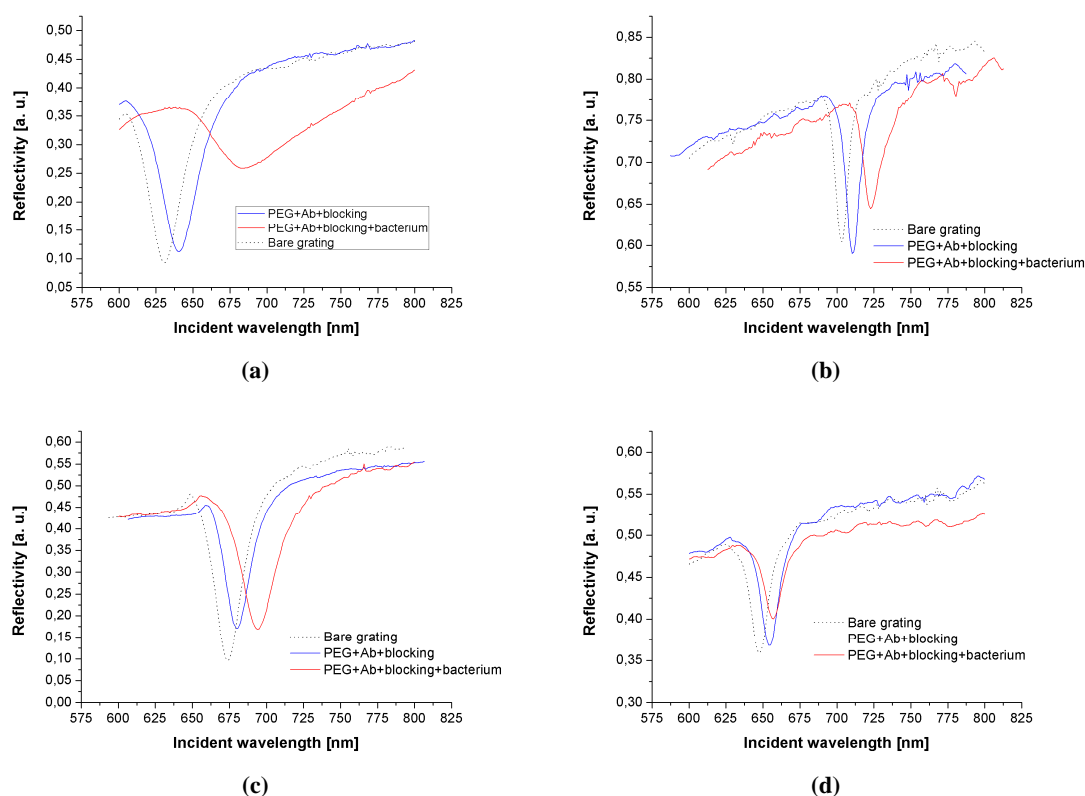
Figure 7. 3. SPR measurements were performed with wavelength interrogation for concentrations of 10^6 (a), 10^4 (b), 10^2 (c) and 10^1 (d) CFU. In the presence of *L. pneumophila* a wavelength shift was detected for each sample tested, from 46.30±0.12 to 2.46±0.04 nm.

Fluorescence array
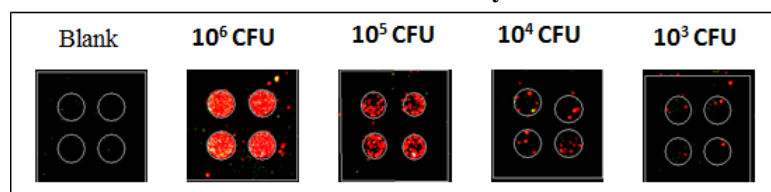
Figure 7. 4. Fluorescence images are reported for all the *L. pneumophila* tested samples, from the blank sample to the lowest detectable concentration used (10^3 CFU). Each measurements was repeated five times and here one concentration set is reported as example. For fluorescence analyses the 10^1 CFU concentration was not tested as a null signal was already detected for 10^3 CFU.

Table 7. 1. SPR *L. pneumophila* and *E. coli* detection results.

For SPR measurements concentration of 10^6, 10^4, 10^2 and 10^1 CFU were tested in the case of *L. pneumophila*. Results were compared with the negative control.

Target	Probe	Bacterium concentration [CFU]	Resonance wavelength shift after PEO, antibody and blocking agent deposition [nm]	Resonance wavelength shift after bacterium deposition [nm]
L. pneumophila	Ab anti *Legionella*	10^6	9.68±0.04	46.30±0.12
L. pneumophila	Ab anti *Legionella*	10^4	6.15±0.12	12.64±0.11
L. pneumophila	Ab anti *Legionella*	10^2	7.04±0.05	13.60±0.05*
L. pneumophila	Ab anti *Legionella*	10^1	6.65±0.05	2.46±0.04
L. pneumophila	no Ab**	10^4	4.67±0.16	0.06±0.16
E. coli	Ab anti *Legionella****	10^4	6.76±0.04	0.07±0.03

*contrary to what we expected, the shift obtained for 10^2 CFU is higher than the one obtained for 10^4 CFU and this could be considered an experimental error that we could be analyzed better in the future after confirming these preliminary results and improving our sensing device for *L. pneumophila*.
**negative control sample: surface adsorption control.
***sensing platform specificity control.

7.4   Conclusions

Although SPR detection experiments will need confirmations as they were preliminary tests and they were performed only once due to the safety conditions needed in the experimental part, we can conclude that at first that the lowest *L. pneumophila* concentration detected was 10^1 CFU is a really a good result. In fact to our knowledge there are few works in which the *L. pneumophila* concentration detected is under the legal limit [215], and the SPR detection of Legionella is generally performed with methods different from the ours leading to output signals significantly lower than the ones obtained by us (~ 0.2° in [214]). Moreover the lowest shift detected using our method (i.e. 2.46±0.04 nm) is not comparable with the error order of magnitude (about 0.01-0.04), giving the possibility of further increase the system sensitivity in term of lowering the bacterium detectable concentration before reaching a quasi-zero shift value as happened with the negative control (0.06±0.16 nm). Finally the detectable concentration of *L. pneumophila* showed by our SPR system is lower than the concentration detected through the standard fluorescence microarray method, allowing the overcoming of experimental limits deriving from standard detection methods.

To the goodness of the preliminary results obtained with SPR detection of *L. pneumophila*, we also add the experiments conducted in parallel with the *E. coli* that allowed us to also check the specificity of our detection method. Following incubation with bacteria not belonging to the *Legionella* group, the shift is recorded is of the same order of magnitude of measurement error instrumental (0.07 ± 0.03), and then close to the zero of the detection system.

8. Conclusions

Sinusoidal plasmonic gratings were fabricated combining laser interference lithography and soft lithography techniques. Thanks to the reproducibility of the fabrication procedure and thanks to the large areas available, it was possible to apply the plasmonic surface to different application fields: the detection of *M. tuberculosis* DNA using PNA probes; the detection of cystic fibrosis DNA through DNA probes; the detection of TNT molecules and of *L. pneumophila* bacteria. The sensing surfaces were characterized under azimuthal control of the grating orientation (azimuthally-controlled grating-coupling surface plasmon resonance, GC-SPR) in order to increase the system sensitivity.

As a general conclusion, plasmonic gratings characterized under azimuthal control have demonstrated a high sensitivity and resolution in the detection of different species showing their applicability to a wide range of sensing field as shown in **Table 8. 1**. A complete study from the biological element choice to the sening surface optimization and then to the real sensing application was performed for *M. tuberculosis* and cystic fibrosis DNA sensors, while for the other sensor types a preliminary working principle demonstration was performed.

The first application (Chapter 4) tested was the detection of *M. tuberculosis* DNA using PNA probes. The objectives of the work were finding a strategy to correlate the sensing response with the amount of molecules adsorbed onto the surface, obtaining a complete surface protection from non-specific adsorptions (antifouling) and obtaining an efficient functionalization strategy in order to maximize the DNA/PNA interaction. After the sensing surface calibration, the antifouling behaviour was optimized testing three poly (ethylene oxide) (PEO) derivatives of different chain lengths: PEO 0.3, 2 and 5 kDa. The results showed that full surface protection in multiple buffer conditions could be achieved only by using high Mw PEOs deposited at high surface density - as the 2 and 5 kDa here used. 2 kDa PEO provided the best compromise between fouling protection and signal detection, in fact it was chosen as the antifouling layer for real sensing applications.

Starting from the optimized sensing surface we applied it to real DNA/PNA sensing. At first we studied the adsorption kinetics of all the molecules of interest: PEO-PNA (the probe), HS-PNA (the probe for comparison) and PEO 2 kDa (the backfiller). In order to optimized the PNA probe detection efficiency we realized a co-immobilization model that allowed us to control the surface composition on term of probe/backifiller ratios. Comparing surfaces covered by different PEO-PNA:PEO or HS-PNA:PEO, we deduced that the best surface composition for DNA sensing was made by a 10% of PEO-PNA and a 90% of PEO. Using these results we analyzed both oligo and genomic or PCR-amplified DNA, comparing SPR and fluorescence measurements. The optimized set-up was able to detect a purified, complementary oligonucleotide DNA at concentrations down to 3.2 pM by SPR measurements and down to 16 nM by fluorescence analyses with a sensitivity of 212 °/RIU (**Table 8. 1**), and we could expect a reliable detection capability even at lower

concentrations with our SPR detection method. Experiments performed using samples containing fragmented human genomic DNA as a model of a real, unamplified clinic sample, showed high levels of interferences, with lowered shifts and a high nonspecific adsorption value, indicating the capability of the developed system to efficiently work only in the presence of PCR amplified and purified samples.

Sensing detection of cystic fibrosis DNA (Chapter 5) showed the possibility of employing azimuthally-controlled GC-SPR for the genotypization of cystic fibrosis mutations, even if the discrimination between homozygous and heterozygous state could be further improved for some of the tested mutations. A discrimination ratio (DR) cut-off for wild type (wt) sample genotypization was set allowing to univocally discriminating between wt and mutant samples. These results clearly showed the possibility of employing azimuthally-controlled GC-SPR for the genotypization of CF mutations, even if the discrimination between homozygous and heterozygous state could be improved by finely controlling and changing the working temperature.

It is interesting to note that, as reported in **Table 8. 1**, the sensitivity obtained with the DNA sensor is higher than which obtained with the PNA sensor. In fact, even if PNA is considered more efficient in the bio-recognition events (Chapter 4), more accurate tests would be needed in order to perfectly know PNA behaviour and to be able to work under the same stringent conditions of DNA-based sensor working (see PNA advantages and disadvantages in **Table 4. 1**).

TNT sensing (Chapter 6) was developed testing two different types of sensing surfaces: a carboxyl-ending self-assembled monolayer (SAM) and a molecularly imprinted polymer (MIP) matrix. Using both the sensing layers we were able to detect TNT traces at a concentration of 45 ppb and this result could be considered the preliminary stage for the realization of a complete explosive sensor. Combining the well-known SAM-based method with the azimuthally-rotated GC-SPR one we were able to monitor the adsorption kinetics of TNT having an idea of the time required by our system for the sensor saturation at room temperature. Starting from these preliminary results we could further improve our TNT sensing platform in future studies. Also the preliminary application of MIP to TNT sensing could be easily improved as it demonstrated its feasibility to explosive detection. As the whole TNT study was at its early stages, future studies and experiments are needed to have an accurate estimation of the sensitivity and to make our sensing substrates an efficient miniaturized device for explosive sensing.

The application of azimuthally-controlled GC SPR to *L. pneumophila* bacteria detection gave a good starting point for the realization of a miniaturized and engineered biosensor (Chapter 7). In fact a bacteria concentration of 10^1 CFU, lower than the law limit of 10^2 CFU, was detected, with a sensitivity of 875 nm/RIU. Moreover the concentration detected using the azimuthally-controlled GC-SPR system was lower than the concentration detected through the standard fluorescence microarray method, allowing the overcoming of experimental limits deriving from standard detection methods. To the goodness of the preliminary results obtained with SPR detection of *L. pneumophila*, we also add the experiments conducted in parallel with the *E. coli* that allowed us to also check the specificity of our detection method.

Starting from previous considerations and results mentioned, the sinusoidal gratings realized in this work showed high versatility as they demonstrated the possibility of being applied to different detection fields only changing the sensing layer and the detection conditions with high sensitivity. Thus the basic studies performed in this work can be considered as the starting point for the realization of a compact and miniaturized SPR sensor for multiple-applications.

Table 8. 1. Performances of sensors realized in this work

Type of sensor	Spacer layer (antifouling)	Probe	Analyte	Type of interrogation	Analyte environment	Sensitivity	Resolution	Chapter
Protein	HS-PEO[1]	biotin	avidin	angular	liquid	200.65°/RIU	4×10^{-4} RIU	4
M. tuberculosis	HS-PEO	PNA[2]	DNA[3]	angular	liquid	212.57°/RIU	9.4×10^{-5} RIU	4
Cystic Fibrosis	HS-PEO	DNA	DNA	angular	liquid	604.60°/RIU	9.9×10^{-5} RIU	5
Explosives	-	6-MNA[4]	TNT[5]	Angular /wavelength	gas	-[6]	-[6]	6
Bacteria	HS-PEO	antibody	*L. pneumophila*	wavelength	liquid	874.68 nm/RIU	1.4×10^{-4} RIU	7

[1]poly (ethylene oxide); [2]peptide nucleic acid; [3]desoxyribonucleic acid; [4] 6-Mercaptonicotinic acid; [5]trinitrotoluene; [6] more experiments would be needed in order to have an accurate estimation of sensitivity and resolution.

Abbreviations

4-MBA	4-mercaptobenzoic acid
6-MNA	6-Mercaptonicotinic acid
Ab	antibody
AFM	atomic force microscopy
APTES	Aminopropyltriethoxysilane
BSA	bovine serum albumin
CF	cystic fibrosis
CFTR	cystic fibrosis transmembrane conductance regulator
CFU	colony forming unit
Cys	cysteine
dCTP	deoxy-cytosine-tri-phosphate
DNA	desoxyribonucleic acid
dNTP	deoxy-nucleotide-tri-phosphate
DR	discrimination ratio
EDC	ethylene dichloride
GC %	guanine-citosine content
GC-SPR	grating coupling SPR
GS	goat serum
LIL	laser interference lithography
m- or b-PEO/PEG	methoxy- or biotin- poly (ethylene oxide)/poly (ethylene glycol)
MES	2-(N-morpholino)ethanesulfonic acid
MIP	molecular imprinted polymer
MPTMS	Mercaptopropyltrimethoxysilane
mut	mutant
(S-)NHS	(sulfo-)N-hydroxysulfosuccinimide
NOA	norland optical adhesive
PBS-B/GS	phosphate sodium chloride (PBS) containing BSA/GS
PCR	polymerase chain reaction
PC-SPR	prism coupling SPR
PDMS	polydimethyl siloxane
PNA	peptide nucleic acid
SAM	self-assembled monolayer
SEM	scanning electron microscopy
SP	surface plasmon
SPP	surface plasmon polariton
SPR	surface plasmon resonance
SPW	surface plasma wave
SSC	saline sodium citrate
TBO	toluidine blue O
Tm	melting temperature
TMOS	Tetramethoxysilane

Appendices

A.1 Spectroscopic ellipsometry

Ellipsometry is a useful technique for the study of optical and geometrical properties of thin films [218]. It is based on the analysis of the polarization state of light reflected by sample surface to obtain information about thickness and refractive index of thin films.

Ellipsometry measures the two values ψ and Δ. These represent the amplitude ratio ψ and phase difference Δ between light waves known as p- and s-polarized light waves. The application area of spectroscopic ellipsometry is quite wide and includes ex situ measurements and real-time monitoring (or in-situ measurements): substrates, thin films, gate dielectrics, lithography films (semiconductor field), polymer films, self-assembled monolayers, proteins, DNA (chemical field), TFT films, transparent conductive oxides, organic LED (display application), high and low dielectrics for anti-reflection coating (optical coating area), phase change media for CD and DVD, magneto-optic layers (data storage field, chemical vapour deposition (CVD), molecular beam epitaxy (MBE),etching, oxidation, thermal annealing, liquid phase processing etc. (real time monitoring).

The advantages of this characterization technique are the high precision (thickness sensitivity~0.1Å), the nondestructive measurements, fast measurement, wide application area, various characterizations including optical constants and film thicknesses are possible, real-time monitoring (feedback control) is possible. On the other end, some disadvantages can be summarized: necessity of an optical model in data analysis (indirect characterization), data analysis tends to be complicated, low spatial resolution (spot size: several mm), difficulty in the characterization of low absorption coefficients ($\alpha < 100 \text{cm}^{-1}$).

Spectroscopic ellipsometry has been applied to evaluate optical constants (n, k or α) and thin-film thicknesses of samples. However, the application area of spectroscopic ellipsometry has been expanded recently, as it allows process diagnosis on the atomic scale from real-time observation.

In **Figure A.1. 1** the scheme of the measurement principle of spectroscopic ellipsometry is reported.

In ellipsometry, p- and s-polarized light waves are irradiated onto a sample at the Brewster angle, and the optical constants and film thickness of the sample is measured from the change in the polarization state by light reflection or transmission.
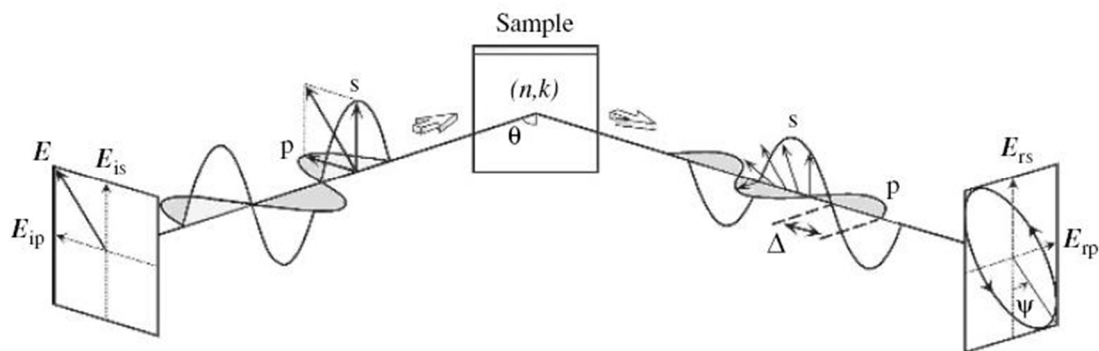
Figure A.1. 1. Measurement principle of spectroscopic ellipsometry.

The typical result of an ellipsometric analysis is expressed in term of the ellipsometric angles ψ and Δ which are defined from the ratio of the amplitude reflection coefficients [219] (Fresnel's coefficients) for p- and s-polarization:

$$\rho = \frac{r_p}{r_s} = \tan \psi \cdot e^{i\Delta} \qquad \text{(A.1. 1)}$$

where r_p and r_s are the reflection coefficients with p- and s- polarizations.

Therefore ψ represents the angle between reflected p- and s-polarizations, while Δ expresses the phase difference:

$$\tan \psi = \frac{r_p}{r_s} \qquad \text{(A.1. 2)}$$

$$\Delta = \delta_{rp} - \delta_{rs} \qquad \text{(A.1. 3)}$$

Thus common ranges for ellipsometric angles are $0° \leq \psi \leq 90°$ and $0° \leq \Delta \leq 360°$.

Ellipsometry allows to know the complex refractive index $\tilde{n} = n + ik$, or the complex dielectric permittivity $\tilde{\varepsilon} = \varepsilon_1 + i\varepsilon_2$ equivalently, starting from a known film thickness, or *viceversa*.

In this work we used the spectroscopic ellipsometer showed in the following figure.

Figure A.1. 2. Picture of the spectroscopic ellipsometer used in this work. (1) Optical bench for focusing and polarization control of the output light (monochromatized by a gating monochromator, located in sequence to a Xe-Neo 75 W lamp), (2) sample holder, (3) rotating goniometer for incidence angle scan, (4) Detector.

A.2   Scanning Electron Microscopy (SEM)

Scanning electron microscope images the sample surface by scanning it with a high energy electron beam [220]. Electrons interact with the atoms that compose the sample and produce signals that yield information about target surface topography, composition and physical properties such as electrical conductivity. Primary electrons are emitted by thermionic emission from a metallic filament cathode (usually tungsten or lanthanum hexaboride) or by a thermal field emission tip (Schottky emitter) and are accelerated towards an anode. The electron beam, with energy typically from a few hundred eV up to 30 keV, is focused by a system of condenser lenses into a beam with a very fine local spot sized 0.4 nm to 5 mm. The electron beam passes through pairs of scanning coils or pairs of deflector plates in the electron column which deflect the beam horizontally and vertically so that it scans in a raster fashion over a rectangular area of the sample surface. Both the column and the target chamber are under high vacuum ($10^{-6} - 10^{-7}$ mbar) in order to avoid electron scattering by air molecules. When primary electrons interacts with the target, they loss energy by repeated scattering and adsorption within a teardrop-shape volume (interaction volume) which extends from less than 100 nm to around μm into the surface. The size of the interaction volume depends on the electron energy and atomic number and density of the target. The interaction between primary electrons and sample results in the back-reflection of high-energy electrons by elastic scattering, production of secondary electrons by inelastic scattering and emission of electromagnetic radiation. The most common imaging technique consists in collecting the low-energy secondary electrons ($E < 50$ eV). These electrons originate within a few nanometres from the surface and are usually detected by an Everhart-Thornley detector which is a type of scintillator-photomultiplier device. The resulting signal is displayed as a two-dimensional intensity distribution. The brightness of the signal depends on the number of secondary electrons reaching the detector: if the beam enters the sample perpendicularly to the surface, the activated region is uniform around the axis of the beam and a certain number of electrons are emitted. As incidence angle increases, the escape distance of one side of the beam will decrease and more secondary electrons will be emitted. In this way steep surfaces and edges tend to be brighter than flat zones, which results in images with a well-defined, three-dimensional appearance. The spatial resolution depends on the size of the electron spot, which is related to the electron energy and the focusing system and it can be also limited by the size of the interaction volume. In our case, resolutions down to few nanometres can be achieved.

A.3   Atomic Force Microscopy (AFM)

Atomic Force Microscopy (AFM) consists in a scanning technique that produces very high resolution 3D images of sample surfaces [220,221]. This technique can be used either in a static or dynamic mode. In the static mode, the sharp tip at the end of a cantilever is bought in contact with the sample surface. During initial contact, atoms at the end of the tip experience a very weak repulsive force due to orbital overlap with atoms on the sample surface. This force causes a cantilever deflection which is measured by optical detectors. Deflection can be measured to within 0.02 nm, so for typical cantilever spring constant of 10N/m, a force as low as 0.2 nN can be detected. In the dynamic operation mode instead, the tip is bought in close proximity (within a few nms) to and not in contact with the sample. The cantilever is deliberately vibrated either in amplitude modulation (AM) or in frequency modulation (FM) mode. Very weak Van Der Waals attractive forces are present at the tip-sample interface. In the two modes, surface topography is measured by laterally scanning the sample under the tip while simultaneously measuring the cantilever deflection or the shift in resonant frequency/amplitude of the cantilever. Piezo-translators are used to scan the sample or alternatively to scan the tip. A cantilever with extremely slow spring constant is required for high vertical and lateral resolutions at small forces, but at the same time a high resonance frequency is desirable (from 10 to 100 kHz) in order to minimize the ratio to vibration noise. This requires a tip with extremely low vertical spring constant (typically from 0.05 to 1 N/m) as well as a low mass (in the order of 1 ng). Common cantilevers are fabricated in silicon, silicon oxide or silicon nitride and lateral dimensions are in the order of 100 μm with thickness of about 1 μm. Tip is required to be robust and have a small curvature radius (∼ 10 nm). The cantilever deflection is measured by means of an optical laser system. The beam is directed onto the back of the cantilever very close to its free end, while the reflected beam is directed onto a quad-photodetector, i.e. two pairs of photodiodes. The differential signal from the different photodiodes provides information on the cantilever deflection. In the dynamic mode, the cantilever is driven into oscillations near its resonance frequency. When the tip approaches the sample, the oscillation is damped, frequency and phase change. The variation is the feedback signal and topography is given by varying the z-position of the sample in order to keep amplitude oscillations constant or the resonance frequency fixed.

A.4 Optimization of functionalization and sensing protocols for CF sensors.

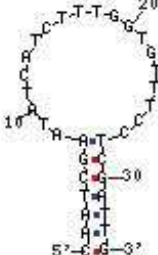**Table A.4. 1. Selected primers characteristics**
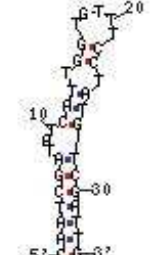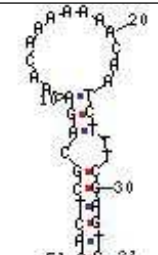
Name	Sequence 5'-3'	nt	GC%	Tm [°C]	Self dimer ΔG max [kcal/mol]	Heterodimer ΔG max [kcal/mol]	Aplicon length (wt/mut)
1 Ex10 F	ATGATGGGTTTTATTTCCAGAC	22	36.4	50.9	-5.02	-5.02	271/268
2 Ex10 R	ATTGGGTAGTGTGAAGGGTTC	21	47.6	54.6	-3.52		
3 Ex13 F	AGCTGTGTCTGTAAACTGATGG	22	45.5	54.8	-6.34	-5.13	465/464
4 Ex13 R	CTCAGAATCTGGTACTAAGGACA	23	43.5	53.3	-5.13		
5 Ex19 F	GCCCGACAAATAACCAAGTGA	21	47.6	55.5	-3.61	-6.21	454/454
6 Ex19 R	GCTAACACATTGCTTCAGGCT	21	47.6	55.8	-3.14		
7 Ex21 F	AATGTTCACAAGGGACTCCA	20	45.0	53.9	-4.64	-4.67	473/473
8 Ex21 R	CAAAAGTACCTGTTGCTCCA	20	45.0	52.9	-3.9		

Table A.4. 2. CFTR wilde type and mutant probes characteristics
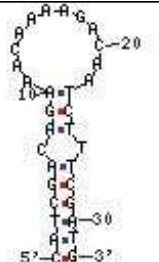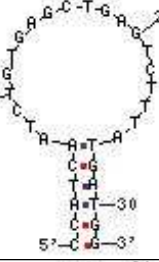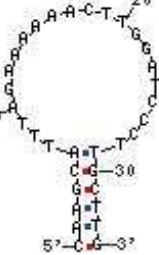
Sequence	Quality	Rating	Probe Sequence	Length [nt]	Tm [°C]	GC%	Hairpin ΔG (Internal)	Hairpin Bond (Internal)	Self Dimer ΔG (Internal)	Self Dimer Bond (Internal)
10	Good	74,2	AATATCATCTTTGGTGTTTCCT	22	49,5	31,8	0	0	-0,4	4
10 mut	Good	71,5	ATATCATTGGTGTTTCCTATGT	22	49	31,8	-0,5	3	-0,5	3
13*	Poor	45,5	CAGAAACAAAAAAACAATCTTT	22	46,8	22,7	-0,6	3	-0,6	3
13 mut*	Poor	41,1	ACAGAAACAAAAGACAATCTTT	22	48,8	27,3	-2,8	5	-2,8	5
19	Best	77,2	TCTGTGAGCCGAGTCTTT	18	50,5	50	0	0	0	0
19 mut	Good	67,6	ATCTGTGAGCTGAGTCTTTA	20	49	40	0	0	-2,9	4
21*	Poor	43,5	TTTAGAAAAAAACTTGGATCCCT	22	49,6	31,8	-0,1	3	-5,7	6
21 mut*	Poor	43,5	TTTAGAAAAAAAGTTGGATCCCT	22	49,6	31,8	-0,1	3	-5,7	6
MEAN				21,25	49,1	33,4	-0,51	2,12	-2,32	3,87
SD				1,48	1,07	8,29	0,95	1,88	2,35	1,96

*poor because of the RUN and dimers, due to sequence composition.

Table A.4. 3. CFTR wilde type and mutant hairpin probes – stem and loop - characteristics

Name	Sequence 5'-3'	Chemical structure	nt	GC%	Tm [°C]	ΔG hairpin portion [kcal/mol]	Tm hairpin portion [°C]	ΔH hairpin portion [kcal/mol]	ΔS hairpin portion [kcal/mol]
CFTR 10	**CAATCG**AATATCATCTTTGGTGTTTCCT**CGATTG**		34	38,2	59,2	-3,2	44,7	-51,5	-162,02
CFTR 10 mut	**CAATCG**ATATCATTGGTGTTTCCTATG**TCGATTG**		34	38,2	59,0	-4,87	43,6	-83	-262,07
CFTR 13	**CACTCG**CAGAAACAAAAAAACAATCTTT**CGAGTG**		34	38,2	60,2	-3,69	41,9	-68,7	-218,04

CFTR 13 mut	**CATCG**ACAGAAACAAAAGACAATCTTT**CGATG**		32	37,5	58,3	-3,69	44,5	-60,2	-189,53
CFTR 19	**CCATCA**TCTGTGAGCCGAGTCTTT**TGATGG**		30	50,0	62,1	-2,24	41,5	-42,8	-136,02
CFTR 19 mut	**CCATCA**ATCTGTGAGCTGAGTCTTTA**TGATGG**		32	43,8	60,1	-2,47	42,9	-43,6	-137,96
CFTR 21	**CAAGCA**TTTAGAAAAAACTTGGATCCCT**TGCTTG**		34	38,2	60,2	-2,52	42,7	-44,9	-142,15

CFTR 21 mut	**CAAGCA**TTTAGAAAAAAGTTGGATCCCT**TGCTTG**		34	38,2	60,2	-2,52	42,7	-44,9	-142,15
	MEAN		33	40,29	**59,91**	-3,15	43,06	-54,95	-173,74
	SD		1,51	4,41	**1,13**	0,90	1,14	14,61	46,06
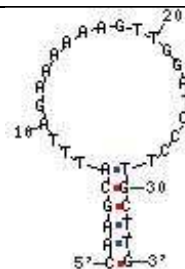
Table A.4. 4. Primers characteristics for exon 10, 13, 19 and 21 products.

Name	Sequence 5'-3'	nt	GC%	Tm [°C]	Self dimer ΔG_{max} [kcal/mol]	Heterodimer ΔG_{max} [kcal/mol]	A
1 Ex10 F	ATGATGGGTTTTATTTCCAGAC	22	36.4	50.9	-5.02		
2 Ex10 R	ATTGGGTAGTGTGAAGGGTTC	21	47.6	54.6	-3.52	-5.02	
3 Ex13 F	AGCTGTGTCTGTAAACTGATGG	22	45.5	54.8	-6.34		
4 Ex13 R	CTCAGAATCTGGTACTAAGGACA	23	43.5	53.3	-5.13	-5.13	
5 Ex19 F	GCCCGACAAATAACCAAGTGA	21	47.6	55.5	-3.61		
6 Ex19 R	GCTAACACATTGCTTCAGGCT	21	47.6	55.8	-3.14	-6.21	
7 Ex21 F	AATGTTCACAAGGGACTCCA	20	45.0	53.9	-4.64		
8 Ex21 R	CAAAAGTACCTGTTGCTCCA	20	45.0	52.9	-3.9	-4.67	

References

[1]   International Union of Pure and Applied Chemistry (IUPAC), Pure Appl. Chem. 71 (1999).

[2]   N. Lubbers, D.W.; Opitz, Eine neue pO2-Messonde zur Messung des pCO2 oder pO2 von Gasen und Flussigkeiten, Zeitschrift Fur Naturforsch. C. 30 (1975) 532–533.

[3]   A. Sassolas, B.D. Leca-Bouvier, L.J. Blum, DNA biosensors and microarrays., Chem. Rev. 108 (2008) 109–39.

[4]   W.E. Moerner, New directions in single-molecule imaging and analysis, Proc. Natl. Acad. Sci. 104 (2007) 12596.

[5]   W.G. Cox, V.L. Singer, Fluorescent DNA hybridization probe preparation using amine modification and reactive dye coupling., Biotechniques. 36 (2004) 114–22.

[6]   X. Fan, I.M. White, S.I. Shopova, H. Zhu, J.D. Suter, Y. Sun, Sensitive optical biosensors for unlabeled targets: a review., Anal. Chim. Acta. 620 (2008) 8–26.

[7]   J. Homola, Surface plasmon resonance sensors for detection of chemical and biological species., Chem. Rev. 108 (2008) 462–93.

[8]   D. Pines, Collective Energy Losses in Losses, Rev. Mod. Phys. 28 (1956) 184–198.

[9]   U. Fano, The theory of anomalous diffraction gratings and of quasi-stationary waves on metallic surfaces (Sommerfeld's waves), J. Opt. Soc. Am. 31 (1941) 213–222.

[10]   R.H. Ritchie, Plasma losses by fast electrons in thin films, Phys. Rev. 106 (1957) 874–881.

[11]   R.W. Wood, On a remarkable case of uneven distribution of light in a diffraction grating spectrum., Proc. Phys. Soc. London. 18 (1902) 269–275.

[12]   J. Zenneck, Über die Fortpflanzung ebener elektromagnetischerWellen längs einer ebenen Leiterfläche und ihre Beziehung zur drahtlosen Telegraphie, Ann. D. Phys. 23 (1907) 846–866.

[13]   A. Sommerfeld, Über die Fortpflanzung electrodynamischerWellen längs eines Drahtes, Ann. Phys. Und Chemie. 67 (1899) 233–290.

[14]   R.P. Willets, K.A.; Van Duyne, Localized Surface Plasmon Resonance Spectroscopy and Sensing, Annu. Rev. Phys. Chem. 58 (2007) 267–297.

[15]   E. Hutter, J.H. Fendler, Exploitation of Localized Surface Plasmon Resonance, Adv. Mater. 16 (2004) 1685–1706.

[16]   S.A. Maier, Plasmonics - Fundamental and Applications, 2007.

[17]   J. Homola, S.S. Yee, G. Gauglitz, Surface plasmon resonance sensors: review, Sensors Actuators B Chem. 54 (1999) 3–15.

[18]   F. Romanato, L. Hong, H. Kang, C. Wong, Z. Yun, W. Knoll, Azimuthal dispersion and energy mode condensation of grating-coupled surface plasmon polaritons, Phys. Rev. B. 77 (2008) 245435.

[19]   F. Romanato, K.H. Lee, H.K. Kang, G. Ruffato, C.C. Wong, Sensitivity enhancement in grating coupled surface plasmon resonance by azimuthal control., Opt. Express. 17 (2009) 12145–54.

[20] F. Romanato, K.H. Lee, G. Ruffato, C.C. Wong, The role of polarization on surface plasmon polariton excitation on metallic gratings in the conical mounting, Appl. Phys. Lett. 96 (2010) 111103.

[21] L.S. Jung, C.T. Campbell, T.M. Chinowsky, M.N. Mar, S.S. Yee, Quantitative Interpretation of the Response of Surface Plasmon Resonance Sensors to Adsorbed Films, 7463 (1998) 5636–5648.

[22] A. Shalabney, I. Abdulhalim, Sensitivity-enhancement methods for surface plasmon sensors, Laser Photon. Rev. 5 (2011) 571–606.

[23] A. Lahav, M. Auslender, I. Abdulhalim, Sensitivity enhancement of guided-wave surface-plasmon resonance sensors., Opt. Lett. 33 (2008) 2539–41.

[24] M. Piliarik, M. Vala, I. Tichý, J. Homola, Compact and low-cost biosensor based on novel approach to spectroscopy of surface plasmons., Biosens. Bioelectron. 24 (2009) 3430–5.

[25] R. Karlsson, R.; Stahlberg, Surface-Plasmon Resonance Detection and Multispot Sensing for Direct Monitoring of Interactions Involving Low-Molecular-Weight Analytes and for Determination of Low Affinities, Anal. Biochem. 228 (1995) 274–280.

[26] J. Breault-Turcot, J.-F. Masson, Nanostructured substrates for portable and miniature SPR biosensors., Anal. Bioanal. Chem. 403 (2012) 1477–84.

[27] J. Homola, I. Koudela, S.S. Yee, Surface plasmon resonance sensors based on diffraction gratings and prism couplers: sensitivity comparison, Sensors Actuators B Chem. 54 (1999) 16–24.

[28] J. et l. Melendez, A commercial solution for surface plasmon sensing, Sensors and Actuators B-Chemical. 35 (1996) 212–216.

[29] J. Dostálek, J. Homola, M. Miler, Rich information format surface plasmon resonance biosensor based on array of diffraction gratings, Sensors Actuators B Chem. 107 (2005) 154–161.

[30] C.J. Alleyne, A.G. Kirk, R.C. McPhedran, N.-A.P. Nicorovici, D. Maystre, Enhanced SPR sensitivity using periodic metallic structures., Opt. Express. 15 (2007) 8163–9.

[31] S. Moon, Y. Kim, Y. Oh, H. Lee, H.C. Kim, K. Lee, et al., Grating-based surface plasmon resonance detection of core-shell nanoparticle mediated DNA hybridization., Biosens. Bioelectron. 32 (2012) 141–7.

[32] D. Kim, Effect of the azimuthal orientation on the performance of grating-coupled surface-plasmon resonance biosensors, Appl. Opt. 44 (2005) 3218–3223.

[33] F. Romanato, H.K. Kang, K.H. Lee, G. Ruffato, M. Prasciolu, C.C. Wong, Interferential lithography of 1D thin metallic sinusoidal gratings: Accurate control of the profile for azimuthal angular dependent plasmonic effects and applications, Microelectron. Eng. 86 (2009) 573–576.

[34] F. Ruffato, G.; Zacco, G.; Romanato, Innovative Exploitation of Grating-Coupled Surface Plasmon Resonance for Sensing, in: K.Y. Kim (Ed.), Plasmon. – Princ. Appl., InTechOpen, 2012: pp. 419–444.

[35] A. Sonato, G. Ruffato, G. Zacco, D. Silvestri, M. Natali, M. Carli, et al., Enhanced sensitivity azimuthally controlled grating-coupled surface plasmon resonance applied to the calibration of thiol-poly(ethylene oxide) grafting, Sensors Actuators B Chem. 181 (2013) 559–566.

[36] J.C. Love, L. a Estroff, J.K. Kriebel, R.G. Nuzzo, G.M. Whitesides, Self-assembled monolayers of thiolates on metals as a form of nanotechnology., 2005.

[37] J.C. Love, D.B. Wolfe, R. Haasch, M.L. Chabinyc, K.E. Paul, G.M. Whitesides, et al., Formation and structure of self-assembled monolayers of alkanethiolates on palladium., J. Am. Chem. Soc. 125 (2003) 2597–609.

[38] C. Ulman, A.; Kang, J. F.; Liao, S.; Jordan, R.; Choi, G. Y.; Zaccaro, J.; Myerson, A. S.; Rafailovich, M.; Sokolov, J.; Fleischer, Self-assembled monolayers of rigid thiols, J. Biotechnol. 74 (2000) 175–188.

[39] A. Ulman, Formation and Structure of Self-Assembled Monolayers., Chem. Rev. 96 (1996) 1533–1554.

[40] G. Della Giustina, G. Zacco, E. Zanchetta, M. Gugliemi, F. Romanato, G. Brusatin, Interferential lithography of Bragg gratings on hybrid organic–inorganic sol–gel materials, Microelectron. Eng. 88 (2011) 1923–1926.

[41] G. Zacco, F. Romanato, A. Sonato, D. Sammito, G. Ruffato, M. Morpurgo, et al., Microelectronic Engineering Sinusoidal plasmonic crystals for bio-detection sensors, Microelectron. Eng. 88 (2011) 1898–1901.

[42] D. Sammito, G. Zacco, P. Zilio, V. Giorgis, a. Martucci, J. Janusonis, et al., Design and fabrication of a light trapping method for photovoltaic devices based on plasmonic gratings, Microelectron. Eng. 98 (2012) 440–443.

[43] V. Malyarchuk, F. Hua, N. Mack, V. Velasquez, J. White, R. Nuzzo, et al., High performance plasmonic crystal sensor formed by soft nanoimprint lithography., Opt. Express. 13 (2005) 5669–75.

[44] J.A. Rogers, R.G. Nuzzo, Recent progress in soft lithography, (2005) 50–56.

[45] M. Salerno, An introduction to Soft Lithography Marco Salerno, (n.d.).

[46] Y. Xia, G.M. Whitesides, SOFT LITHOGRAPHY, (1998).

[47] J. a. Shackleford, R. Grote, M. Currie, J.E. Spanier, B. Nabet, Integrated plasmonic lens photodetector, Appl. Phys. Lett. 94 (2009) 083501.

[48] T. Jia, M. Baba, M. Suzuki, R. a Ganeev, H. Kuroda, J. Qiu, et al., Fabrication of two-dimensional periodic nanostructures by two-beam interference of femtosecond pulses., Opt. Express. 16 (2008) 1874–8.

[49] M.M. Alkaisi, R.J. Blaikie, S.J. McNab, Nanolithography in the Evanescent Near Field, Adv. Mater. 13 (2001) 877–887.

[50] G. Chandezon, J.; Maystre, D.; Raoult, A new theoretical method for diffraction gratings and it numerical application, J. Opt. Rev. D'optique. 11 (1980) 235–241.

[51] A. Sonato, D. Silvestri, G. Ruffato, G. Zacco, F. Romanato, M. Morpurgo, Quantitative control of poly(ethylene oxide) surface antifouling and biodetection through azimuthally enhanced grating coupled-surface plasmon resonance sensing, Appl. Surf. Sci. 286 (2013) 22–30.

[52] A. Sonato, G. Ruffato, M. Natali, G. Zacco, M. Morpurgo, D. Silvestri, et al., Plasmonic Platforms for Biodetection Devices, 2011 Int. Work. Biophotonics. (2011) 1–3.

[53] J. Labuda, A.M.O. Brett, G. Evtugyn, M. Fojta, M. Mascini, M. Ozsoz, et al., Electrochemical nucleic acid-based biosensors: Concepts, terms, and methodology (IUPAC Technical Report), Pure Appl. Chem. 82 (2010) 1161–1187.

[54]   C. Briones, M. Moreno, Applications of peptide nucleic acids (PNAs) and locked nucleic acids (LNAs) in biosensor development., Anal. Bioanal. Chem. 402 (2012) 3071–89.

[55]   J. Wang, DNA biosensors based on Peptide Nucleic Acid (PNA) recognition, 13 (1998) 757–762.

[56]   A. Porcheddu, G. Giacomelli, Peptide nucleic acids (PNAs), a chemical overview., Curr. Med. Chem. 12 (2005) 2561–99.

[57]   N. Prabhakar, K. Arora, S.K. Arya, P.R. Solanki, M. Iwamoto, H. Singh, et al., Nucleic acid sensor for M. tuberculosis detection based on surface plasmon resonance., Analyst. 133 (2008) 1587–92.

[58]   a Rachkov, S. Patskovsky, a Soldatkin, M. Meunier, Surface plasmon resonance detection of oligonucleotide sequences of the rpoB genes of Mycobacterium tuberculosis., Talanta. 85 (2011) 2094–9.

[59]   B.R. Bloom, C.J.L. Murray, All use subject to JSTOR Terms and Conditions Tuberculosis : Commentary on a Reemergent Killer, 257 (2014) 1055–1064.

[60]   J.M. Musser, Antimicrobial agent resistance in mycobacteria: molecular genetic insights., Clin. Microbiol. Rev. 8 (1995) 496–514.

[61]   WHO/HTM/TB, Anti-tuberculosis drug resistance in the world, 2010.

[62]   G.A. Heifets, L.B.; Cangelosi, Drug susceptibility testing of Mycobacterium tuberculosis: a neglected problem at the turn of the century, Int. J. Tuberc. LUNG Dis. 3 (1999) 564–581.

[63]   M. Duman, E. Piskin, Detection of Mycobacterium tuberculosis complex and Mycobacterium gordonae on the same portable surface plasmon resonance sensor., Biosens. Bioelectron. 26 (2010) 908–12.

[64]   Y. Xie, Z.-G. He, Characterization of physical interaction between replication initiator protein DnaA and replicative helicase from Mycobacterium tuberculosis H37Rv., Biochem. Biokhimii͡a. 74 (2009) 1320–7.

[65]   M. Dettin, D. Silvestri, R. Danesin, E. Cretaio, G. Picariello, E. Casarin, et al., Synthesis and Chromatography-Free Purification of PNA-PEO Conjugates for the Functionalisation of Gold Sensors, (2012) 11026–11045.

[66]   P.E. Nielsen, M. Egholm, R.H. Berg, O. Buchardt, Sequence-selective recognition of DNA by strand displacement with a thymine-substituted polyamide., Science. 254 (1991) 1497–500.

[67]   M. Egholm, P.E. Nielsen, O. Buchardt, Recognition of Guanine and Adenine, (1992) 9677–9678.

[68]   M. Egholm, O. Buchardt, P.E. Nielsen, No Title, 1 (1992) 1895–1897.

[69]   B. Hyrup, M. Egholm, P.E. Nielsen, P. Wittung, B. Nordc, O. Buchardt, Structure-Activity Studies of the Binding of Modified Peptide Nucleic Acids (PNAs) to DNA1, (1994) 7964–7970.

[70]   J. Wang, E. Palecek, P.E. Nielsen, G. Rivas, X. Cai, H. Shiraishi, et al., Peptide Nucleic Acid Probes for Sequence-Specific DNA Biosensors, 7863 (1996) 7667–7670.

[71]   K.K. Jensen, H. Orum, P.E. Nielsen, B. Nordén, Kinetics for hybridization of peptide nucleic acids (PNA) with DNA and RNA studied with the BIAcore technique., Biochemistry. 36 (1997) 5072–7.

[72]   E. Mateo-martí, C. Pradier, A Novel Type of Nucleic Acid-based Biosensors : the Use of PNA Probes , Associated with Surface Science and Electrochemical Detection Techniques, (2010).

[73]   C. Briones, E. Mateo-Martí, C. Gómez-Navarro, V. Parro, E. Román, J. a. Martín-Gago, Structural and functional characterization of self-assembled monolayers of peptide nucleic acids and its interaction with complementary DNA, J. Mol. Catal. A Chem. 228 (2005) 131–136.

[74]   E. Mateo-Martí, C. Briones, E. Román, E. Briand, C.M. Pradier, J. a Martín-Gago, Self-assembled monolayers of peptide nucleic acids on gold surfaces: a spectroscopic study., Langmuir. 21 (2005) 9510–7.

[75]   C. Briones, E. Mateo-Marti, C. Gómez-Navarro, V. Parro, E. Román, J. Martín-Gago, Ordered Self-Assembled Monolayers of Peptide Nucleic Acids with DNA Recognition Capability, Phys. Rev. Lett. 93 (2004) 208103.

[76]   P.E. Nielsen, Peptide nucleic acids: on the road to new gene therapeutic drugs., Pharmacol. Toxicol. 86 (2000) 3–7.

[77]   M. et al. Egholm, PNA hybridizes to complementary oligonucleotides obeying the Watson-Crick hydrogen-bonding rules, Nature. 365 (1993) 566–568.

[78]   T. Ratilainen, a Holmén, E. Tuite, P.E. Nielsen, B. Nordén, Thermodynamics of sequence-specific binding of PNA to DNA., Biochemistry. 39 (2000) 7781–91.

[79]   L.N.A. Dna, D. Formation, P.M. Mctigue, R.J. Peterson, J.D. Kahn, Sequence-Dependent Thermodynamic Parameters for Locked Nucleic Acid, (2004) 5388–5405.

[80]   K.J. Breslauer, R. Frank, H. Blöcker, L. a Marky, Predicting DNA duplex stability from the base sequence., Proc. Natl. Acad. Sci. U. S. A. 83 (1986) 3746–50.

[81]   P. Eriksson, M; Nielsen, Solution structure of a peptide nucleic acid DNA duplex, Nat. Struct. Biol. 3 (1996) 410–413.

[82]   S.S. Menchise V, De Simone G, Tedeschi T, Corradini R, P.C. Marchelli R, Capasso D, Saviano M, Insights into peptide nucleic acid (PNA) structural features: the crystal structure of a D-lysine-based chiral PNA-DNA duplex, Proc Natl Acad Sci U S A. 100 (2003) 12021–12026.

[83]   T. Endo, K. Kerman, N. Nagatani, Y. Takamura, E. Tamiya, Label-Free Detection of Peptide Nucleic Acid - DNA Hybridization Using Localized Surface Plasmon Resonance Based Optical Biosensor related to tumor necrosis factor . The nanoparticle layer, 77 (2005) 6976–6984.

[84]   D. a Braasch, D.R. Corey, Synthesis, analysis, purification, and intracellular delivery of peptide nucleic acids., Methods. 23 (2001) 97–107.

[85]   B. Hyrup, M. Egholm, O. Buchardt, P.E. Nielsena, A FLEXIBLE AND POSITIVELY CHARGED PNA ANALOGUE WITH AN ETHYLENE-LINKER TO THE NUCLEOBASE : SYNTHESIS AND HYBRIDIZATION PROPERTIES Center for Biomolecular Recognition , Department of Chemistry , University of Copenhagen , Universitetsparken 5 , DK-2100 Cop, 6 (1996) 1083–1088.

[86]   M. et al. DEMIDOV, VV; POTAMAN, VN; FRANKKAMENETSKII, Stability of peptide nucleic acids in human serum and cellular extracts., Biochem. Pharmacol. 48 (1994) 1310 –3.

[87]   U. Koppelhus, P.E. Nielsen, C ellular delivery of peptide nucleic acid (PNA), 55 (2003) 267–280.

[88]   A. Ray, B. Nordén, Peptide nucleic acid (PNA): its medical and biotechnical applications and promise for the future., FASEB J. 14 (2000) 1041–60.

[89]   a W. Peterson, R.J. Heaton, R.M. Georgiadis, The effect of surface probe density on DNA hybridization., Nucleic Acids Res. 29 (2001) 5163–8.

[90]   D. Ozkan, P. Kara, K. Kerman, B. Meric, A. Erdem, F. Jelen, et al., DNA and PNA sensing on mercury and carbon electrodes by using methylene blue as an electrochemical label., Bioelectrochemistry. 58 (2002) 119–26.

[91]   D. Ozkan, A. Erdem, P. Kara, K. Kerman, J. Justin Gooding, P.E. Nielsen, et al., Electrochemical detection of hybridization using peptide nucleic acids and methylene blue on self-assembled alkanethiol monolayer modified gold electrodes, Electrochem. Commun. 4 (2002) 796–802.

[92]   S. Tomac, M. Sarkar, T. Ratilainen, P. Wittung, P.E. Nielsen, B. Norde, et al., Ionic Effects on the Stability and Conformation of Peptide Nucleic Acid Complexes, 7863 (1996) 5544–5552.

[93]   T. Ratilainen, A. Holme, E. Tuite, G. Haaima, L. Christensen, P.E. Nielsen, Hybridization of Peptide Nucleic Acid †, 2960 (1998) 12331–12342.

[94]   H. Park, A. Germini, S. Sforza, R. Corradini, R. Marchelli, W. Knoll, Effect of ionic strength on PNA-DNA hybridization on surfaces and in solution., Biointerphases. 2 (2007) 80–8.

[95]   C. Ananthanawat, T. Vilaivan, W. Mekboonsonglarp, V.P. Hoven, Thiolated pyrrolidinyl peptide nucleic acids for the detection of DNA hybridization using surface plasmon resonance., Biosens. Bioelectron. 24 (2009) 3544–9.

[96]   K. Kerman, M. Vestergaard, N. Nagatani, Y. Takamura, E. Tamiya, Electrochemical Genosensor Based on Peptide Nucleic Acid-Mediated PCR and Asymmetric PCR Techniques : Electrostatic Interactions with a Metal Cation with redox-active metal cation cobalt (III) hexamine ([Co-, (2006) 2182–2189.

[97]   F.R. Raymond, H.-A. Ho, R. Peytavi, L. Bissonnette, M. Boissinot, F.J. Picard, et al., Detection of target DNA using fluorescent cationic polymer and peptide nucleic acid probes on solid support., BMC Biotechnol. 5 (2005) 10.

[98]   O. Brandt, J.D. Hoheisel, Peptide nucleic acids on microarrays and other biosensors., Trends Biotechnol. 22 (2004) 617–22.

[99]   H.F. Arlinghaus, M. Schröder, J.C. Feldner, O. Brandt, J.D. Hoheisel, D. Lipinsky, Development of PNA microarrays for gene diagnostics with TOF-SIMS, Appl. Surf. Sci. 231-232 (2004) 392–396.

[100]   P. Wittung-Stafshede, M. Rodahl, B. Kasemo, P. Nielsen, B. Norden, Detection of point mutations in DNA by PNA-based quartz-crystal biosensor, Colloids Surfaces A Physicochem. Eng. Asp. 174 (2000) 269–273.

[101]   J.B. Raoof, R. Ojani, S.M. Golabi, E. Hamidi-Asl, M.S. Hejazi, Preparation of an electrochemical PNA biosensor for detection of target DNA sequence and single nucleotide mutation on p53 tumor suppressor gene corresponding oligonucleotide, Sensors Actuators B Chem. 157 (2011) 195–201.

[102]   K. Hashimoto, Y. Ishimori, Preliminary evaluation of electrochemical PNA array for detection of single base mismatch mutations., Lab Chip. 1 (2001) 61–3.

[103]   R.S. Kane, P. Deschatelets, G.M. Whitesides, N. York, Kosmotropes Form the Basis of Protein-Resistant Surfaces, (2003) 2388–2391.

[104]   K.V. Gobi, H. Iwasaka, N. Miura, Self-assembled PEG monolayer based SPR immunosensor for label-free detection of insulin., Biosens. Bioelectron. 22 (2007) 1382–9.

[105]   Y. Martin, P. Vermette, C. Jh, Low-Fouling Amine-Terminated Poly (ethylene glycol) Thin Layers and Effect of Immobilization Conditions on Their Mechanical and Physicochemical Properties, (2006) 8083–8091.

[106] E.F. Murphy, J.R. Lu, J. Brewer, J. Russell, The Reduced Adsorption of Proteins at the Phosphoryl Choline Incorporated Polymer - Water Interface, 2 (1999) 1313–1322.

[107] R. Schlapak, P. Pammer, D. Armitage, R. Zhu, P. Hinterdorfer, M. Vaupel, et al., Glass surfaces grafted with high-density poly(ethylene glycol) as substrates for DNA oligonucleotide microarrays., Langmuir. 22 (2006) 277–85.

[108] K. Yoshimoto, T. Hirase, J. Madsen, S.P. Armes, Y. Nagasaki, Non-Fouling Character of Poly[2-(methacryloyloxy)ethyl Phosphorylcholine]-Modified Gold Surfaces Fabricated by the "Grafting to" Method: Comparison of its Protein Resistance with Poly(ethylene glycol)-Modified Gold Surfaces., Macromol. Rapid Commun. 30 (2009) 2136–2140.

[109] M. Heuberger, T. Drobek, N.D. Spencer, Interaction forces and morphology of a protein-resistant poly(ethylene glycol) layer., Biophys. J. 88 (2005) 495–504.

[110] K. Uchida, H. Otsuka, M. Kaneko, K. Kataoka, Y. Nagasaki, A reactive poly(ethylene glycol) layer to achieve specific surface plasmon resonance sensing with a high S/N ratio: the substantial role of a short underbrushed PEG layer in minimizing nonspecific adsorption., Anal. Chem. 77 (2005) 1075–80.

[111] H. Du, P. Chandaroy, S.W. Hui, Grafted poly-(ethylene glycol) on lipid surfaces inhibits protein adsorption and cell adhesion., Biochim. Biophys. Acta. 1326 (1997) 236–48.

[112] P. Harder, M. Grunze, R. Dahint, D. Heidelberg, Molecular Conformation in Oligo (ethylene glycol) -Terminated Self-Assembled Monolayers on Gold and Silver Surfaces Determines Their Ability To Resist Protein Adsorption, 5647 (1998) 426–436.

[113] S. Sofia, V. Premnath, E. Merrill, Poly(ethylene oxide) Grafted to Silicon Surfaces: Grafting Density and Protein Adsorption., Macromolecules. 31 (1998) 5059–70.

[114] J. Harris, Poly(ethylene glycol) Chemistry: Biotechnical and Biomedical Applications, New York, 1992.

[115] S. Harris, J.; Zalipsky, Poly(ethylene glycol): Chemistry and Biological Applications, Washington, DC, 1997.

[116] J.D. Jeon, S.I.; Andrade, Protein surface interactions in the presence of polyethylene oxide.2. Effect of protein size, J. Colloid Interface Sci. 142 (1991) 159–166.

[117] J.D. Jeon, S.I.; Lee, J.H.; Andrade, Protein surface interactions in the preence of polyethylene oxide .1. Simplified theory, J. Colloid Interface Sci. 142 (1991) 149–158.

[118] F.S. Damos, R.C.S. Luz, L.T. Kubota, Determination of thickness, dielectric constant of thiol films, and kinetics of adsorption using surface plasmon resonance., Langmuir. 21 (2005) 602–9.

[119] R.F. Debono, G.D. Loucks, D. Della Manna, U.J. Krull, Self-assembly of short and long-chain n-alkyl thiols onto gold surfaces : A real-time study using surface plasmon resonance techniques, 688 (1996) 677–688.

[120] L.D. Unsworth, Z. Tun, H. Sheardown, J.L. Brash, Chemisorption of thiolated poly(ethylene oxide) to gold: surface chain densities measured by ellipsometry and neutron reflectometry., J. Colloid Interface Sci. 281 (2005) 112–21.

[121] K. a. Peterlinz, R. Georgiadis, In Situ Kinetics of Self-Assembly by Surface Plasmon Resonance Spectroscopy, Langmuir. 12 (1996) 4731–4740.

[122] A. Silvestri, Davide; Sonato, Optimized PEO-PNA/PE surface dressing for SPR sensing application in the detection of Mycobacterium tuberculosis related DNA, (2013).

[123] A. et al. Silvestri, D. and Sonato, Optimized PEO-PNA/PEO surface dressing for SPR sensing application in the detection of Mycobacterium tuberculosis related DNA, (2013).

[124] M. Morpurgo, E. a Bayer, M. Wilchek, N-hydroxysuccinimide carbonates and carbamates are useful reactive reagents for coupling ligands to lysines on proteins., J. Biochem. Biophys. Methods. 38 (1999) 17–28.

[125] M.T. Mccammon, J.S. Gillette, D.P. Thomas, S. V Ramaswamy, E.A. Graviss, B.N. Kreiswirth, et al., Detection of rpoB Mutations Associated with Rifampin Resistance in Mycobacterium tuberculosis Using Denaturing Gradient Gel Electrophoresis, 49 (2005) 2200–2209.

[126] D.A. Stuart, A.J. Haes, C.R. Yonzon, E.M. Hicks, R.P. Van Duyne, Biological applications of localised surface plasmonic phenomenae, 152 (2005).

[127] A.I.K. Lao, X. Su, K.M.M. Aung, SPR study of DNA hybridization with DNA and PNA probes under stringent conditions., Biosens. Bioelectron. 24 (2009) 1717–22.

[128] J.B. Fiche, a Buhot, R. Calemczuk, T. Livache, Temperature effects on DNA chip experiments from surface plasmon resonance imaging: isotherms and melting curves., Biophys. J. 92 (2007) 935–46.

[129] S. Neidle, The structures of quadruplex nucleic acids and their drug complexes., Curr. Opin. Struct. Biol. 19 (2009) 239–50.

[130] M. Morpurgo, S. Facchin, M. Pignatto, D. Silvestri, E. Casarin, N. Realdon, Characterization of multifunctional nanosystems based on the avidin-nucleic acid interaction as signal enhancers in immuno-detection., Anal. Chem. 84 (2012) 3433–9.

[131] S. Busse, V. Scheumann, B. Menges, Sensiti v ity studies for specific binding reactions using the biotin / strepta v idin system by e v anescent optical methods, 17 (2002) 704–710.

[132] A. Paul, R.M. Watson, P. Lund, Y. Xing, K. Burke, Y. He, et al., Charge Transfer through Single-Stranded Peptide Nucleic Acid Composed of Thymine Nucleotides, J. Phys. Chem. C. 112 (2008) 7233–7240.

[133] Bhat_2005_Polymer Grafting.pdf, (n.d.).

[134] Z. Ma, G. Zhang, X. Zhai, L. Jin, X. Tang, M. Yang, et al., Fractal crystal growth of poly(ethylene oxide) crystals from its amorphous monolayers, Polymer (Guildf). 49 (2008) 1629–1634.

[135] X. Zhu, Y. Jun, D.R. Staarup, R.C. Major, S. Danielson, V. Boiadjiev, et al., Grafting of High-Density Poly (Ethylene Glycol) Monolayers on Si (111), 2778 (2001) 7798–7803.

[136] S. Tokumitsu, A. Liebich, S. Herrwerth, W. Eck, M. Himmelhaus, M. Grunze, Grafting of Alkanethiol-Terminated Poly (ethylene glycol) on Gold, (2002) 8862–8870.

[137] T. Mcpherson, A. Kidane, I. Szleifer, K. Park, W. Lafayette, Prevention of Protein Adsorption by Tethered Poly (ethylene oxide) Layers : Experiments and Single-Chain Mean-Field Analysis, 7463 (1998) 176–186.

[138] D.L. Allara, M. Hill, R.G. Nuzzo, T.B. Laboratories, Spontaneously Organized Molecular Assemblies. 2. Quantitative Infrared Spectroscopic Determination of Equilibrium Structures of Solution-Adsorbed, (1985) 52–66.

[139] Y.T. Kim, R.L. McCarley, A.J. Bard, Observation of n-octadecanethiol multilayer formation from solution onto gold, Langmuir. 9 (1993) 1941–1944.

[140] T.W. Schneider, D.A. Buttry, Electrochemical Quartz Crystal Microbalance Studies of Adsorption and Desorption of Self-Assembled Monolayers of Alkyl Thiols on Gold, 17 (1993) 12391–12397.

[141] A. Surface, D.L. Allara, M. Hill, R.G. Nuzzo, T.B. Laboratories, Spontaneously Organized Molecular Assemblies. 1. Formation, Dynamics, and Physical Properties of, (1985) 45–52.

[142] E.B.T.Y. Tao, J. Evall, Formation of Monolayer Films by the Spontaneous Assembly of Organic Thiols from Solution onto Gold', 335 (1989) 321–335.

[143] L.L. Rouhana, M.D. Moussallem, J.B. Schlenoff, Adsorption of short-chain thiols and disulfides onto gold under defined mass transport conditions: coverage, kinetics, and mechanism., J. Am. Chem. Soc. 133 (2011) 16080–91.

[144] W. Pan, C.J. Durning, N.J. Turro, Kinetics of Alkanethiol Adsorption on Gold, Langmuir. 12 (1996) 4469–4473.

[145] K. Hu, A.J. Bard, In Situ Monitoring of Kinetics of Charged Thiol Adsorption on Gold Using an Atomic Force Microscope, 7463 (1998) 4790–4794.

[146] D.S. Karpovich, G.J. Blanchard, Direct Measurement of the Adsorption Kinetics of Alkanethiolate Self-Assembled Monolayers on a Microcrystalline Gold Surface, (1994) 3315–3322.

[147] C.D. Bain, H.A. Biebuyck, G.M. Whitesides, Comparison of Self -Assembled Monolayers on Gold: Coadsorption of Thiols and Disulfides1, (1989) 723–727.

[148] M. Surfaces, P.E. Laibinis, G.M. Whitesides, D.L. Allara, Comparison of the Structures and Wetting Properties of Self-Assembled Monolayers of, (1991) 7152–7167.

[149] a. Halperin, Polymer Brushes that Resist Adsorption of Model Proteins: Design Parameters, Langmuir. 15 (1999) 2525–2533.

[150] Y. Liu, M.K. Shipton, J. Ryan, E.D. Kaufman, S. Franzen, D.L. Feldheim, Synthesis, stability, and cellular internalization of gold nanoparticles containing mixed peptide-poly(ethylene glycol) monolayers., Anal. Chem. 79 (2007) 2221–9.

[151] B.R. Pistillo, L. Detomaso, E. Sardella, P. Favia, R. d'Agostino, RF-Plasma Deposition and Surface Characterization of Stable (COOH)-Rich Thin Films from CyclicL-Lactide, Plasma Process. Polym. 4 (2007) S817–S820.

[152] K.T. Chong, X. Su, E.J.D. Lee, S.J.O. Shea, Polyethylene- co -acrylic Acid as Coating for Biosensor Application : A Quartz Crystal Microbalance Study, (2002) 9932–9936.

[153] S. Sano, K. Kato, Y. Ikada, Introduction of functional groups onto the surface of polyethylene for protein immobilization., Biomaterials. 14 (1993) 817–22.

[154] E.T. Kang, K.L. Tan, K. Kato, Y. Uyama, Y. Ikada, Surface Modification and Functionalization of Polytetrafluoroethylene Films, 9297 (1996) 6872–6879.

[155] D.Y. Cherny, B.P. Belotserkovskii, M.D. Frank-kamenetskii, M. Egholm, O.L.E. Buchardtf, R.H. Berg, et al., DNA unwinding upon strand-displacement binding of a thymine-substituted polyamide to double-stranded DNA, 90 (1993) 1667–1670.

[156] N. Zhang, D.H. Appella, Colorimetric detection of anthrax DNA with a Peptide nucleic acid sandwich-hybridization assay., J. Am. Chem. Soc. 129 (2007) 8424–5.

[157] J. Liu, S. Tian, L. Tiefenauer, P.E. Nielsen, W. Knoll, P.S. Institut, Simultaneously Amplified Electrochemical and Surface Plasmon Optical Detection of DNA Hybridization Based on Ferrocene - Streptavidin Conjugates Stv) conjugates for the simultaneously amplified electro- target hybridization to peptide nucleic acid-modifi, 77 (2005) 2756–2761.

[158] L.-Q. Chu, R. Förch, W. Knoll, Surface-plasmon-enhanced fluorescence spectroscopy for DNA detection using fluorescently labeled PNA as "DNA indicator"., Angew. Chem. Int. Ed. Engl. 46 (2007) 4944–7.

[159] R. D'Agata, R. Corradini, C. Ferretti, L. Zanoli, M. Gatti, R. Marchelli, et al., Ultrasensitive detection of non-amplified genomic DNA by nanoparticle-enhanced surface plasmon resonance imaging., Biosens. Bioelectron. 25 (2010) 2095–100.

[160] R. D'Agata, R. Corradini, G. Grasso, R. Marchelli, G. Spoto, Ultrasensitive detection of DNA by PNA and nanoparticle-enhanced surface plasmon resonance imaging., Chembiochem. 9 (2008) 2067–70.

[161] A.L. Boat, T.; Welsh, M.; Beaudet, Cystic fibrosis, 1989.

[162] D.H. Andersen, Cystic fibrosis of the pancreas and its relation to celiac disease: a clinical and pathological study, Am. J. Dis. Child. 56 (1938) 344–399.

[163] A. Kerem, B.S.; Rommens, J.M.; Buchanan, J.A.; Markiewicz, D.;Cox ,T.K.; Chakravarti, Identification of the cystic fibrosis gene: genetic analysis, Science (80-.). 245 (1989) 1073–1080.

[164] H. Nasef, V. Beni, C.K. O'Sullivan, Methylene blue as an electrochemical indicator for DF508 cystic fibrosis mutation detection., Anal. Bioanal. Chem. 396 (2010) 1423–32.

[165] S. et al. Rendine, Genetic history of cystic fibrosis mutations in Italy. I. Regional distribution, Ann. Humman Genet. 61 (1997) 411–424.

[166] L. Picci, M. Cameran, O. Marangon, D. Marzenta, S. Ferrari, A.C. Frigo, et al., A 10-year large-scale cystic fibrosis carrier screening in the Italian population., J. Cyst. Fibros. 9 (2010) 29–35.

[167] G. Feriotto, M. Lucci, N. Bianchi, C. Mischiati, R. Gambari, Detection of the Δ F508 (F508del) Mutation of the Cystic Fibrosis Gene by Surface Plasmon Resonance and Biosensor Technology, 400 (1999) 390–400.

[168] N. Saiki, R.K.; Scharf, S.; Faloona, F.; Mullis, K.B.; Horn, G.T.; Erlich, H.A.; Arnhein, Enzymatic amplification of Beta-globin genomic sequences and restriction site analysis for diagnosis of sickle cell anemia, Science (80-.). 230 (1985) 1350–1354.

[169] C.T. Ballabio, A.; Gibbs, R.A.; Caskey, PCR test for cystic fibrosis deletion, Nature. 343 (n.d.).

[170] L.-C. Ng, Y.S.; Pace, R.; Richard M.V.; Kobayashi, K.; Kerem, B.; Tsui, B. AL., Methods for analysis of multiple cystic fibrosis mutations, Hum. Genet. 87 (1991) 613–617.

[171] R.C.. D. Richards, B.; Skoletsky, J.; Shuber, A.P.; Balfour, R.; Stern, K.W. H.L.; Parad, R.B.; Witt, D.; Klinger, Multiplex PCR amplification from the CFTR gene using DNA prepared from buccal brushes/swabs, Hum. Mol. Genet. 2 (1993) 159–163.

[172] J. Chehab, F.F.; Wall, Detection of multiple cystic fibrosis mutations by reverse dot blot hybridization: a technology for carrier screening, Hum. Genet. 89 (1992) 163–168.

[173] R.P. Rommens, J.M.; Kerem, B.; Greer, W.; Chang, P.;, Tsui L-C, Rapid non radioactive detection of the major cystic fibrosis mutation, Hum. Gnetics. 46 (1990) 395–396.

[174] C.C. Grade, K.; Grunewald, I.; Graupner, I.; Beherens, F.;, Identification of three novel mutations in the CFTR gene using temperature-optimized non-radioactive conditions for SSCP analysis, Hum. Genet. 94 (1994) 154–158.

[175] T. Orita, M.; Iwahana, H.; Kanazawa, H.; Hayashi, K.; Sekiya, Dtection of polymorphisms of human DNA by gel electrophoresis as single-strand conformation polymorphisms, Natl Acad Sci USA. 86 (1989) 2766–2770.

[176] C. Ferec, C.; Audrezet, M.P.; Mercier, B.; Guillermit, H.; Moullier, P.; Quere, I.; Verlingue, Detection of over 98% cystic fibrosis mutations in a Celtic population, Nat. Genet. 1 (1992) 188–191.

[177] Y. Shoshani, T.; Augarten, A.; Gazit, E.; Bashan, N.; Yahav, Y.; Rivlin, K.B. Tal A, Seret H, Yaar L, Kerem E, Association of a nonsense mutation (W1282X), the most common mutation in the Ashkenazi Jewish Cystic Fibrosis patients in Israel, with presentation of severe disease, Am. J. Hum. Genet. 50 (1992) 222–228.

[178] J. Chehab, F.F.; Wall, Detection of multiple cystic fibrosis mutations by reverse dot blot hybridization: a technology for carrier screening, Hum. Genet. 89 (1992) 163–168.

[179] G. Feriotto, a Ferlini, a Ravani, E. Calzolari, C. Mischiati, N. Bianchi, et al., Biosensor technology for real-time detection of the cystic fibrosis W1282X mutation in CFTR., Hum. Mutat. 18 (2001) 70–81.

[180] G. Feriotto, R. Corradini, S. Sforza, N. Bianchi, C. Mischiati, R. Marchelli, et al., Peptide nucleic acids and biosensor technology for real-time detection of the cystic fibrosis W1282X mutation by surface plasmon resonance., Lab. Invest. 81 (2001) 1415–27.

[181] R. Corradini, G. Feriotto, S. Sforza, R. Marchelli, R. Gambari, Enhanced recognition of cystic fibrosis W1282X DNA point mutation by chiral peptide nucleic acid probes by a surface plasmon resonance biosensor., J. Mol. Recognit. 17 (2004) 76–84.

[182] D. Murphy, G. Redmond, Optical detection and discrimination of cystic fibrosis-related genetic mutations using oligonucleotide-nanoparticle conjugates., Anal. Bioanal. Chem. 381 (2005) 1122–9.

[183] P.-A. Nilsson, P.; Persson, B.; Larsson, A.; Uhlen, M.; Nygren, Detection of mutations in PCR products from clinical samples by surface plasmon resonance, J. Mol. Recognit. 10 (1997) 7–17.

[184] F. Lucarelli, G. Marrazza, M. Mascini, Design of an optimal allele-specific oligonucleotide probe for the efficient discrimination of a thermodynamically stable (G x T) mismatch., Anal. Chim. Acta. 603 (2007) 82–6.

[185] G. Castaldo, E. Rippa, G. Sebastio, V. Raia, P. Ercolini, G. de Ritis, et al., Molecular epidemiology of cystic fibrosis mutations and haplotypes in southern Italy evaluated with an improved semiautomated robotic procedure., J. Med. Genet. 33 (1996) 475–9.

[186] G. Castaldo, a Fuccio, C. Cazeneuve, L. Picci, D. Salvatore, V. Raia, et al., Detection of five rare cystic fibrosis mutations peculiar to Southern Italy: implications in screening for the disease and phenotype characterization for patients with homozygote mutations., Clin. Chem. 45 (1999) 957–62.

[187] Oligonucleotide property calculator - http://www.basic.northwestern.edu/biotools/oligocalc.html, (n.d.).

[188] L.M. Dorozhkin, V.A. Nefedov, A.G. Sabelnikov, V.G. Sevastjanov, Detection of trace amounts of explosives and / or explosive related compounds on various surfaces by a new sensing technique / material, 99 (2004) 568–570.

[189] 2012- Current trends in explosive detection techniques.pdf, (n.d.).

[190] L. Senesac, T.G. Thundat, Nanosensors for trace explosive detection, 11 (2008) 28–36.

[191] P.A. Pella, Measurement of the vapor pressures of TNT, 2,4-DNT, 2,6-DNT and EGDN, J. Chem. Thermodyn. 9 (1977) 301–305.

[192] K.G. Furton, L.J. Myers, The scientific foundation and efficacy of the use of canines as chemical detectors for explosives., Talanta. 54 (2001) 487–500.

[193] M.B. Pushkarsky, I.G. Dunayevskiy, M. Prasanna, A.G. Tsekoun, R. Go, C.K.N. Patel, High-sensitivity detection of TNT, (2006).

[194] A.R. Krause, C. Van Neste, L. Senesac, T. Thundat, E. Finot, Trace explosive detection using photothermal deflection spectroscopy, J. Appl. Phys. 103 (2008) 094906.

[195] L.. Pinnaduwage, T. Thundat, J.. Hawk, D.. Hedden, P.. Britt, E.. Houser, et al., Detection of 2,4-dinitrotoluene using microcantilever sensors, Sensors Actuators B Chem. 99 (2004) 223–229.

[196] A. Boisen, S. Dohn, S.S. Keller, S. Schmid, M. Tenje, Cantilever-like micromechanical sensors, Reports Prog. Phys. 74 (2011) 036101.

[197] J. Janni, B.D. Gilbert, R.W. Field, J.I. Steinfeld, Infrared absorption of explosive molecule vapors, 53 (1997) 1375–1381.

[198] Dual-SAM functionalization on integrated cantilevers for specific trace-explosive sensing and non-specific adsorption suppression, Nanotechnology. 18 (2007).

[199] C. Alexander, H.S. Andersson, L.I. Andersson, R.J. Ansell, N. Kirsch, I. a Nicholls, et al., Molecular imprinting science and technology: a survey of the literature for the years up to and including 2003., J. Mol. Recognit. 19 (2006) 106–80.

[200] G. Vasapollo, R. Del Sole, L. Mergola, M.R. Lazzoi, A. Scardino, S. Scorrano, et al., Molecularly imprinted polymers: present and future prospective., Int. J. Mol. Sci. 12 (2011) 5908–45.

[201] G. Guan, B. Liu, Z. Wang, Z. Zhang, Imprinting of Molecular Recognition Sites on Nanostructures and Its Applications in Chemosensors, Sensors. 8 (2008) 8291–8320.

[202] E.L. Holthoff, D.N. Stratis-Cullum, M.E. Hankus, A nanosensor for TNT detection based on molecularly imprinted polymers and surface enhanced Raman scattering., Sensors (Basel). 11 (2011) 2700–14.

[203] B.M. Riskin, R. Tel-vered, I. Willner, Imprinted Au-Nanoparticle Composites for the Ultrasensitive Surface Plasmon Resonance Detection of, (2010) 1387–1391.

[204] I. Kondepudi , D.; Prigogine, Modern Thermodynamics, 1998.

[205] S. Stephenson, R.; Malanowski, Handbook of the thermodynamics of organic compounds, New York, 1987.

[206] A.P. Gershanik, Y. Zeiri, Sublimation Rate of TNT Microcrystals in Air, (2010) 12403–12410.

[207] I. Langmuir, The adsorption of gases on plane surfaces of glass, mica and platinum, 16 (1918) 1361–1403.

[208] D. Duong D.; Do, Adsorption Analysis: Equilibria and Kinetics, 1998.

[209] O.M. Jakšić, Ž.D. Čupić, Z.S. Jakšić, D. V. Randjelović, L.Z. Kolar-Anić, Monolayer gas adsorption in plasmonic sensors: Comparative analysis of kinetic models, Russ. J. Phys. Chem. A. 87 (2013) 2134–2139.

[210] D.A. Prescott, L.M.; Harley, J.P.; Klein, Microbiology, Third, 1996.

[211] WHO Library Cataloguing-in-Publication Data, Legionella and the prevention of legionellosis, World Health Organization, 2007.

[212] P.S. Fraser, D W; Tsai, T R; Orenstein, W; Parkin, W E; Beecham, H J; Sharrar, R G; Harris, J; Mallison, G F; Martin, S M; McDade, J E; Shepard, C C; Brachman, Legionnaires' disease: description of an epidemic of pneumonia, N. Engl. J. Med. 297 (1977) 1189–97.

[213] D.L. Enrico, M.G. Manera, G. Montagna, F. Cimaglia, M. Chiesa, P. Poltronieri, et al., SPR based immunosensor for detection of Legionella pneumophila in water samples, Opt. Commun. 294 (2013) 420–426.

[214] B. Oh, Y. Kim, W. Lee, Y. Min, W. Hong, J. Choi, Immunosensor for detection of Legionella pneumophila using surface plasmon resonance, 18 (2003) 605–611.

[215] H. Lin, Y. Tsao, W. Tsai, Y. Yang, T. Yan, B. Sheu, Development and application of side-polished fiber immunosensor based on surface plasmon resonance for the detection of Legionella pneumophila with halogens light and 850 nm-LED, 138 (2007) 299–305.

[216] D.S. Regione Piemonte, Raccomandazioni per la sorveglianza, la prevenzione e il controllo delle polmoniti da Legionella nelle strutture sanitarie piemontesi pubbliche e private, 2005.

[217] I. J.A. Woollam Co., Ellipsometry solutions, n.d.

[218] H. Fujiwara, Spectroscopic Ellipsometry – Principles and Applications, 2007.

[219] M. Bass, Handbook of Optics, second, 1995.

[220] Z.L. Yao, N.; Wang, Handbook of Microscopy for Nanotechnology, 2005.

[221] B. Bhushan, Handbook of Nanotechnology, 2004.

Ringraziamenti

Al termine di questo dottorato di ricerca, passaggio molto importante per una crescita sia personale che scientifica ci tengo a ringraziare chi ha contribuito affinchè si realizzasse e si concludesse al meglio.

Prima di tutto ringrazio il mio supervisore, prof. Filippo Romanato, e con lui chi ha lavorato direttamente con me: la prof.ssa Margherita Morpurgo, Davide Silvestri, Gabriele Zacco, Gianluca Ruffato, Enrico Gazzola, Gioia della Giustina, Agnese Antognoli, Anna Meneghello ed Erica Cretaio. Ringrazio anche tutti gli altri colleghi di laboratorio e di dottorato, anche chi ha cambiato percorso.

Un grazie particolare va alla mia famiglia, supporto fondamentale in tutti questi anni, in particolare al nonno Silvio, il "nonno tecnologico", e alla zia che fino all'ultimo mi sono stati vicini e a cui ho pensato molto durante la scrittura della tesi.

Un grazie speciale va a Gianluca per il supporto e per avermi resa felice sempre, anche nei momenti più difficili.

Grazie anche alle amiche e agli amici tra cui in particolare Marta, Bianca, Verena, Maria Chiara, Valentina, Elisa, Stefano, Gabriele e Valeria. Non posso dimenticarmi della redazione di PLaNCK!, persone che da non molto occupano un grande posto nella mia vita.

Un grazie va anche a tutte le altre persone che hanno avuto e hanno tuttora un ruolo in quello che faccio; anche se il ruolo è piccolo, tutto è importante: GRAZIE!